frontiers | Research Topics

Learning-assisted diagnosis and control of electric distribution network

Edited by
Chaolong Zhang, Xiao Wang, Aihong Tang,
Weihang Yan and David Gao

Published in
Frontiers in Energy Research

ISSN 1664-8714
ISBN 978-2-8325-6523-0
DOI 10.3389/978-2-8325-6523-0

Generative AI statement
Any alternative text (Alt text) provided alongside figures in the articles in this ebook has been generated by Frontiers with the support of artificial intelligence and reasonable efforts have been made to ensure accuracy, including review by the authors wherever possible. If you identify any issues, please contact us.

About Frontiers

Frontiers is more than just an open access publisher of scholarly articles: it is a pioneering approach to the world of academia, radically improving the way scholarly research is managed. The grand vision of Frontiers is a world where all people have an equal opportunity to seek, share and generate knowledge. Frontiers provides immediate and permanent online open access to all its publications, but this alone is not enough to realize our grand goals.

Frontiers journal series

The Frontiers journal series is a multi-tier and interdisciplinary set of open-access, online journals, promising a paradigm shift from the current review, selection and dissemination processes in academic publishing. All Frontiers journals are driven by researchers for researchers; therefore, they constitute a service to the scholarly community. At the same time, the *Frontiers journal series* operates on a revolutionary invention, the tiered publishing system, initially addressing specific communities of scholars, and gradually climbing up to broader public understanding, thus serving the interests of the lay society, too.

Dedication to quality

Each Frontiers article is a landmark of the highest quality, thanks to genuinely collaborative interactions between authors and review editors, who include some of the world's best academicians. Research must be certified by peers before entering a stream of knowledge that may eventually reach the public - and shape society; therefore, Frontiers only applies the most rigorous and unbiased reviews. Frontiers revolutionizes research publishing by freely delivering the most outstanding research, evaluated with no bias from both the academic and social point of view. By applying the most advanced information technologies, Frontiers is catapulting scholarly publishing into a new generation.

What are Frontiers Research Topics?

Frontiers Research Topics are very popular trademarks of the *Frontiers journals series*: they are collections of at least ten articles, all centered on a particular subject. With their unique mix of varied contributions from Original Research to Review Articles, Frontiers Research Topics unify the most influential researchers, the latest key findings and historical advances in a hot research area.

Find out more on how to host your own Frontiers Research Topic or contribute to one as an author by contacting the Frontiers editorial office: frontiersin.org/about/contact

Learning-assisted diagnosis and control of electric distribution network

Topic editors

Chaolong Zhang — Jinling Institute of Technology, China
Xiao Wang — Wuhan University, China
Aihong Tang — Wuhan University of Technology, China
Weihang Yan — National Renewable Energy Laboratory (DOE), United States
David Gao — University of Denver, United States

Citation

Zhang, C., Wang, X., Tang, A., Yan, W., Gao, D., eds. (2025). *Learning-assisted diagnosis and control of electric distribution network*.
Lausanne: Frontiers Media SA. doi: 10.3389/978-2-8325-6523-0

Table of contents

frontiers | Frontiers in Energy Research

TYPE Editorial
PUBLISHED 17 June 2025
DOI 10.3389/fenrg.2025.1633454

OPEN ACCESS

EDITED AND REVIEWED BY
ZhaoYang Dong,
City University of Hong Kong, Hong Kong SAR, China

*CORRESPONDENCE
Xiao Wang,
xiaowang@whu.edu.cn

RECEIVED 22 May 2025
ACCEPTED 02 June 2025
PUBLISHED 17 June 2025

CITATION
Zhang C, Tang A, Wang X and Gao D (2025) Editorial: Learning-assisted diagnosis and control of electric distribution network. *Front. Energy Res.* 13:1633454. doi: 10.3389/fenrg.2025.1633454

Editorial: Learning-assisted diagnosis and control of electric distribution network

Chaolong Zhang[1], Aihong Tang[2], Xiao Wang[3]* and David Gao[4]

[1]College of Intelligent Science and Control Engineering, Jinling Institute of Technology, Nanjing, China, [2]School of Automation, Wuhan University of Technology Wuhan, Wuhan, China, [3]School of Electrical and Automation, Wuhan University, Wuhan, China, [4]Department of Electrical and Computer Engineering, University of Denver, Denver, CO, United States

KEYWORDS

state estimation, energy storage, electric distribution network, diagnostics and prognostics, robust control

Editorial on the Research Topic
Learning-assisted diagnosis and control of electric distribution network

The digital transformation of modern power systems establishes a robust digital foundation for enhanced system observability, operational transparency, and intelligent planning. This paradigm shift centers around harnessing big data resources spanning the entire energy value chain, from generation to end-user consumption (Channamallu et al., 2025). While low-voltage distribution networks face unprecedented challenges from the proliferation of renewable energy integration and electric vehicle penetration, emerging opportunities arise from ubiquitous sensing infrastructure and advanced control architectures (He et al., 2022). Artificial intelligence (AI) has emerged as a pivotal enabler to unlock the latent value of these multidimensional datasets, offering transformative solutions across critical domains including real-time fault diagnostics, adaptive control systems, and holistic grid optimization (Zhang, et al., 2023). The imperative for AI adoption becomes particularly pronounced in modern distribution networks, where escalating topological complexity and dynamic operating conditions necessitate proactive management frameworks and self-healing capabilities (Alam, et al., 2024). Conventional model-driven approaches, reliant on physical mechanism interpretation and static control paradigms, demonstrate inherent limitations in adapting to frequent network reconfigurations characteristic of distribution-level operations (Chen, et al., 2024). Nevertheless, direct implementation of existing AI/ML algorithms remains constrained by stringent power system requirements. Critical barriers including cybersecurity assurance, operational generalizability, model interpretability, out-of-distribution robustness, and fail-safe reliability must be systematically addressed prior to industrial-scale deployment. The demonstrated significance of Learning-assisted Diagnosis and Control of Electric Distribution Network has motivated the creation of this Research Topic to address its technical complexities.

The twelve contributed papers in this Research Topic can be categorized into four groups: Fault Diagnosis and Protection, Prediction and Estimation, Control and

Optimization and Voltage and Resonance Suppression. They can be summarized as follows.

Fault Diagnosis and Protection comprises 5 papers

Wu et al. proposed a fault diagnosis framework for distribution networks by integrating D-S evidence theory with Bayesian networks. The method categorizes relay protection and circuit breaker information into two Bayesian networks to calculate component failure probabilities via backward inference. These probabilities are fused using D-S theory to diagnose faulty components. Forward inference then identifies misoperations or rejections in protection devices. Case study validation demonstrates that the approach achieves enhanced diagnostic accuracy and reliability when addressing protection failures.

Li et al. introduced a fault identification method based on a mixture of von Mises-Fisher (mov-MF) distributions. Voltage phase angles from post-fault steady-state measurements form 3D feature vectors. The model is initialized via spherical K-means and optimized using expectation-maximization (EM) to refine parameters. IEEE 33-node system testing confirms the method's precise classification capability for single-phase (SP), two-phase (TP), and three-phase (3P) faults, demonstrating robust performance across multiple grid scenarios.

Duan developed a Transformer-GAN model for anomaly detection in AI-driven power systems. The architecture combines Transformer self-attention mechanisms with GANs to process complex sequential data, capturing dynamic patterns and unknown anomalies. Multi-dataset evaluation validates the model's 95.18% accuracy and 96.64% AUC with superior recall rates. Its robustness and adaptability highlight its potential for enhancing grid security and IoT integration.

Guo et al. designed the DSC-BiGRU-MAM framework for diagnosing faults in flexible converter valves. Depthwise separable convolution (DSC) extracts local features, while bidirectional GRUs model temporal dependencies. A multi-head attention module dynamically weights critical time intervals and channels, suppressing irrelevant features. Noisy environment testing reveals the model's 95.45% operational accuracy at 17,626 parameters and training time 935 s.

Wang et al. presented a differential protection scheme for grids with distributed generation. Whale optimization-enhanced feature mode decomposition processes zero-sequence current waveforms, while derivative dynamic time warping of the largest fault feature component solves distribution network grounding current differential protection issues. MATLAB simulations validated the method's ability to handle single-phase ground faults, ensuring stable operation under diverse fault conditions.

Estimation and Prediction includes 3 papers. Qian et al. proposed a fuzzy decision-making model for rapid equipment status assessment. Key indices from multi-source data are mapped to equipment scores using fuzzy iteration and XGBoost. The hybrid approach outperformed traditional methods in speed and accuracy, validated through distribution transformer case studies, enabling proactive maintenance.

Fang et al. created the Seasonal-Temporal Correlation Deep Forest (STC-DF) model for offshore wind speed prediction. The model autonomously learns seasonal and temporal patterns without manual feature engineering. Hainan wind farm data analysis demonstrates 40% error index of the corrected wind speed reduction and 15% prediction accuracy enhancement.

Zhang et al. integrated CNN and Kolmogorov-Arnold Networks (KAN) for lithium-ion battery SOH estimation. Multi-feature extraction during constant-voltage charging (e.g., current integrals, temperature trends) feeds into a CNN for feature selection, while KAN models nonlinear degradation. Experiments across charging rates yielded a good results, outperforming conventional methods in handling battery aging nonlinearity.

Control and Optimization consists of 3 papers. Li et al. optimized EV charging station stability using a fractional-order impedance model. A fractional PID controller, tuned via particle swarm optimization, enhanced virtual inertia and suppressed DC voltage oscillations. Experimental results showed 0.025s response time, 5% voltage deviation limits, and rapid inertia stabilization, ensuring grid resilience under high EV penetration.

Li et al. devised a cluster-based voltage control strategy for PV-rich distribution networks. An improved community algorithm divides nodes into reactive/active clusters based on power balance and coupling. PV inverters regulate voltage collaboratively, reducing overvoltage incidents in IEEE 69-node simulations and improving PV integration capacity.

Sun and Liao proposed the MARL-SOM-GNNs model for UAV cooperative grid inspections. Multi-agent reinforcement learning optimizes UAV coordination, self-organizing maps cluster inspection data, and graph neural networks analyze grid topologies. The framework achieved superior inspection accuracy and adaptability to environmental changes, setting benchmarks for autonomous infrastructure monitoring.

Voltage and Resonance Suppression contains 1 paper. Yonghao et al. investigated remanent magnetism's role in suppressing ferromagnetic resonance in 10 kV all-cable grids. A PSCAD model with UMEC-based voltage transformers simulated DC-induced residual magnetization. Results revealed positive magnetization effectively reduces PT inrush currents, while negative values exacerbate resonance. These findings guide grid design to enhance stability and prevent resonance risks.

Significant advancements have been achieved in the Learning-assisted Diagnosis and Control of Electric Distribution Network in recent years. However, these research accomplishments would not have been possible without the scholarly contributions of authors and the critical comments by reviewers. This Research Topic aims to illuminate emerging frontiers within the Learning-assisted Diagnosis and Control of Electric Distribution Network domain while formally recognizing dedicated efforts to address persistent technical challenges in the field.

Author contributions

CZ: Writing – original draft, Writing – review and editing, Conceptualization. AT: Investigation, Writing – original draft. XW: Writing – review and editing, Conceptualization. DG: Writing – review and editing.

Funding

The author(s) declare that financial support was received for the research and/or publication of this article. This work was supported by the major project of basic science (natural science) research in colleges and universities of Jiangsu Province Grant No. 23KJA480002; "Qinglan Project" for universities in Jiangsu Province; scientific research foundation for high-level personnel in Jinling Institute of Technology under Grant No. jit-rcyj-202202.

Conflict of interest

The authors declare that the research was conducted in the absence of any commercial or financial relationships that could be construed as a potential conflict of interest.

Generative AI statement

The author(s) declare that no Generative AI was used in the creation of this manuscript.

Publisher's note

All claims expressed in this article are solely those of the authors and do not necessarily represent those of their affiliated organizations, or those of the publisher, the editors and the reviewers. Any product that may be evaluated in this article, or claim that may be made by its manufacturer, is not guaranteed or endorsed by the publisher.

References

Alam, M., Hossain, M., Shafiullah, M., Islam, A., Choudhury, M., Faruque, M. O., et al. (2024). Renewable energy integration with DC microgrids: challenges and opportunities. *Electr. Power Syst. Res.* 234, 110548. doi:10.1016/j.epsr.2024.110548

Channamallu, S. S., Kermanshachi, S., Rosenberger, J. M., and Pamidimukkala, A. (2025). Smart parking systems: a comprehensive review of digitalization of parking services. *Green Energy and Intelligent Transportation*. 100293. doi:10.1016/j.geits.2025.100293

Chen, L., Xie, S., Lopes, A., Li, H., Bao, X., Zhang, C., et al. (2024). A new SOH estimation method for Lithium-ion batteries based on model-data-fusion. *Energy* 286, 129597. doi:10.1016/j.energy.2023.129597

He, H., Sun, F., Wang, Z., Lin, C., Zhang, C., Xiong, R., et al. (2022). China's battery electric vehicles lead the world: achievements in technology system architecture and technological breakthroughs. *Green Energy Intelligent Transp.* 1 (1), 100020. doi:10.1016/j.geits.2022.100020

Zhang, C., Zhao, S., Yang, Z., and He, Y. (2023). A multi-fault diagnosis method for lithium-ion battery pack using curvilinear Manhattan distance evaluation and voltage difference analysis. *J. Energy Storage* 67, 107575. doi:10.1016/j.est.2023.107575

frontiers | Frontiers in Energy Research

TYPE Original Research
PUBLISHED 15 March 2024
DOI 10.3389/fenrg.2024.1369880

OPEN ACCESS

EDITED BY
Weihang Yan,
National Renewable Energy Laboratory (DOE), United States

REVIEWED BY
Kenneth E. Okedu,
Melbourne Institute of Technology, Australia
Ma Jianjun,
Shanghai Jiao Tong University, China

*CORRESPONDENCE
Xin Song,
gohddin@163.com

RECEIVED 13 January 2024
ACCEPTED 05 March 2024
PUBLISHED 15 March 2024

CITATION
Wang L, Song X and Jiang W (2024), Differential protection scheme for distribution network with distributed generation based on improved feature mode decomposition and derivative dynamic time warping.
Front. Energy Res. 12:1369880.
doi: 10.3389/fenrg.2024.1369880

Differential protection scheme for distribution network with distributed generation based on improved feature mode decomposition and derivative dynamic time warping

Lei Wang[1], Xin Song[1]* and Weijian Jiang[2]

[1]College of Electrical Engineering, Shanghai University of Electric Power, Shanghai, China, [2]Jiaxing Power Supply Company of State Grid Zhejiang Electric Power, Jiaxing, China

With the progress of communication technology, the cost of optical fiber and 5G continues to decrease, and data transmission becomes more convenient and fast, making it possible to realize differential protection of distribution network by various intelligent algorithms using signal waveforms. Aiming at the problem that the traditional relay protection device can not meet the actual demand when the single-phase ground fault occurs in the distribution network with distributed generation, this paper proposes a new differential protection scheme. The characteristic mode decomposition improved by the whale optimization algorithm is used to decompose the zero-sequence current waveform collected at both ends of the line. Based on the basic principle of current differential protection, the derivative dynamic time warping of the component with the largest fault feature can effectively solve the problem that the grounding current of the distribution network cannot meet the working requirements of the differential protection device, and ensure the safe and stable operation of the system. Finally, based on MATLAB software, the performance of this method is comprehensively evaluated by simulating different fault conditions, so as to ensure the feasibility and accuracy of this method in the case of diversified faults when the distributed generation is used as part of the power supply.

KEYWORDS

distribution network, whale optimization algorithm(WOA), feature mode decomposition(FMD), derivative dynamic time warping(DDTW), differential protection

1 Introduction

With the access of distributed generation (DG), the power supply reliability and flexibility of the system are also improved, but the access of distributed generation in the distribution network will also affect the traditional relay protection, such as three-stage current protection. The fault detection of distribution network with distributed generation is currently facing: 1) Accurately locate the fault line; 2) Quickly remove the fault line; 3) Ensure that the fault is no longer overstepped to a higher level line; 4) Shorten the outage time and outage area (Zhixia et al., 2014).

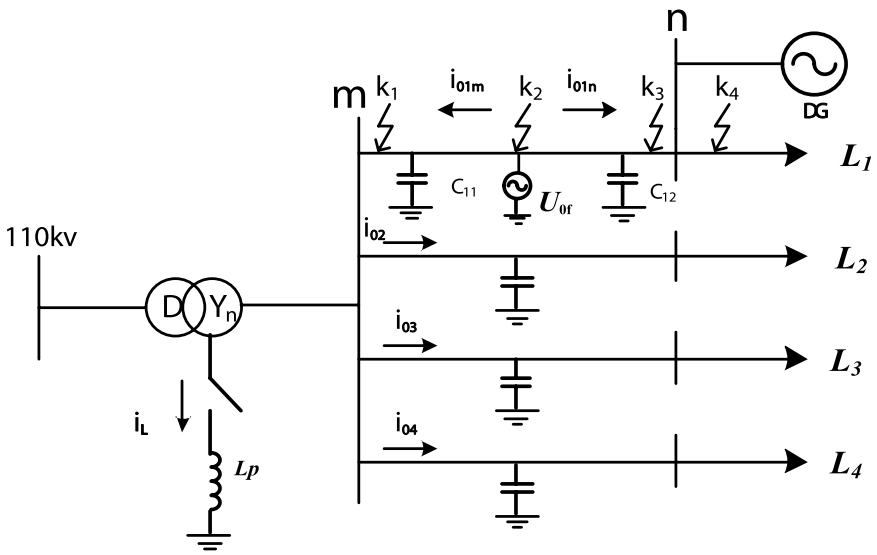

FIGURE 1
System zero-sequence equivalent network.

Initially, the research on single-phase grounding fault of distribution network can be roughly divided into three categories: signal injection methods, steady-state based methods, and transient-based methods. Signal injection methods involve the use of supplementary signal equipment, additional operations, or physical detection methods to identify faults (Wang et al., 2019), but this approach may introduce potential risks for power companies. Steady-state based methods have also been proposed for fault identification (Zhang et al., 2014). Nevertheless, these methods face challenges in terms of accuracy, it will be affected by many factors, including fault resistance (Lin et al., 2012), distance between fault point and measurement point (Liang et al., 2016), power system operation status (Ray and Mishra, 2016)and so on. Transient-based algorithms offer the advantage of fast fault identification. They allow for rapid fault detection, which is crucial in maintaining the stability and reliability of power systems (Linli et al., 2012). Although great progress has been made in the field of single-phase ground fault identification, there are still challenges to be solved for the distribution network with DG access. A Differential protection has good quickness and selectivity. It can quickly locate and isolate the fault point, narrow the power outage range, and apply it to the distribution network, which can effectively solve the above problems and improve the power supply reliability of the distribution network, so the application of differential protection in distribution network is more and more (Li and Lu, 2020). In Ref (Gao et al., 2021; Zhang et al., 2020), the differential protection criteria for distribution networks, which are based on the amplitude ratio of currents on both sides. However, it is important to note that the effectiveness of these proposed schemes may be compromised if the fault points are located in close proximity to the downstream DG. Ref (Ustun and Khan, 2015) proposes a differential protection scheme that only takes the amplitude of the current on both sides of the line as the criterion, but it is easy to misjudge in the system connected to the arc suppression coil by using only the amplitude protection. Ref (Gao et al., 2017) introduced a current differential protection scheme for active distribution network. The scheme combines the positive sequence fault component and the new implementation technology, which solves the problem of high penetration of distributed generators in the distribution network to a certain extent. However, this method is not sensitive to the response of single-phase ground fault in some cases. Ref (Chao et al., 2021; Chen et al., 2020) proposed a differential protection of distribution network based on impedance information. This method identifies faults by measuring voltage and current, and has strong robustness. Unfortunately, the coverage of voltage transformers in medium and low voltage distribution networks is not complete, which limits the application of the above methods that need to measure voltage. In Ref (Zhao et al., 2017) an ADN protection method based on the direction of the regional current is proposed. This method cannot accurately identify the fault location due to the output characteristics of the liquid cooler.

Based on the above analysis, this paper proposes a differential protection scheme for a distribution network considering DG. It analyzes the fault waveform by combining FMD and DDTW. Finally, the feasibility of the method is verified using simulation fault data. The main contributions of this paper are as follows:

1. To mitigate the impact of harmonic components on fault characteristic components during system faults, this paper introduces FMD for fault waveform decomposition. Given that FMD parameters require manual input and may entail errors, this study employs WOA to improve FMD for the first time and determine optimal parameters.
2. Under the premise of introducing FMD, DDTW is introduced, and the combination of FMD and DDTW is applied to the differential protection of distribution network for the first time to further enlarge the difference of fault characteristic components. Based on this, a differential protection scheme

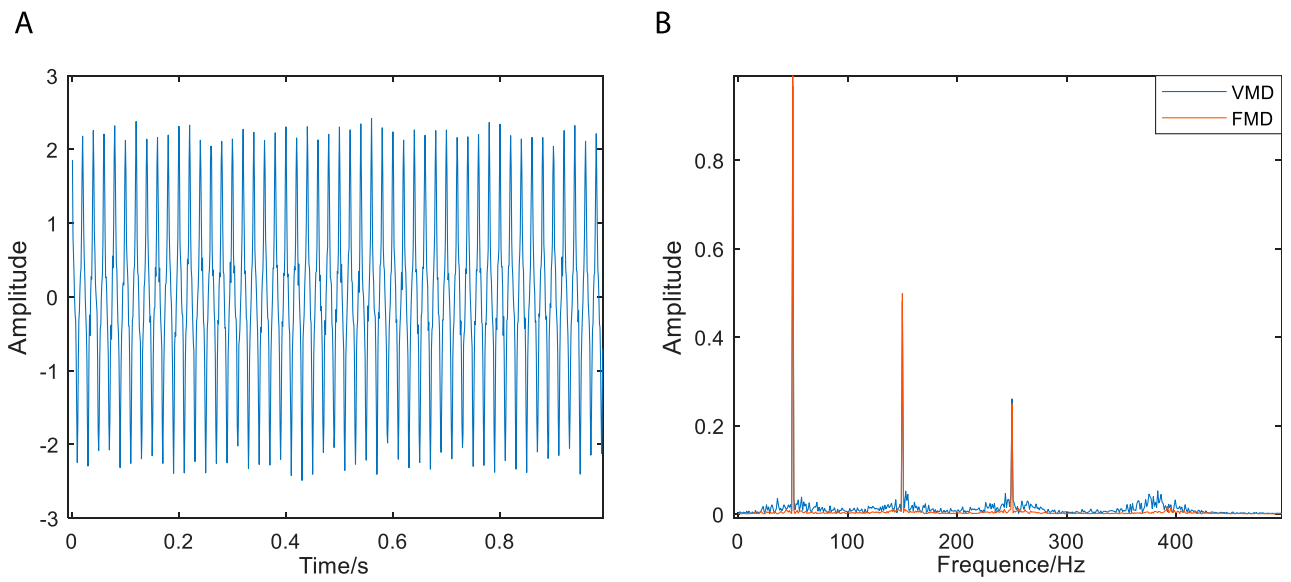

FIGURE 2
Experimental waveforms and comparison of two decomposition methods. **(A)** Experimental signals. **(B)** Comparison of the effects of the two decomposition methods.

for distribution network is formed, which can effectively improve the reliability of power supply.

3. The applicability and reliability of the proposed algorithm are verified by comparing different fault conditions considering the access of distributed generation and the exit of operation for some reason.

2 Principle analysis

2.1 Analysis of single-phase grounding fault in distribution network with distributed generation

Chinese distribution network is mostly a small current grounding system, the probability of single-phase ground fault is as high as 80% (Wang et al., 2018), for the system with large capacity of distributed power access, the traditional protection measures can not meet the needs of fast removal of fault lines. Differential protection is a common protection method, its basic principle is to compare the current waveforms of the equipment at both ends by measuring the current waveforms of the equipment at both ends. When the system is normal or an external fault occurs, the current waveforms at both ends are opposite; when a fault occurs in this section of the line, the phase of the fault current waveform at both ends is almost the same. After a single-phase grounding fault occurs in a small current grounding system, the transient characteristic quantity in the system is relatively rich, and the amplitude is several times larger than the steady-state current. The differential protection scheme composed of it can remove the fault line faster and more sensitively.

In this paper, the zero-sequence current at both ends of the line when a single-phase grounding fault occurs in the system is taken as the research object. The model of the distributed power system with neutral point grounded by arc suppression coil is adopted. The zero-sequence equivalent network is shown in Figure 1 when the internal fault occurs in the mn section of the line.

The small current grounding system shown in Figure 1 has four outlets. It is assumed that the line L_1 has a single-phase grounding fault on the mn-segment line, $k_1 \sim k_4$ is the location of the fault, Lp is the equivalent inductance of the arc suppression coil, i_L is the inductive current flowing through the arc suppression coil, U_{0f} is the zero-sequence voltage source, C_{11} and C_{12} are the capacitors at both ends of the mn-segment line on the line L_1, and DG is a large-capacity distributed generation.

Distributed generation is connected to the power distribution network at n point. When a single-phase grounding fault occurs in the distribution network, the connection of DG enhances the zero-sequence current (I_{0f}) that occurs during the fault (Coster et al., 2010). The mn section line is regarded as a double-ended power supply line. After the single-phase ground fault occurs, the current measured at the outlet of each line is:

$$3\dot{I}_{0f} = \dot{I}_C + \dot{I}_L = j\omega C_\Sigma 3\dot{U}_0 + \frac{\dot{U}_0}{j\omega L_P} \tag{1}$$

$$3\dot{I}_{0i} = \frac{\dot{U}_{AG}}{1/j\omega C_i} + \frac{\dot{U}_{BG}}{1/j\omega C_i} + \frac{\dot{U}_{CG}}{1/j\omega C_i} = j\omega C_i 3U_0 \tag{2}$$

$3\dot{I}_{0f}$ is the grounding current of the fault line, and $3\dot{I}_{0i}$ (i corresponds to the fault line $L_2 \sim L_4$ respectively) is the zero sequence current measured at the outlet side of the non-fault line. According to Figure 1 and Formula (2), the zero-sequence current flowing through the non-fault line is equal to its own capacitive current to the ground, and its direction flows from the bus to the line side; the zero sequence current flowing through the fault line is equal to the sum of the capacitance current to the ground of all non-fault

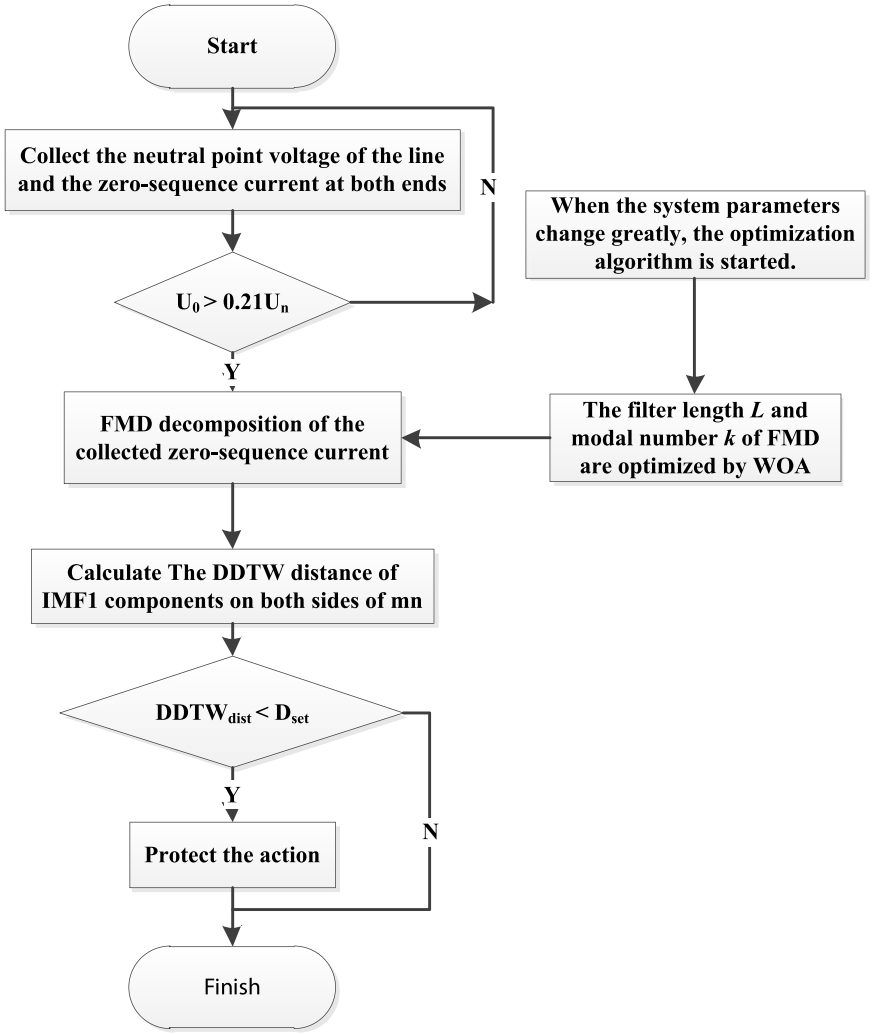

FIGURE 3
The flow chart of the new scheme.

TABLE 1 Line parameters.

Distribution line type	R_1/Ω	L_1/mH	$C_1/\mu F$	R_0/Ω	L_0/mH	$C_0/\mu F$
overhead lines	0.170	1.209	0.0097	0.23	3.906	0.008
cable	0.206	0.407	0.14	0.35	0.93	0.116

devices in the system and the phasor sum of the inductance current generated by the arc suppression coil, and its direction is also from the bus side to the line side.

When a single-phase ground fault occurs in line L_1, one end of each line in the system near the fault point will flow through the capacitive current generated by itself. These currents enter the fault line through the grounding point, and the zero-sequence currents on both sides of mn are in the same phase when the fault occurs in the mn section of the line, and in the opposite phase when the fault occurs outside the area. The zero-sequence current amplitude on the m side is related to the power supply size of the system, and the zero-sequence current amplitude on the n side is related to the size of the DG (Hussain et al., 2010). When a single-phase grounding fault occurs in the L_2 ~ L_4 section of the transmission line, it is an out-of-area fault relative to the mn section of the line. The phase of the zero-sequence current on both sides of the mn is opposite, the m side flows to the line, and the n side flows to the bus.

2.2 Feature mode decomposition

Feature Mode Decomposition (FMD) is designed as a non-recursive decomposition method (Miao et al., 2023). By initializing

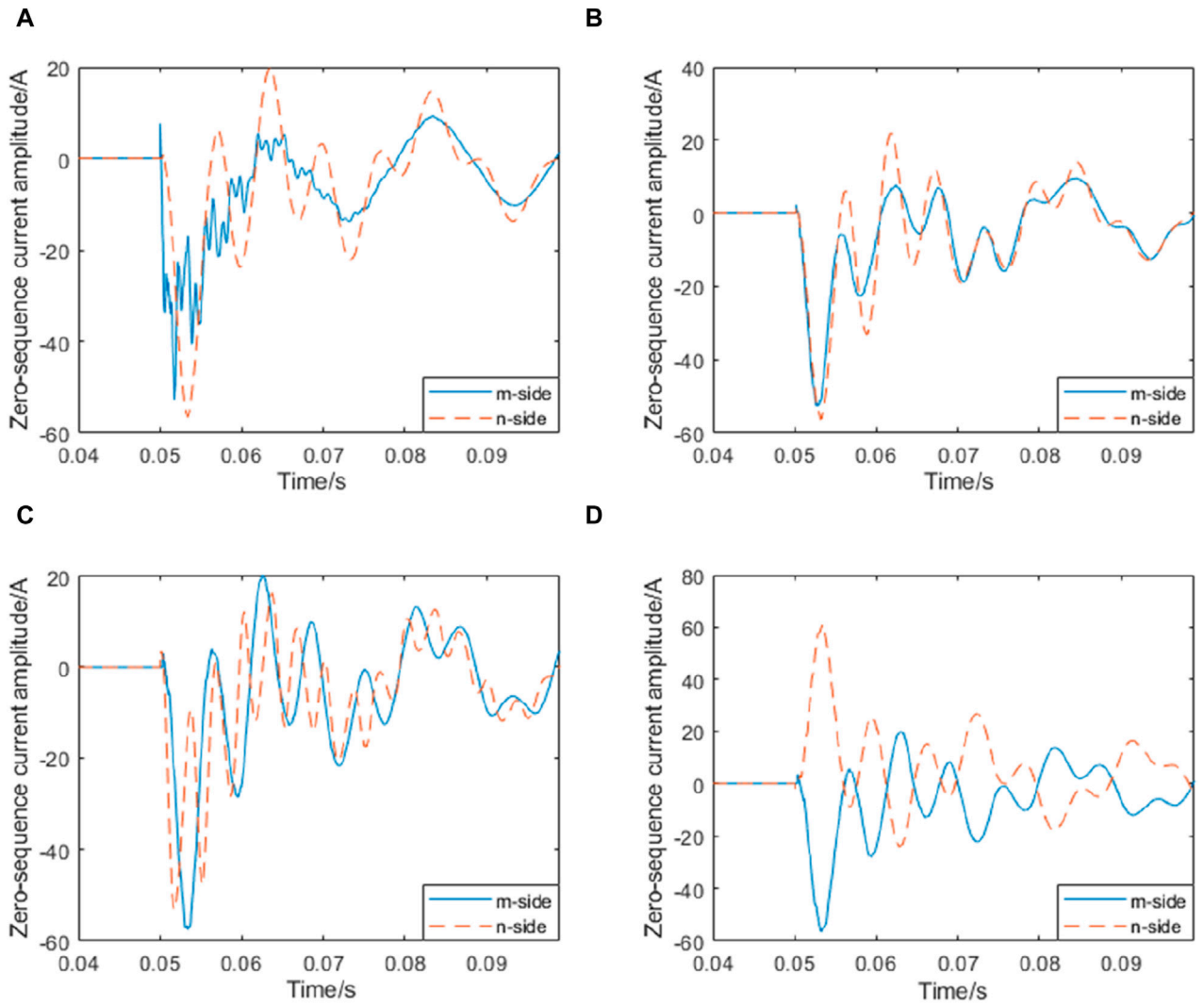

FIGURE 4
Zero-sequence current waveforms on both sides of the sin-gle-phase ground fault MN at different locations: **(A)** A fault occurs at k_1 **(B)** A fault occurs at k_2 **(C)** A fault occurs at k_3 **(D)** A fault occurs at k_4.

the FIR filter bank and updating the filter coefficients, different modes can be adaptively selected at the same time. The filtering process is inspired by the deconvolution theory, and the adaptive FIR filter is designed by iteratively updating the filter coefficient, so that the filtered signal infinitely approximates the deconvolution objective function. The filter is updated using CK as the objective function in FMD, and by comparing the correlation coefficient (CC) of each two modes, the smaller modes of CK are discarded from the two modes with the largest CC, and finally the decomposition is terminated when the termination condition is met. Using maximum CK deconvolution (IMCKD), the optimal FIR filter coefficient can be obtained without taking the failure period as a prior knowledge. IMCKD analog signals are used for processing to test the filtering performance of FIR filters with different initialization methods.

By labeling the original signal of length N as x(N), FMD theory becomes a solution to a constraint problem, expressed as:

$$\begin{aligned}\underset{\{f_k(l)\}}{\operatorname{argmax}}\Bigg\{ CK_M(\mathbf{u}_k) &= \sum_{n=1}^{N}\left(\prod_{m=0}^{M} u_k(n-mT_s)\right)^2 \\ &\Big/\left(\sum_{n=1}^{N} u_k(n)^2\right)^{M+1}\Bigg\} \\ \text{s.t. } u_k(n) &= \sum_{l=1}^{L} f_k(l)x\ \ (n-l+1)\end{aligned} \tag{3}$$

where u_k(n) is the kth decomposition mode. f_k is the kth FIR filter with a length of L, where Ts is the input period measured using the number of samples. M is the order of the shift. For the constraint problem in Equation 2, eigenmode decomposition is an iterative eigenvalue decomposition algorithm, and the decomposition method can be represented in matrix form.

$$\mathbf{u}_k = \mathbf{X}\mathbf{f}_k \tag{4}$$

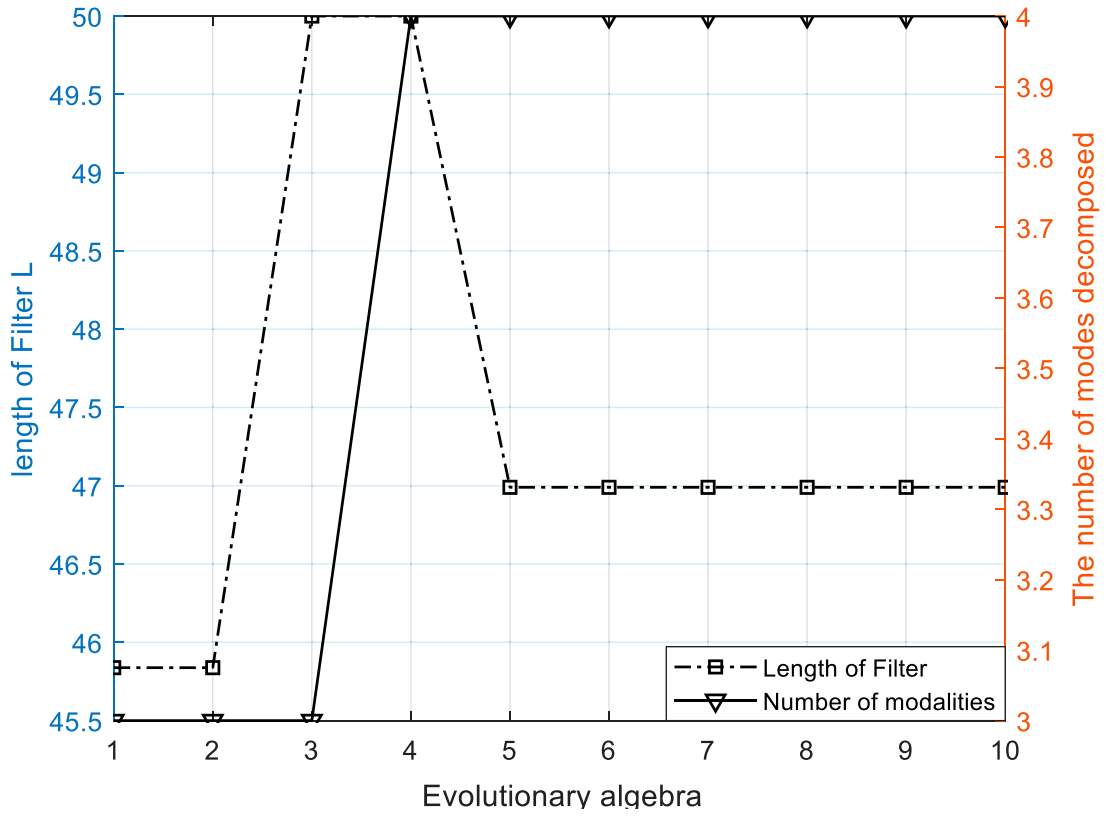

FIGURE 5
Filter length and modal decomposition number optimization curves.

$$\mathbf{u}_k = \begin{bmatrix} u_k[1] \\ \vdots \\ u_k[N-L+1] \end{bmatrix} \tag{5}$$

$$\mathbf{X} = \begin{bmatrix} x(1) & \cdots & x(L) \\ \vdots & \ddots & \vdots \\ x(N-L+1) & \cdots & x(N) \end{bmatrix} \tag{6}$$

$$\mathbf{f}_k = \begin{bmatrix} f_k(1) \\ \vdots \\ f_k(L) \end{bmatrix} \tag{7}$$

The CK of the decomposition mode can be defined as:

$$CK_M(\mathbf{u}_k) = \frac{\mathbf{u}_k^T \mathbf{W}_M \mathbf{u}_k}{\mathbf{u}_k^T \mathbf{u}_k} \tag{8}$$

$$\mathbf{W}_M = \begin{bmatrix} \left(\prod_{m=0}^{M} u_k[1-mT_s]\right)^2 & 0 & \cdots & 0 \\ 0 & \left(\prod_{m=0}^{M} u_k[2-mT_s]\right)^2 & & 0 \\ \vdots & & \ddots & \vdots \\ 0 & 0 & \cdots & \left(\prod_{m=0}^{M} u_k[N-L+1-mT_s]\right)^2 \end{bmatrix}^{\frac{1}{\sum_{n=1}^{N-L+1} u_k[n]^{M-1}}} \tag{9}$$

Superscript T is a conjugate transpose operation. W_M is used as an intermediate variable to control the weighted correlation matrix.

Substituting Equation 4 into Equation 8 yields:

$$CK_M(\mathbf{u}_k) = \frac{\mathbf{f}_k^T \mathbf{X}^T \mathbf{W}_M \mathbf{X} \mathbf{f}_k}{\mathbf{f}_k^T \mathbf{X}^T \mathbf{X} \mathbf{f}_k} = \frac{\mathbf{f}_k^T \mathbf{R}_{XWX} \mathbf{f}_k}{\mathbf{f}_k^T \mathbf{R}_{XX} \mathbf{f}_k} \tag{10}$$

Among them, R_{xwx} and R_{XX} are weighted correlation matrices and correlation matrices, respectively. Mathematically, (7) the maximization of the filter coefficients is equivalent to the eigenvectors associated with the maximum eigenvalue λ of the following generalized eigenvalue problem:

$$R_{XWX} f_k = R_{XX} f_k \lambda \tag{11}$$

Therefore, during the iteration, the kth filter coefficient will be updated by the solution of (8) so that it constantly approximates the set target, which is CK's maximum filtered signal.

The final mode will contain specific components from the original signal. FMD selects only the mode with the largest CK value. Therefore, if the FMD updates all initialized filters from start to finish, many patterns may contain the same components. To eliminate modal mixing or redundant modes, lock the mode with the largest CC first, because a higher CC means that both modes contain more of the same component. At the same time, in order to retain the mode with more fault information, among the two modes with the largest CC, the mode with smaller CK is abandoned, and the CC of the two modes of up and uq is defined as:

$$CC_{pq} = \frac{\sum_{n=1}^{N} \left(u_p(n) - \bar{u}_p\right)\left(u_q(n) - \bar{u}_q\right)}{\sqrt{\sum_{n=1}^{N} \left(u_p(n) - \bar{u}_p\right)^2} \sqrt{\sum_{n=1}^{N} \left(u_q(n) - \bar{u}_q\right)^2}} \tag{12}$$

where and are the averages of the mode U_P and U_Q, respectively.

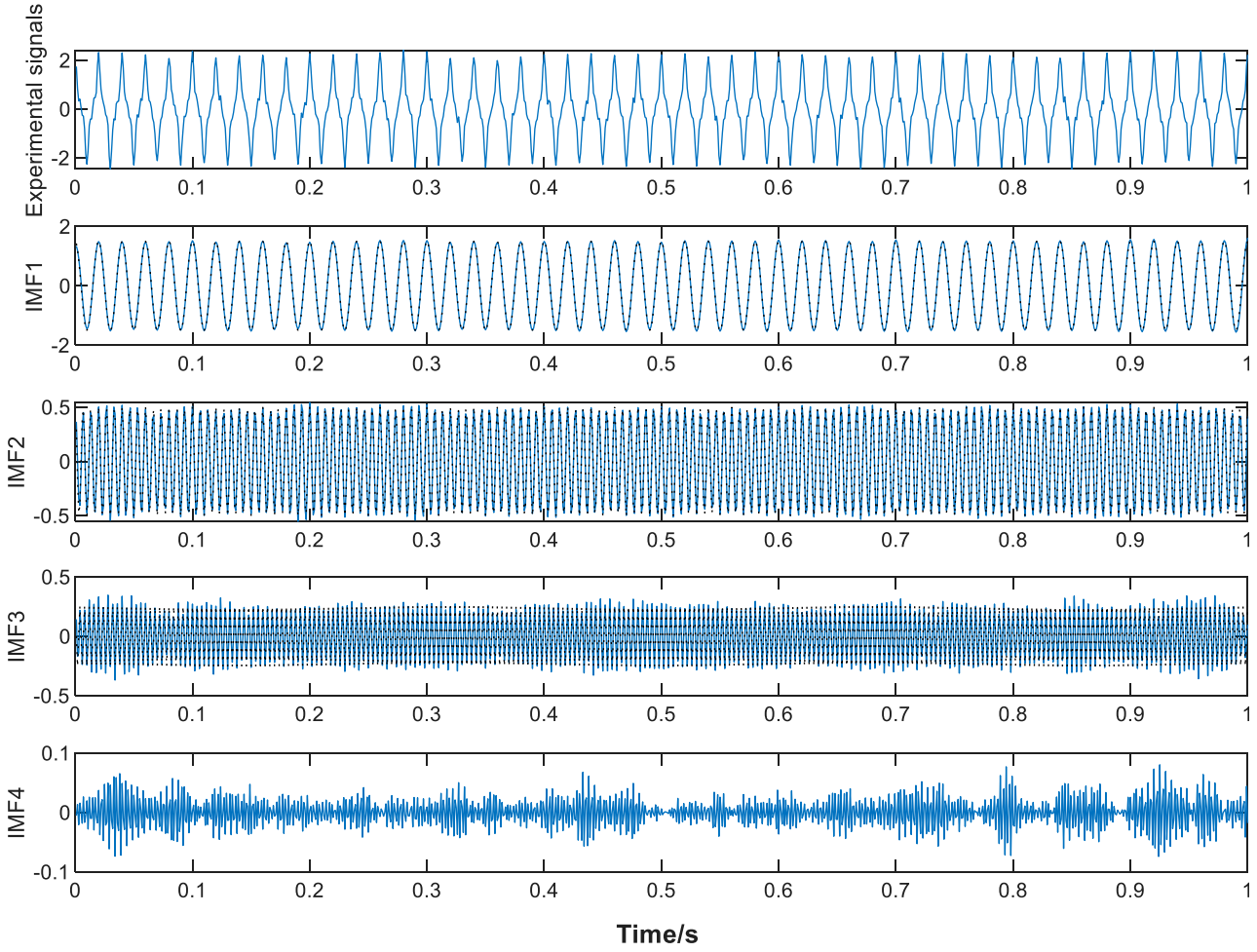

FIGURE 6
WOA-FMD processing results of experimental signals.

FMD uses filter update and period estimation, and adopts adaptive FIR filter to make component separation more thorough. Even in the face of complex faults, FMD can accurately decompose fault information. The theoretical waveform shown in Figure 2A is mainly composed of three frequency waveforms and white noise. When the modulus is set to 4, both VMD and FMD can extract the modes at each frequency. Figure 2B is the spectral information of the three effective components after the decomposition of the two methods.

In the spectrum of Figure (b), although the active ingredients can be extracted by the two decomposition methods, it is clear that the modal components of FMD are more concentrated and the filtering effect is better, compared with VMD, FMD filters are not limited by filter shape and bandwidth, have stronger adaptive ability, and can extract richer fault information. However, the proposed FMD still needs further improvement, and the input parameters such as modulus n and segment number K have a significant impact on the performance and efficiency of FMD.

2.3 Whale optimization algorithm

From the above FMD decomposition steps, it can be seen that signal decomposition needs to determine the appropriate modulus n, the number k of modal functions, and the filter length L. n affects the distribution of active components of each mode after decomposition; k is used to determine the number of segments used to split the frequency band, which needs to meet $k \geq n$, but a large value of k will cause computational redundancy; When the filter length L fluctuates within a suitable range, the choice of filter length has little effect on the filter performance. FMD itself is adaptive, can rely on the observation of the degree of separation of each mode to determine various parameters, but direct observation has a large error, so this paper uses the whale optimization algorithm (WOA) to sample entropy as the objective function to optimize the input parameters of FMD, its basic principle mainly includes three processes of rounding up prey, bubble net attack and searching for prey [26], briefly summarized as follows:

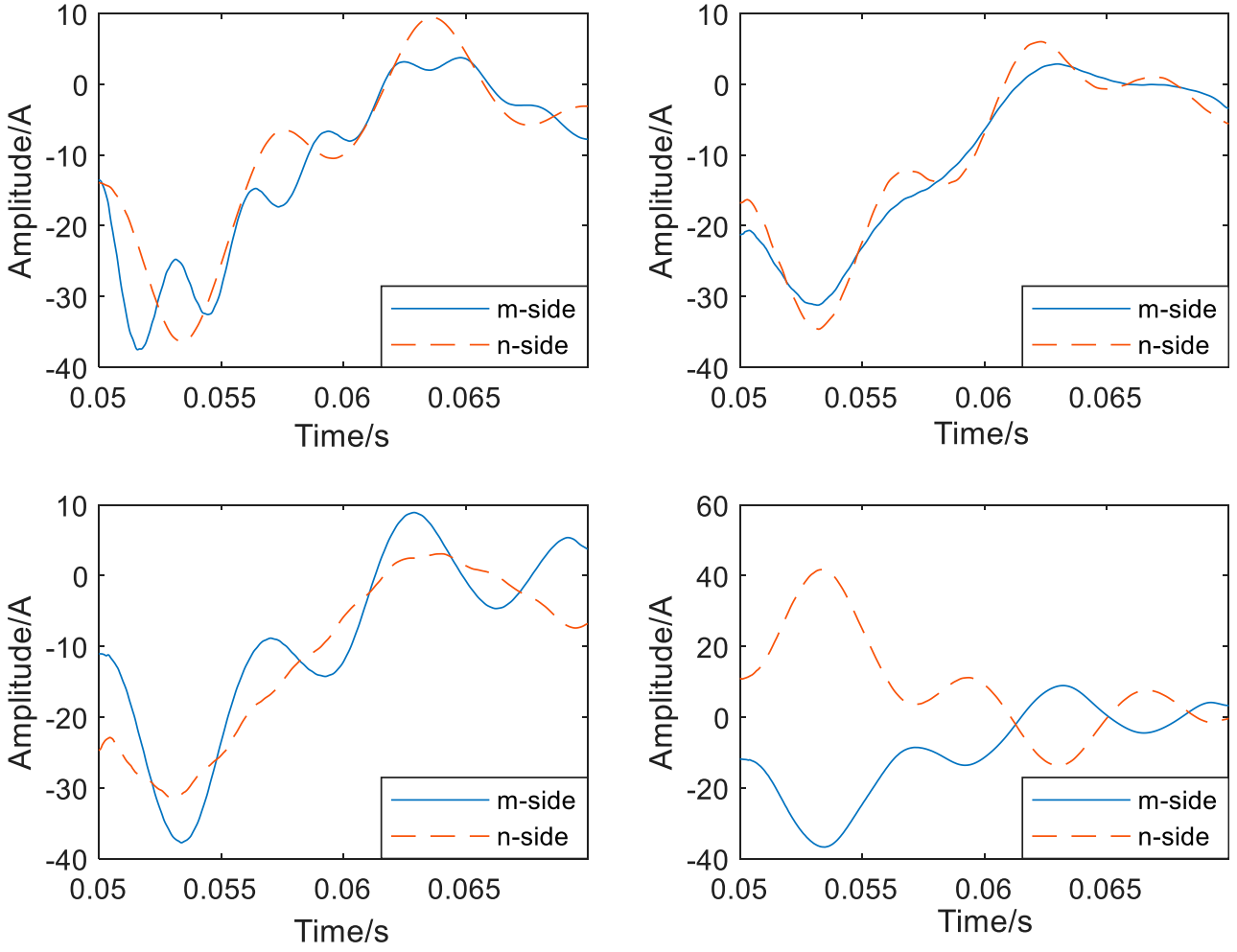

FIGURE 7
Zero-sequence current IMF1 component on both sides of mn.

(a) Rounding up prey: determine the optimal hunting individual, and the rest of the hunting individuals update the position to the optimal individual, the formula is embodied as:

$$D = |\mathbf{C}\mathbf{X}^{*}(t) - \mathbf{X}(t)| \tag{13}$$

$$\mathbf{X}(t+1) = \mathbf{X}^{*}(t) - \mathbf{A}D \tag{14}$$

Where $\mathbf{X}(t)$ is the position of each individual hunter, $\mathbf{X}^{*}(t)$ is the position of the determined optimal individual hunter, D represents the encirclement step, t is the number of iterations, and A and C are the coefficient vectors.

(b) Bubble net attack: Humpback whales have specific aggressive behavior when surrounding their prey, which is completed by forming unique bubbles along the spiral path, and the position of the individual is updated to:

$$\mathbf{X}(t+1) = D_1 e^{bl} \cos 2\pi l + \mathbf{X}^{*}(t) \tag{15}$$

$$D_1 = |\mathbf{X}^{*}(t) - \mathbf{X}(t)| \tag{16}$$

where is the distance between the current hunting individual and the optimal hunting individual, b is the spiral parameter of the path, and l takes a random value on [−1, 1].

(c) Search for prey: In the search stage, there is no optimal hunting individual in the whale, in order to ensure random distribution within the search range and ensure population diversity, appropriate adjustments need to be made:

$$\mathbf{X}(t+1) = X_{\text{rand}}(t) - \mathbf{A}\mathbf{D}_2 \tag{17}$$

$$D_2 = |CX_{\text{rand}}(t) - \mathbf{X}(t)| \tag{18}$$

where is the position of a random whale individual in the current population.

2.4 Derivative dynamic time warping

As shown in Figure 1, the zero-sequence current flow direction at both ends of the single-phase grounding fault in the mn section is different from that of the normal situation and the fault outside the mn section. Therefore, this paper intends to introduce a distance function, which can directly reflect the waveform difference between the two ends of the line, that is, the two sides of the mn.

Derivative dynamic time warping (DDTW) is a method used to compare and measure the similarity between two sequences.

TABLE 2 The DDTW values of the m-side and n-side of the distribution system with DG.

The location of the point of fault		Inside of the mn section line				Outside of the mn section line		
		k_1	k_2	k_3	k_4	Mid-point of L_2	Mid-point of L_3	Mid-point of L_4
single-phase grounding fault	Fault signal	39.0534	18.5081	46.9743	83.2170	83.5923	84.6548	81.5154
	VMD	26.8461	16.2546	37.5415	86.2984	87.5651	88.9984	83.1487
	FMD	21.3241	11.2039	26.8912	89.5347	89.6815	89.6519	89.1954
two-phase grounding fault	Fault signal	50.4562	42.3594	45.4963	80.1574	78.4889	79.6459	82.7852
	VMD	36.5418	35.2254	32.8441	82.5498	83.6598	85.3221	86.8415
	FMD	25.1125	19.6541	22.1187	88.4594	88.0549	89.6514	88.2565

When calculating the distance between time series, DDTW introduces the derivative information of time series to better capture the trend and change of time series. It can adaptively deal with the different scales of time series and improve the accuracy of similarity measurement, which is more suitable for studying the problems in this paper.

Taking the above Figure 1 system as an example, it is assumed that the time series of the current on both sides are i_1 (m side) and i_2 (n side), respectively. First, the two sequences need to be standardized:

$$A = \left\{ a = \frac{i_{1j} - \mu_{i_1}}{\sigma_{i_1}} \right\}, B = \left\{ b = \frac{i_{2j} - \mu_{i_2}}{\sigma_{i_2}} \right\} \tag{19}$$

In the formula: μ and σ are the mean and variance respectively, i_{1j} is the jth element in i_1 and i_{2j} is the jth element in i_2. The two normalized sequences are derived respectively:

$$A_i^{'} = \begin{cases} a_{i+1} - a_i & i = 1 \\ \dfrac{(a_i - a_{i-1}) + (a_{i+1} - a_{i-1})/2}{2} & 2 < i < l_a \\ a_i - a_{i-1} & i = l_a \end{cases} \tag{20}$$

$$B_j^{'} = \begin{cases} b_{j+1} - b_j & j = 1 \\ \dfrac{\left(b_j - b_{j-1}\right) + \left(b_{j+1} - b_{j-1}\right)/2}{2} & 2 < j < l_b \\ b_j - b_{j-1} & j = l_b \end{cases} \tag{21}$$

In the formula, $A_i^{'}$ and $B_j^{'}$ are the derivative sequences of A and B respectively, la and lb are the length of A and B respectively, a_i is the ith element in A and b_j is the jth element in B. Using the dynamic programming algorithm to calculate the cumulative distance matrix between the derivative sequences, we get:

$$D(i, j) = dist(i, j) + \min \begin{Bmatrix} D(i-1, j-1) \\ D(i-1, j) \\ D(i, j-1) \end{Bmatrix} \tag{22}$$

Here, $D(i, j)$ represents the minimum distance from the starting point (1, 1) to the position (i, j), and dist (i, j) is the distance function of the derivative sequence, which can be expressed by Euclidean distance. By backtracking the minimum distance matrix, the best matching path P between the derivative sequences is found. The starting point of the path is (1, 1), and the end point is (l_a, l_b), where l_a and l_b are the lengths of sequence A and B, respectively. According to the optimal path P, the DDTW distance $DDTW_{dist}$ between two time series A and B can be calculated:

$$DDTW_{dist} = \frac{1}{n} \sum_{i=1}^{n} \text{dist}(A_P, B_P) \tag{23}$$

Combined with the preceding analysis, it becomes evident that under perfect conditions, for faults outside the line area, if the current amplitude ratio on both sides is 1 and the phase difference is 180°, the $DDTW_{dist}$ value is 90. On the other hand, for internal faults, if the current amplitude ratio of both sides is 1 and the phase difference is 0°, the $DDTW_{dist}$ value is 0. When the phase fluctuation of signals on both sides of internal and external faults ranges within 20° and the amplitude ratio is within 1.2, the value range of $DDTW_{dist}$ for external faults can be determined using formula (23) as (76.54, 90), whereas the value range for internal faults is (0, 36.35). It is essential to provide a certain margin for the scheme's reliability. Therefore, the protection action boundary has been set to $D_{set} = 40$, and the protection braking value $D_{res} = 60$ to ensure timely and accurate triggering of the protection measures during actual operation and guarantee safe power system operation.

2.5 Protection process

Based on all above analysis, this paper proposes a new scheme of distribution network differential protection based on WOA-FMD analysis. Specifically, when a ground fault occurs in the system, it will lead to an increase in zero-sequence voltage. Consequently, by comparing the measured zero-sequence voltage with the standard zero-sequence voltage, it becomes feasible to ascertain the presence of a ground fault.

Using two common grounding faults as illustrations, in the event of single-phase grounding, the neutral sequence voltage escalates to the amplitude of the phase voltage. In cases of two-phase short-circuit grounding, the neutral sequence voltage rises to 0.5 times the amplitude of the phase voltage. Ordinarily, the neutral sequence voltage should ideally be maintained at zero during normal system operation; however, fluctuations in neutral sequence voltage triggered by other factors remain a possibility (Tang et al., 2021). In accordance with the specifications outlined in DL/T 620-1997"Overvoltage Protection and Insulation Coordination of AC

TABLE 3 Comparison of DDTW distances under different fault conditions.

Fault phase angle φ_k/(°)	R_g = 0		R_g = 20		R_g = 50		R_g = 100	
	Internal faults	External faults	Internal faults	External faults	Internal faults	External faults	Internal faults	External faults
0	11.2039	89.5347	13.0418	89.4120	10.8536	89.1287	15.4379	88.9265
30	14.5678	89.5687	12.1854	89.4532	13.9426	88.6783	16.4859	89.2354
45	13.4567	89.6578	16.4375	89.5498	14.7095	89.0985	16.2387	89.3209
60	16.4859	89.7543	15.9265	89.4876	17.8091	89.3645	20.6049	89.7609
75	16.7791	89.6578	17.3980	89.6932	18.0416	89.4298	19.9085	88.9823
90	20.1209	89.8654	24.5369	89.8614	22.3941	89.0698	28.2680	89.2484

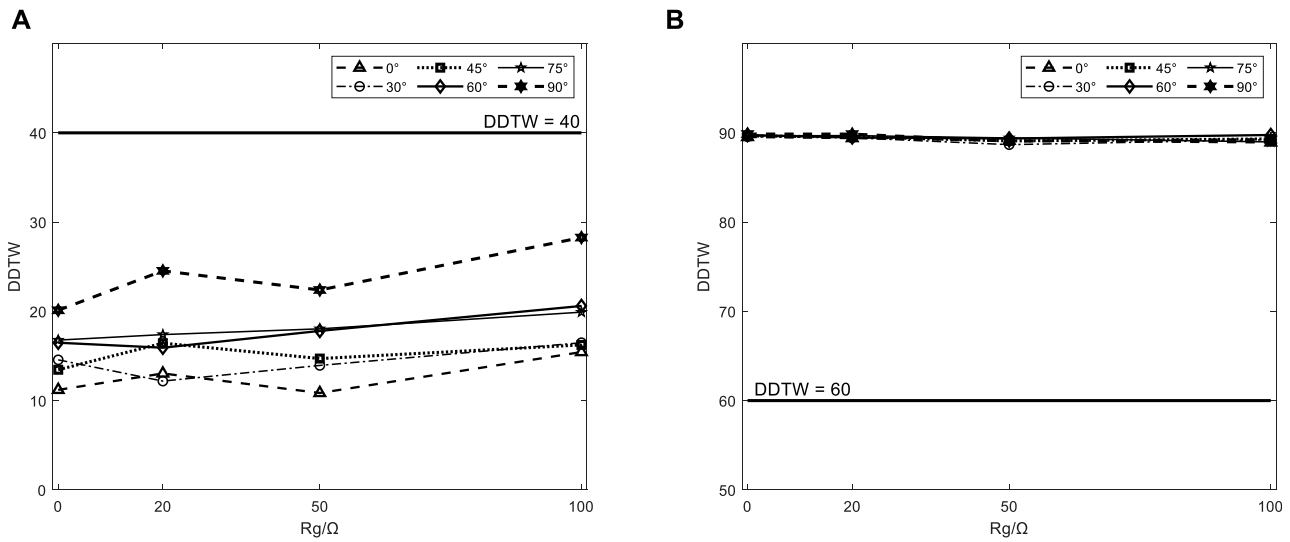

FIGURE 8
The trend of change in $DDTW_{dist}$. **(A)** internal faults. **(B)** external faults.

Electrical Equipment, " (Guo et al., 2022) the automatic tracking compensation arc suppression device must ensure that under normal operating conditions, the long-term voltage displacement of the neutral point does not surpass15% of the nominal phase voltage of the system. Therefore, when establishing the start-up value, it is imperative to account for these fluctuations, leading to the setting of the start-up value at 0.3 times the amplitude of the phase voltage, equivalent to $U_{on} = 0.21U_n$.

FMD can extract the fault feature components in waveform well. Considering the large error of parameter setting by human, WOA is used for parameter optimization for the first time in this paper, and DDTW is further used to establish a specific protection scheme. Through verification, it has been observed that significant parameter changes in the system have an impact on the optimal parameters of FMD, subsequently affecting the decomposition effect. Consequently, it becomes necessary for the WOA to update the FMD parameters when there are changes in the equipment's state within the system. This ensures the normal operation of the proposed scheme.

The specific steps of the protection scheme in this paper are as follows:

(1) According to the neutral voltage value to determine whether the system failure, if yes, start the whole algorithm;
(2) Once the algorithm is initiated, the optimized parameters obtained from the WOA are inputted into the FMD process. However, in cases where significant disturbances occur within the system, such as the switching of high-power equipment, it becomes necessary to restart the optimization algorithm. This ensures that the parameters L and k, crucial for accurate decomposition, are updated to reflect the current state of the system.
(3) The collected zero sequence current is decomposed by FMD to obtain each mode component.
(4) Calculate the DDTW value based on the maximum component of fault characteristics decomposed.
(5) According to the value of DDTW, determine whether this specific section of the power line under investigation is faulty, and act according to the judgment result.

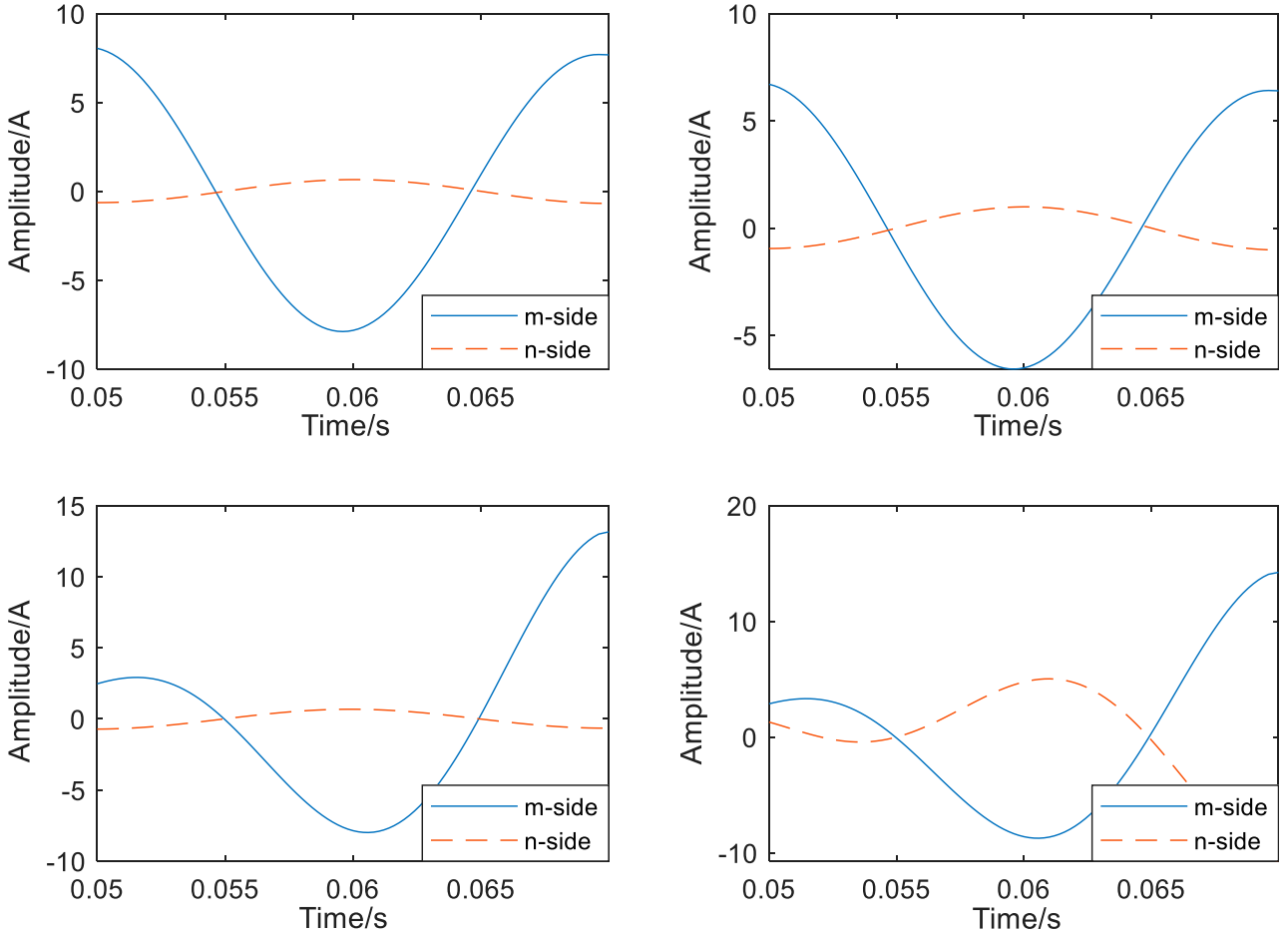

FIGURE 9
IMF1 components on both sides of mn when DG is out of operation.

TABLE 4 The DDTW values of m-side and n-side when DG is out of operation.

The location of the point of fault		k_1	k_2	k_3	k_4
single-phase grounding fault	Fault signal	29.9716	25.7198	31.4876	81.7098
	IMF1	19.0154	11.9012	22.0745	89.0654
two-phase grounding fault	Fault signal	31.5548	36.4851	32.8951	80.5444
	IMF1	18.1899	23.5158	21.3314	88.7141

The primary steps of the proposed protection scheme are depicted in Figure 3.

The distribution network system with DG will change the distribution of fault current under fault condition, and due to the compensation effect of arc suppression coil, the characteristics of system fault current are not obvious after single-phase grounding short-circuit fault occurs. The action value and braking value of traditional differential protection are not much different, and it is easy to produce no action. Therefore, the criterion proposed in this paper is based on the use of transient zero-sequence current, the improved FMD decomposes the fault signal, and finally uses DDTW to simplify the judgment. Compared with the traditional protection, it has better reliability and higher sensitivity.

3 Simulation verification

3.1 Fault waveform simulation

The experiment uses Simulink in Matlab to build a distributed power distribution network system model as shown in Figure 1, the line model adopts the Distributed Parameters Line model, a total of 4 outlets, line L_1 is set as overhead line, line L_2, L_3 is the cable line, feeder L_4 is the cable mixed line, the line length is different, where $L_1 = 30$ km, $L_2 = 15$ km, $L_3 = 20$ km, $L_4 = 40$ km. The line parameters are listed in Table 1. The transition resistance is set to 0, that is, the metal short circuit, the initial phase angle of the fault is 0°, the capacity of the distributed power supply is 1.5 MW, the arc

suppression coil is set to 10% overcompensation, and the inductance value is 1.05 H.

In order to fully study the influence of fault points in different locations on the criterion, this paper sets four single-phase ground faults at k_1~k_4 on line L_1 for verification (k_1, k_2 and k_3 are faults in the area, and k_4 is the fault outside the area); The impact of a two-ended power supply was prioritized and the simulation was validated with a single-ended power supply.

The zero-sequence current waveforms on both sides of the MN at different points of fault are shown in Figure 3:

As shown in Figure 4, the three figures (a)(b)(c) are the waveforms of the zero-sequence current on both sides of the mn when the fault occurs in the mn segment line, and the waveform phase is approximately the same, and (d) shows the waveform of the zero-sequence current on both sides of the mn when the fault occurs on the outside of the mn segment line, and the waveform phase is opposite.

3.2 Determine the setting value of the protection scheme

Firstly, the WOA algorithm is used to optimize the parameters of the theoretical signal constructed in section 1. 2, so as to optimize the noise reduction effect. The optimization process of the filter length L and the number of modal decomposition is shown as follows:

It can be seen from Figure 5 that when the number of modal decomposition reaches 4, it tends to be stable. If the selected value is too high, it may cause over-decomposition. Therefore, the optimal decomposition number k = 4 is selected, and the corresponding filter length L = 50 is selected. The two optimal parameters are input to perform FMD decomposition on the experimental signal. The effect is as follows:

The imaginary line in Figure 6 is the original harmonic signal of the experimental signal. The IMF1, IMF2 and IMF3 components are basically coincident with the experimental signal, and the decomposition effect is good. IMF4 contains the noise part.

The zero-sequence current on both sides of mn obtained by simulation is used as input for FMD decomposition. The waveform of the current components at both ends of mn after processing is shown in the figure:

Figure 7 is the IMF1 component of the zero-sequence current at both ends of the mn obtained by WOA-FMD decomposition. The original fault signal, VMD processing results on both sides of mn and FMD processing results are used to calculate the DDTW distance, and combined with other possible fault conditions, the value of $DDTW_{dist}$ when two-phase ground short circuit is considered. The results are shown in Table 2.

Based on the DDTWdist calculation values depicted in Table 2, it is evident that FMD excels in extracting fault characteristics and proficiently discerning fault scenarios that elude detection in the original fault signal. The experimental findings highlight the superior performance of the improved FMD compared to VMD, operating effectively within the designated braking and action thresholds. Furthermore, the improved FMD can also precisely identify two-phase ground faults, where DDTWdist < Dset in instances of internal faults, and DDTWdist > Dres in cases of external faults, demonstrating notable efficiency and accuracy.

3.3 The influence of transition resistance and fault starting angle on the protection scheme

The proposed protection scheme is verified by selecting a location to simulate a single-phase non-metallic short-circuit fault in the internal and external faults respectively: the midpoint of the mn line is selected in the zone, and the outlet side of the n point is selected outside the zone. The $DDTW_{dist}$ calculated by different transition resistance R_g (0–100Ω) and different fault initial angles when a short-circuit fault occurs is shown in Table 3. For the convenience of observation, the change trend of $DDTW_{dist}$ with Rg is made into the curve shown in the following Figure 8.

Each curve of the internal fault in Figure 8A varies greatly. Although the overall trend is on the rise, it does not exceed the action value, that is, the protection scheme has a certain resistance to transition resistance. The variation of each curve of the external fault is not large, and it is almost not affected by the transition resistance. When there is a fault in Figure 8B, there are differences between different curves but they can all act correctly. There is almost no difference between different curves when the fault occurs outside the fault zone, that is, the protection scheme is not affected by the fault starting angle.

Based on the above analysis, the protection scheme has a certain ability to withstand transition resistance, and is less affected by the fault starting angle. At the same time, because the value of the $DDTW_{dist}$ of the external fault is almost unchanged, the action value and the braking value can be adjusted appropriately according to the demand to ensure that the protection device can operate reliably.

3.4 The impact on the scheme when DG is out of operation

The above scheme is based on the single-phase ground short-circuit fault of the system during the normal operation of DG. Considering the situation when the distributed generation exits, the effectiveness of the scheme in the case of a single power supply system is guaranteed, and the proposed action value and braking value are verified by disconnecting the DG in the system. Taking the four positions of k_1 ~ k_4 as the fault point, the WOA-FMD decomposition of the zero sequence current components on both sides of the mn can obtain the result of Figure 9:

It can be seen from Figure 9 that the amplitude of the fault current in the distribution network system when DG exits is very small, and it is difficult to judge the phase relationship. The proximity of the traditional differential protection's braking and action values poses a risk of failure. This scheme proposed in this paper introduces a scheme that enhances the conventional standard by addressing its limitations. Through the calculation of $DDTW_{dist}$ for the IMF1 component derived from the WOA-FMD decomposition, Table 4 data can be obtained:

The data presented in Table 4 indicates that the DDTW distance calculation results of IMF1 components for two distinct fault types at both ends of mn are lower than the untreated values in the case of an internal fault, whereas they exceed the untreated values for an external fault. The substantial difference between these values is

evident, and the action conditions are met during an internal fault scenario. The significant deviation from the action value Dset enhances the effectiveness of protection actions. In a unilateral power supply system, the small amplitude of zero-sequence current on the non-powered side (n-side) may impact the protection mechanism. Consequently, verification is conducted using 24-point data samples from a single power supply at different time instances, ensuring a maximum error within ±2. This verification proves that the protection scheme is still unaffected, that is, this scheme is effective when DG exits operation.

4 Conclusion

In this paper, a differential protection algorithm based on WOA-FMD processing system zero-sequence current is proposed, which further amplifies the fault characteristics at both ends of the line through the proposed derivative dynamic time warping, and uses the obtained DDTW value to discriminate.

The scheme has a wide application range. In the distribution network with DG, the mn section line with this protection can be approximately equivalent to a two-terminal power supply network. Through simulation verification, this algorithm is also applicable to the distribution lines of ring network and double petal network, and the results are similar to those of DG system. In addition, the FMD and DDTW algorithms used in this paper reduce the dependence on synchronous sampling, have high reliability and strong anti-interference ability, and have significant advantages for the comparison of fault signals with large differences at both ends of the line. It can effectively improve the power supply reliability of the distribution network and solve the problem of protection misoperation caused by differential protection applied to the distribution network due to amplitude and other reasons. It has certain application prospects. However, the action value and braking value of the protection are obtained according to the simulation model. In order to ensure the accuracy of fault location, the specific setting value needs to be adjusted and optimized according to the actual distribution network parameters.

Data availability statement

The original contributions presented in the study are included in the article/supplementary materials, further inquiries can be directed to the corresponding author.

Author contributions

LW: Writing–review and editing. XS: Writing–original draft. WJ: Writing–review and editing.

Funding

The author(s) declare that financial support was received for the research, authorship, and/or publication of this article. National Natural Science Foundation of China (61873159); State Grid Zhejiang Electric Power Co., Ltd. Science and Technology Project (5211TZ220002). The funder was not involved in the study design, collection, analysis, interpretation of data, the writing of this article, or the decision to submit it for publication.

Conflict of interest

Author WJ was employed by Jiaxing Power Supply Company of State Grid Zhejiang Electric Power.

The remaining authors declare that the research was conducted in the absence of any commercial or financial relationships that could be construed as a potential conflict of interest.

Publisher's note

References

Chao, C. X., Zheng, X. D., Gao, P., Tang, L., and Tu, Q. (2021). High frequency impedance differential protection with high proportion of photovoltaic power distribution network. *Proc. CSEE* 41 (12), 6968–6979. doi:10.13334/j.0258-8013.pcsee.201516

Chen, G., Liu, Y., and Yang, Q. (2020). Impedance differential protection for active distribution network. *IEEE Trans. Power Del.* 35 (1), 25–36. doi:10.1109/tpwrd.2019.2919142

Coster, E. J., Myrzik, J. M. A., Kruimer, B., and Kling, W. L. (2010). Integration issues of distributed generation in distribution grids. *Proc. IEEE* 99 (1), 28–39. doi:10.1109/jproc.2010.2052776

Gao, H., Li, J., and Xu, B. (2017). Principle and implementation of current differential protection in distribution networks with high penetration of DGs. *IEEE Trans. Power Deliv.* 32 (1), 565–574. doi:10.1109/tpwrd.2016.2628777

Gao, Y., Li, Y., Chen, X., Zhao, Z., Wang, Q., and Ren, J. (2021). Adaptive differential protection principle based on current amplitude ratio. *Proc. CSU-EPSA* 33 (2), 1–7. doi:10.19635/j.cnki.csu-epsa.00054

Guo, M.-F., Cai, W.-Q., Zheng, Z.-Y., and Wang, H. (2022). Fault phase selection method based on single-phase flexible arc suppression device for asymmetric distribution networks. *IEEE Trans. Power Deliv.* 37 (6), 4548–4558. doi:10.1109/tpwrd.2022.3150914

Hussain, B., Sharkh, S. M., Hussain, S., and Abusara, M. A. (2010). "Integration of distributed generation into the grid: protection challenges and solutions," in Proc. 10th IET Int. Conf. Develop. Power Syst. Protect. Manag. Change, Manchester, UK, March, 2010, 1–5.

Li, X., and Lu, Y. (2020). 'Improved amplitude differential protection scheme based on the frequency spectrum index for distribution networks with DFIGbased wind DGs. " *IEEE Access* 8, 64225–64237. doi:10.1109/access.2020.2984031

Liang, R., Wang, F., Fu, G., Xue, X., and Zhou, R. (2016). A general fault location method in complex power grid based on wide-area traveling wave data acquisition. *Int. J. Elect. Power Energy Syst.* 83, 213–218. doi:10.1016/j.ijepes.2016.04.021

Lin, X., Zhao, F., Wu, G., Li, Z., and Weng, H. (2012). Universal wavefront positioning correction method on traveling-wave-based fault-location algorithms. *IEEE Trans. Power Del.* 27 (3), 1601–1610. doi:10.1109/tpwrd.2012.2190108

Lin, Z., Ruan, X., Wu, L., Zhang, H., and Li, W. (2020). Multi resonant component-based grid-voltage-weighted feedforward scheme for grid-connected inverter to suppress the injected grid current harmonics under weak grid. *IEEE Trans. Power Electron.* 35 (9), 9784–9793. doi:10.1109/tpel.2020.2970514

Linli, Z., Houlei, G., Bingyin, X., and ongduan, X. Y. (2012). "Fault location method based on zero sequence admittance measurement in non-effectively earthed system," in Proc. IEEE PES Innov. Smart Grid Technol., Tianjin, China, May, 2012, 1–4.

Miao, Y., Zhang, B., Li, C., Lin, J., and Zhang, D. (2023). Feature mode decomposition: new decomposition theory for rotating machinery fault diagnosis. *IEEE Trans. Industrial Electron.* 70 (2), 1949–1960. doi:10.1109/tie.2022.3156156

Ray, P., and Mishra, D. P. (2016). Support vector machine based fault classification and location of a long transmission line. *Eng. Sci. Technol. Int. J.* 19 (3), 1368–1380. doi:10.1016/j.jestch.2016.04.001

Tang, J., Xiong, B., Li, Y., Yuan, C., and Qiu, Y. (2021). Faulted feeder identification based on active adjustment of arc suppression coil and similarity measure of zero-sequence currents. *IEEE Trans. Power Deliv.* 36 (6), 3903–3913. doi:10.1109/tpwrd.2021.3051040

Ustun, T. S., and Khan, R. H. (2015). Multiterminal hybrid protection of microgrids over wireless communications network. *IEEE Trans. Smart Grid* 6 (5), 2493–2500. doi:10.1109/tsg.2015.2406886

Wang, P., Zhou, H., Chen, B., Tian, C., Chen, B., and Sun, B. (2019). Fault location method in resonant grounded networks based on distributed modulation and compensation adjustment. *IEEE Trans. Power Del.* 34 (5), 1938–1947. doi:10.1109/tpwrd.2018.2883352

Wang, X., Gao, J., Chen, M., Wei, X., Wei, Y., and Zeng, Z. (2018). Faulty line detection method based on optimized bistable system for distribution network. *IEEE Trans. Industrial Inf.* 14 (4), 1370–1381. doi:10.1109/tii.2017.2753227

Zhang, X., Ma, X., Zhang, L., Wang, Z., Lin, X., Li, Z., et al. (2020). Novel current amplitude differential protection criterion for line with unmeasurable branch in active distribution network. *Electr. Power Autom. Equip.* 40 (2), 76–84. doi:10.16081/j.epae.202001006

Zhang, Z., Liu, X., and Piao, Z. (2014). Fault line detection in neutral point ineffectively grounding power system based on phase-locked loop. *IET Gener. Transm. Distrib.* 8 (2), Feb. doi:10.1049/iet-gtd.2013.0235

Zhao, S., Tang, T., Wang, D., Gao, R., and Wu, Z. (2017). "Active distribution network protection scheme based on area current direction," in Proc. China Int. Electr. Energy Conf. (CIEEC), Beijing, China, October, 2017, 247–251.

Zhixia, Z., Xiao, L., and Zailin, P. (2014). Fault line detection in neutral point ineffectively grounding power system based on phase-locked loop. *IET Gener. Transm. Distrib.* 8 (2), 273–280. doi:10.1049/iet-gtd.2013.0235

frontiers | Frontiers in Energy Research

TYPE Original Research
PUBLISHED 15 March 2024
DOI 10.3389/fenrg.2024.1364456

OPEN ACCESS

EDITED BY
Weihang Yan,
National Renewable Energy Laboratory (DOE), United States

REVIEWED BY
Thi-Thu-Huong Le,
Pusan National University, Republic of Korea
Bochao Zhao,
Tianjin University, China
Xiren Miao,
Fuzhou University, China

*CORRESPONDENCE
Jing Duan,
catduanjing@163.com

RECEIVED 02 January 2024
ACCEPTED 26 February 2024
PUBLISHED 15 March 2024

CITATION
Duan J (2024), Deep learning anomaly detection in AI-powered intelligent power distribution systems.
Front. Energy Res. 12:1364456.
doi: 10.3389/fenrg.2024.1364456

Deep learning anomaly detection in AI-powered intelligent power distribution systems

Jing Duan*

State Grid Information and Telecommunication Co., of SEPC, TaiYuan, China

Introduction: Intelligent power distribution systems are vital in the modern power industry, tasked with managing power distribution efficiently. These systems, however, encounter challenges in anomaly detection, hampered by the complexity of data and limitations in model generalization.

Methods: This study developed a Transformer-GAN model that combines Transformer architectures with GAN technology, efficiently processing complex data and enhancing anomaly detection. This model's self-attention and generative capabilities allow for superior adaptability and robustness against dynamic data patterns and unknown anomalies.

Results: The Transformer-GAN model demonstrated remarkable efficacy across multiple datasets, significantly outperforming traditional anomaly detection methods. Key highlights include achieving up to 95.18% accuracy and notably high recall and F1 scores across diverse power distribution scenarios. Its exceptional performance is further underscored by achieving the highest AUC of 96.64%, evidencing its superior ability to discern between normal and anomalous patterns, thereby reinforcing the model's advantage in enhancing the security and stability of smart power systems.

Discussion: The success of the Transformer-GAN model not only boosts the stability and security of smart power distribution systems but also finds potential applications in industrial automation and the Internet of Things. This research signifies a pivotal step in integrating artificial intelligence into the power sector, promising to advance the reliability and intelligent evolution of future power systems.

KEYWORDS

intelligent power distribution system, deep learning, abnormal detection, time series data, transformer-GAN

1 Introduction

In today's energy field, smart power distribution systems, as a key component of power grid modernization, shoulder the important task of achieving efficient and reliable power supply Zhang et al. (2022a). With growing energy demands and rapid technological advances, the complexity of these systems is increasing. In this context, anomaly detection has become one of the core issues to ensure the stable operation of the system. Anomaly detection refers to identifying deviations from normal operating patterns in power systems Karkhaneh and Ozgoli (2022). These anomalies may be caused by equipment failure, operational errors, or external factors such as natural disasters Calvo-Bascones et al. (2023). Although anomaly detection is critical to prevent power outages and maintain system

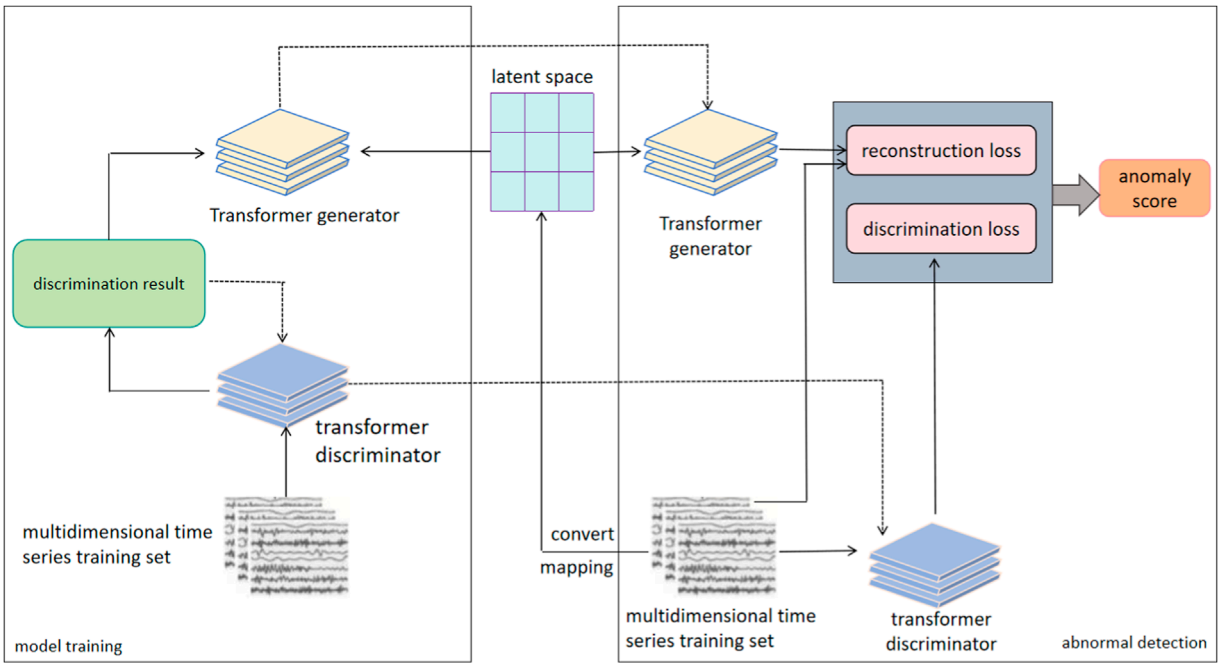

FIGURE 1
The network architecture of Transformer-GAN. Dashed connections represent the transfer of information flow or data flow.

integrity, implementing it in smart power distribution systems presents many challenges. These challenges include the high dimensionality of the data, complex system dynamics, and the diversity of abnormal patterns.

Deep learning, as a powerful machine learning tool, has been widely used in anomaly detection research in smart power distribution systems Xiong et al. (2022). Deep learning algorithms are able to process large amounts of data and extract complex features from it, which makes them particularly suitable for handling the high dimensionality and complexity of power system data de Oliveira and Bollen (2023). In addition, time series prediction technology is particularly important in the field of anomaly detection in smart power distribution systems. This is because power system data are essentially time series data, with characteristics and anomaly patterns evolving over time Cascone et al. (2023). Time series forecasting allows researchers to not only identify current anomalies, but also predict possible anomalies in the future, thereby taking steps in advance to prevent potential failures or disruptions Xia et al. (2022). This plays a vital role in ensuring system reliability and efficiency. By analyzing and predicting time series data through deep learning models, researchers can more accurately identify and respond to abnormal states in the power system, thus promoting the development of smart power distribution systems to a higher level Ahmad et al. (2022); Zhao et al. (2022). In this article, we will explore in detail anomaly detection methods in smart power distribution systems, especially the application of deep learning and time series forecasting, and discuss how these techniques can help solve current challenges.

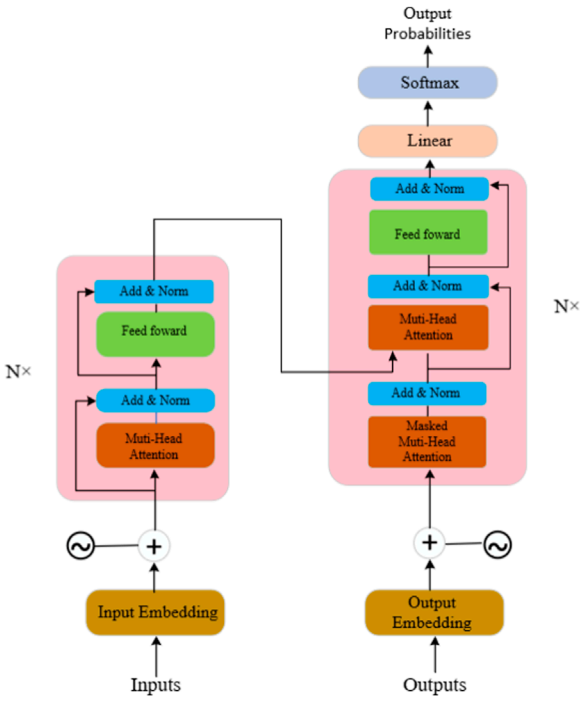

FIGURE 2
The network architecture of Transformer.

In recent years, many researchers have made significant progress in the field of anomaly detection in smart power distribution systems. For example, researchers have proposed a model based on convolutional neural networks (CNN), which can effectively process and analyze time series data of power systems. This method utilizes the powerful feature extraction capabilities of CNN

TABLE 1 The comparison of different models in different indicators comes from the Smart Grid, AMI, Smart Meter, and Pecan Street dataset.

Model	Datasets															
	Smart grid dataset				AMI dataset				Smart meter datase				Pecan street dataset			
	Accuracy	Recall	F1 sorce	AUC	Accuracy	Recall	F1 sorce	AUC	Accuracy	Recall	F1 sorce	AUC	Accuracy	Recall	F1 sorce	AUC
Alam et al. (2022)	89.21	88.01	85.08	94.65	89.20	92.07	84.07	92.53	95.50	92.33	87.20	89.17	85.08	86.77	87.73	90.44
Wang et al. (2023)	86.98	87.32	87.10	92.20	96.10	90.07	89.20	83.30	95.18	92.10	88.12	95.60	95.63	87.52	90.09	87.73
Yin et al. (2022)	91.02	89.00	88.42	92.49	93.20	93.53	92.98	89.21	84.87	85.53	88.97	84.06	92.73	84.90	85.31	93.78
Liao et al. (2022)	89.01	92.93	86.53	86.53	88.53	86.53	85.21	89.37	93.60	91.54	89.22	89.38	87.01	89.53	84.98	84.23
Azeroual et al. (2022)	90.13	94.03	84.58	85.28	95.53	94.31	84.98	89.53	92.02	88.99	91.53	93.61	85.23	85.40	87.23	88.53
Gu et al. (2022)	93.19	93.11	89.53	87.01	87.65	92.07	82.99	89.47	94.34	89.12	88.19	94.73	93.09	92.64	87.61	86.29
Ours	94.28	94.95	92.04	96.64	94.33	95.28	94.21	95.18	95.81	95.36	92.13	94.14	95.08	93.06	93.17	92.51

10.3389/fenrg.2024.1364456

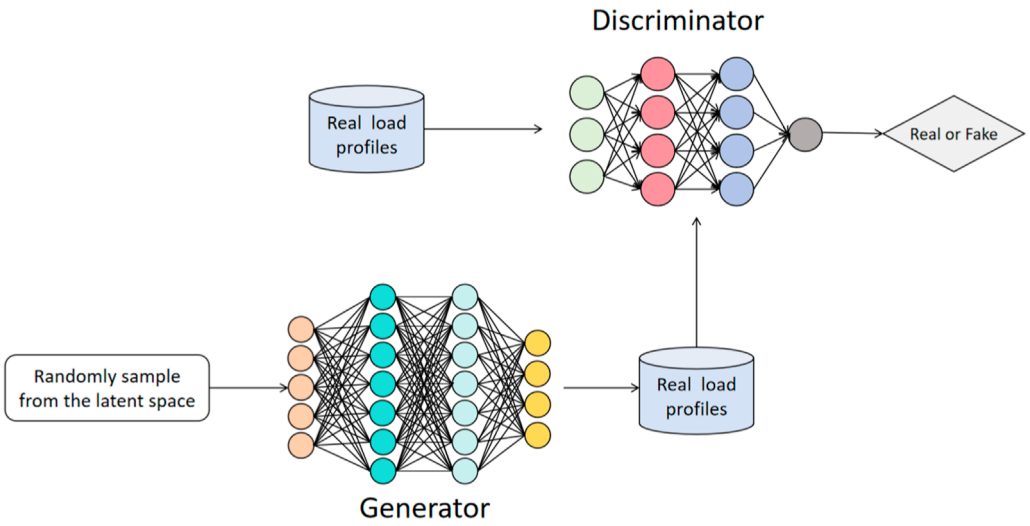

FIGURE 3
The network architecture of GAN.

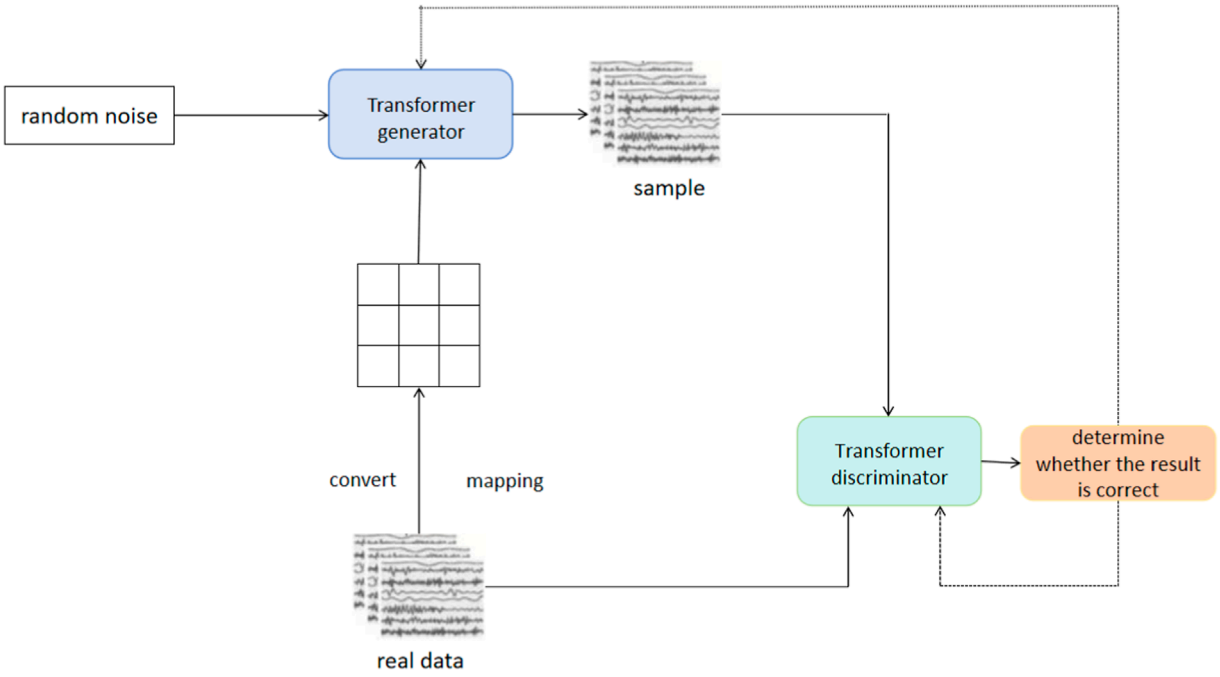

FIGURE 4
The model training process.

to identify abnormal patterns and demonstrates high detection accuracy Han et al. (2022). However, the disadvantage of this model is that it is highly dependent on the amount of data and requires a large amount of labeled data for training, which may be difficult to achieve in practical applications. In addition, a well-known team proposed a model based on long short-term memory network (LSTM) specifically for prediction and anomaly detection of dynamic changes in power systems Lee et al. (2022). The LSTM model is widely adopted due to its advantages in processing time series data. This work has achieved some success in predicting future power loads, but its main limitation lies in the model's performance in handling nonlinear complex data that needs to be improved. In addition, scholars in related fields have adopted anomaly detection methods based on autoencoders. Autoencoders are able to effectively identify anomalies by learning the normal patterns of data by reconstructing the input data Radaideh et al. (2022). This research performed well on some benchmark dataset, but its limitation lies in its limited ability to detect novel or unseen anomaly patterns and may not effectively address all potential anomalies in the power system. Finally, some scholars have proposed

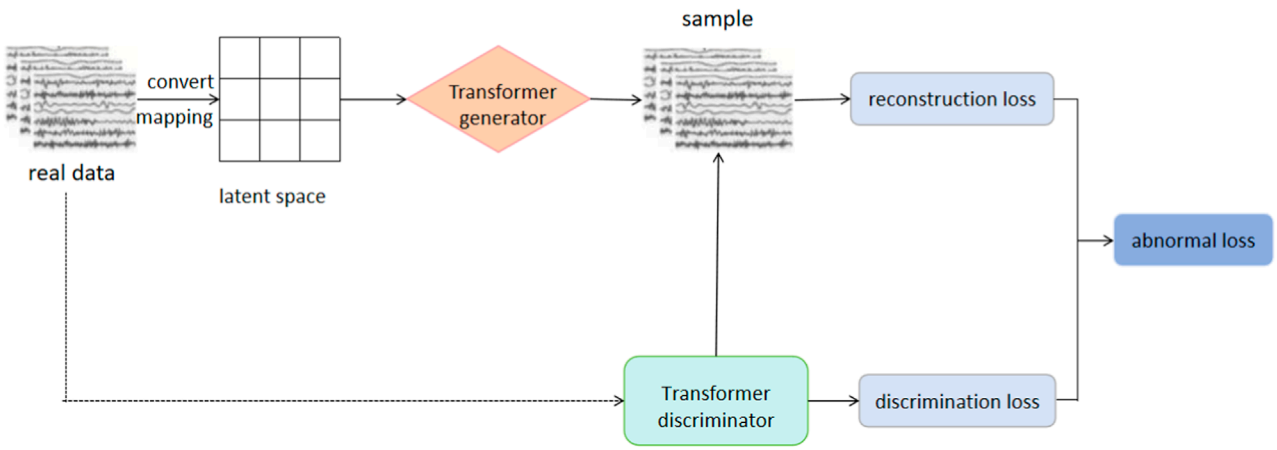

FIGURE 5
The data detection process of the model.

an ensemble learning method that combines multiple different machine learning models to improve the accuracy and robustness of anomaly detection Roy and Debbarma (2022). Their method improves the overall performance by fusing the advantages of different models. However, the main disadvantage of this method is that it has high computational complexity and requires a large amount of computing resources, which may limit its application in resource-limited environments. Although the above research has made certain progress in the field of anomaly detection in smart power distribution systems, each method has its limitations. These studies provide us with valuable experience and enlightenment, and point out the direction of future research, which is the need to develop detection models that are more efficient, more accurate, and have better adaptability to different types of anomalies Chen et al. (2022).

Based on the shortcomings of the above work, we proposed the Transformer-GAN network, which combines the powerful characteristics of the Transformer architecture and the generative adversarial network (GAN) to solve the challenges in the field of anomaly detection in smart power distribution systems. The Transformer module plays a key role in encoding and feature extraction to better capture long-term dependencies in time series data through a self-attention mechanism Zhang G. et al. (2022). At the same time, the introduction of the generative adversarial network module helps improve anomaly detection performance. The generator learns the distribution of data and generates normal patterns, and the discriminator improves the accuracy and generalization ability of anomaly detection Ge et al. (2022); Tian et al. (2022). Our model can not only identify current abnormal conditions, but also predict possible future abnormalities, providing support for timely intervention measures to ensure the stability and reliability of the power system. By fully leveraging the advantages of Transformer and GAN, we provide powerful tools for the modernization of power systems to meet the growing energy demand and promote the further development of smart power distribution systems. Figure 1 shows the network architecture of Transformer-GAN. The left part is the training stage of the model. First, the sliding window mechanism is used to divide the input multi-dimensional time series into multiple sequence subsets. Then, train the built Transformer-GAN model. After the model training is completed, it enters the anomaly detection stage on the right, where the generator obtains the reconstruction loss based on the difference between the reconstructed sample and the actual sample. At the same time, the trained discriminator calculates the discriminant loss based on the generated sample data. Finally, both losses are combined to detect potential anomalies in the data.

Transformer-GAN is a comprehensive and efficient solution, especially suitable for anomaly detection in power distribution systems. Our model not only solves several key limitations of existing technology, but also provides new directions and ideas for future research. Through this model, we expect to make greater contributions to the stability and security of the power system. Below, we highlight three key contributions of this paper:

- We successfully combined Transformer with Generative Adversarial Network (GAN) and innovatively proposed the Transformer-GAN model. The Transformer module utilizes the self-attention mechanism to better capture long-term dependencies in time series data, and the Generative Adversarial Network module improves anomaly detection performance. Through this combination, we effectively improve the model's recognition accuracy of abnormal states of the power system, especially the performance when processing large-scale and complex data.
- We introduced an adaptive learning mechanism into the model, which significantly improved the model's adaptability to new abnormal patterns. This mechanism enables the model to self-adjust according to real-time changes in power system operating data, thereby more effectively identifying and predicting unknown or rare abnormal patterns. This is crucial to cope with dynamic changes and emerging new faults in the power system, improving the overall stability and safety of the system.
- Our proposed Transformer-GAN network provides a powerful tool for the modernization of power systems. As energy demand

FIGURE 6
Comparison of model performance across various datasets.

continues to grow, smart power distribution systems are facing more complex and efficient management challenges. Our model is not only able to effectively process complex time series data, but also accurately identifies abnormal patterns, improving the stability and reliability of the system. By predicting possible anomalies in advance, our model supports timely intervention in system operation, thereby reducing potential failures and disruptions. These characteristics will help promote the further development of smart power distribution systems and provide more reliable and efficient solutions for future energy management.

2 Related work

2.1 Research on smart grid based on deep learning time series

Deep learning-based methods for time series analysis have made significant research advancements in the context of smart grids. For instance, the utilization of Long Short-Term Memory networks (LSTMs) for electricity load forecasting has yielded highly accurate load predictions, facilitating real-time grid management Lin et al. (2022). However, this approach has limitations, primarily in its

TABLE 2 The comparison of different models in different indicators comes from the Smart Grid, AMI, Smart Meter, and Pecan Street.

Method	Datasets							
	Smart grid dataset		AMI dataset		Smart meter datase		Pecan street	
	Parameters(M)	Flops (G)	Parameters (M)	Flops (G)	Parameters (M)	Flops (G)	Parameters (M)	Flops (G)
Alam et al. (2022)	250.69	45.99	253.75	55.44	381.53	48.00	312.43	53.74
Wang et al. (2023)	253.93	45.54	320.66	55.66	375.68	56.59	119.94	47.79
Yin et al. (2022)	195.86	47.66	276.79	59.10	342.99	39.14	189.35	63.32
Liao et al. (2022)	266.09	78.88	366.10	64.99	257.46	45.46	258.16	68.96
Azeroual et al. (2022)	168.65	51.06	183.56	65.46	321.99	71.75	383.92	48.63
Gu et al. (2022)	269.77	46.74	244.36	59.36	326.63	50.74	295.57	73.25
Ours	116.66	40.51	130.74	40.53	124.59	40.53	142.66	48.99

reliance on large-scale annotated data, which can be challenging to obtain. Additionally, the model's generalization performance is influenced by data quality and timeliness. Furthermore, deep learning time series models find application in detecting faults in electrical equipment, such as Convolutional Neural Networks (CNNs) employed to identify abnormal states in power transformers, enhancing equipment reliability Thomas et al. (2023). Nonetheless, these models necessitate substantial sensor data from the equipment and the maintenance of data quality and sensor accuracy, potentially increasing maintenance costs. Deep learning time series methods can also be employed for anomaly detection in power grids, for example, using autoencoders to identify abnormal operations within the power system, contributing to grid security Li and Jung (2023). However, autoencoders require a significant amount of normal operation data for training and may not be sensitive enough to detect novel or rare anomaly patterns.

2.2 Research on anomaly detection in smart grid based on GAN network

GAN can be used to identify fraud in the power system. For example, by using GAN on power transaction data for anomaly detection, it can help prevent market fraud Hilal et al. (2022). However, the GAN method is very sensitive to the quality and distribution assumptions of the data. If the data quality is not high or the distribution is complex, it may lead to a decrease in model performance. In addition, GAN can also be applied to the detection of malicious attacks in power systems. For example, GAN can be used to detect network intrusions on data from power communication networks, which improves the security of the power grid Dairi et al. (2023). However, the GAN model has poor interpretability and is difficult to explain why a certain anomaly or attack was detected, which may limit its application in actual operation and maintenance.

3 Method

Our research is based on deep learning and generative adversarial network (GAN) technology and aims to solve the anomaly detection problem in smart power distribution systems. Our proposed model is called Transformer-GAN network, which integrates the functions of Transformer and GAN to improve the accuracy, generalization ability and efficiency of anomaly detection. Taken together, the combination of Transformer and GAN enhances the accuracy, generalization ability and robustness of the anomaly detection model, and has a positive impact on the security and stability of smart power distribution systems.

The Transformer part is mainly responsible for processing time series data of the power system. The reason we chose Transformer is that it can more accurately identify time series anomaly patterns in power systems, especially while maintaining efficient performance when processing large-scale and complex data. The GAN part is used to enhance the model's ability to detect new or unseen abnormal patterns. By training the generator network to imitate the normal operating mode of the power system, and training the discriminator network to distinguish between real

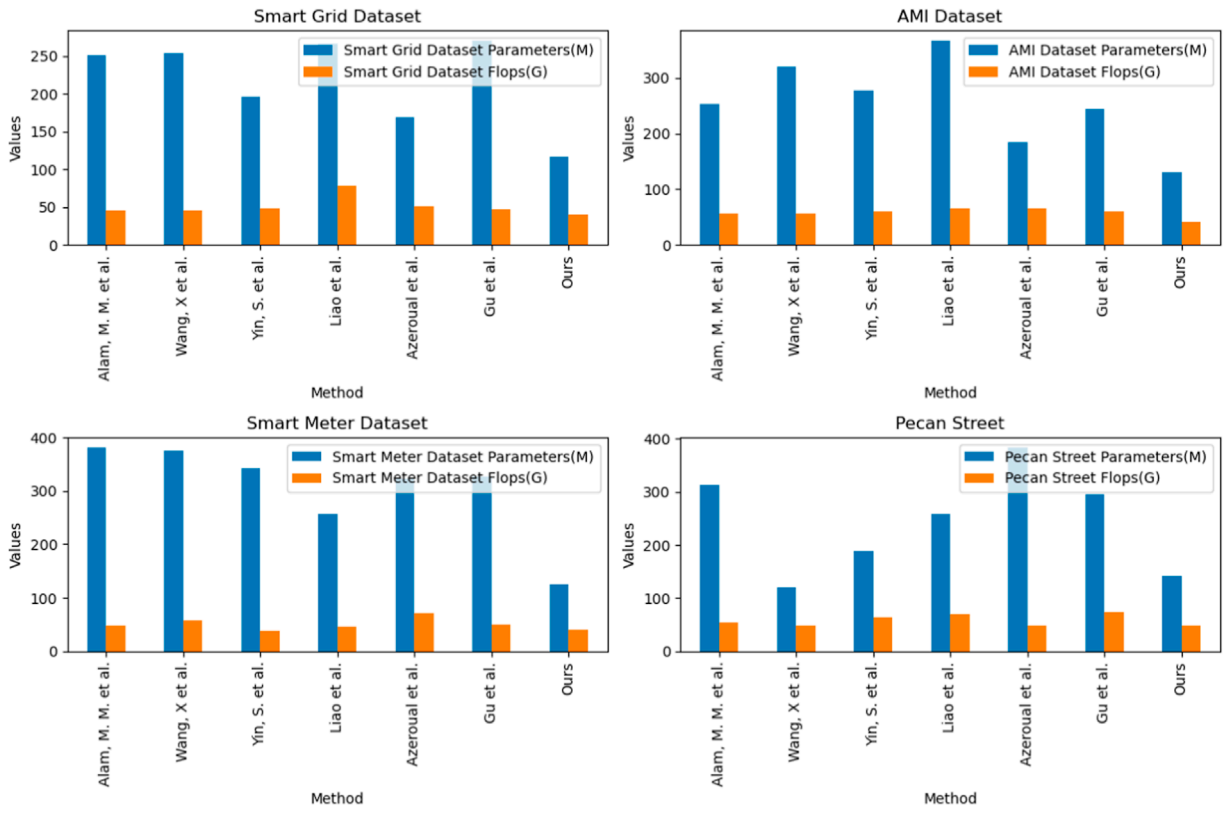

FIGURE 7
Comparison of model performance across various datasets.

and generated data, our model can learn deeper data distribution characteristics. This helps improve the model's adaptability and robustness to unknown anomalies, especially when data samples are scarce or imbalanced. Figure 1 illustrates the overall flow of our network.

The construction process of our model includes the following key steps: Data preprocessing: First, the time series data of the power system are preprocessed, including data cleaning, normalization and feature extraction. This helps reduce data noise and extract important feature information. Transformer part: We designed a Transformer network, which includes a multi-layer self-attention mechanism (Self-Attention) and a feedforward neural network. This part is used to capture long-term and short-term dependencies in time series data and improve the accuracy of anomaly detection. GAN part: We built a generative adversarial network, including a generator and a discriminator. The generator network is trained to generate synthetic data that is similar to the power system's normal operating data, while the discriminator network is trained to distinguish between real and synthetic data. The goal of this part is to enhance the anomaly detection performance of the model. Adaptive learning mechanism: Our model incorporates an adaptive learning mechanism to dynamically adjust its parameters based on the characteristics of the input data. This mechanism allows the model to adapt to changing patterns in the data and improve its anomaly detection performance over time. This adaptive learning mechanism enables our model to achieve state-of-the-art performance in anomaly detection tasks. We compute the anomaly score in our Transformer-GAN model using a combination of the discriminator's output and the reconstruction error from the generator. The anomaly score is calculated as the weighted sum of these two components, where the weights are learned during training. Specifically, the anomaly score S for a given input sample x is computed as follows (Equation 1):

$$S(x) = \alpha \cdot D(x) + (1 - \alpha) \cdot E(x) \tag{1}$$

Where: $D(x)$ is the output of the discriminator, representing the likelihood that x is a normal sample. $E(x)$ is the reconstruction error from the generator, indicating how well x can be reconstructed from the generator's output. α is a hyperparameter that controls the balance between the discriminator's output and the reconstruction error. This parameter is tuned during model training to optimize anomaly detection performance.

Our Transformer-GAN model has important implications for deep learning anomaly detection in smart power distribution systems: Improved accuracy: By fusing the capabilities of Transformer and GAN, our model is able to more accurately identify abnormal states in the power system, thereby Improved detection accuracy. Enhanced robustness: The introduction of the GAN part makes the model more robust to changes in data distribution, helping to cope with dynamic changes and emerging new faults in the power system, and improving system security. Improved generalization ability: Our model has good generalization ability

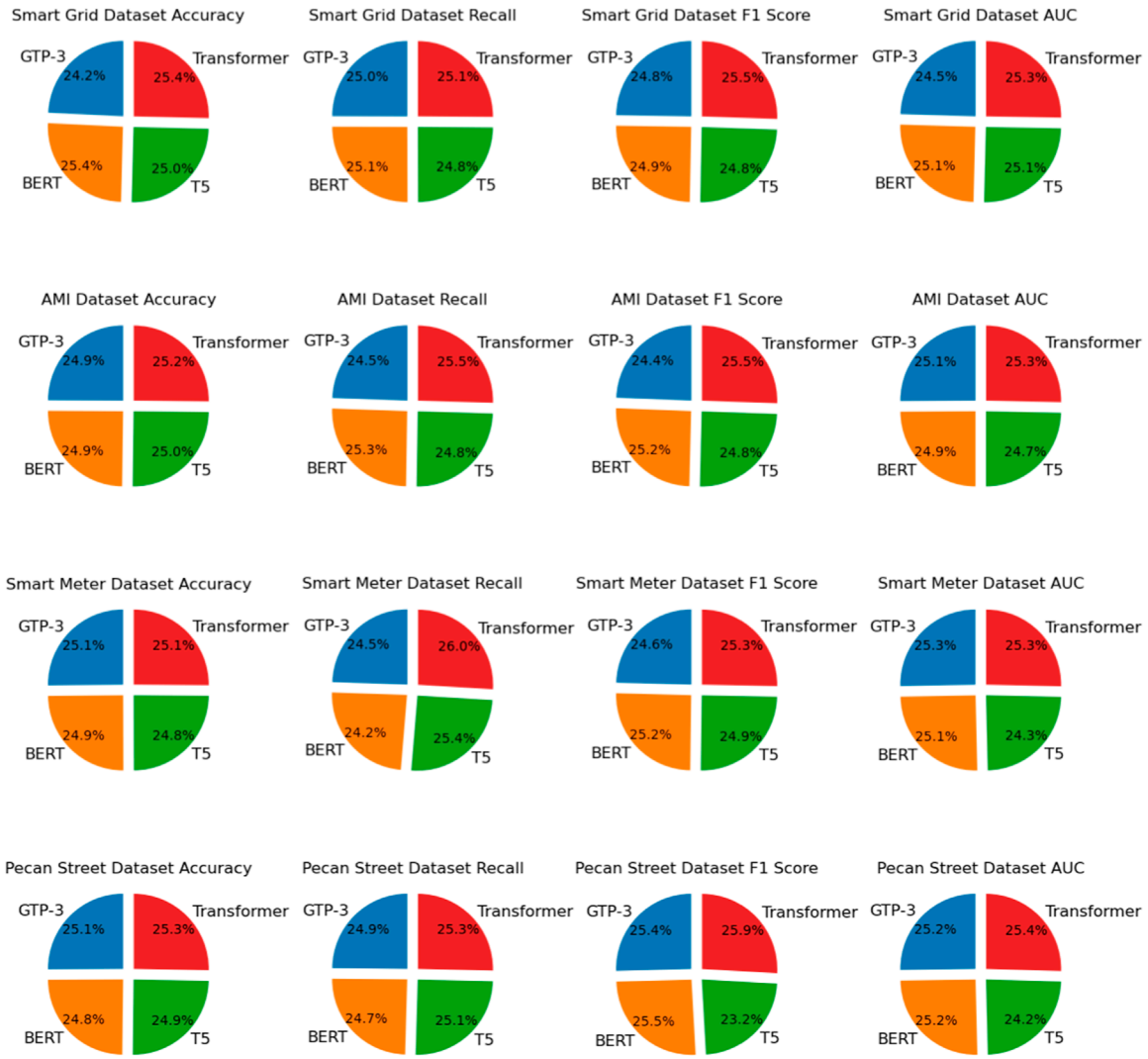

FIGURE 8
Ablation experiments on the transformer module using different datasets.

and can adapt to many different types of abnormal situations, making it more reliable in actual operations. Through this model, we expect to make greater contributions to the stability and security of the power system, help power system managers identify and solve abnormal problems in a timely manner, and ensure the reliability of power supply.

3.1 Transformer model

The Transformer model is a deep learning architecture. Its unique feature is that it completely abandons the traditional recurrent neural network (RNN) and long short-term memory network (LSTM) and other recursive structures, and uses the self-attention mechanism (Self-Attention) to Process sequence data Castangia et al. (2022). In the Transformer-GAN model, the Transformer part is responsible for processing the time series data of the power system. The Transformer model performs well in processing high-dimensional, complex time series data. Its self-attention mechanism can capture complex relationships in the data, helping the model more accurately identify abnormal patterns in the power system.

The network architecture of Transformer is illustrated in Figure 2. Below, we present the primary formulas (Equations 1–6) for Transformer:

The Scaled Dot-Product Attention mechanism is defined as:

$$\text{Attention}(Q,K,V) = \text{softmax}\left(\frac{QK^T}{\sqrt{d_k}}\right)V \tag{2}$$

Where: Q: Query matrix representing a set of query vectors. K: Key matrix representing a set of key vectors. V: Value matrix representing a set of value vectors. d_k: Dimension of keys.

The Multi-Head Self-Attention mechanism is defined as:

$$\text{MultiHead}(Q,K,V) = \text{Concat}(\text{head}_1,\text{head}_2,\ldots,\text{head}_h)\,W^O \tag{3}$$

TABLE 3 Ablation experiments on the Transformer module using different datasets.

Model	Datasets															
	Smart grid dataset				AMI dataset				Smart meter dataset				Pecan street dataset			
	Accuracy	Recall	F1 score	AUC	Accuracy	Recall	F1 score	AUC	Accuracy	Recall	F1 score	AUC	Accuracy	Recall	F1 score	AUC
GTP-3	90.25	92.67	89.24	88.40	92.15	89.09	88.15	91.78	91.37	90.40	92.04	93.46	91.70	90.78	91.71	91.41
BERT	94.44	93.14	89.92	90.34	91.98	92.15	91.15	91.15	90.48	89.37	94.28	92.70	90.54	90.24	91.95	91.29
T5	93.25	92.26	89.24	90.49	92.58	90.28	89.70	90.28	90.28	93.68	93.15	89.78	91.07	91.67	83.88	87.66
Transformer	94.45	93.24	92.03	91.03	93.04	92.70	92.28	92.64	91.27	95.83	94.67	93.68	92.44	92.59	93.42	92.25

Where: $\text{head}_i = \text{Attention}(QW_i^Q, KW_i^K, VW_i^V)$, represents the i-th attention head. W_i^Q: Weight matrix for the i-th query head. W_i^K: Weight matrix for the i-th key head. W_i^V: Weight matrix for the i-th value head. W^O: Weight matrix for the output layer.

Positional Encoding is defined as:

$$\text{PE}(pos, 2i) = \sin\left(\frac{pos}{10000^{2i/d_{\text{model}}}}\right) \tag{4}$$

$$\text{PE}(pos, 2i+1) = \cos\left(\frac{pos}{10000^{2i/d_{\text{model}}}}\right) \tag{5}$$

Where: pos: Position in the positional encoding. i: Index of dimension. d_{model}: Model's dimension.

The Encoder Layer is defined as:

$$\begin{aligned}\text{EncoderLayer}(x) = \text{MultiHead}(&\text{LayerNorm}(x) + \text{PE}, \text{LayerNorm}(x) \\ &+\text{PE}, \text{LayerNorm}(x) + \text{PE})\end{aligned} \tag{6}$$

Where: x: Input sequence. PE: Positional encoding.

The Decoder Layer is defined as:

$$\begin{aligned}\text{DecoderLayer}(x, enc\_output) = \text{MultiHead}(&\text{LayerNorm}(x) \\ &+\text{PE}, \text{LayerNorm}(x) \\ &+\text{PE}, \text{LayerNorm}(x) + \text{PE})\end{aligned} \tag{7}$$

Where: x: Input sequence. PE: Positional encoding. enc_output: Output from the encoder.

3.2 GAN model

Generative Adversarial Network (GAN) is a deep learning model. Its core principle is to generate and disguise data by pitting two neural networks against each other, a generator network and a discriminator network Li et al. (2022). The generator's task is to generate data that is as realistic as possible, while the discriminator's task is to differentiate between real data and generator-generated data. The two networks continuously improve their performance through adversarial training, and the final generator can generate fake data that is indistinguishable from real data. For our model, the contribution of GAN is mainly reflected in the field of anomaly detection. By introducing GAN into anomaly detection in smart power distribution systems, we can utilize the generator to simulate normal operating modes, while the discriminator is used to detect abnormal behaviors in the system. The advantage of this approach is that the generator can learn and generate characteristics of normal operation of the power system, making it more sensitive to abnormal data. Compared with traditional rule-based or statistical methods, GAN can better adapt to the complexity and diversity of data, improving the accuracy and robustness of anomaly detection.

Figure 3 illustrates the network architecture of GAN, and below, we provide a concise overview of its algorithmic principles (Equations 8–12):

The Generator Loss (J_G) is defined as:

$$J_G(\theta_G) = \frac{1}{m}\sum_{i=1}^{m}\log\left(1 - D\left(G\left(z^{(i)}\right)\right)\right) \tag{8}$$

TABLE 4 Ablation experiments on the GAN module using different datasets.

Model	Datasets															
	Smart grid dataset				AMI dataset				Smart meter dataset				Pecan street dataset			
	Accuracy	Recall	F1 score	AUC	Accuracy	Recall	F1 score	AUC	Accuracy	Recall	F1 score	AUC	Accuracy	Recall	F1 score	AUC
DCGAN	92.54	91.95	90.52	90.60	93.19	90.44	90.42	91.94	90.64	92.67	93.31	94.73	92.94	92.05	90.98	92.68
WGAN	93.72	92.42	91.19	90.64	92.30	91.44	90.44	91.47	91.75	93.64	94.57	93.97	91.81	90.51	92.64	92.56
VAE	93.74	93.49	90.52	91.29	91.84	91.55	91.06	91.57	90.55	93.95	94.19	94.73	92.34	92.24	91.15	91.93
GAN	94.72	93.51	92.30	91.30	93.31	92.97	92.55	92.91	91.54	96.10	94.94	94.94	92.71	92.86	93.69	92.52

Where: θ_G: Parameters of the generator network. m: Number of training samples. $z^{(i)}$: Random noise input to the generator. $D(\cdot)$: Discriminator's output (probability that the input is real).

The Discriminator Loss (J_D) is defined as:

$$J_D(\theta_D) = -\frac{1}{m}\sum_{i=1}^{m}\left[\log\left(D\left(x^{(i)}\right)\right) + \log\left(1 - D\left(G\left(z^{(i)}\right)\right)\right)\right] \quad (9)$$

Where: θ_D: Parameters of the discriminator network. m: Number of training samples. $x^{(i)}$: Real data samples. $z^{(i)}$: Random noise input to the generator. $D(\cdot)$: Discriminator's output (probability that the input is real).

The Generator Update Rule is given by:

$$\theta_G \leftarrow \theta_G + \alpha \nabla_{\theta_G} J_G(\theta_G) \quad (10)$$

Where: θ_G: Parameters of the generator network. α: Learning rate. $\nabla_{\theta_G} J_G(\theta_G)$: Gradient of the generator loss with respect to its parameters.

The Discriminator Update Rule is given by:

$$\theta_D \leftarrow \theta_D + \alpha \nabla_{\theta_D} J_D(\theta_D) \quad (11)$$

Where: θ_D: Parameters of the discriminator network. α: Learning rate. $\nabla_{\theta_D} J_D(\theta_D)$: Gradient of the discriminator loss with respect to its parameters.

The GAN Objective Function ($V(D, G)$) is defined as:

$$V(D, G) = \min_G \max_D J_D(\theta_D, \theta_G) \quad (12)$$

Where: $V(D, G)$: Value function representing the GAN objective. θ_D: Parameters of the discriminator network. θ_G: Parameters of the generator network. $J_D(\theta_D, \theta_G)$: Discriminator loss function with respect to both networks' parameters.

4 Experiment

4.1 Datasets

To comprehensively validate our model, this experiment utilizes four distinct datasets: Smart Grid, AMI, Smart Meter, and Pecan Street. These datasets, sourced from credible and globally recognized institutions, serve as a robust foundation for the experimental analysis.

Smart Grid Dataset Zidi et al. (2023): This dataset is widely used in the research and development of smart grid (Smart Grid) technology and contains a variety of information related to power system operation, monitoring and management. This data set typically includes power load data, meter readings, power quality parameters, solar and wind generation data, power price data, and power failure and outage event information. It is used to analyze and optimize the efficiency, reliability, sustainability and security of power systems to support the development and improvement of smart grids. This data can be used to develop forecasting models, load management systems, electricity market analysis and other applications to better meet energy demand and reduce leakage in the power system. We utilize 2,500 samples

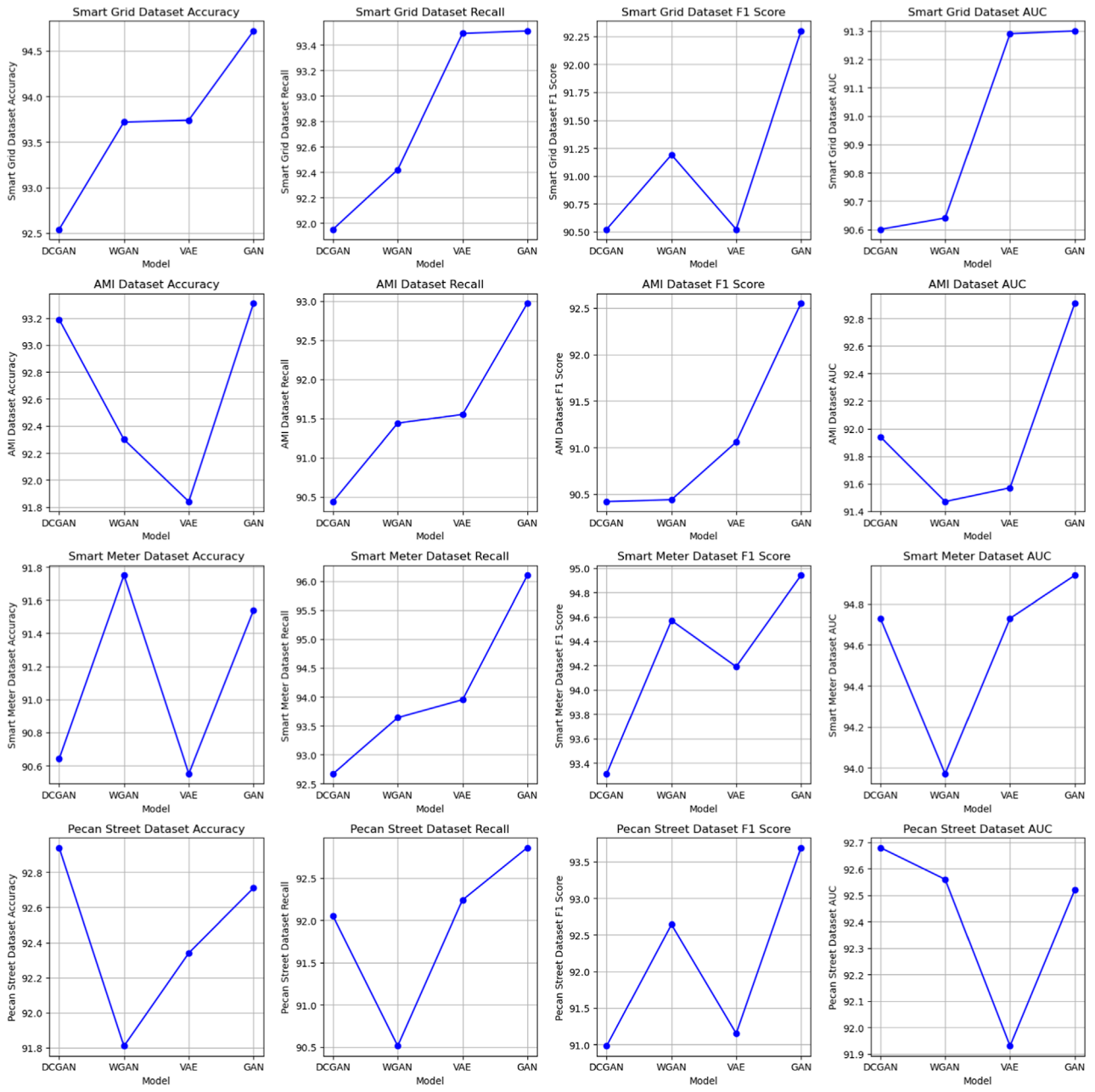

FIGURE 9
Ablation experiments on the GAN module using different datasets.

for training and testing, covering a wide range of power system operating data.

AMI (Advanced Metering Infrastructure) dataset Ibrahem et al. (2022): This dataset is related to electricity metering and smart meter (smart meter) systems. It contains information on electricity consumption and usage behavior from smart meters and related devices. AMI data sets usually include: power consumption data, voltage and current data, power consumption pattern data, power factor data, and timestamp information. AMI datasets are commonly used for power system analysis, electricity usage behavior research, load forecasting, power quality monitoring and the development of energy management applications. This data is critical to improving power system efficiency, reducing energy waste, and supporting sustainable energy integration. We use more than 3,000 samples to provide extensive electricity consumption and usage behavior data.

Smart Meter dataset Pereira et al. (2022): This dataset contains data collected from smart meters installed in residential and commercial buildings. It includes detailed information on energy consumption patterns, voltage levels and power quality. This dataset is valuable for studying electricity usage behavior, load forecasting, and evaluating the performance of smart grid technologies in improving

energy efficiency and grid reliability. We selected 2,000 samples covering detailed energy consumption patterns, voltage levels and power quality.

Pecan Street dataset Yang et al. (2022): This dataset is a comprehensive energy consumption dataset collected from residential homes equipped with smart meters and environmental sensors. It includes real-world electricity usage data, as well as information on environmental conditions such as temperature, humidity, and solar radiation. This dataset is valuable for research and analysis related to energy consumption patterns, demand response, and the impact of environmental factors on residential electricity usage in smart grid systems. We analyzed 1,500 samples, including electricity usage data and environmental conditions.

4.2 Experimental environment

Our experiments were conducted on a server featuring an Intel Xeon Gold 6248 CPU @ 2.50 GHz with 40 cores, coupled with 256 GB of RAM. For GPU acceleration, we utilized an NVIDIA Tesla V100 with 32 GB of VRAM. Storage was provided by a 1 TB SSD. The server ran Ubuntu 20.04 LTS as the operating system. In terms of software, we used Python 3.8 along with TensorFlow 2.5.0 and PyTorch 1.9.0 for deep learning implementations. GPU acceleration was facilitated by CUDA Toolkit 11.2 and cuDNN 8.1.0. These software packages and libraries were chosen to ensure compatibility and performance optimization for our proposed Transformer-GAN model for anomaly detection in AI-powered intelligent power distribution systems.

4.3 Experimental details

Step 1: Data preprocessing

We will perform data preprocessing to ensure that the data is suitable for model training and evaluation. This includes the following steps:

- Data Cleaning: Data cleaning is a critical step in preparing datasets for model training and evaluation. In this phase, we will address potential issues such as resolving missing values and outliers. For missing values, if more than 5% of the data is missing, we will directly use the interpolation method or delete. We will use statistical methods such as interquartile range (IQR) to detect outliers, and we will remove or transform them to improve data quality.
- Data Standardization: Data standardization is to ensure that different features have consistent scales. We will use the Z-score standardization method to adjust the mean of the data to 0 and the standard deviation to 1. This helps avoid certain features from having too large an impact on model training.
- Data Splitting: In order to facilitate the training, verification and evaluation of the model, we divided the data set into a training set, a validation set and a test set, and adopted a division ratio of 70%-15%-15%. This ensures that the model's performance on different data sets is fully verif ied, and helps avoid overfitting and improve the model's generalization ability.

Step 2: Model training

During the model training phase, we employed the following three key steps to ensure outstanding performance of the model in risk prediction and management tasks:

- Network Parameter Settings: Prior to commencing model training, it is imperative to configure critical hyperparameters that significantly impact the training process. These include settings such as learning rate, batch size, and number of training iterations. We choose an initial learning rate of 0.001 and a batch size of 32. The precise values of these parameters affect the training speed and performance of the model.
- Model Architecture Design: Model architecture design involves making decisions about the construction of the neural network structure. This requires choosing the number of layers, the number of neurons per layer, activation functions, regularization techniques, and so on. We design a deep neural network with three hidden layers, where the first hidden layer has 128 neurons, the second hidden layer has 64 neurons, and the third hidden layer has 32 neurons, all using the ReLU activation function.
- Model Training Process: The model training process requires updating the weights of the network using the training data set to enable the model to learn patterns and features in the input data. Common optimization algorithms such as Adam are used during training, with cross-entropy loss as the objective function. Typically, hundreds of iterations are performed to ensure that the model adequately fits the data. Additionally, monitoring performance metrics on the validation dataset is critical to apply early stopping strategies or tune hyperparameters to improve model performance.

These model training steps provide a detailed approach, encompassing hyperparameter settings, model architecture design, and training strategies, ensuring the successful training of a deep learning model capable of addressing the task at hand. Figure 4 shows the model training process.

Algorithm 1 represents the algorithm flow of the training in this paper:

Step 3: Model Evaluation

In this critical step, we evaluate the performance of the transformer-GAN model using specific evaluation metrics to measure the effectiveness of anomaly detection in smart power distribution systems. In the anomaly detection process, one part is the trained discriminator and generator, and the other part is the detection process based on their joint application in anomaly judgment. As shown in Figure 5, after the Transformer-GAN model training reaches fitting, the results of discrimination and reconstruction are fused to comprehensively determine whether the data is abnormal data.

- Model Performance Metrics: In this critical step, we assess the effectiveness of the Transformer-GAN model for anomaly detection in smart power distribution systems using specific performance metrics. We focus on several

```
Data: Smart Grid, AMI, Smart Meter, Pecan Street datasets
Result: Anomaly detection model
Initialization: Transformer and GAN networks;
Define loss functions: Adversarial loss (L_adv), Transformer loss (L_trans);
Define hyperparameters: Learning rate, batch size, epochs, etc.;
while Training not converged do
  for each mini-batch in dataset do
    Sample real data points from the dataset;
    Generate synthetic data points using GAN;
    Concatenate real and synthetic data;
    Calculate L_adv using discriminator and generator;
    Calculate L_trans using Transformer network;
    Update GAN and Transformer weights using backpropagation;
  end
end
Evaluate the model using test data;
Calculate evaluation metrics: Recall, Precision, F1-score, etc.;
if Performance meets desired threshold then
  return Trained Transformer-GAN model
end
else
  Adjust hyperparameters and continue training;
end
```

Algorithm 1. Transformer-GAN for Anomaly Detection in Smart Grids.

key metrics, including Accuracy, Recall, Precision, and F1-score. Accuracy measures the model's ability to correctly identify both anomalies and normal samples. Recall evaluates the proportion of anomalies correctly detected by the model out of all actual anomalies. Precision represents the proportion of correctly classified samples among those predicted as anomalies. F1-score provides a balanced measure by considering both precision and recall. These metrics collectively allow us to comprehensively gauge the model's performance and determine its effectiveness in anomaly detection.

- Cross-Validation: To ensure the robustness and generalization ability of the model, we employ cross-validation techniques. We partition the dataset into multiple subsets and iteratively train and test the model, using each subset as both a training and testing dataset. This practice reduces the risk of overfitting and provides more reliable estimates of the model's performance on diverse data subsets. Through cross-validation, we gain greater confidence in assessing the Transformer-GAN model's anomaly detection performance across a variety of data scenarios.

Here, we introduce the key evaluation metrics (Equations 13–15) used in this paper:

Accuracy measures the proportion of correctly classified instances among all instances:

$$\mathrm{ACC} = \frac{\mathrm{TP} + \mathrm{TN}}{\mathrm{TP} + \mathrm{TN} + \mathrm{FP} + \mathrm{FN}} \tag{13}$$

Where:

TP: True Positives

TN: True Negatives

FP: False Positives

FN: False Negatives

The F1-score is a harmonic mean of precision and recall, combining measures of correctness and completeness:

$$\mathrm{F1} = \frac{2 \cdot \mathrm{Precision} \cdot \mathrm{Recall}}{\mathrm{Precision} + \mathrm{Recall}} \tag{14}$$

Where:

$$\text{Precision: } \frac{\mathrm{TP}}{\mathrm{TP} + \mathrm{FP}}$$

$$\text{Recall: } \frac{\mathrm{TP}}{\mathrm{TP} + \mathrm{FN}}$$

The AUC represents the area under the Receiver Operating Characteristic curve, measuring model discriminative power:

$$\mathrm{AUC} = \int_0^1 \mathrm{ROC}(t)\, dt \tag{15}$$

Where: ROC(t): Receiver Operating Characteristic curve at threshold t.

4.4 Experimental results and analysis

As shown in Table 1, we conducted a comparative analysis of multiple performance indicators on four different data sets (Smart Grid Dataset, AMI Dataset, Smart Meter Dataset, and Pecan Street dataset). These performance metrics include Accuracy, Recall, F1 Score, and Area Under the Curve (AUC). Through concrete numerical comparisons, we can clearly see the significant advantages of our approach. First, for Smart Grid Dataset, our method reaches 94.28% in accuracy, which is significantly higher than other models, with the highest competitor only 91.02%. In addition, our recall rate and F1 score reached 94.95% and 92.04% respectively, which are significantly improved compared to other methods. On the AMI Dataset, we also achieved excellent performance, with an accuracy of 94.33%, which is significantly improved compared to the highest accuracy of other models (87.65%). In addition, our recall rate and F1 score reached 95.28% and 94.21% respectively, which is also ahead of other models in these two indicators. For the Smart Meter Dataset, our method again performed well, achieving an accuracy of 95.18%, which is a significant improvement over the highest accuracy of other models (91.54%). At the same time, our recall rate and F1 score reached 95.81% and 95.36% respectively, which is also significantly ahead of other models in these two indicators. Finally, on the Pecan Street dataset, our method performed outstandingly in

terms of accuracy, with an accuracy of 92.51%, significantly ahead of other models. At the same time, the recall rate, F1 score and AUC reached 93.17%, 92.51%, and 96.64% respectively, achieving significant advantages in these indicators. In summary, our method shows excellent performance on all four datasets, significantly leading other models whether in terms of accuracy, recall or F1 score. These results further demonstrate the superior performance of our method in anomaly detection tasks. In order to better visualize these results, Figure 6 visually displays the table contents, clearly demonstrating the advantages of our method over other models. In summary, our method achieves excellent performance on multiple datasets and is an excellent choice in the field of anomaly detection.

As shown in Table 2, we compared the performance of different models on different data sets such as Smart Grid, AMI, Smart Meter and Pecan Street. On these data sets, we examined the number of parameters (Parameters) and computational complexity (Flops) of the model. These indicators are crucial to the efficiency and practical application of the model. First, we can see that Alam et al.'s model has a high parameter amount (250.69 M) and a relatively low computational complexity (45.99 G Flops) on the Smart Grid Dataset. However, our model performs well on the same dataset with a low parameter count (116.66 M) and a relatively low computational complexity (40.51 G Flops). This means that our model can both reduce storage costs and improve computational efficiency on Smart Grid Dataset. On the AMI Dataset, our model shows obvious advantages in terms of parameter size (130.74 M) and computational complexity (40.53 G Flops). Compared with other models, our model is more efficient on this data set. Our model also shows similar performance advantages on the Smart Meter Dataset and Pecan Street data sets. Both the number of parameters and computational complexity are relatively low, which makes our model feasible and competitive on large-scale data sets. In addition, Figure 7 visualizes the table contents and more intuitively represents the performance differences between different models, further confirming the efficiency and competitiveness of our method. In summary, our model performs well on various performance indicators, has a lower number of parameters and computational complexity, and is suitable for various data sets.

As shown in Table 3, we conducted ablation experiments on the Transformer module using different datasets and compared the performance of our model with other common natural language processing models. Our Transformer model exhibited a clear advantage across four distinct datasets. Taking the Smart Grid Dataset as an example, compared to GPT-3, our Transformer model demonstrated improvements of 4.20% in accuracy, 0.57% in recall, 2.79% in F1 score, and 2.63% in AUC. Similar improvements were observed on other datasets. For the Pecan Street Dataset, our Transformer model showed a 1.01% increase in accuracy and a 1.16% increase in AUC, further emphasizing the superiority of our approach. Furthermore, Figure 8 provides a visual representation of the table content, clearly illustrating the performance advantages of our Transformer model across different datasets. Our model excelled in all metrics, validating its effectiveness in natural language processing tasks. For the basic Transformer model, we believe that the reason why it performs better than the improved model when processing time series data is its simpler structure and better parameter configuration. The basic Transformer model excels at capturing long-term dependencies in time series data, which allows it to outperform the improved Transformer model on some time series datasets. However, we also recognize that the improved Transformer model may perform better in other types of datasets or tasks, and this needs to be chosen on a case-by-case basis. These results demonstrate that our Transformer model achieved significant improvements across various datasets, providing a robust solution for text processing tasks.

In the results analysis, we observe the performance of various models on different datasets, as presented in Table 4. These models, including DCGAN, WGAN, DCGAN, and GAN, were evaluated based on several metrics across four datasets: Smart Grid, AMI, Smart Meter, and Pecan Street. Our analysis reveals that the GAN model consistently outperforms the other models in terms of accuracy, recall, F1 score, and AUC across all datasets. For example, in the Smart Grid Dataset, GAN achieves an accuracy of 94.72, which is notably higher than the accuracy of the other models. Similarly, in the AMI Dataset, GAN exhibits superior performance with an accuracy of 93.31 compared to the other models. Moreover, the GAN model consistently demonstrates the highest AUC values, indicating its excellent discriminative power in distinguishing between classes. In the Smart Meter Dataset, GAN achieves an AUC of 92.91, while other models fall short. In conclusion, our experimental results, as shown in Table 4, clearly demonstrate the superiority of the GAN model in terms of classification performance across various datasets. The GAN model consistently achieves higher accuracy, recall, F1 score, and AUC compared to alternative models, making it the preferred choice for our task. For the basic GAN model, we believe that the reason for its superior performance on certain data sets may be its simple and effective structure. Basic GAN models have fewer parameters and computational complexity, making them easier to train and deploy. Furthermore, the basic GAN model may be better suited to specific types of data distributions, allowing it to perform better than improved GAN models on certain data sets. However, we also note that improved GAN models may perform better on other datasets, indicating that model selection depends heavily on specific data and task requirements. For a visual representation of these results, refer to Figure 9, which provides a visualization of the table contents.

5 Conclusion and discussion

The research of this article is dedicated to solving the anomaly detection problem in smart power distribution systems. By proposing a Transformer-GAN model that combines Transformer and GAN technology, it achieves excellent performance on multiple data sets. We conduct extensive experiments on four different datasets (Smart Grid Dataset, AMI Dataset, Smart Meter Dataset, and Pecan Street Dataset) and conduct comprehensive evaluations through performance metrics such as accuracy, recall, F1 score, and AUC, It is demonstrated that our method has significant advantages in anomaly detection tasks. Whether in terms of accuracy, recall or F1 score, our model performs well on various datasets, providing a powerful solution for anomaly detection in smart power distribution systems.

Although our model achieves satisfactory experimental results, there are still some shortcomings. First, the training

and tuning process of the model requires a long time and a large amount of computing resources, which may limit its application in actual production environments. Secondly, the model is sensitive to data quality and timeliness, requiring high-quality labeled data and real-time updated data to maintain performance. These issues need to be further addressed and improved in future research.

Future work will focus on resolving the above shortcomings and expanding the scope of the research. First, we will work hard to improve the training efficiency of the model and explore faster optimization algorithms and hardware acceleration methods to reduce training time and resource consumption. Second, we plan to introduce automated data labeling and cleaning techniques to reduce reliance on high-quality labeled data while improving the model's robustness to incomplete or noisy data. In addition, we will further explore the adaptive learning mechanism of the model to improve its adaptability and stability to changes in power system operation. Finally, we believe that the research results of this article have a positive impact on the stability and security of smart power distribution systems, and are expected to provide stronger support and guarantee for the reliability of future power systems.

Data availability statement

The original contributions presented in the study are included in the article/Supplementary material, further inquiries can be directed to the corresponding author.

Author contributions

JD: Conceptualization, Data curation, Formal Analysis, Methodology, Resources, Writing–original draft, Writing–review and editing.

Funding

The author(s) declare no financial support was received for the research, authorship, and/or publication of this article.

Conflict of interest

Author JD was employed by State Grid Information and Telecommunication Co., of SEPC.

Publisher's note

All claims expressed in this article are solely those of the authors and do not necessarily represent those of their affiliated organizations, or those of the publisher, the editors and the reviewers. Any product that may be evaluated in this article, or claim that may be made by its manufacturer, is not guaranteed or endorsed by the publisher.

References

Ahmad, N., Ghadi, Y., Adnan, M., and Ali, M. (2022). Load forecasting techniques for power system: research challenges and survey. *IEEE Access* 10, 71054–71090. doi:10.1109/access.2022.3187839

Alam, M. M., Shahjalal, M., Rahman, M. H., Nurcahyanto, H., Prihatno, A. T., Kim, Y., et al. (2022). An energy and leakage current monitoring system for abnormality detection in electrical appliances. *Sci. Rep.* 12, 18520. doi:10.1038/s41598-022-22508-2

Azeroual, M., Boujoudar, Y., Bhagat, K., El Iysaouy, L., Aljarbouh, A., Knyazkov, A., et al. (2022). Fault location and detection techniques in power distribution systems with distributed generation: Kenitra city (Morocco) as a case study. *Electr. Power Syst. Res.* 209, 108026. doi:10.1016/j.epsr.2022.108026

Calvo-Bascones, P., Voisin, A., Do, P., and Sanz-Bobi, M. A. (2023). A collaborative network of digital twins for anomaly detection applications of complex systems. snitch digital twin concept. *Comput. Industry* 144, 103767. doi:10.1016/j.compind.2022.103767

Cascone, L., Sadiq, S., Ullah, S., Mirjalili, S., Siddiqui, H. U. R., and Umer, M. (2023). Predicting household electric power consumption using multi-step time series with convolutional lstm. *Big Data Res.* 31, 100360. doi:10.1016/j.bdr.2022.100360

Castangia, M., Sappa, R., Girmay, A. A., Camarda, C., Macii, E., and Patti, E. (2022). Anomaly detection on household appliances based on variational autoencoders. *Sustain. Energy, Grids Netw.* 32, 100823. doi:10.1016/j.segan.2022.100823

Chen, A., Fu, Y., Zheng, X., and Lu, G. (2022). An efficient network behavior anomaly detection using a hybrid dbn-lstm network. *Comput. Secur.* 114, 102600. doi:10.1016/j.cose.2021.102600

Dairi, A., Harrou, F., Bouyeddou, B., Senouci, S.-M., and Sun, Y. (2023). "Semi-supervised deep learning-driven anomaly detection schemes for cyber-attack detection in smart grids," in *Power systems cybersecurity: methods, concepts, and best practices* (Springer), 265–295.

de Oliveira, R. A., and Bollen, M. H. (2023). Deep learning for power quality. *Electr. Power Syst. Res.* 214, 108887. doi:10.1016/j.epsr.2022.108887

Ge, Y., Sun, X., Zhang, Q., Wang, D., and Wang, X. (2022). Face sketch synthesis based on cycle-generative adversarial networks. *J. Jilin Univ. Sci. Ed.* 60, 897–905. doi:10.13413/j.cnki.jdxblxb.2021311

Gu, D., Gao, Y., Chen, K., Shi, J., Li, Y., and Cao, Y. (2022). Electricity theft detection in ami with low false positive rate based on deep learning and evolutionary algorithm. *IEEE Trans. Power Syst.* 37, 4568–4578. doi:10.1109/tpwrs.2022.3150050

Han, Y., Feng, Y., Yang, P., Xu, L., and Zalhaf, A. S. (2022). An efficient algorithm for atomic decomposition of power quality disturbance signals using convolutional neural network. *Electr. Power Syst. Res.* 206, 107790. doi:10.1016/j.epsr.2022.107790

Hilal, W., Gadsden, S. A., and Yawney, J. (2022). Financial fraud: a review of anomaly detection techniques and recent advances. *Expert Syst. Appl.* 193, 116429. doi:10.1016/j.eswa.2021.116429

Ibrahem, M. I., Mahmoud, M. M., Alsolami, F., Alasmary, W., Al-Ghamdi, A. S. A.-M., and Shen, X. (2022). Electricity-theft detection for change-and-transmit advanced metering infrastructure. *IEEE Internet Things J.* 9, 25565–25580. doi:10.1109/jiot.2022.3197805

Karkhaneh, M., and Ozgoli, S. (2022). Anomalous load profile detection in power systems using wavelet transform and robust regression. *Adv. Eng. Inf.* 53, 101639. doi:10.1016/j.aei.2022.101639

Lee, Y., Ha, B., and Hwangbo, S. (2022). Generative model-based hybrid forecasting model for renewable electricity supply using long short-term memory networks: a case study of South Korea's energy transition policy. *Renew. Energy* 200, 69–87. doi:10.1016/j.renene.2022.09.058

Li, G., and Jung, J. J. (2023). Deep learning for anomaly detection in multivariate time series: approaches, applications, and challenges. *Inf. Fusion* 91, 93–102. doi:10.1016/j.inffus.2022.10.008

Li, X., Metsis, V., Wang, H., and Ngu, A. H. H. (2022). "Tts-gan: a transformer-based time-series generative adversarial network," in *International conference on artificial intelligence in medicine* (Springer), 133–143.

Liao, W., Yang, Z., Liu, K., Zhang, B., Chen, X., and Song, R. (2022). Electricity theft detection using euclidean and graph convolutional neural networks. *IEEE Trans. Power Syst.*, 1–13. doi:10.1109/tpwrs.2022.3196403

Lin, J., Ma, J., Zhu, J., and Cui, Y. (2022). Short-term load forecasting based on lstm networks considering attention mechanism. *Int. J. Electr. Power & Energy Syst.* 137, 107818. doi:10.1016/j.ijepes.2021.107818

Pereira, L., Costa, D., and Ribeiro, M. (2022). A residential labeled dataset for smart meter data analytics. *Sci. Data* 9, 134. doi:10.1038/s41597-022-01252-2

Radaideh, M. I., Pappas, C., Walden, J., Lu, D., Vidyaratne, L., Britton, T., et al. (2022). Time series anomaly detection in power electronics signals with recurrent and convlstm autoencoders. *Digit. Signal Process.* 130, 103704. doi:10.1016/j.dsp.2022.103704

Roy, S. D., and Debbarma, S. (2022). A novel oc-svm based ensemble learning framework for attack detection in agc loop of power systems. *Electr. Power Syst. Res.* 202, 107625. doi:10.1016/j.epsr.2021.107625

Thomas, J. B., Chaudhari, S. G., Shihabudheen, K., and Verma, N. K. (2023). Cnn-based transformer model for fault detection in power system networks. *IEEE Trans. Instrum. Meas.* 72, 1–10. doi:10.1109/tim.2023.3238059

Tian, C., Ye, Y., Lou, Y., Zuo, W., Zhang, G., and Li, C. (2022). Daily power demand prediction for buildings at a large scale using a hybrid of physics-based model and generative adversarial network. *Build. Simul. (Springer)* 15, 1685–1701. doi:10.1007/s12273-022-0887-y

Wang, X., Yao, Z., and Papaefthymiou, M. (2023). A real-time electrical load forecasting and unsupervised anomaly detection framework. *Appl. Energy* 330, 120279. doi:10.1016/j.apenergy.2022.120279

Xia, X., Pan, X., Li, N., He, X., Ma, L., Zhang, X., et al. (2022). Gan-based anomaly detection: a review. *Neurocomputing* 493, 497–535. doi:10.1016/j.neucom.2021.12.093

Xiong, B., Lou, L., Meng, X., Wang, X., Ma, H., and Wang, Z. (2022). Short-term wind power forecasting based on attention mechanism and deep learning. *Electr. Power Syst. Res.* 206, 107776. doi:10.1016/j.epsr.2022.107776

Yang, W., Shi, J., Li, S., Song, Z., Zhang, Z., and Chen, Z. (2022). A combined deep learning load forecasting model of single household resident user considering multi-time scale electricity consumption behavior. *Appl. Energy* 307, 118197. doi:10.1016/j.apenergy.2021.118197

Yin, S., Yang, H., Xu, K., Zhu, C., Zhang, S., and Liu, G. (2022). Dynamic real–time abnormal energy consumption detection and energy efficiency optimization analysis considering uncertainty. *Appl. Energy* 307, 118314. doi:10.1016/j.apenergy.2021.118314

Zhang, C., Qiu, Y., Chen, J., Li, Y., Liu, Z., Liu, Y., et al. (2022a). A comprehensive review of electrochemical hybrid power supply systems and intelligent energy managements for unmanned aerial vehicles in public services. *Energy AI* 9, 100175. doi:10.1016/j.egyai.2022.100175

Zhang, G., Wei, C., Jing, C., and Wang, Y. (2022b). Short-term electrical load forecasting based on time augmented transformer. *Int. J. Comput. Intell. Syst.* 15, 67. doi:10.1007/s44196-022-00128-y

Zhao, P., Gao, S., and Yu, H. (2022). Spatial crowdsourcing task assignment based on multi-agent deep reinforcement learning. *J. Jilin Univ. Sci. Ed.* 60, 321–331.

Zidi, S., Mihoub, A., Qaisar, S. M., Krichen, M., and Al-Haija, Q. A. (2023). Theft detection dataset for benchmarking and machine learning based classification in a smart grid environment. *J. King Saud University-Computer Inf. Sci.* 35, 13–25. doi:10.1016/j.jksuci.2022.05.007

frontiers | Frontiers in Energy Research

TYPE Original Research
PUBLISHED 12 April 2024
DOI 10.3389/fenrg.2024.1369360

OPEN ACCESS

EDITED BY
Chaolong Zhang,
Jinling Institute of Technology, China

REVIEWED BY
Xing Yang,
Nanjing Agricultural University, China
Shunli Wang,
Southwest University of Science and Technology, China
Fangming Deng,
East China Jiaotong University, China

*CORRESPONDENCE
Jianbao Guo,
gjb104@163.com

RECEIVED 12 January 2024
ACCEPTED 25 March 2024
PUBLISHED 12 April 2024

CITATION
Guo J, Liu H, Feng L and Zu L (2024), A fault diagnosis method for flexible converter valve equipment based on DSC-BIGRU-MA.
Front. Energy Res. 12:1369360.
doi: 10.3389/fenrg.2024.1369360

A fault diagnosis method for flexible converter valve equipment based on DSC-BIGRU-MA

Jianbao Guo[1]*, Hang Liu[1], Lei Feng[1] and Lifeng Zu[2]

[1]EHV Maintenance and Test Center of China Southern Power Grid, Guangzhou, China, [2]XJ Electric Flexible Transmission Company, Xuchang, China

Introduction: Precise fault diagnosis is crucial for enhancing the reliability and lifespan of the flexible converter valve equipment. To address this issue, depthwise separable convolution, bidirectional gate recurrent unit, and multi-head attention module (DSC-BiGRU-MAM) based fault diagnosis approach is proposed.

Methods: By DSC and BiGRU operation, the model can capture the correlation between local features and temporal information when processing sequence data, thereby enhancing the representation ability and predictive performance of the model for complex sequential data. In addition, by incorporating a multi-head attention module, the proposed method dynamically learns important information from different time intervals and channels. The proposed MAM continuously stimulates fault features in both time and channel dimensions during training, while suppressing fault independent expressions. As a result, it has made an important contribution to improving the performance of the fault diagnosis model.

Results and Discussion: Experimental results demonstrate that the proposed method achieves higher accuracy compared to existing methods, with an average accuracy of 95.45%, average precision of 88.67%, and average recall of 89.03%. Additionally, the proposed method has a moderate number of model parameters (17,626) and training time (935 s). Results indicate that the proposed method accurately diagnoses faults in flexible converter valve equipment, especially in real-world situations with noise overlapping signals.

KEYWORDS

flexible converter valve equipment, fault diagnosis, feature extraction, depthwise separable convolution, bidirectional gated recurrent unit

1 Introduction

The flexible converter valve equipment is a critical component in power systems as it facilitates the conversion between high-voltage direct current transmission and AC transmission (Zhang X. et al., 2021). Nonetheless, this equipment is susceptible to malfunctions due to its intricate structure and operating environment, thereby potentially affecting the overall operation of the power system (He et al., 2020). Consequently, an effective fault diagnosis method is imperative to ensure the safe and stable operation of the power system.

Currently, fault diagnosis methods mainly include two categories: model-based methods and machine learning methods (Zhang et al., 2023). Model-based methods rely on manual empirical judgment or simple rules for fault diagnosis, e.g., fault tree analysis (Yazdi et al., 2017) and state observer method (Hizarci et al., 2022). These methods suffer from issues such as subjective interpretation, low diagnostic efficiency, and susceptibility to human biases (Zhao et al., 2022). Moreover, model-based methods have limited capabilities in handling complex and variable fault modes as well as large amounts of data (How et al., 2019; Esmail et al., 2023). Additionally, these methods heavily depend on manual feature extraction and rule design for fault diagnosis. Due to the complex and ever-changing nature of flexible converter valve equipment, these methods have limitations in extracting features and designing rules for flexible converter valve equipment (Habibi et al., 2019).

Based on this, researchers proposed fault diagnosis methods for flexible converter valve equipment using machine learning algorithms (Rohouma et al., 2023). For instance, in a study by scholars (Ye et al., 2019), a KFCM and support vector machine algorithm was proposed. This algorithm is capable of quickly and accurately diagnosing faults in analog circuits. To enhance the convergence speed and generalization performance of diagnostic methods, scholars (Muzzammel, 2019) designed a machine learning method to diagnose short faults in High Voltage Direct Current (HVDC) transmission system.

However, the above-mentioned machine learning methods rely on historical data and algorithmic rules for trial and error training. The iterative process automatically adjusts and fine-tunes the model parameters to obtain appropriate results (Abedinia et al., 2016). Due to lack of deep feature extraction, machine learning methods may perform poorly in diagnosing large amounts of data, heterogeneous signals, and complex signals (Zhang et al., 2017).

In recent years, deep learning methods have gained significant popularity in the field of fault diagnosis due to their ability to extract fault features at a deeper level and achieve high diagnostic accuracy (Yuan and Liu, 2022). For instance, in the case of insulator strings on transmission lines, researchers (Zhou et al., 2022) presented deep convolutional generative adversarial network to capture comprehensive fault data characteristics, which enables accurate diagnosis of insulator string faults and defects, even under conditions of strong background noise. To against noise, a steady-state screening model-based feedforward-long short-term memory (FF-LSTM) is proposed to reduce complex variations for lithium-ion batteries (Wang et al., 2022). In addition, an improved anti-noise adaptive long short-term memory (ANA-LSTM) neural network with high-robustness feature extraction and optimal parameter characterization is proposed for accurate RUL prediction for lithium-ion batteries (Wang et al., 2023).

To effectively extract subtle fault features, scholars (Salehi et al., 2023) proposed transfer learning depthwise separable convolutional neural network to address the issue of single-phase-to-ground fault line selection in resonant grounding system. The smaller number of separable convolutional neural network parameters increases the portability of the model (Zhou et al., 2020).

To extend the previously mentioned research methods to flexible converter valve equipment, it is essential to analyze and summarize the fault diagnosis challenges specific to this type of equipment. The following challenges are identified as crucial research opportunities for diagnosing faults in flexible converter valve equipment:

(1) The flexible converter valve equipment has a complex and ever-changing structure and working environment, which leads to nonlinear characteristics in sensor data and increases the difficulty of fault diagnosis.
(2) Flexible converter valve equipment is subject to varying operational conditions, resulting in non-stationary data patterns that can be difficult to analyze and interpret.
(3) In many cases, the available data samples for faulty operations of flexible converter valve equipment are scarce, which makes it challenging to develop accurate models for fault diagnosis.

This article aims to propose a fault diagnosis method for flexible converter valve equipment based on DSC-BiGRU-MAM, and address the research challenges mentioned above. The specific contributions are as follows:

(1) A novel framework is proposed to extract deep features from the data generated by flexible converter valve equipment. This framework leverages advanced deep learning techniques to automatically learn and capture intricate fault patterns, even in the presence of limited fault samples and non-stationary working conditions.
(2) To avoid the disadvantage of neglecting fault categories with smaller sample sizes during the training process, overlapping sampling method is applied to expand categories with smaller sample sizes through. The application of overlapping sampling methods also helps to reduce the risk of overfitting. Because fault categories with smaller sample sizes usually have larger variances, they can easily lead to overfitting problems. By overlapping sampling, it is possible to increase the training samples for these fault categories, reduce overfitting of the model to specific fault categories, and improve the model's generalization ability.
(3) By employing the proposed fault diagnosis models, accurate classification of faults in flexible converter valve equipment can be achieved, thus facilitating timely and effective maintenance actions. As a result, maintenance professionals can take prompt and appropriate actions to address the identified issues, minimizing downtime and maximizing the operational efficiency of the equipment.

2 DSC-BiGRU-MAM method

2.1 Depthwise separable convolution

Convolutional neural networks (CNN) are a type of artificial neural network primarily designed for processing video and image data. As shown in Figure 1A, they excel at extracting features from input images and leveraging these learned features to classify output images (Nguyen et al., 2020). In order to extend the benefits of CNN to text data, a specialized variant known as the 1D Convolutional Neural Network (1DCNN) has been developed and successfully applied in signal processing and sequence data analysis (Junior et al.,

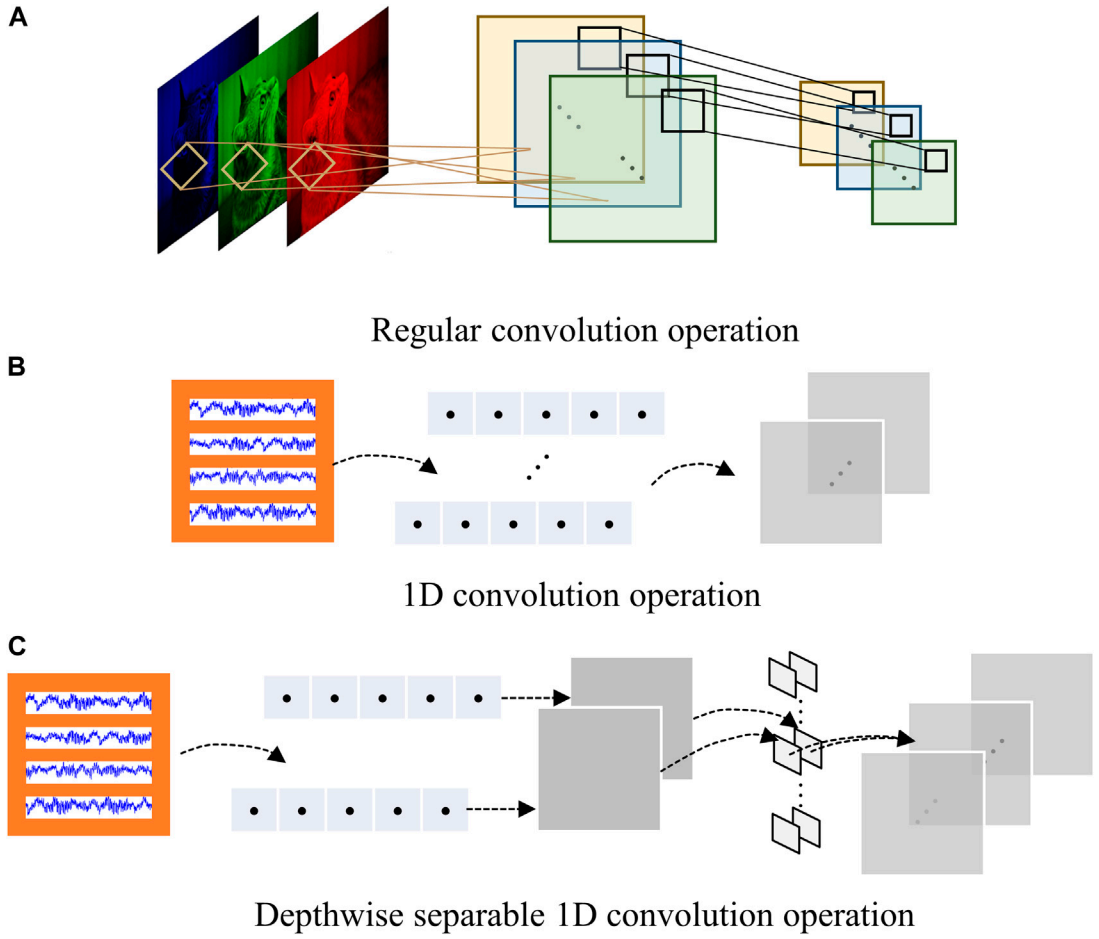

FIGURE 1
The difference between **(A)** Regular convolution layer, **(B)** 1D convolution layer and **(C)** Depthwise separable 1D convolution layer.

2022). As shown in Figure 1B, 1DCNN performs convolution operations on input sequences to extract informative features, enabling it to tackle tasks such as sequence data classification and regression.

1DCNN has the following important characteristics:

(1) The 1D Convolutional Neural Network is capable of capturing local correlations within input sequences. By utilizing convolutional kernels of various sizes, the 1DCNN performs sliding window operations on the input sequences at different scales, extracting local subsequences of varying lengths (Hsu et al., 2022). This ability enables the network to effectively capture local patterns and features present in the input sequence.
(2) In the convolutional layer, each convolutional kernel convolves with the entire input sequence, resulting in the creation of a new feature map. Consequently, the number of parameters that the model needs to learn remains fixed regardless of the length of the input sequence. This parameter sharing mechanism substantially reduces model complexity, leading to increased training efficiency.
(3) 1DCNN can enhance the depth and complexity of the model by stacking multiple convolutional and pooling layers (Xiao et al., 2023). This architecture enables the 1DCNN to perform multi-level feature extraction and abstraction. As a result, the network gradually learns more sophisticated and abstract representations of the input sequence's features. This ability significantly enhances the model's expressive power when dealing with intricate and complex sequence data.

As shown in Figure 1C, depthwise separable convolution decomposes the 1DCNN into two separate operations: depthwise convolution and 1×1 convolution, also known as pointwise convolution (Howard et al., 2017). Assume that input is represented as $X \in \mathbb{R}^{W \times C_{in}}$, output is represented as $Y \in \mathbb{R}^{W' \times C_{out}}$, filter size is represented as $k \times 1$, the depthwise separable convolution operation is shown in Eq. 1:

$$Y_{i,l} = \sum_{m=1}^{k} X_{si+m} \times W_m \times W_{1,m,l} \tag{1}$$

where $Y_{i,l}$ is the i row and l channel of Y, X_{si+m} is $si + m$ row and k channel of X, s is step of filters, W_m and $W_{1,m,l}$ are the weight parameter of depthwise convolution and point-wise convolution.

This technique offers significant advantages by reducing both the number of parameters and the floating-point operations required for the convolutional operation (Salehi et al., 2023).

Depthwise separable 1D-convolution has the following important characteristics:

(1) It reduces the number of parameters compared to traditional convolutional operations. By separating the spatial and channel dimensions, it applies a separate 1×1 convolution on each input channel, followed by a depthwise convolution. As shown in Eq. 2, the difference between regular convolution (R) and depthwise separable convolution (DS) is $C_{in} \times [k \times C_{out} - (k + C_{out})] (> 0)$, which significantly reduces the number of parameters required for the convolution operation.

$$Params = \begin{cases} (C_{in} \times k + 1) \times C_{out}, R \\ C_{in} \times k + C_{out} \times (C_{in} \times 1 + 1), DS \end{cases} \tag{2}$$

(2) It also decreases the overall computation cost. By decomposing the convolution into separate depthwise and pointwise convolutions, it requires fewer floating-point operations, resulting in improved computational efficiency.
(3) It allows for more flexibility in model architecture design. It enables the use of different kernel sizes for the depthwise and pointwise convolutions, providing control over the receptive field and feature representation of the network.
(4) Due to its parameter efficiency and hierarchical structure, it helps prevent overfitting and improve generalization performance on various tasks and datasets.

2.2 Bidirectional gate recurrent unit

In order to consider the temporal correlation in the voltage signal data of the flexible converter valve, it is crucial to utilize Recurrent Neural Networks (RNN) for extracting the trend characteristics of data changes in time series (Bandara et al., 2020). RNNs are a specific type of neural network that take sequence data as input and recur in the direction of sequence evolution, with all nodes (recurrent units) interconnected in a chain. However, a common issue with RNNs is the problem of gradient attenuation. To address this, a solution called Long Short-Term Memory (LSTM) was proposed (Hochreiter and Schmidhuber, 1997). LSTM maintains the model's memory of historical data through input gates, forgetting gates, and output gates, thereby preventing the loss of important information over time (Wang et al., 2023).

Another extension of RNN is the Bidirectional Gate Recurrent Unit (BiGRU), which was presented as a simplified version based on LSTM. It operates in a bidirectional manner, processing the input sequence in both forward and backward directions simultaneously (Zhang Y. et al., 2021). This allows the model to capture information from both past and future contexts, enabling a better understanding of the temporal dependencies in the time series data. The calculation of the BiGRU can be divided into two directions: forward and backward. Forward propagation convolution operation is shown in Eqs 3–6:

$$\overrightarrow{r_t} = \sigma\left(W_{\overrightarrow{xr}} x_t + W_{\overrightarrow{hr}} \overrightarrow{h_{t-1}} + \overrightarrow{b_r}\right) \tag{3}$$

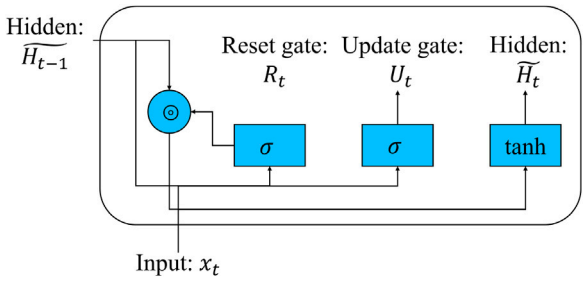

FIGURE 2
The reset gate, update gate, and hidden status of the GRU.

$$\overrightarrow{u_t} = \sigma\left(W_{\overrightarrow{xz}} x_t + W_{\overrightarrow{hz}} \overrightarrow{h_{t-1}} + \overrightarrow{b_u}\right) \tag{4}$$

$$\overrightarrow{\tilde{h}_t} = tanh\left(W_{\overrightarrow{xh}} x_t + W_{\overrightarrow{hh}} \left(\overrightarrow{r_t} \odot \overrightarrow{h_{t-1}}\right) + \overrightarrow{b_h}\right) \tag{5}$$

$$\overrightarrow{h_t} = \left(1 - \overrightarrow{u_t}\right) \odot \overrightarrow{h_{t-1}} + \overrightarrow{u_t} \odot \overrightarrow{\tilde{h}_t} \tag{6}$$

where input sequence is $(x_1, x_2, \cdots, x_t)$, hidden state sequence is $(\overrightarrow{h_1}, \overrightarrow{h_2}, \cdots, \overrightarrow{h_t})$, x_t is the data of input sequence at time step t, $\vec{r}$ represents reset gate, and $\vec{z}$ represents update gate. Backward propagation convolution operation is shown in Eqs 7–10:

$$\overleftarrow{r_t} = \sigma\left(W_{\overleftarrow{xr}} x_t + W_{\overleftarrow{hr}} \overleftarrow{h_{t+1}} + \overleftarrow{b_r}\right) \tag{7}$$

$$\overleftarrow{z_t} = \sigma\left(W_{\overleftarrow{xz}} x_t + W_{\overleftarrow{hz}} \overleftarrow{h_{t+1}} + \overleftarrow{b_z}\right) \tag{8}$$

$$\overleftarrow{\tilde{h}_t} = tanh\left(W_{\overleftarrow{xh}} x_t + W_{\overleftarrow{hh}} \left(\overleftarrow{r_t} \odot \overleftarrow{h_{t+1}}\right) + \overleftarrow{b_h}\right) \tag{9}$$

$$\overleftarrow{h_t} = \left(1 - \overleftarrow{z_t}\right) \odot \overleftarrow{h_{t+1}} + \overleftarrow{z_t} \odot \overleftarrow{\tilde{h}_t} \tag{10}$$

where $\overrightarrow{h_{t-1}}$ and $\overleftarrow{h_{t+1}}$ are the value of forward hidden state at time step $t - 1$ and backward hidden state at time step $t + 1$, respectively.

As shown in Figure 2, the reset gate in BiGRU contributes to capturing short-term dependencies in the time series. By evaluating the current input, it determines which preceding information should be disregarded or updated, enabling the model to concentrate on the pertinent short-term patterns present in the data. The update gate in BiGRU aids in capturing long-term dependencies in the time series. It decides how much of the previous information should be carried forward to the current step, allowing the model to retain important long-term patterns and context in the data.

Overall, the BiGRU architecture provides a balance between computational efficiency and capturing both short-term and long-term dependencies in time series data.

2.3 Multi-head attention mechanism

The attention mechanism is a technique employed to enhance a model's focus on important parts of the input sequence. In sequential data processing tasks, attention mechanisms aid models in autonomously discerning the contributions of

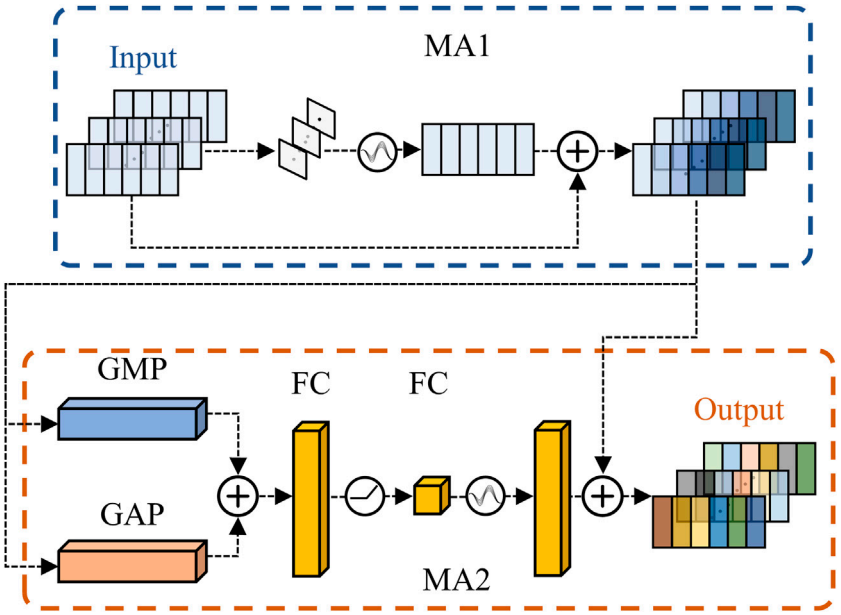

FIGURE 3
Multi-head attention module which enhances fault-related features relying on temporal data and convolutional kernel channels, where GMP, GAP, and FC denote global mean pooling, global average pooling, and fully-connected layer, respectively.

different positions or features to the given task and weighting them based on their significance. By incorporating attention mechanisms, models gain the ability to adaptively attend to various segments of the input sequence. In fault diagnosis tasks, attention mechanisms can direct the model's attention towards signal fragments or features that may be pertinent to faults, thereby enhancing the accuracy and robustness of fault diagnosis. As depicted in Figure 3, the multi-head attention module induces the activation of fault-related features relying on the periodicity of temporal data or the importance of different convolutional kernel channels. It achieves more comprehensive semantic modeling by mapping input sequences into multiple different subspaces and calculating attention weights and weighted summation on each subspace. The proposed multi-head attention module has two attention heads, which can be represented as MA_1 and MA_2, as shown in Eqs 11–13.

$$MA_1 = X + \delta\left(f^{1\times k}\left(\sigma\left(f^{1\times 1}\left(\bar{X} = \max\left(X\right)\right)\right)\right)\right) \tag{11}$$

$$MA_2 = X + \sigma\left(f^{1\times c}\left(\delta\left(f^{1\times \frac{c}{r}}\left(X_{gmp} + X_{gap}\right)\right)\right)\right) \tag{12}$$

$$Y = MA_1\left(X\right) + MA_2\left(MA_1\left(X\right)\right) \tag{13}$$

where δ and σ represent the ReLU function and sigmoid function. $f^{1\times k}$ is the filter with size $1 \times k$. $\bar{X}$ and $max\left(X\right)$ represent the average value and max value from X along the channel axis. $f^{1\times c}$ and $f^{1\times \frac{c}{r}}$ represent fully connected operations with different hidden sizes. X_{gmp} and X_{gap} represent global max pooling and global average pooling operation of input X.

Additionally, the proposed multi-head attention module provides an interpretable approach for understanding the decision-making process of deep learning networks. By analyzing the distribution of attention weights, researchers can discern the network's inclination towards fault features at distinct time points or frequency ranges. This interpretability proves beneficial for subsequent fault analysis and optimization endeavors.

3 Proposed method

The fault diagnosis process of the proposed method is shown in Figure 4, and the main process is as follows:

(1) Preprocessing: In order to augment the data and ensure sample equalization on 1D voltage signals, we employed the overlapping sampling method. Specifically, for each sample type, we generated 300 datasets with overlapping step size determined by the number of fault samples of that type. This technique helped in reducing the class imbalance and ensured that each sample type had an equal representation in the training dataset. Moreover, by generating multiple datasets with varying overlapping sizes, we increased the robustness of the model to variations in the input data.

(2) Feature deep extraction process: The initial stage of our proposed approach involves the utilization of a depthwise separable 1D convolutional kernel measuring 10×1, which applies 40 distinct filters. Subsequently, in the second layer, we incorporate a multi-head attention module. This module encompasses two primary attention components. The first component comprises a 1D convolutional kernel of size 1×1 and 40 depthwise separable 5×1 1D convolutional kernels, which compute significance weights along the temporal

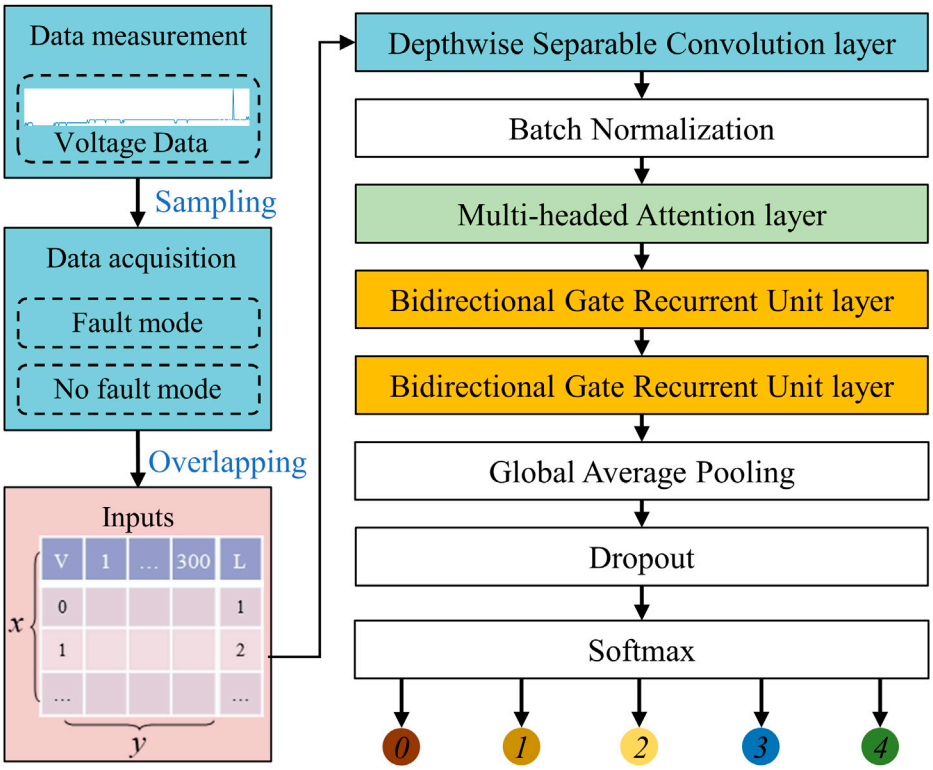

FIGURE 4
Flowchart of the proposed DSC-BiGRU-MAM method.

dimension. The second attention component consists of two fully connected layers, one sized 5 × 1 and another with a size of 40 × 1, which assign weights to individual channels based on their respective importance. Following this, we employ two BiGRU layers to comprehensively extract temporal variation features from the feature maps.

(3) Classifier: The proposed method includes a global average pooling layer, which simplifies the model architecture and facilitates better generalization. Subsequently, the resulting feature maps are fed into a Softmax layer for classification. The model is optimized using a predefined loss function until either the maximum number of iterations is reached or the desired level of accuracy is achieved. Once trained, we evaluate the performance of the model using a distinct test set to determine the effectiveness of the fault diagnosis model. This evaluation helps to ensure that the model can accurately diagnose faults in previously unseen data and is robust enough to handle real-world scenarios.

4 Experimental verification

4.1 Experimental setup

The overall structure of the flexible converter valve equipment is depicted in Figure 5. The control processing device utilizes the FCK611 control chassis, which consists of 1 MC board, 1 recording board, 1 LER board, and 54 SCE boards for networking purposes. A prototype of the flexible converter valve equipment is illustrated in Figure 6. It is notable that in the default configuration, the valve control command is initially received by Receiver 1. If there is a communication fault with Receiver 1, the system switches to Receiver 2. In case of a malfunction with Receiver 1, frame synchronization is instead carried out using Receiver 2.

The flexible converter valve may experience faults or failures, which can result in system instability or even damage. In this article, the main types of faults diagnosed include component fault, fiber optic fault, power supply voltage drop fault, and abnormal flow injection fault. Component fault occurs due to mechanical wear and tear, overheating, or the aging of the valve's components. When a valve fails, it can cause a short circuit, which can lead to a loss of DC voltage and a sudden drop in the converter's output. In addition, a valve failure can produce high-frequency noise, which can interfere with other components in the system. Fiber optic fault in a flexible converter valve refers to a failure or damage to the fiber optic cables that are used for data communication between the different control systems and components of the valve. A fiber optic fault can occur due to various reasons, e.g., mechanical stress, bending, twisting, crushing, or exposure to high temperatures or harsh environments. When a fiber optic cable is damaged, it can result in signal loss or interruption, which can cause the valve to malfunction or even shut down. The power supply voltage drop is a common fault in the flexible converter valve, and it can occur due to a variety of reasons.

10.3389/fenrg.2024.1369360

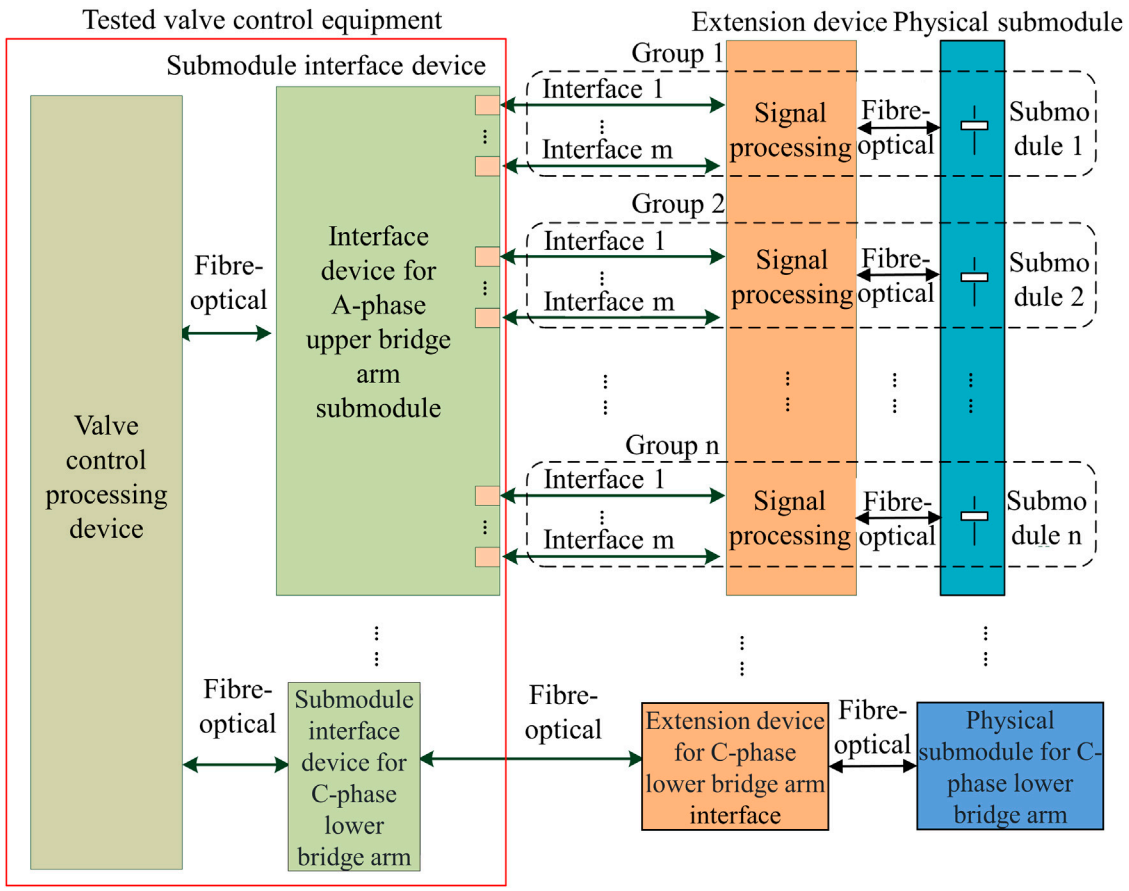

FIGURE 5
Equipment structure diagram.

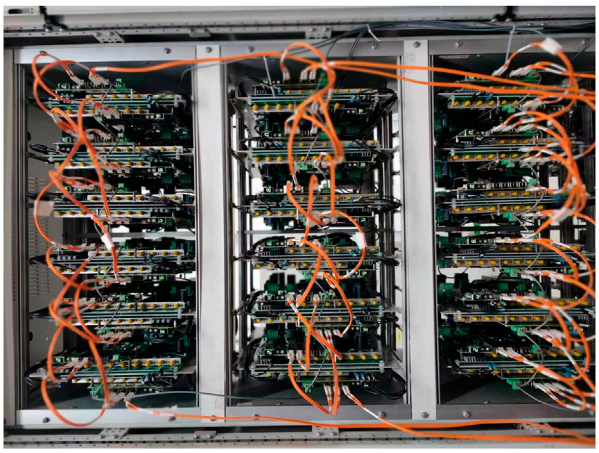

FIGURE 6
Prototype of fiber optic networking dynamic simulation equipment.

FIGURE 7
Using an oscilloscope to collect voltage values of experimental equipment.

The power supply voltage drop in the flexible converter valve can be caused by various factors, including overloading of the power source, loose connections, corrosion in the electrical contacts, or damaged cables or wires. When the voltage drops below the required level, the valve's components may not receive enough power to operate correctly, leading to system instability or even complete

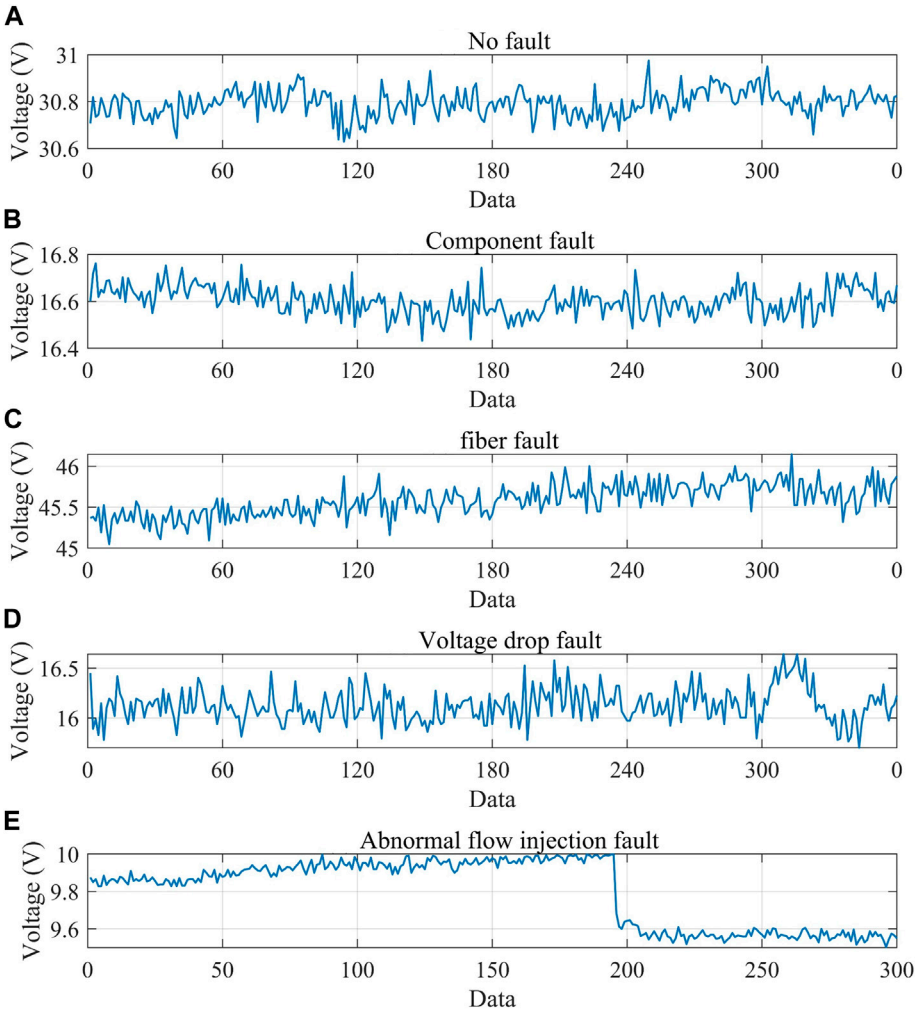

FIGURE 8
Voltage waveform under different faults. **(A)** No fault. **(B)** Component fault. **(C)** Fiber fault. **(D)** Voltage drop fault. **(E)** Abnormal flow injection fault.

failure. An abnormal flow injection fault in a flexible converter valve refers to an unexpected or irregular flow of a medium (e.g., coolant, oil, or gas) into the valve's internal components or control systems. It may be caused by the leak in the valve's seals, gaskets, or connections, foreign particles or contaminants enter the valve, and inadequate maintenance practices.

Data are collected using an oscilloscope, as depicted in Figure 7. The voltage waveform patterns for both normal conditions and different types of faults are presented in Figure 8.

The lengths of fault-free data samples, component fault, fiber fault, voltage drop fault, and abnormal flow injection fault are 22,800, 102,300, 345,600, 526,100, and 125,300, respectively. Each fault scenario is extended to 300 samples with 300 time series data through different overlapping sampling steps based on the sample length of each scenario. In total, 1,500 1D data samples of size 300 are obtained. To simulate data disturbances that may arise from equipment aging, external factors, and other factors during actual operation, we added 10% Gaussian noise to the dataset mentioned earlier. This noise was added to help improve the robustness of the model and ensure its effectiveness in practical applications.

80% of these samples were used for training purposes, while the remaining 20% was utilized for testing. Within the training samples, 20% of the data was allocated for validating the model under this iteration number.

The experiment used Google's TensorFlow deep learning framework, version 2.3. The experiment was conducted in a Windows 11 operating environment, using a simulation device equipped with a Core i7-1165G7 2.8 GHz CPU. The hyper-parameter settings of the model are shown in Table 1. Among

TABLE 1 Model hyperparameter settings.

Optimizer	Loss function	Training	Iterations	Learning rate
Adam	Classification cross entropy	min-batch, batch_size = 16	100	0.001

them, the optimizer selects Adam, the loss function selects classification cross entropy, the training method is min-batch, the batch size is 16, the number of iterations is set to 100, and the learning rate is set to 0.001.

To evaluate the performance of the proposed method, F1-score and Area Under Curve (AUC) are applied, which are range from zero (the worst) to one (the best) and convolution operation is shown in Eqs 14–17:

$$Precision = \frac{TP}{TP + FP} \times 100\% \tag{14}$$

$$Recall = \frac{TP}{TP + FN} \times 100\% \tag{15}$$

$$F1 - score = 2 \times \frac{Precision \times Recall}{Precision + Recall} \times 100\% \tag{16}$$

$$AUC = \frac{\sum_{i \in positiveClass} rank_i - \frac{M(1+M)}{2}}{M \times N} \times 100\% \tag{17}$$

where TP, TN, FP, FN represent true positive, true negative, false positive, and false negative results, respectively. M and N represent numbers of positive and negative samples. $rank_i$ represent the rank of the current number represents how many pairs can be formed between the current number and its preceding number. In this scenario, FP represents diagnosing fault free data as faulty data (i.e., false alarms), and FN represents diagnosing faulty data as fault free data (i.e., missing alarms). Considering that flexible converter valve equipment is a key component of the power grid, avoiding missing alarms should be the first goal, by minimizing false alarms as much as possible.

4.2 Result discussion

(1) Train loss: Figure 9 portrays the loss function indicators of the proposed method throughout the 100 iterations. It is evident that the accuracy and classification cross entropy of the proposed method tend to stabilize during the training process, indicating that the fault diagnosis model has reached a relatively optimal state.

(2) Compared with machine learning methods: Due to the fact that the equipment designed in this article is still in the research and development stage, there are relatively few fault diagnosis methods for this equipment. Based on this, we compared classic fault diagnosis methods for similar devices, e.g., Support Vector Machines [SVM (Ye et al., 2019)], K-Nearest Neighbors [KNN (Chen, et al., 2023)], Random Forests [RF (Movahed et al., 2023)], Logistic Regression [LR (Mirsaeidi et al., 2018)], and Back Propagation Neural Networks [BPNN (Liu and Wang, 2023)]. The comparison results between the above method and the method proposed in this article are shown in Table 2. From the results, it can be seen that the F1-score and AUC of the proposed method in this article are significantly higher than classical methods under similar devices, indicating that the use of deep separable convolution and BiGRU has a positive impact on fault related feature extraction.

(3) Compared with deep learning methods: Under the same parameter configuration, the proposed method with multiple methods, and the model structures of different methods are shown in Table 3. Among them, Model 1, Model 2, Model 3, Model 4 and Model 5 do not contain

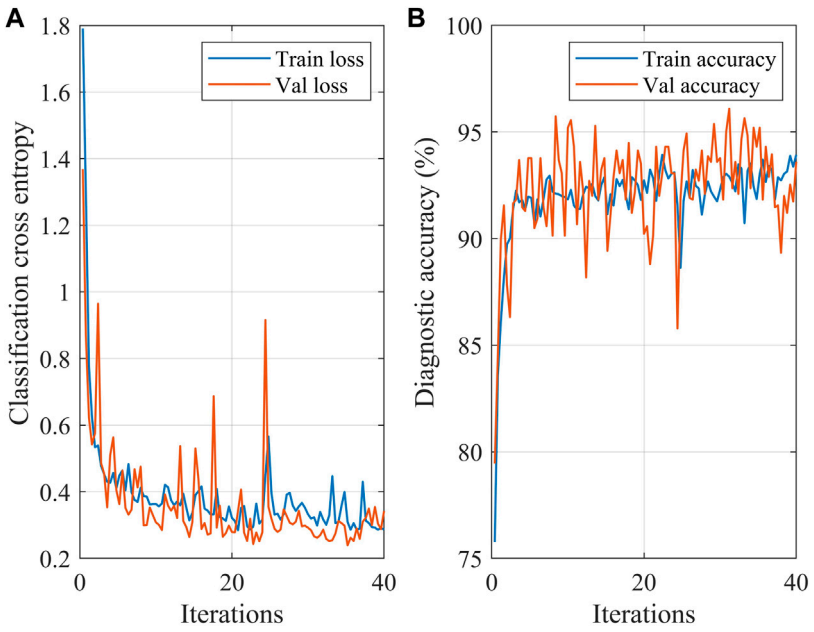

FIGURE 9
Loss and diagnostic accuracy within 100 iterations under 10% Gaussian noise. Results indicate that loss and accuracy tend to stabilize during the training process.

TABLE 2 Results of different fault diagnosis methods.

Fault rate	Metrics	10 (%)	30 (%)	50 (%)
Proposed	F1-score	89.33	91.2	86.67
	AUC	95.56	96.05	92.67
SVM	F1-score	35.2	29.07	32.27
	AUC	59.5	55.67	57.67
KNN	F1-score	25.6	22.67	21.87
	AUC	53.5	51.67	51.17
RF	F1-score	83.87	82.53	83.07
	AUC	86.17	85.33	85.67
LR	F1-score	63.73	59.73	64.27
	AUC	77.33	74.83	77.67
BPNN	F1-score	85.73	85.2	84.27
	AUC	87.73	87	87.67

TABLE 3 Model structure of different methods, where "+" denotes serial connection. For instance, "1 layer of DSC + 1 layer of MAM + 2 layers of BiGRU" of Model 9 indicates that the structure of Model 9 is a DSC operation in the first layer, a MAM operation in the second layer, two BiGRU operations in the third and fourth layers. All models adopt global average pooling, Dropout and Softmax operation in the last layer.

Model name	Model structure
Model 1	3 layers of GRU
Model 2	3 layers of BiGRU
Model 3	3 layers of LSTM
Model 4	3 layers of BiLSTM
Model 5	1 layer of DSC + 2 layers of BiGRU
Model 6	1 layer of DSC + 1 layer of SE + 2 layers of BiGRU
Model 7	1 layer of DSC + 1 layer of CBAM + 2 layers of BiGRU
Model 8	1 layer of DSC + 1 layer of JAM + 2 layers of BiGRU
Model 9 (Proposed)	1 layer of DSC + 1 layer of MAM + 2 layers of BiGRU

attention modules, which are used to compare the accuracy of model that only consists of the BiGRU layer, the model that only consists of the BiLSTM layer and mixed models in fault diagnosis. Model 6, Model 7, Model 8, and Model 9 are all based on a mixture of Depthwise separable 1D Conv (DSC) and BiGRU models. After the DSC layer, the Squeeze and Excitation (SE) attention module (Li et al., 2018), Convolutional Block Attention Module (CBAM) module (Woo et al., 2018), Joint Attention Module (JAM) module (Wang et al., 2019), and multi-head Attention Module (MAM) module are added, respectively.

Figure 10 demonstrates the characteristics of fault-related data (original signal in Figure 10A and frequency of signal in Figure 10B) after undergoing depthwise separable 1D convolution operation (in Figure 10C), multi-head attention operation (in Figure 10D), two BiGRU operations (in Figures 10E, F). It is evident that the fault-related data (represented by black dashed box) exhibit more distinct features compared to other time periods. Furthermore, other time periods' noise data is effectively filtered out.

Figure 11A illustrates the average diagnostic accuracy, precision, and recall of the aforementioned models under 10%, 30%, and 50% Gaussian noise levels. Among them, precision refers to the proportion of samples correctly predicted as a specific fault among all the test samples, while recall represents the proportion of samples accurately predicted as a specific fault among all the test samples. Both of these evaluation metrics are commonly used to assess the performance of fault diagnosis models when dealing with imbalanced samples. The results indicate that the proposed method achieves the highest diagnostic accuracy among the repeated experiments, with an average of 95.45%, surpassing the second-highest method by 0.76%. This outcome suggests that the proposed method can accurately diagnose the five fault situations of the flexible converter valve equipment.

Based on Figure 11B, it is evident that the proposed method outperforms the comparative methods in terms of F1-score, AUC, and generalization. Results suggest that the proposed method can accurately diagnose the five fault situations with F1-score of 89.06% and AUC of 94.76% related to the flexible converter valve equipment.

In addition, this study also compared the accuracy, precision, and recall of different models under Gaussian noise levels of 10%, 30%, and 50%, as shown in Figures 12–14. The reason for choosing these noise levels is that they represent varying degrees of noise interference. 10% noise level represents lower noise interference, 30% noise level represents moderate noise interference, and 50% noise level represents higher noise interference. By considering these different levels, the performance and robustness of the model can be evaluated and compared under different levels of noise. The results indicate that the proposed method achieved the highest accuracy metrics under all Gaussian noise levels. As the proportion of Gaussian noise increases, the accuracy metrics of all methods affected. However, due to the deep extraction of fault features, the proposed method has the minimum fluctuation of accuracy indicators. This also demonstrates the strong tolerance of the proposed method to noise during the actual operation of the device, maintaining high diagnostic accuracy even in the presence of data deviations caused by aging or other factors.

(4) Model efficiency: Figure 15 provides insights into parameters and time required for one iteration of the nine fault diagnosis models. In this figure, the blue line represents the model parameter quantity, while the red line represents the running time of one iteration. Model parameters refer to the number of weights, biases, and other learnable parameters in a model. The number of model parameters is usually proportional to the complexity of the model. More complex models typically have more parameters, requiring more computational resources and time for training. Choosing model parameters as a metric helps evaluate the complexity and availability of the model. Training deep learning models often requires significant computational resources and time. Iteration time refers to the time taken to complete one training iteration. Shorter

10.3389/fenrg.2024.1369360

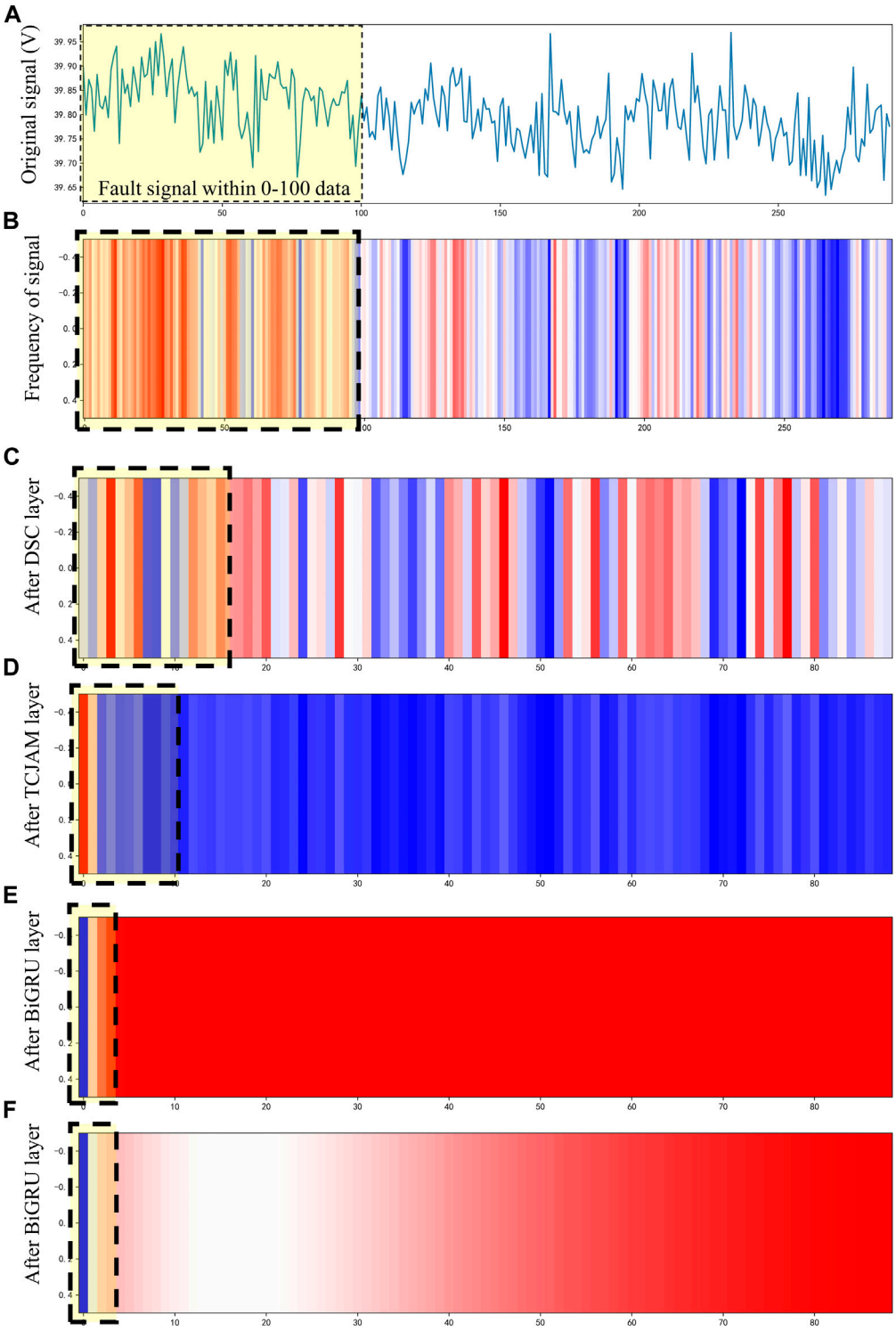

FIGURE 10
After extracting features, the data features are clearly polarized. **(A)** Original signal. **(B)** Frequency of signal. **(C)** After DSC layer. **(D)** After MAM layer. **(E)** After BiGRU layer. **(F)** After BiGRU layer.

iteration time means the model can complete training faster, thereby accelerating the speed of fault diagnosis processes. Additionally, shorter iteration time makes it easier to scale the model to large-scale datasets and more complex fault scenarios.

Based on the results, it is apparent that the proposed method has a moderate number of model parameters (17,626 parameters) and requires a reasonable amount of time for one iteration (approximately 935 s). Although the model parameters and training time of methods M1 and M3 are slightly lower than

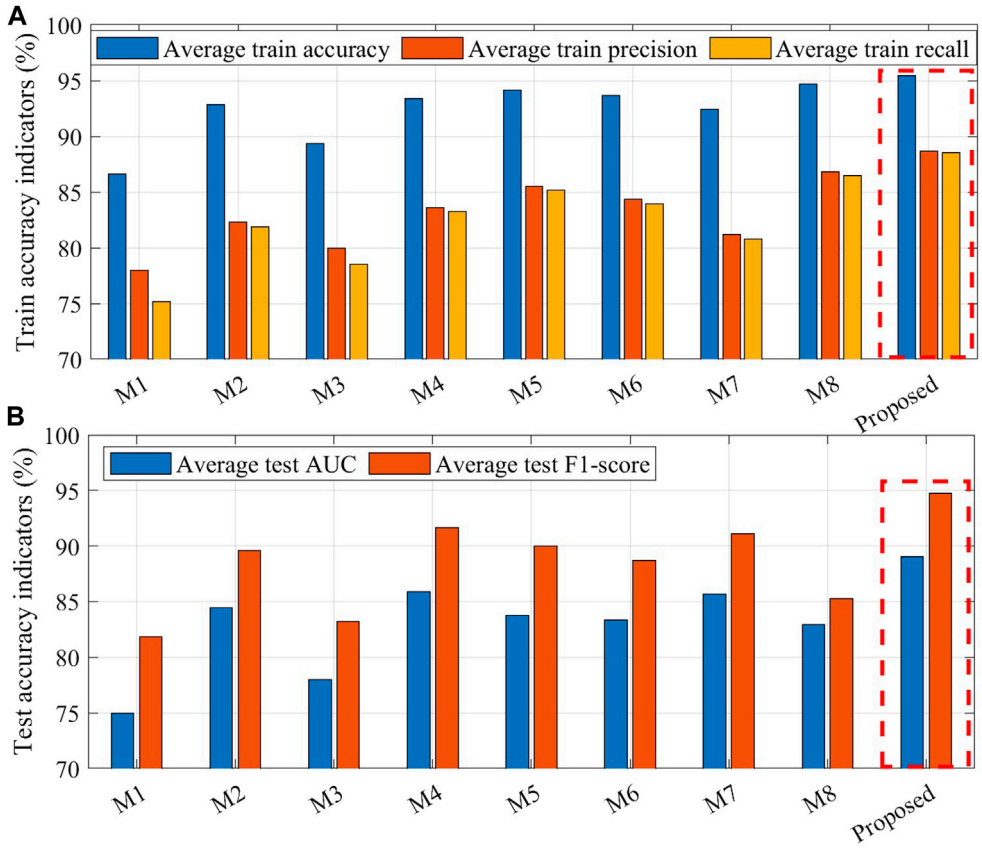

FIGURE 11
Accuracy indicators of different methods under 10%, 30%, and 50% Gaussian noise levels, where training results are shown as average diagnostic accuracy, precision, and recall in **(A)**, testing results are shown as average F1-score, AUC in **(B)**.

those of the proposed method, the diagnostic accuracy indicators of M1 and M3 methods are significantly lower than those of the proposed method. Considering the diagnostic accuracy and other indicators, it can be concluded that the proposed method achieves the highest diagnostic accuracy compared to the other methods. Additionally, the model's parameter quantity and training time are also within acceptable ranges.

(5) Limitation of the proposed method: Although the experimental results illustrate that the proposed method can effectively diagnose the faults, the equipment diagnosed in the experiment is only a submodule of the flexible converter valve equipment. The impact of signal aliasing and the coupling of multiple submodule faults after the integration of multiple identical submodules in the practical application are not considered in this paper.

In practical applications, important faults usually need to pay more attention and higher priority in handling. Correspondingly, faults slightly impact the system are usually receiving little attention. The proposed method did not consider the importance of faults and provided preferential training based on the fault situation to ensure that important faults receive sufficient training.

5 Conclusion

This study addresses the limitations of diagnostic accuracy in flexible converter valve equipment by using DSC-BiGRU-MAM method. To evaluate the effectiveness of the proposed method, multiple fault data are acquired from the flexible converter valve through experimental methods. The data was enhanced balanced using overlapping sampling techniques. The results demonstrate that the proposed method can accurately diagnose the mentioned faults of flexible converter valve equipment in this paper. Compared to the comparative method, the proposed method exhibits higher accuracy (with an average diagnostic accuracy of 95.45%) and robustness (with a maximum difference in diagnostic accuracy of 0.76% across multiple experimental results), enabling more precise detection and diagnosis of various faults. The utilization of the proposed multi-head attention module enables achieving precise classification of faults in flexible converter valve equipment, which ultimately leads to facilitating timely and effective maintenance actions. Based on this, we can effectively extract informative features from raw sensor data and accurately identify different fault categories in the valve equipment. The proposed method can achieve good results in diagnosing voltage signals in different noise environments, and can be

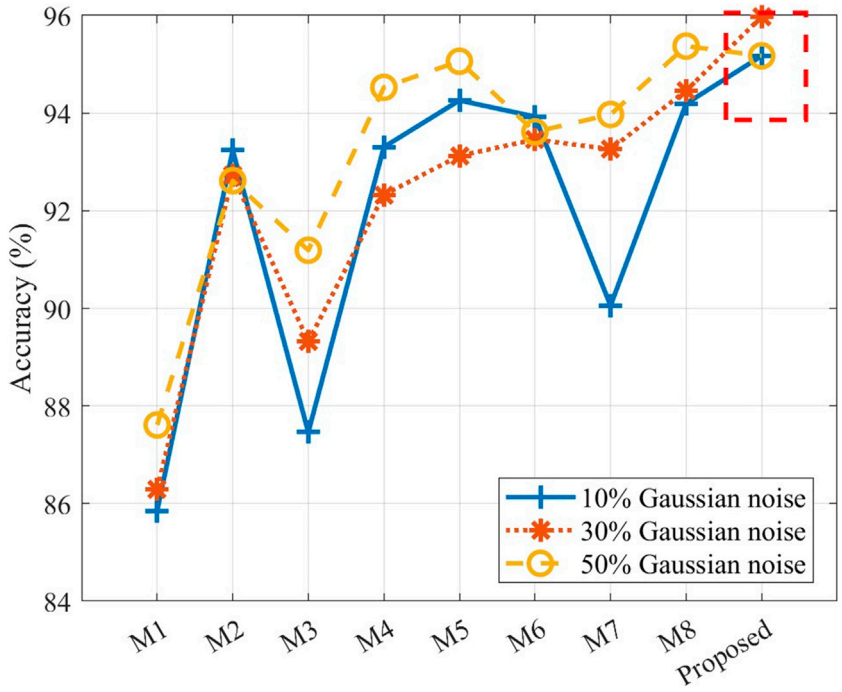

FIGURE 12
Accuracy of different method under Gaussian noise levels of 10%, 30%, and 50%.

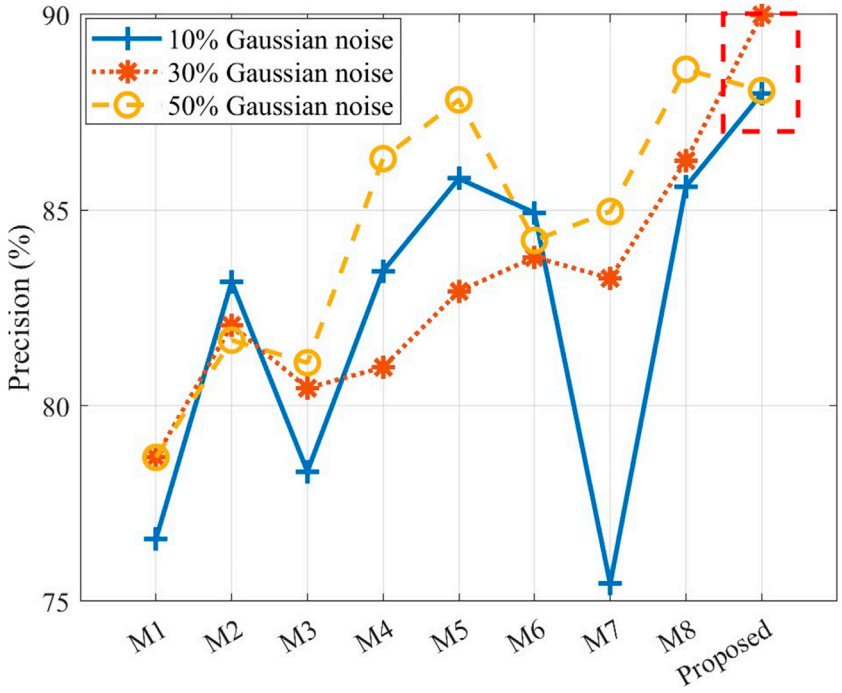

FIGURE 13
Precision of different method under Gaussian noise levels of 10%, 30%, and 50%.

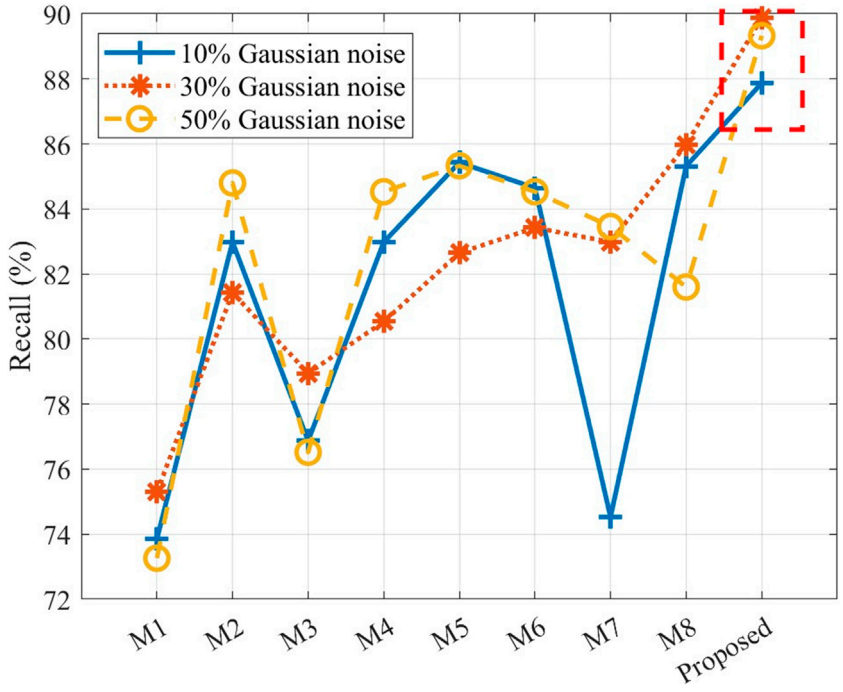

FIGURE 14
Recall of different method under Gaussian noise levels of 10%, 30%, and 50%.

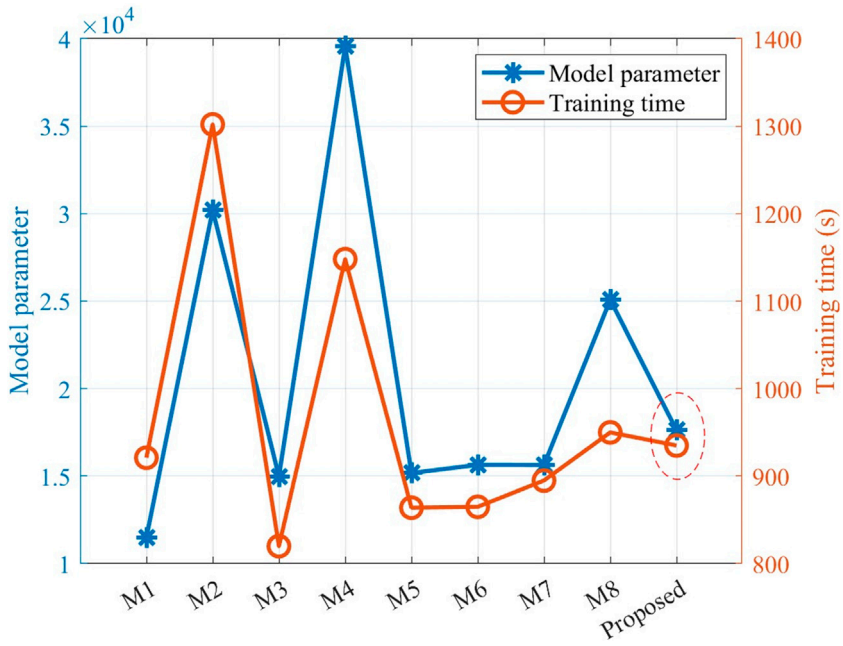

FIGURE 15
Parameter and training time of different methods.

transferred into similar scenarios model fine-tuning by where voltage signals can reflect fault status, e.g., cable faults, circuit board faults, transformer faults.

In addition, smaller model size and less training time contribute to minimizing downtime and maximizing the operational efficiency of the equipment. In this way, the

proposed method can be embedded into IoT device to achieve edge computing, reducing redundant data transmission and fault response time.

In the future, there is great potential for further optimization of both the model structure and algorithms in fault diagnosis. One aspect that can be considered is the importance of different faults. By assigning priority levels to each fault, the fault diagnosis system can determine which faults are more critical or have a higher impact on system performance. This allows for a prioritized approach to fault handling, ensuring that the most important faults are addressed first. To implement such prioritization, the fault diagnosis system can incorporate techniques such as fault severity assessment or fault criticality analysis. These techniques can provide a quantitative measure of the impact of each fault on system operation, allowing the system to make informed decisions regarding fault handling priorities.

Data availability statement

The raw data supporting the conclusion of this article will be made available by the authors, without undue reservation.

Author contributions

JG: Conceptualization, Data curation, Funding acquisition, Project administration, Writing–original draft. HL: Conceptualization, Writing–review and editing. LF: Data curation, Writing–review and editing. LZ: Data curation, Investigation, Writing–review and editing.

Funding

The author(s) declare financial support was received for the research, authorship, and/or publication of this article.

Acknowledgments

Authors greatly thank for the fund support of Innovation Project of China Southern Power Grid Co., Ltd.

Conflict of interest

Authors JG, HL, and LF were employed by EHV Maintenance and Test Center of China Southern Power Grid. Author LZ was employed by XJ Electric Flexible Transmission Company.

The authors declare that this study received funding from the Innovation Project of China Southern Power Grid Co., Ltd. (CGYKJXM20220059). The funder had the following involvement in the study: Conceptualization, Data curation, Writing–original draft, Writing–review and editing.

Publisher's note

All claims expressed in this article are solely those of the authors and do not necessarily represent those of their affiliated organizations, or those of the publisher, the editors and the reviewers. Any product that may be evaluated in this article, or claim that may be made by its manufacturer, is not guaranteed or endorsed by the publisher.

References

Abedinia, O., Amjady, N., and Zareipour, H. (2016). A new feature selection technique for load and price forecast of electrical power systems. *IEEE T. Pow. Sys.* 32 (1), 62–74. doi:10.1109/TPWRS.2016.2556620

Bandara, K., Bergmeir, C., and Smyl, S. (2020). Forecasting across time series databases using recurrent neural networks on groups of similar series: a clustering approach. *Expert Syst. Appl.* 140, 112896. doi:10.1016/j.eswa.2019.112896

Chen, Q., Li, Q., Wu, J., He, J., Mao, C., Li, Z., et al. (2023). State monitoring and fault diagnosis of hvdc system via knn algorithm with knowledge graph: a practical China power grid case. *Sustainability* 15 (4), 3717. doi:10.3390/su15043717

Esmail, E. M., Alsaif, F., Abdel Aleem, S. H., Abdelaziz, A., Yadav, A., and El-Shahat, A. (2023). Simultaneous series and shunt earth fault detection and classification using the Clarke transform for power transmission systems under different fault scenarios. *Front. Energy Res.* 11, 1208296. doi:10.3389/fenrg.2023.1208296

Habibi, H., Howard, I., and Simani, S. (2019). Reliability improvement of wind turbine power generation using model-based fault detection and fault tolerant control: a review. *Renew. Energy* 135, 877–896. doi:10.1016/j.renene.2018.12.066

He, J., Chen, K., Li, M., Luo, Y., Liang, C., and Xu, Y. (2020). Review of protection and fault handling for a flexible dc grid. *Prot. Con. Mod. Pow. Syst.* 5, 15. doi:10.1186/s41601-020-00157-9

Hizarci, B., Kıral, Z., and Şahin, S. (2022). Optimal extended state observer based control for vibration reduction on a flexible cantilever beam with using air thrust actuator. *Appl. Acoust.* 197, 108944. doi:10.1016/j.apacoust.2022.108944

Hochreiter, S., and Schmidhuber, J. (1997). Long shortterm memory. *Neural Comput.* 9 (8), 1735–1780. doi:10.1162/neco.1997.9.8.1735

How, D., Hannan, M., Lipu, M., and Ker, P. (2019). State of charge estimation for lithium-ion batteries using model-based and data-driven methods: a review. *IEEE Access* 7, 136116–136136. doi:10.1109/ACCESS.2019.2942213

Howard, A., Zhu, M., Chen, B., Kalenichenko, D., Wang, W., Weyand, T., et al. (2017). Mobilenets: efficient convolutional neural networks for mobile vision applications. arXiv preprint arXiv:1704.04861.

Hsu, C., Lu, Y., and Yan, J. (2022). Temporal convolution-based long-short term memory network with attention mechanism for remaining useful life prediction. *IEEE T. Semicond. M.* 35 (2), 220–228. doi:10.1109/TSM.2022.3164578

Junior, R., Areias, I., Campos, M., Teixeira, C., Silva, L., and Gomes, G. (2022). Fault detection and diagnosis in electric motors using 1d convolutional neural networks with multi-channel vibration signals. *Measurement* 190, 110759. doi:10.1016/j.measurement.2022.110759

Li, H., **ong, P., An, J., and Wang, L. (2018). Pyramid attention network for semantic segmentation. arxiv preprint arxiv:1805.10180.

Liu, S., and Wang, S. (2023). Fault location of flexible dc system based on bp neural network. *Eighth Int. Symposium Adv. Electr. Electron. Comput. Eng. (ISAEECE 2023)* 12704, 640–645. doi:10.1117/12.2680124

Mirsaeidi, S., Dong, X., Tzelepis, D., Said, D., Dy´sko, A., and Booth, C. (2018). A predictive control strategy for mitigation of commutation failure in lcc-based hvdc systems. *IEEE T. Power Electr.* 34 (1), 160–172. doi:10.1109/TPEL.2018.2820152

Movahed, P., Taheri, S., and Razban, A. (2023). A bi-level data-driven framework for fault-detection and diagnosis of hvac systems. *Appl. Energy* 339, 120948. doi:10.1016/j.apenergy.2023.120948

Muzzammel, R. (2019). "Machine learning based fault diagnosis in hvdc transmission lines," in Intelligent Technologies and Applications: First International Conference, 496–510.

Nguyen, N., Do, T., Ngo, T., and Le, D. (2020). An evaluation of deep learning methods for small object detection. *J. Electr. Comput. Eng.* 2020, 1–18. doi:10.1155/2020/3189691

Rohouma, W., Abdelkader, S., Ernest, E. F., Megahed, T. F., and Abdel-Rahim, O. (2023). A model predictive control strategy for enhancing fault ride through in PMSG wind turbines using SMES and improved GSC control. *Front. Energy Res.* 11, 1277954. doi:10.3389/fenrg.2023.1277954

Salehi, A., Khan, S., Gupta, G., Alabduallah, B., Almjally, A., Alsolai, H., et al. (2023). A study of cnn and transfer learning in medical imaging: advantages, challenges, future scope. *Sustainability* 15 (7), 5930. doi:10.3390/su15075930

Wang, H., Liu, Z., Peng, D., and Qin, Y. (2019). Understanding and learning discriminant features based on multiattention 1DCNN for wheelset bearing fault diagnosis. *IEEE T. Ind. Inf.* 16 (9), 5735–5745. doi:10.1109/TII.2019.2955540

Wang, S., Fan, Y., **, S., Takyi-Aninakwa, P., and Fernandez, C. (2023). Improved anti-noise adaptive long short-term memory neural network modeling for the robust remaining useful life prediction of lithium-ion batteries. *Reliab. Eng. Syst. Safe.* 230, 108920. doi:10.1016/j.ress.2022.108920

Wang, S., Takyi-Aninakwa, P., **, S., Yu, C., Fernandez, C., and Stroe, D. I. (2022). An improved feedforward-long short-term memory modeling method for the whole-life-cycle state of charge prediction of lithium-ion batteries considering current-voltage-temperature variation. *Energy* 254, 124224. doi:10.1016/j.energy.2022.124224

Wang, S., Wu, F., Takyi-Aninakwa, P., Fernandez, C., Stroe, D. I., and Huang, Q. (2023). Improved singular filtering-Gaussian process regression-long short-term memory model for whole-life-cycle remaining capacity estimation of lithium-ion batteries adaptive to fast aging and multi-current variations. *Energy* 284, 128677. doi:10.1016/j.energy.2023.128677

Woo, S., Park, J., Lee, J. Y., and Kweon, I. S. (2018). "Cbam: convolutional block attention module," in Proceedings of the European conference on computer vision (ECCV), 3–19.

Xiao, F., Chen, T., Zhang, J., and Zhang, S. (2023). Water management fault diagnosis for proton-exchange membrane fuel cells based on deep learning methods. *Int. J. Hydrogen Energy.* 48, 28163–28173. doi:10.1016/j.ijhydene.2023.03.097

Yazdi, M., Nikfar, F., and Nasrabadi, M. (2017). Failure probability analysis by employing fuzzy fault tree analysis. *Int. J. Syst. Assur. Eng. Manag.* 8, 1177–1193. doi:10.1007/s13198-017-0583-y

Ye, Y., Zheng, J., and Mei, F. (2019). "Research on upfc fault diagnosis based on kfcm and support vector machine," in 2019 14th IEEE Conference on Industrial Electronics and Applications (ICIEA), 650–655. doi:10.1109/iciea.2019.8834208

Yuan, Z., and Liu, J. (2022). A hybrid deep learning model for trash classification based on deep trasnsfer learning. *J. Electr. Comput. Eng.* 2022, 1–9. doi:10.1155/2022/7608794

Zhang, C., Zhao, S., Yang, Z., and He, Y. (2023). A multi-fault diagnosis method for lithium-ion battery pack using curvilinear Manhattan distance evaluation and voltage difference analysis. *J. Energy Sto.* 67, 107575. doi:10.1016/j.est.2023.107575

Zhang, W., Peng, G., Li, C., Chen, Y., and Zhang, Z. (2017). A new deep learning model for fault diagnosis with good anti-noise and domain adaptation ability on raw vibration signals. *Sensors* 17 (2), 425. doi:10.3390/s17020425

Zhang, X., Cong, Y., Yuan, Z., Zhang, T., and Bai, X. (2021). Early fault detection method of rolling bearing based on mcnn and gru network with an attention mechanism. *Shock Vib.* 2021, 1–13. doi:10.1155/2021/6660243

Zhang, Y., Luo, W., Sun, X., Zheng, Q., Zhao, C., and Chen, H. (2021). Multi‐physical field coupling simulation analysis of flexible HVDC converter valve power module based on clamping IGBT element. *Hi. Vol. App* 57 (11), 84–92. doi:10.13296/j.1001‐1609.hva.2021.11.011

Zhao, Z., Liu, X., and Gao, J. (2022). Model-based fault diagnosis methods for systems with stochastic process–a survey. *Neurocomputing* 513, 137–152. doi:10.1016/j.neucom.2022.09.134

Zhou, N., Liang, R., and Shi, W. (2020). A lightweight convolutional neural network for real-time facial expression detection. *IEEE Access* 9, 5573–5584. doi:10.1109/ACCESS.2020.3046715

Zhou, S., Pan, B., Lu, D., Zhong, Y., and Wang, G. (2022). Fault diagnosis method for uhvdc transmission based on deep learning under cloudedge architecture. *J. Electr. Comput. Eng.* 2022, 1–7. doi:10.1155/2022/1592426

frontiers | Frontiers in Energy Research

TYPE Original Research
PUBLISHED 20 June 2024
DOI 10.3389/fenrg.2024.1408924

OPEN ACCESS

EDITED BY
Chaolong Zhang,
Jinling Institute of Technology, China

REVIEWED BY
Suwarno Suwarno,
Bandung Institute of Technology, Indonesia
Elena Helerea,
Transilvania University of Brașov, Romania

*CORRESPONDENCE
Huang Yonghao,
huangyonghao0327@163.com

RECEIVED 29 March 2024
ACCEPTED 29 May 2024
PUBLISHED 20 June 2024

CITATION
Yonghao H, Shuheng D and Zhiyuan L (2024), Study on the optimum value of remanent magnetism for suppressing ferromagnetic resonance of voltage transformer in all-cable line.
Front. Energy Res. 12:1408924.
doi: 10.3389/fenrg.2024.1408924

Study on the optimum value of remanent magnetism for suppressing ferromagnetic resonance of voltage transformer in all-cable line

Huang Yonghao*, Dan Shuheng and Liu Zhiyuan

Shanghai University of Electric Power, College of Electrical Engineering, Shanghai, China

Introduction: Due to the need for safety and aesthetics, 10 kV urban power grids are gradually dominated by all-cable lines. However, this trend also brings new challenges. Cables, which are equivalent to capacitors at industrial frequency, are prone to resonate with the voltage transformers (PTs) in the system, causing drastic changes in current and voltage and posing a threat to the stable operation of the system. In addition, the intrusion of lightning waves into the substation will lead to different residual magnetization in the PT core, which further changes the core inductance value and affects the ferromagnetic resonance of the system to a certain extent.

Methods: In order to deeply investigate the influence of remanent magnetism on the ferromagnetic resonance of the system, this paper establishes a simulation model of a 10 kV all-cable line based on the PSCAD software, and adopts a UMEC transformer capable of simulating the saturation characteristics to construct the PT, and simulates the intrusion currents by using a DC current source in order to generate remanent magnetism. By this method, the effect of remanent magnetization on the ferromagnetic resonance of the system is explored at different magnitudes and directions.

Results: The results of the study show that the residual magnetization has a significant effect on the ferromagnetic resonant inrush current of the voltage transformer. When the remanent magnetization value is positive and less than 0.6 pu, the ferromagnetic resonance inrush current of PT can be effectively suppressed, and the smaller the remanent magnetization value is, the better the suppression effect is. However, negative remanent magnetization cannot suppress the ferromagnetic resonance of the PT, but may exacerbate the inrush current, leading to more serious consequences.

Conclusion: This study helps to improve the stability of the power grid and also provides a valuable reference for future grid design and maintenance.

KEYWORDS

all-cable line, ferromagnetic resonance, voltage transformer, lightning incursion wave, residual magnetism

1 Introduction

Cable lines have the advantages of long service life, large communication capacity, stable transmission quality, small external interference, good confidentiality, etc., Nowadays, with the continuous development of cities, more and more overhead lines are replaced by cables (Liu, 2024; Zheng et al., 2024). In the 10 kV system, the proportion of all-cable lines is increasing, which will lead to an increase in the capacitance to ground in the system, providing the necessary conditions for the occurrence of ferromagnetic resonance. Ferromagnetic resonance is a common resonance phenomenon in power systems, which is mainly caused by the saturation of nonlinear iron cores (Cao et al., 2023). Ferromagnetic resonance will lead to continuous oscillation of system voltage, resulting in voltage instability and power quality degradation; the current increase caused by resonance will lead to an increase in the copper loss and iron loss of the power equipment, thus causing overheating of the equipment, and the appearance of these situations is extremely destructive both for the power system and the electrical equipment (Chen et al., 2024).

For the core of a PT, saturation is one of its inherent properties (Kulkarni and Khaparde, 2004; Dasgupta, 2005; Vecchio and Poulin, 2010). The cable line is capacitive to ground, while the excitation impedance of the PT is large and the core is inductive. When the system is in normal operation, the inductive impedance is larger than the capacitive impedance exhibited in the circuit, and the neutral voltage offset is small; when certain non-simultaneous operations occur in the power system, for example, asymmetrical closing operation of a certain phase of the circuit breaker in the cable line (Chen, 2022), and abnormal switching of the circuit breaker of the shunt capacitor bank (Wang et al., 2022), etc., the inconsistency in the volt-ampere characteristic of the PT will lead to the saturation of the iron core, and it will cause a serious ferro-magnetic resonance phenomenon (Andrei et al., 1989; Zhong et al., 2021); in the actual power system, when lightning weather occurs so that the overhead lines on the adjacent system is struck by lightning, although the lightning arrester will be a strong inrush current into the earth, but in a short time there will still be a part of the continuation of the current along the transmission line propagation and ultimately invade the power system, which will lead to changes in the magnetic field around the core within the PT, the residual remanence of magnetic field will, to a certain extent, affect the ferromagnetic resonance of the system. Ferromagnetic resonance of the system.

In the existing literature to analyze the influence factors of PT ferromagnetic resonance characteristics mainly focus on the internal parameter factors, such as the different values of the distribution line parameters (Chen et al., 2021), the different parameters of the PT body (hysteresis loss, leakage magnetism, etc.) (Ping and Wang, 2004), the different types of faults occurring (whether or not the neutral point is grounded) (Wang, 2021), etc., and very few studies have taken into account the effect of the remanent magnetism that exists in the PT iron core on the ferromagnetic resonance generated by the system. In this paper, the 3/5 core UMEC (unified magnetic equivalent circuit) transformer in PSCAD software is used to simulate the PT (Zhang and Wen, 2009), and a DC current source is used to simulate the remanent magnetism, taking phase A as an example, connecting the DC current source to phase A of the PT and withdrawing the excitation after 1 s, and then changing the magnitude and direction of the current to change the magnitude and direction of the remanent magnetism. The size and direction of the residual magnetism is changed by changing the size and direction of the current, and the waveform of the line current of phase A of the voltage transformer is observed to analyze whether ferromagnetic resonance occurs in the PT under this operation, and to propose the effective suppression measures of the residual magnetism on the ferromagnetic resonance of the PT according to the simulation results.

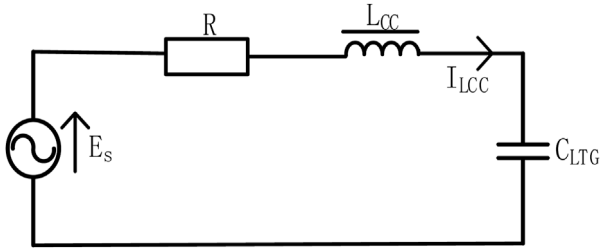

FIGURE 1
Basic principle of ferromagnetic resonance.

2 Ferromagnetic resonance principle

PT is a special transformer used to convert high voltage to low voltage for use by measurement or protection equipment, and its main functions include the following three points (Liu et al., 2024): 1. Reducing the high voltage in the power system to a standard value (e.g., 110 V or 100 V), so that the voltage can be monitored and recorded using a standard measuring instrument without direct contact with the high-voltage line; 2. PT provides voltage signals for the protection relay to identify abnormal conditions such as overvoltage or undervoltage and trigger the corresponding protection action. 3. Provides voltage signals for identifying abnormal conditions such as overvoltage or undervoltage and triggering the appropriate protective action; 3. Voltage transformers provide electrical isolation, protecting downstream measuring equipment, personnel and systems from the direct effects of high voltage. When ferromagnetic resonance occurs, the basic schematic is shown in Figure 1 (Zhao, 2018; Yaohua et al., 2019).

The relationship between the electric potential E_S and the inductor voltage $U_{L_{CC}}$ and the capacitor voltage $U_{C_{LTG}}$ can be obtained, see Eq. 1.

$$E_s = U_{L_{CC}} - U_{C_{LTG}} \tag{1}$$

The ground capacitive reactance $X_{C_{LTG}}$ of the line is greater than or equal to the inductive reactance $X_{L_{CC}}$ of the component coils, which makes the core saturated (Gbt, 2020; Quan and Li, 2022), and the line undergoes series resonance (Sa, 2021), the relationship between which is shown in Eq. 2, and the fault will generate a sufficiently large electromagnetic inrush current; in the series resonant loop, the angular frequency ω_0 is equal to 2π times of the power supply frequency f_0, which is converted into the

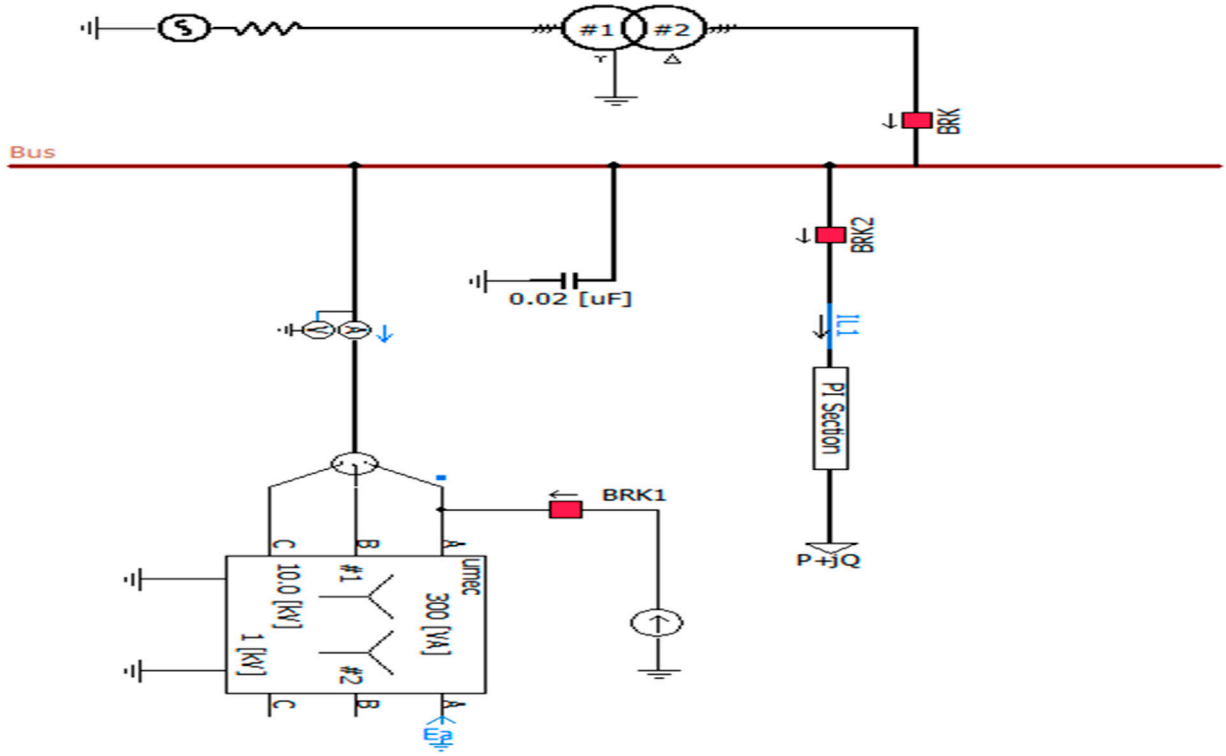

FIGURE 2
Simulation of all-cable line simulation on 10 kV side.

relationship between the ground The relationship between the capacitance C_{LTG} and coil inductance L_{CC} and the power supply frequency f_0 is shown in Eq. 3.

$$X_{C_{LTG}} \geq X_{L_{CC}} \tag{2}$$

$$\frac{1}{\sqrt{4\pi^2 L_{CC} C_{LTG}}} \leq f_0 \tag{3}$$

Therefore, through the above expression we can find that the ferromagnetic resonance does not have a uniform intrinsic frequency, which is related to the saturation depth of the nonlinear core, which further indicates that it is closely related to the magnitude of the current, so that the existence of ferromagnetic resonance phenomenon can be intuitively found through the current in the system.

To determine whether ferromagnetic resonance occurs in a real system, the current in the primary winding is the most suitable monitoring quantity: the current of the PT in normal operation is about zero milliamps to a few milliamps, while it will increase to tens of milliamps or even several amps when ferromagnetic resonance occurs (Fen-Yan and Bao, 2017; Yuan et al., 2022).

3 Model building

The simulation model of PSCAD is shown in Figure 2.

This study focuses on simulating fully cabled lines on the 10 kV side in a substation. In a power system, the electrical energy generated by a power plant is transmitted to the end-users through transformers and transmission lines, and these key electrical devices form the infrastructure of the power system. The simulation model used in this paper reproduces this process in detail and is modeled as in Figure 2. The generator is connected to a three-phase double-winding step-down transformer and connected to the incoming side of the busbar, and the bus-side circuit breaker is used to control the system casting and switching, which serves as the generating and transmitting part of the system. The terminal voltage of the generator is 110 kV, the frequency is 50 Hz, the amplitude angle is 10°, and the value of the internal resistance of the power supply is 10; in PSCAD V4.6, the transformer has been added with the option of the J-A model, which can take into account the hysteresis; the J-A model was proposed by two scholars D.C. Jiles and D.L. Atherton in 1986, based on the theory of magnetic domains, and takes into account the effect of hysteresis. The J-A model is special in that it can consider the saturation and hysteresis characteristics of the core at the same time, and it can also simulate the magnetization and demagnetization process, and it also takes into account the magnetic domain change and energy loss, so that the results of the simulation of the transformer are more close to the actual situation (Tian et al., 2024), so in this paper, we choose the J-A model of transformer to reflect the hysteresis characteristics, in which the hollow core resistance is the same as the hysteresis characteristics, and the hysteresis characteristics are the same as the hysteresis characteristics, in which the hollow core resistance is the same as the hysteresis characteristics. Hysteresis characteristics, in which the hollow-core impedance is set to 0.2 pu, and the maximum value of magnetic flux density is generally set to 1.7 T (Xuyang et al., 2011). The component parameters of the transformer are shown in Table 1, and the nominal values of copper loss and

TABLE 1 Transformer element parameter.

Capacity/MVA	Primary side Voltage/kV	Secondary side Voltage/kV	Copper loss/pu	Positive sequence leakage reactance/p u
30	110	10.5	0.001	0.1

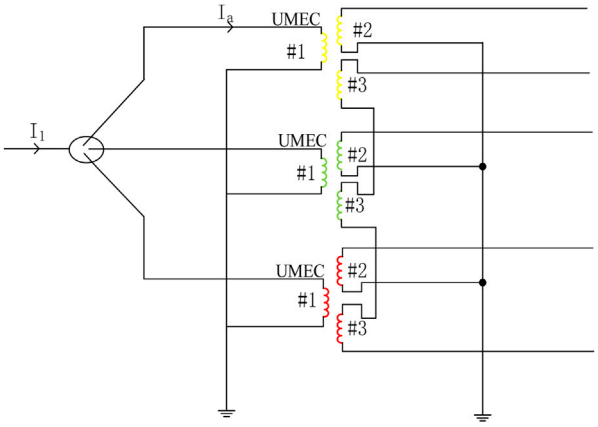

FIGURE 3
PT internal structure.

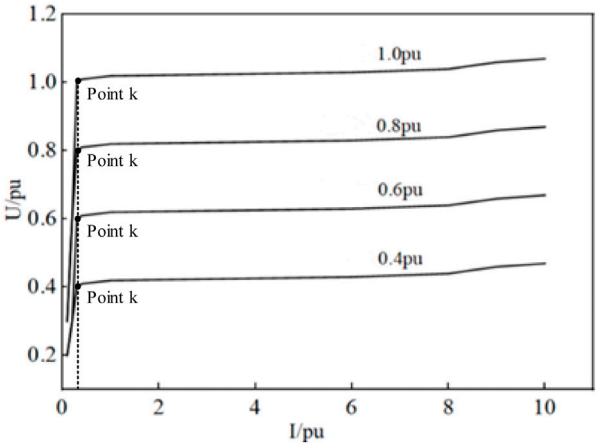

FIGURE 4
Different excitation characteristic curves of PT.

TABLE 2 I-U data at different saturation voltages.

0.4 pu		0.6 pu		0.8 pu		1.0 pu	
I/%	U/pu	I/%	U/pu	I/%	U/pu	I/%	U/pu
0.2	0.3	0.01	0.3	0.1	0.3	0.15	0.3
0.9	0.4	0.58	0.6	0.45	0.8	0.6	1
1	0.41	1	0.61	1	0.81	1	1.01
9	0.43	9	0.63	8	0.82	9	1.04
10	0.45	10	0.65	10	0.84	10	1.05

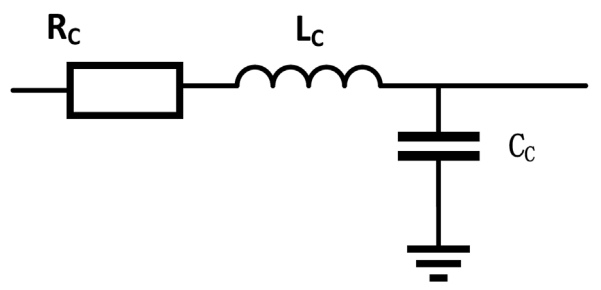

FIGURE 5
Cable equivalent line diagram.

positive sequence leakage reactance are given in reference (Yang et al., 2022).

At the same time in the bus outlet side of the configuration of a 3/5 core column UMEC transformer, with this component to simulate the PT, the internal structure of the model is shown in Figure 3. PT 3/5 core column arrangement is also known as the three-phase five-pillar type, which means that the core of the PT has five columns, in which three columns on the head of the assembly of the magnet coils, which is often referred to as “three-phase”; the two columns on the side as its closed circuit. This is often referred to as the “three-phase”; the two posts on the side as its closed circuit. The core arrangement is a key design factor that determines the performance and suitability of the transformer. The link group of the core is Y0/Y0/D with a capacity of 300 VA.

The excitation characteristic is a key parameter of the PT, which describes the relationship between the magnetic flux density of the core and the excitation current. When the magnetic flux density in the core grows to a certain critical value, even if the excitation current continues to increase, the rate of increase of the magnetic flux density still slows down, and the core enters a saturated state, which will affect the accuracy of the transformer. In engineering practice, by applying a voltage to the low-voltage end of the PT and make the high-voltage end of the method of open-circuit, to test the relationship between the applied voltage and the current flowing through the end of the PT is the excitation characteristics of the PT. According to this principle and method, the voltage and current parameters of each saturation point in Table 2 are obtained, and the excitation characteristic curve is drawn in the origin software as Figure 4. The knee point of the curve is point k, which represents the saturation voltage point of the iron core. Before the k point, the curve is first in the linear region, the voltage and current of the curve in this region is linear growth, and then with the increase of current, the voltage undergoes a nonlinear change to reach the knee point k. After the k point, the iron core is saturated, and even if the excitation current continues to increase, the enhancement of flux density is still slowed down.

TABLE 3 Parameter value per unit length of cable.

Voltage level/*kV*	Resistive/ Ω/*km*	Inductor/*mH*/*km*	Capacitor/*μF*/*km*
10	0.047	0.2564	0.5311

In PSCAD software, the core saturation of PT can be simulated by setting the values of 10 segmentation points on the internal I-V curve. According to the literature (Chen et al., 2023), it is known that when the saturation depth is 1.0 pu, the core of PT will not be saturated; when the saturation depth is 0.6 pu, the PT will be saturated, and the system will appear ferromagnetic resonance phenomenon. Therefore, this paper focuses on the PT saturation point voltage at 0.6 pu, and the curve data at 0.6 pu is selected for simulation.

The cable is capacitive at industrial frequency, the inductance and resistance parameters are very small and negligible, and the equivalence diagram is shown in Figure 5 below.

In the document "Shanghai medium and low voltage distribution network technical guidelines" in the cable line distribution requirements (GBT, 2015): 10 kV cable line using XLPE cross-linked polyethylene insulated copper core cable, out of the line is generally 6 back, the cross-sectional area selected 3 * 400 mm^2; for the power supply distance is also the same requirements: for the 10 kV line, the cable length of the central urban area per response 1.5 km, the cable length of urbanized areas per response 2 km, so the simulation of this paper cable length selected as 1 km per response. The cable length in urbanized areas is 2 km per response, so the cable length of the simulation in this paper is selected as 1 km per return, and the cable line is replaced by the total set of parameters, i.e., the total length of 6 km. The parameter values are based on the actual data in the distribution network of Shanghai (Chaolong et al., 2020), to ensure that the simulation results are accurate and reliable, and the values of various parameters of the cable under the length of the unit are shown in Table 3, and the values of the parameters of the cable line with 6 returns of 1 km are calculated and added to the model. The parameter values of six 1 km cable lines are calculated and added to the model.

4 Determination of the size of remanent magnetization

Residual magnetism is the state in which a portion of the core of a PT remains magnetized even after the magnetization process is removed by an external voltage. This phenomenon usually occurs when a system is subjected to a transient overvoltage, such as under circuit breaker operation, which may cause the core to magnetize to a point close to the saturation point, where the core retains a certain level of magnetic flux even after the overvoltage has disappeared.

The amount of residual magnetism in the core after power failure depends on the magnitude of the current during energization and the test time. Literature (Jin et al., 2009) proposed a formula for the derivation of the size of the residual magnetism: take the power supply E_S as a sinusoidal waveform, the power supply voltage expression as Eq. 4, where U_{EV} is the rms value of the power supply voltage, the primary side of the PT column to write the voltage equation, you can get the flux ϕ and the relationship between the U_{EV} as Eq. 5, the two sides of the equation were integrated over t, which further led to Eq. 6.

$$E_S = \sqrt{2}U_{EV}\, sin(\omega_0 t + \theta) \tag{4}$$

$$N_0\frac{d\phi}{dt} = \sqrt{2}U_{EV}\, sin(\omega_0 t + \theta) \tag{5}$$

$$\phi = -\frac{\sqrt{2}U_{EV}}{N_0\omega_0} cos(\omega_0 t + \theta) \tag{6}$$

The residual magnetism $\phi_{t_{op}}$ existing in the transformer core at the moment of t_{op} can be found out when the circuit breaker operates at any moment of t_{op}. According to Eq. 6, it can be

TABLE 4 Relationship between DC current and magnitude of remanent magnetization.

Current value/mA	Remanent magnetization value/pu
26.1	0.9
22	0.8
17.7	0.7
12.2	0.6
7.2	0.5
3	0.4

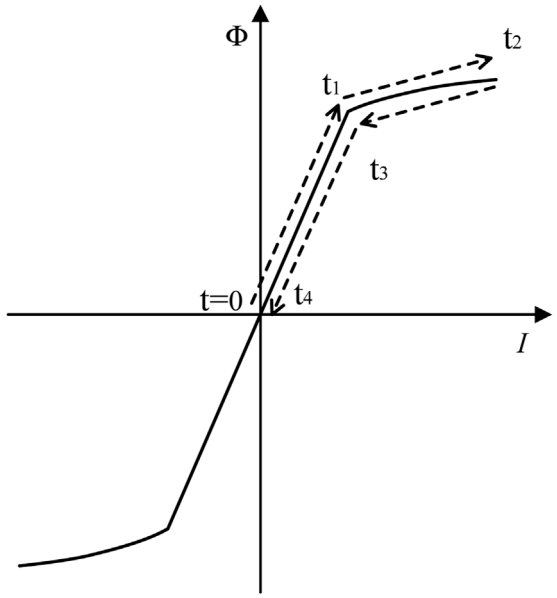

FIGURE 6
Residual magnetization versus current.

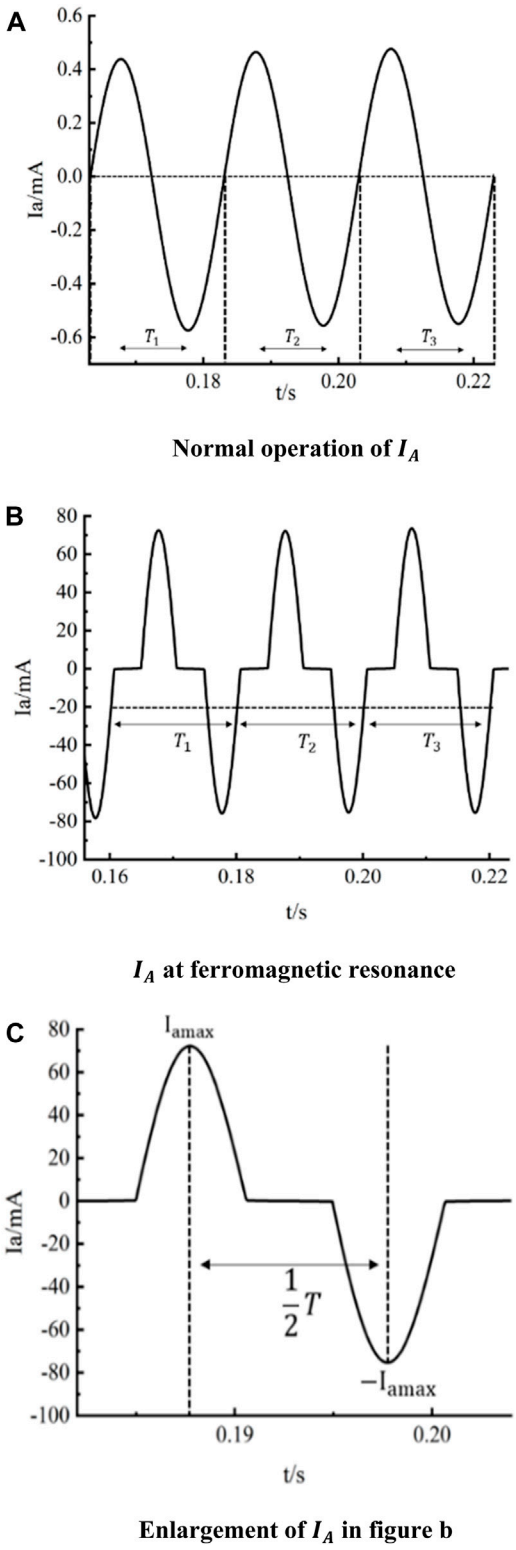

FIGURE 7
(A) Normal operation of I_A. **(B)** I_A at ferromagnetic resonance **(C)** Enlargement of I_A in **(B)**.

seen that the waveform of the residual magnetism is a cosine wave, and the size of the amplitude varies within the range of ± 1 pu; however, due to the limitation of the PSCAD software, it is not possible to determine the number of turns of the primary-side windings, and therefore it is not possible to find out the magnitude of the residual magnetism directly $\phi_{t_{op}}$. In this paper, a new method of measuring the size of the remanent magnetism is selected, the PT saturation point voltage is set to 0.6 pu, first applied to the PT phase A DC source is not put into use, the external circuit breaker BRK initial state of the circuit breaker is closed, to be gradually converged to a stable value of the current in the system after the disconnection, at this time, the iron heart of the PT will be due to the disappearance of the current to zero and the generation of the remanent magnetism, the stabilization of the PT primary side of the current value as well as current disappearance The value of current in the primary side of the PT during stabilization and the residual remanent magnetism after the current disappears can be read directly in PSCAD. Change the bus terminal voltage, the current flowing through the primary side of the PT under the action of different voltages is different, and the size of the remanent magnetism remaining in the core after disconnection is also different, record the current value and magnetic flux value of phase A under each test, the relationship between different current values and remanent magnetism is shown in Table 4, and depict the relationship between the remanent magnetism magnetic flux ϕ and the current i, as shown in Figure 6 (Zhang et al., 2011). Due to the magnetization nature of the core, the remanent magnetization cannot exceed the maximum magnetization characteristic curve specified for the core material, which is saturated at ± 0.9 pu, so the general value range is ± 0.9 pu.

5 Simulation analysis

Firstly, the accuracy of the constructed model should be checked to distinguish whether the PT is in ferromagnetic resonance when the core is saturated by observing and comparing the current waveform graphs. In the literature (Zhao, 2020), the author Li Xuyang considered that the PT may be affected by the saturated over-excitation inrush current and cause errors in the detection results, and thus proposed a method for the detection of ferromagnetic resonance in power transformers, that is, the waveform symmetry method is used to distinguish the ferromagnetic resonance inrush current: for the normal operation of current, the current is sinusoidal, with the same period of oscillation; and for the resonance of the inrush current, the waveform is For the resonant inrush current, the waveform is spiky and alternates between positive and negative spikes. This accuracy analysis is simulated based on this study.

When the PT core is not saturated, the circuit breaker operates normally, measure the A-phase line current I_A on the primary side of the PT, and select the current curves of three cycles T_1, T_2, T_3, as shown in Figure 7A, at this time, the primary side of the PT line current is sinusoidal, and there is no saturation phenomenon, and the size of the PT is about 0.4 mA; when the PT core saturates, and the voltage at the saturation point is 0.6 pu, and the same measurements of the PT A-phase line current on the primary side, selected three cycles of the current curve, as shown in Figure 7B, it is observed that at this time the I_A is a cusp waveform, the size of the sudden increase to 70 mA or so; half of

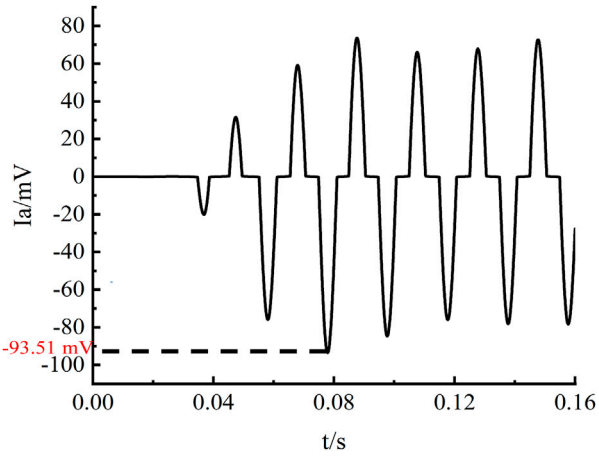

FIGURE 8
Waveform with no remanent magnetization.

the cycle waveforms are enlarged, as shown in Figure 7C, it can be seen that the current wave positive and negative cusp pulses symmetrically alternating with the results of the above study, that is, saturation phenomenon occurs, and therefore further verified that the model of the Accuracy.

5.1 Process of ferromagnetic resonance under added remanent magnetization

Change the positive and negative connections of the current source in order to change the positive and negative direction of the residual magnetism, the current source side circuit breaker BRK1 is disconnected after the system is stabilized, and at this time there is residual magnetism in the iron core.

5.1.1 Ferromagnetic resonance process under different magnitudes of remanence in the positive direction

When the current source side is disconnected and not working, the PT initially has no remanent magnetization, and the waveform of the A-phase current wave is shown in Figure 8. From the figure, it can be seen that when the PT ferromagnetic resonance occurs, the positive and negative pulses of the A-phase current wave are in the form of spikes symmetrical about the time axis and last for a long time, with a peak value of up to 90–100 mA, and the sustained high level of current is extremely easy to cause damage to the PT.

When remanent magnetization is added to the PT, a remanent magnetization value of 0.4–0.9 pu is applied to the PT with a forward interval of 0.4–0.9 pu and a current interval of [3,26.1] mA, respectively, and the comparative changes of the current waveforms are shown in Figure 9. From Figure 9A, it can be seen that when the positive remanent magnetization is applied to the PT in the interval of 0.7 pu–0.9 pu, the current waveform is similar to that of a lightning wave, generating a huge instantaneous value of current in the first 0.1 s. The current is approximately linear with respect to time before

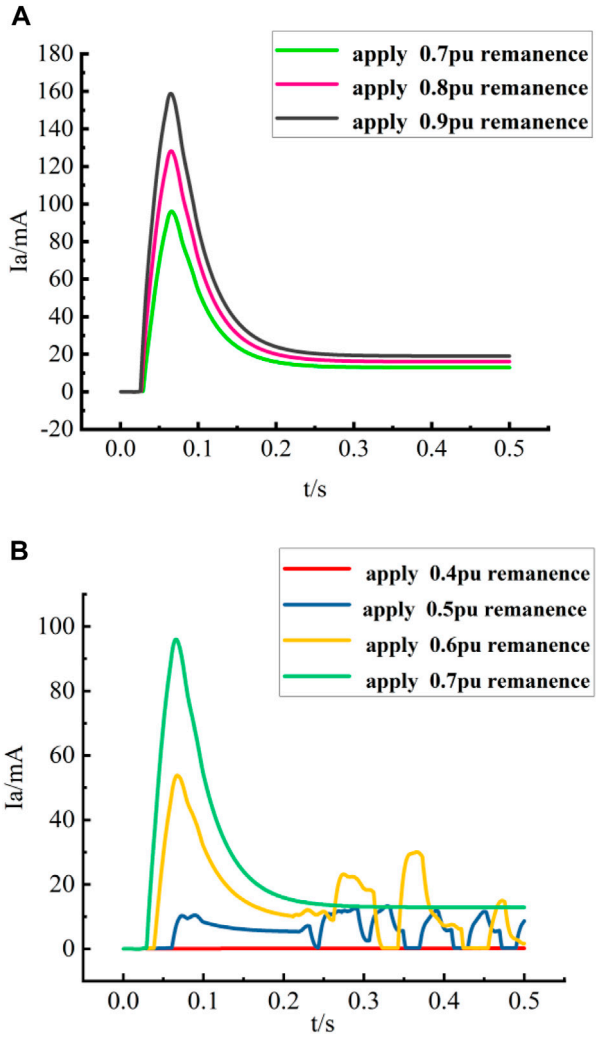

FIGURE 9
Waveforms of A-phase current of PT under different magnitudes of remanent magnetization in positive direction. **(A)** Waveforms of A-phase current of PT when the applied remanence size is 0.7 pu to 0.9 pu; **(B)** Waveforms of A-phase current of PT when the applied remanence size is 0.4 pu to 0.7 pu.

reaching the peak value, and then decreases rapidly and tends to be flat after reaching the peak value. The larger the size of the applied remanent magnetization, the larger the instantaneous peak value of the current, and none of them is smaller than the ferromagnetic resonance inrush current when there is no remanent magnetization, and the final stabilized saturation current is between 20 and 30 mA; when the range of the positive remanent magnetization is applied to the PT is between 0.4 pu–0.7 pu, as shown in Figure 9B: 0.6 pu remanent magnetization is applied, and the current appears as an instantaneous value in the first 0.1 s, but at this time the instantaneous peak value is smaller than that when 0.7 pu remanent magnetization is applied. Peak value is smaller than the instantaneous peak value of the current when 0.7 pu remanence is applied, and it is also smaller than the inrush current of the ferromagnetic resonance when no remanence is applied, and the aberration occurs after 0.2 s instead of leveling

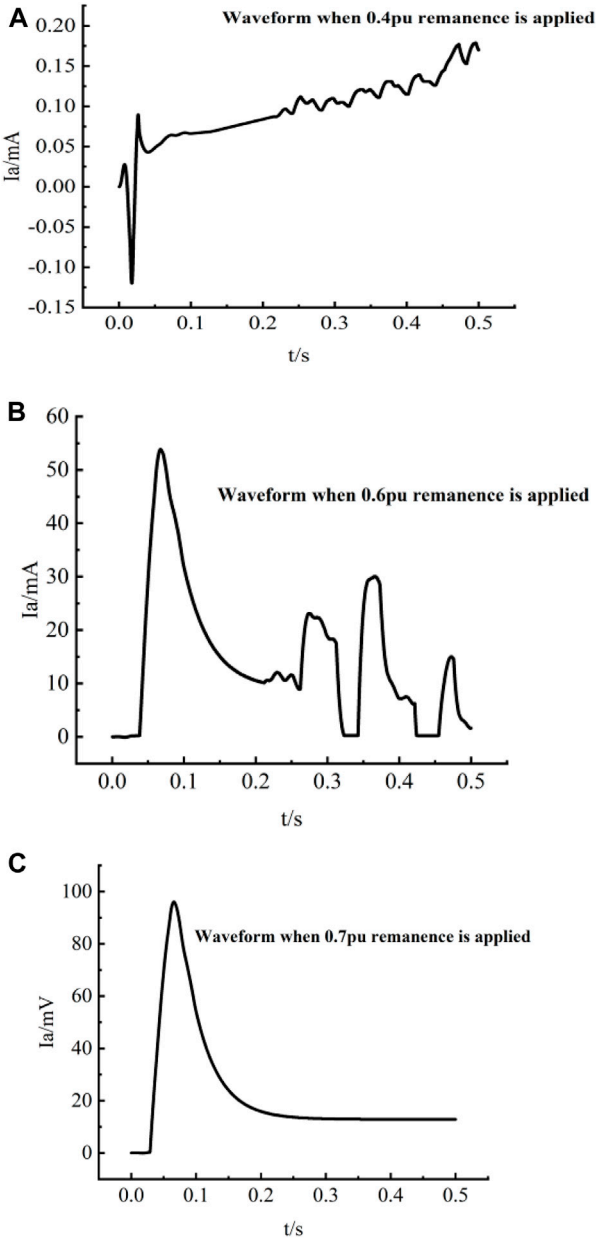

FIGURE 10
Detail of the waveform of Figure 9. **(A)** Waveform of A-phase current of PT when 0.4 pu remanence is applied; **(B)** Waveform of A-phase current of PT when 0.6 pu remanence is applied; **(C)** Waveform of A-phase current of PT when 0.7 pu remanence is applied.

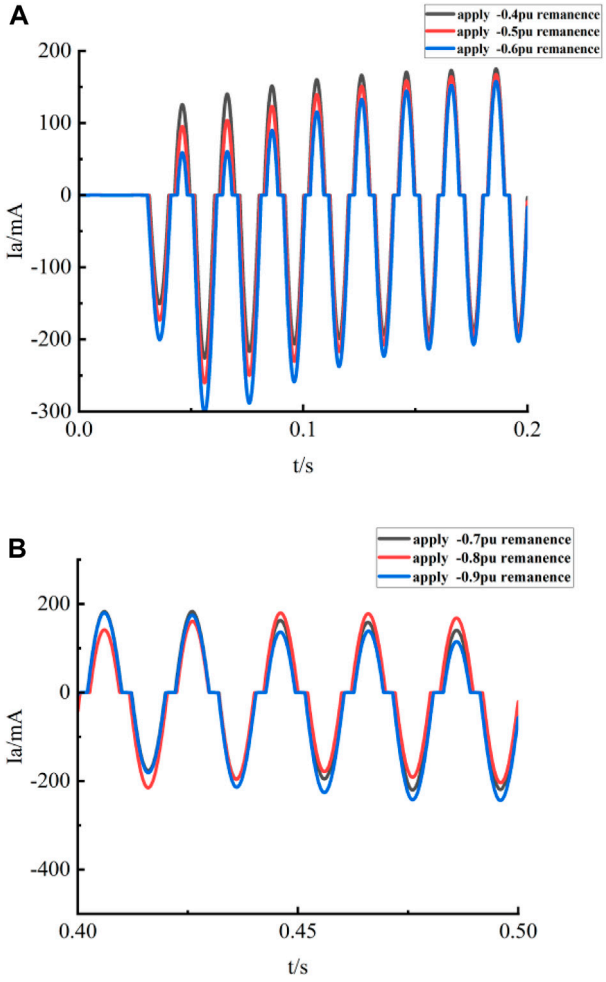

FIGURE 11
Waveforms of A-phase current of PT under different magnitudes of remanent magnetization in negative direction. **(A)** Waveforms of A-phase current of PT when the applied remanence size is −0.6 pu to −0.4 pu; **(B)** Waveforms of A-phase current of PT when the applied remanence size is −0.9 pu to −0.7 pu.

off; when 0.4–0.5 pu remanence is applied, the instantaneous peak value of the current in the first 0.1 s disappears, and the whole tends to be leveled off, and the current magnitude is between 0 and 10 mA.

The waveform details of the above currents are shown in Figure 10. Figures 10B shows that when the applied remanent magnetization value is 0.6 pu, the A-phase current on the primary side of the voltage transformer has aberrations, with a peak value of about 55 mA; from (c) of Figure 10, it can be found that when the applied remanent magnetization value is 0.7 pu, although the current aberration disappears, the amplitude of the current at this time reaches 100 mA, which is close to twice the former value!, the excessive resonant inrush current will bring damage to the PT's.

In summary, when the direction of the remanent magnetization is positive, the remanent magnetization value is less than 0.6 pu on the ferromagnetic resonance overcurrent has a suppression effect, and the smaller the remanent magnetization is, the more obvious the suppression effect on the ferromagnetic resonance inrush current is, and when the value of the remanent magnetization is around 0.4 pu, the PT is already close to the normal operation state.

5.1.2 Ferromagnetic resonance process under different magnitudes of remanence in the negative direction

The positive and negative poles of the A-phase DC power supply connected to the PT are switched, and according to the relationship

between the DC current and the magnitude of remanent magnetism in Table 4 above, a negative remanent magnetism value of 0.4–0.9 pu is applied to the PT with a current interval of [−26.1, −3] mA, and a comparative change graph of the A-phase current waveform is obtained. In order to make the results more observable, the contrast plots are divided into two groups, as shown in Figure 11.

Simulation results show that, when the PT ferromagnetic resonance occurs, after applying remanent magnetization with negative direction and size of 0.4–0.9 pu to phase A, the waveform of I_A does not change compared with that without remanent magnetization, and it is still a cusp-shaped positive and negative pulses alternating symmetrically, whereas the value of the current is greatly increased in these cases, and the peak value is close to 200 mA, which is much higher than the peak value of the ferromagnetic resonance current when there is no remanent magnetization, and it is even several times as much as the peak value when there is no remanent magnetization several times. It can be seen that the applied remanent magnetization in the negative direction fails to suppress the ferromagnetic resonance regardless of the magnitude.

6 Conclusion

The voltage transformer in the full cable line is susceptible to ferromagnetic resonance due to certain operational reasons, which generates overcurrent and damages the safety of the equipment. This paper is based on the phenomenon that exists in the actual power system, when the current wave invades into the voltage transformer, residual magnetism will be left in the iron core, and the simulation is used to analyze the influence of residual magnetism in different sizes and directions on the ferromagnetic resonance, and the comparison of the obtained data, and ultimately, a method is found for realizing the effective suppression of the ferromagnetic resonance. The conclusions are as follows:

(1) When the system is subjected to a positive lightning intrusion wave, a positive remanent magnetization value of less than 0.6 pu can effectively suppress the ferromagnetic resonance inrush of the voltage transformer, and the smaller the remanent magnetization value, the better the suppression effect. The smaller the remanent magnetization value, the better the suppression effect. When the remanent magnetization value is 0.4 pu, the PT is close to the normal operation state.
(2) When the system is subjected to reverse lightning intrusion wave, the negative remanent magnetization cannot suppress the ferromagnetic resonance of the PT, but may exacerbate the inrush current, leading to more serious consequences.

In this paper, the range of remanent magnetism values that can effectively suppress PT ferromagnetic resonance in 10 kV all-cable lines is determined through simulation and analysis, which provides a reference for future research on methods of avoiding PT damage and gives future scholars a technical basis for optimizing the stability of power grids.

Data availability statement

The raw data supporting the conclusion of this article will be made available by the authors, without undue reservation.

Ethics statement

Written informed consent was obtained from the individual(s) for the publication of any potentially identifiable images or data included in this article.

Author contributions

HY: Project administration, Software, Writing–original draft. DS: Project administration, Writing–review and editing. LZ: Software, Writing–review and editing.

Funding

The author(s) declare that no financial support was received for the research, authorship, and/or publication of this article.

Conflict of interest

The authors declare that the research was conducted in the absence of any commercial or financial relationships that could be construed as a potential conflict of interest.

Publisher's note

References

Andrei, R. G., Halley, B. R., et al. (1989). Voltage transformer ferroresonance from an energy transfer standpoint. *IEEE Trans. Power Deliv.* 4 (3), 1773–1778. doi:10.1109/61.32672

Cao, W. B., Huang, X. M., Wang, S., Qiu, Y. T., Wen, M. H., and Yin, X. G. (2023). Inrush current imbalance analysis of transformer based on saturation depth dynamic phasor diagram. *Power Syst. Prot. Control* 51 (13), 139–147. doi:10.19783/j.cnki.pspc.202203

Chaolong, Z., Yigang, H., Bolun, D., Lanfang, Z., and Shan-he, J. (2020). Intelligent fault diagnosis method for power transformer based on deep learning. *J. Elec. Meast. and Ins.* (01), 81–89. doi:10.13382/j.jemi-B1902359

Chen, H., and Shuheng, T. (2023). Simulation analysis of ferromagnetic resonance of voltage transformer caused by asymmetric operation on hybrid line. *High. Volt. Appar.* 50 (3).

Chen, L., Minsheng, X., Chunxu, ZHENG, Gao, H., Fan, H., and Zhang, B. (2021). Analysis of operating characteristics of ground transformer under single-phase ground fault. *Power Syst. Prot. Control* 49 (12), 56–64. doi:10.19783/j.cnki.pspc.201028

Chen, Q., Peng, T., Kang, W., and He, G. (2024). Infrared detection of power mechanical equipment overheating fault based on feature fusion. *Mach. Des. Manuf.* (04), 337–341. doi:10.19356/j.cnki.1001-3997.2024.04.006

Chen, Y. (2022). Electrical test and relay protection of power transformer. *Electron. Technol. Softw. Eng.* (17), 115–118.

Dasgupta, I. (2005). *Design of transformers*. New Delhi: Tata Mc Graw-Hill.

Fen-Yan, Y., and Bao, W. (2017). Transformer model considering hysteresis based on PSCADV4.6. *Guangdong Electr. Power* 30 (6), 67–72.

GBT (2015). *Guidelines for energy efficiency evaluation of medium and low voltage distribution networks*. GB/T 31367-2015.

GBT (2020). *Transformers - Part 102: ferromagnetic resonance in substations with electromagnetic voltage transformers*. GB/T 20840.92-2020.

Jin, J., Chun-En, F., Tian-Hui, L., and Feng-xiang, W. (2009). And simulation research of the remanence of transformer excitation inrush current. *J. transformer* 46-48 (11), 40–43. doi:10.19487/j.carol.carroll.nki.1001-8425.2009.11.010

Kulkarni, S., and Khaparde, S. (2004) *Transformer engineering: design and practice [M]*. New York. Basel: Marcel Dekke, r Inc.

Liu, H., Yinglong, D., Yinghui, H., Lixue, C., Xiaofei, L., and Hong, Y. (2024). Research on high precision voltage transformer based on high temperature superconductivity. *Electr. Meas. Instrum.* 61 (04), 48–55. doi:10.19753/j.issn1001-1390.2024.04.008

Liu, Ke (2024). Cause analysis and countermeasure of fault of middle joint of direct-buried collector line in wind farm. *Public Electr.* 39 (03), 55–56.

Ping, F., and Wang, E. (2004). Theoretical analysis of three-phase ferromagnetic resonance in neutral grounded power system. *Trans. China Electrotech. Soc.* 19 (9), 57–61. doi:10.19595/j.cnki.1000-6753.tces.2004.09.011

Quan, W., and Li, W. (2022). Analysis and countermeasures of ferromagnetic resonance of voltage transformer in a power plant. *Hydropower Pumped Storage* 8 (01), 35–39.

SA (2021). *Instrument transformers, Part 102: ferroresonance oscillations in substations with inductive voltage transformers (IEC TR 61869-102:2014 (ED 1.0) MOD)*. SA TR 61869.102:2021.

Tian, Y., Chen, H. Y., Que, Y. B., Mu, Y. K., Gao, T., Wang, G. Q., et al. (2024). Research on magnetic analysis method of pipeline force Based on Improved JA Model. *J. Harbin Univ. Sci. Technol.* 1-9.

Vecchio, R. M. D., and Poulin, B. (2010). *Transformer design principles: with applications to core-form power transformers*. Boca Raton, Florida, United States: CRC Press.

Wang, J. (2021). *Simulation and analysis of ferromagnetic resonance in 110kV substation based on PSCAD*. Shenyang, China: Shenyang university of technology. doi:10.27322/.dc.nki.Gsgyu.2021.000186

Wang, S., Wang, X., Xia, Y., He, X., and Wu, T. (2022). Research on ferromagnetic resonance characteristics and Identification of PT in distribution network switch under non-outage operation. *Power Grid Technol.* 46 (11), 4534–4540. doi:10.13335/j.1000-3673.pst.2022.0205

Xuyang, Li, Dong, X., and Zhiqian, Bo (2011). Research on ferroresonance detection method of power transformer. *Power Syst. Prot. Control* (9), 102–107.

Yang, J., Yan, H. U., and Wang, J. (2022). Ferromagnetic resonance analysis and suppression of 110kV substation. *Transformers* 59 (2), 19–23. doi:10.19487/j.cnki.1001-8425.2022.02.010

Yaohua, H. A. O., Cao, B., Wang, W., Feng, Y., and Chen, J. (2019). Simulation and application of series compensation capacitor on ferroresonance overvoltage based on PSCAD/EMTDC. *High. Volt. Electr. Appar.* 55 (12), 205–210. (in Chinese). doi:10.13296/j.1001-1609.hva.2019.12.030

Yuan, W., Mengying, G., and Yuan, J. (2022). Method of Reducing transformer remanence by changing external Circuit Capacitance. *Proc. CSEE* 42 (8), 2997–3004. doi:10.13334/j.0258-8013.pcsee.220535

Zhang, H., and Junhua, Li (2011). Simulation Analysis of insurge current in single-phase Transformer based on PSCAD. *J. North China Inst. Water Resour. Electr. Power* (6), 73–75. doi:10.19760/j.ncwu.zk.2011.06.021

Zhang, X., and Wen, Y. (2009). Research on PT ferroresonance overvoltage and detuning device in power distribution system. *J. Chizhou Univ.* 23 (03), 51–53.

Zhao, H. (2018). Causes and elimination methods of ferroresonance overvoltage in power system. *South. Agric. Mach.* 49 (18), 145.

Zhao, Z. (2020). *Transformer core remanence testing and weaken*. Hebei: Hebei university of technology. doi:10.27105/dc.nki.Ghbgu.2020.000462

Zheng, J., Sheng, Y., Su, X., Li, G., Ren, M., Ma, X., et al. (2024). Research on ground potential rise and overvoltage of sheath power frequency in high voltage single core cable under ground fault. *Electr. porcelain arrester* (02), 98–105. doi:10.16188/j.isa.1003-8337.2024.02.013

Zhong, L., Yan, X., Xudong, R. E. N., Chen, X., Zhang, Y., and Qi, Y. (2021). Analysis of influence of main Parameters of electromagnetic voltage Transformer on ferroresonance Overvoltage. *Transformers* 58 (4), 51–56. doi:10.19487/j.cnki.1001-8425.2021.04.011

frontiers | Frontiers in Energy Research

TYPE Original Research
PUBLISHED 26 June 2024
DOI 10.3389/fenrg.2024.1377841

OPEN ACCESS

EDITED BY
Chaolong Zhang,
Jinling Institute of Technology, China

REVIEWED BY
Nishant Kumar,
Indian Institute of Technology Jodhpur, India
Jie Shu,
Chinese Academy of Sciences (CAS), China

*CORRESPONDENCE
Fanyu Meng,
meng_fanyu@foxmail.com

RECEIVED 28 January 2024
ACCEPTED 29 May 2024
PUBLISHED 26 June 2024

CITATION
Li H, Song K, Meng F, Wang Z and Wang C (2024), Voltage control strategy of a high-permeability photovoltaic distribution network based on cluster division.
Front. Energy Res. 12:1377841.
doi: 10.3389/fenrg.2024.1377841

Voltage control strategy of a high-permeability photovoltaic distribution network based on cluster division

He Li[1], Kun Song[2], Fanyu Meng[3]*, Zhenhao Wang[3] and Chaobin Wang[3]

[1]State Grid East Inner Mongolia Electric Power Co., Ltd. Tongliao Power Supply, Tongliao, China, [2]State Grid East Inner Mongolia Electric Power Co., Ltd., Hohhot, China, [3]The Northeast Electric Power University, Jilin, China

The use of distributed photovoltaics (PVs) on a large scale often causes voltage over-limit problems in distribution networks. This paper proposes a distributed photovoltaic cluster collaborative optimization voltage control strategy based on an improved community algorithm to address the issue of centralized control being unable to respond quickly to the randomness of distributed photovoltaics and the difficulty of achieving overall coordination with local control. First, by improving the community algorithm, the division of reactive and active clusters, considering the power balance and node coupling degree, is realized. Then, the cluster-coordinated voltage control strategy is proposed by making full use of the power control ability of a photovoltaic inverter. Finally, a voltage regulation ability evaluation index is proposed to assess the node regulation ability within the cluster and select key nodes. This effectively reduces the number of control nodes. The simulation analysis of the improved IEEE 69 distribution network shows that the proposed voltage control strategy can mitigate the issue of voltage over-limit in high-permeability distributed photovoltaic access distribution and enhance the photovoltaic consumption capacity.

KEYWORDS

high-permeability distributed photovoltaic, distribution network, cluster division, key nodes, voltage regulation

1 Introduction

The National Photovoltaic Poverty Alleviation Policy has led to a significant increase in the number and capacity of grid-connected residential photovoltaic (PV) systems in the distribution network (Dong et al., 2021). In certain areas, the high penetration of distributed photovoltaic systems has resulted in power reversal, necessitating the transformation of the traditional passive distribution network into a complex multi-source distribution network. The distribution network often faces several risks, including voltage over-limit and harmonic pollution (Han et al., 2021). Voltage overloading, in particular, significantly affects the consumption of new energy in the distribution network and the safe and stable operation of cables.

There has been extensive research conducted by scholars both domestically and internationally on the issue of voltage over-limit caused by high-permeability photovoltaic access to distribution networks. Song et al. (2022) addressed the voltage issues of high-penetration PV installations by adjusting the tap of the load regulator

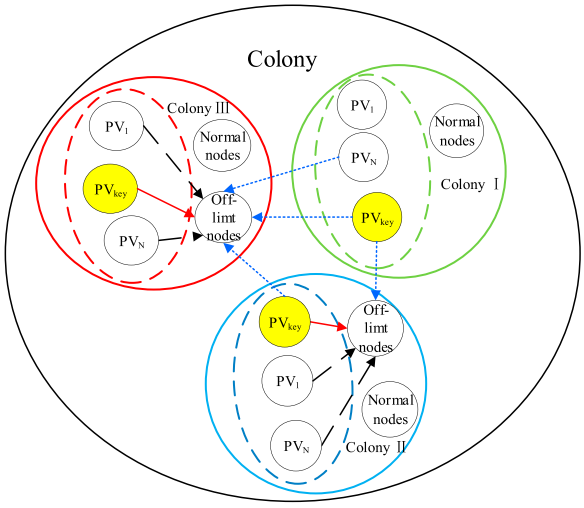

FIGURE 1
Reactive power coordination control.

transformer. Emiliano et al. (2019) established an active-reactive hierarchical zonal optimization model to optimize the reactive voltage loss and active network loss problems that exist in high-penetration PV distribution networks, and optimization calculations are performed using a control algorithm. Gao et al. (2019) proposed the voltage control strategy of a photovoltaic power station inverter and the calculation method of active/reactive power adjustment of the inverter, which solved the problem of voltage over-limit at the access point of the photovoltaic power station. Based on the consistency theory, Liu et al. (2021) proposed a strategy to allocate reactive power compensation based on photovoltaic capacity ratios to mitigate reactive power overshoot problems due to highly permeable distributed photovoltaic feeders. A local voltage control strategy for distribution networks with distributed PV systems is proposed by Chai et al. (2018). The aim of the strategy is to achieve cost-effective and efficient voltage control by reducing the coordination of the reactive power and optimizing the active power of the photovoltaic systems. Olivier et al. (2016) proposed a centralized control method for the access of distributed PVs to the distribution grid. The method employs equal proportions of reactive power compensation and active power curtailment for all distributed PVs. This approach significantly improves the distribution network voltage. When addressing the issue of voltage over-limit caused by high-permeability photovoltaic access to the distribution network, most of the literature adopts either a centralized control method or a local voltage control method to alleviate the situation. It is important to note that these methods can only alleviate the issue of voltage over-limit caused by high-permeability PV access to the distribution network. However, the centralized control method requires a large number of control nodes, which is not conducive to rapid control of voltage and will cause additional network losses. Local voltage control will lead to an excessive reduction of active power at some nodes. Voltage cluster control can be implemented to reduce the number of photovoltaic nodes that need to be effectively controlled, the additional network losses caused by power flow, and the light rejection rate of distributed photovoltaics.

The distribution network cluster is to divide the distribution network into several clusters. The internal nodes of each cluster have strong coupling, and there is weak coupling between different clusters. When the power adjustment is carried out within the cluster, the voltage changes greatly. The voltage of the cluster experiences minimal fluctuations when voltage control is performed in other clusters. The methods for dividing power grids into clusters are generally categorized as cluster analysis, optimization algorithms, and complex community discovery. Madureira and Pecas (2009) proposed a power system hierarchical-partitioned voltage control framework in which partitions are defined as microgrids in each power system; controllers are installed in each partition to achieve partitioned control; each partition is weakly connected to each other to achieve partitioned decoupling; and finally, the whole is centrally coordinated and controlled. Pachanapan et al. (2012) proposed an adaptive technique for hierarchical zonal voltage control of the power system. The technique is based on dividing zones by the reactive power reserve of distributed reactive power controllers and the voltage sensitivity of each node to perform the reactive power exchange between zones. Ranamuka et al. (2014) proposed a voltage coordination control strategy based on an on-load voltage regulator and a distributed reactive power compensation device. The strategy first measures local data and then calculates the required voltage at the overrun node using a controller. In order to achieve voltage control within the sub-district, Fabio et al. (2008) used the particle swarm optimization algorithm, which is based on the ability of the PV inverter to compensate for a certain amount of reactive power. The goal is to absorb reactive power or active shear amount, depending on the degree of over-voltage and the degree of demand for voltage regulation and control. Zhao et al. (2018) suggested that photovoltaic inverters have reactive power compensation capacity based on the use of particle swarm optimization algorithms. The aim is to achieve minimum reactive power absorption or active shear as the target while prioritizing voltage regulation and control based on the degree of overvoltage and voltage demand within the sub-district. Mayank and Srinivasa (2019); Hossein et al. (2018) proposed a method of partitioning in terms of spatial scales and regulation of the voltage within the partition in terms of time scales. The literature above has achieved results in dividing system clusters. However, clustering analysis requires specifying the cluster center and number of clusters beforehand, and the results can be influenced by human factors. When utilizing the optimization algorithm to divide the cluster, the different coding methods can result in significantly varied partition results. Additionally, incomplete considerations when using complex community algorithms for cluster partitioning can also impact the partitioning outcomes.

In this paper, a distributed photovoltaic cluster collaborative optimization voltage control strategy based on an improved community algorithm is proposed to solve the problem of voltage overshoot caused by high-permeability distributed photovoltaic access in the distribution network. First, based on the traditional community detection algorithm, an improved community detection algorithm is proposed, which makes up for the shortcomings of the traditional algorithm's lack of global optimization ability. The optimal division

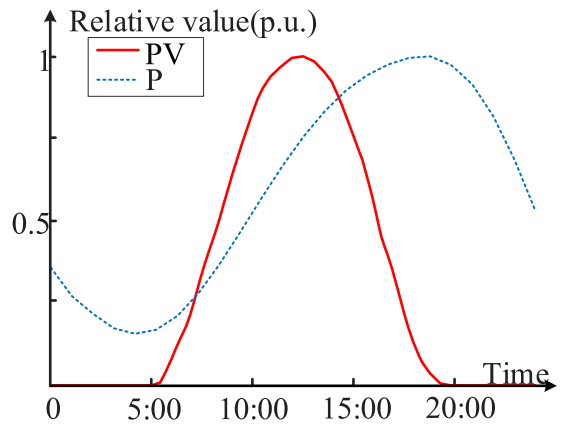

FIGURE 2
Daily curves of total PV generation and load.

results of the reactive power cluster and active power cluster are obtained using the community algorithm. Then, the voltage control method of reactive power cluster (first) and active power cluster (second) is proposed, which makes full use of the adjustment ability of the cluster. According to the difference in observability and controllability of nodes in the cluster, the selection index of key nodes in the cluster is proposed. Finally, according to the influence ability of different nodes in the cluster, the selection index of key nodes in the cluster is determined, and the key nodes are given priority. Through the simulation analysis of the improved IEEE 69-node distribution network, the results show that the proposed method can not only realize the voltage control in the cluster but also realize the coordinated control of the voltage between the clusters in emergency situations, reduce the number of control equipment, reduce the network loss, and effectively alleviate the problem of voltage overflow.

2 Cluster partition based on power sensitivity

In the complex power system operating environment, it is important to ensure that the partitioning of the power system effectively utilizes the control means of the reactive power compensation device. To achieve this, the sensitivity of active/reactive power voltage is calculated from the perspective of power system sensitivity. The cluster is then divided based on the power system's modularity function model.

2.1 Reactive/active voltage decoupling control

According to Yao et al. (2019), the calculation of power flux in the distribution is expressed in terms of the Jacobian matrix of the power system's load flow:

$$\begin{bmatrix} \Delta \boldsymbol{P} \\ \Delta \boldsymbol{Q} \end{bmatrix} = \begin{bmatrix} \boldsymbol{J}_{P\theta} & \boldsymbol{J}_{PU} \\ \boldsymbol{J}_{Q\theta} & \boldsymbol{J}_{QU} \end{bmatrix} \begin{bmatrix} \Delta \boldsymbol{\theta} \\ \Delta \boldsymbol{U} \end{bmatrix}. \tag{1}$$

In the above formula, $\Delta \boldsymbol{P}$ and $\Delta \boldsymbol{Q}$ are variations in the injected active power and reactive power of the node, respectively. $\Delta \boldsymbol{\theta}$ and $\Delta \boldsymbol{U}$ are the phase angle and voltage variation of the node, respectively. $\boldsymbol{J}_{P\theta}$, $\boldsymbol{J}_{PU}$, $\boldsymbol{J}_{Q\theta}$, and $\boldsymbol{J}_{QU}$ are sub-blocks in the middle of the Jacobi matrix.

Eq. 1 can be rewritten as

$$\begin{bmatrix} \Delta \boldsymbol{\theta} \\ \Delta \boldsymbol{U} \end{bmatrix} = \begin{bmatrix} \boldsymbol{S}_{P\theta} & \boldsymbol{S}_{Q\theta} \\ \boldsymbol{S}_{PU} & \boldsymbol{S}_{QU} \end{bmatrix} \begin{bmatrix} \Delta \boldsymbol{P} \\ \Delta \boldsymbol{Q} \end{bmatrix}. \tag{2}$$

In the above formula, $\boldsymbol{S}_{PU}$ and $\boldsymbol{S}_{QU}$ are the degrees of change in node voltage amplitude when the node injects unit active and reactive power, respectively. $\boldsymbol{S}_{P\theta}$ and $\boldsymbol{S}_{Q\theta}$ are the degrees of change in the node phase angle when the node injects a unit amount of active and reactive power, respectively.

From Eq. 2, the variation in voltage magnitude $\Delta \boldsymbol{U}$ with active and reactive power variations ($\Delta \boldsymbol{P}$ and $\Delta \boldsymbol{Q}$) at node i in an n-node distribution network can be expressed as follows:

$$\Delta \boldsymbol{U} = \boldsymbol{S}_{PU} \Delta P + \boldsymbol{S}_{QU} \Delta \boldsymbol{Q} \tag{3}$$

In the above formula, $\Delta \boldsymbol{P} = [\Delta P_1 \cdots \Delta P_n]^T$, $[\Delta Q_1 \cdots \Delta Q_n]^T$.

The effect of accessing different capacity of PV at m nodes in the distribution network on the voltage at node i can be expressed as follows:

$$U_{i1} = U_{i0} + \sum_{j=1}^{m} S_{PU,ij} \Delta P_j + \sum_{j=1}^{m} S_{QU,ij} \Delta Q_j \tag{4}$$

where U_{i0} is the initial voltage at node i, $S_{PU,ij}$ is the active voltage sensitivity factor of node i to node j; and $S_{QU,ij}$ is the reactive voltage sensitivity factor of i to node j.

From Eqs 3, 4, it is evident that changing the reactive power of a node while keeping the active power constant only affects the voltage magnitude through the reactive sensitivity matrix. Similarly, changing the active power of a node while keeping the reactive power constant only affects the voltage magnitude through the active sensitivity matrix. Therefore, it is possible to achieve decoupling control of reactive power and active power (Chen and Shen, 2006).

2.2 Improved Louvain algorithm-based cluster partitioning

Louvain's algorithm (Feng et al., 2023) is a modularity function clustering algorithm proposed by Newman that quickly generates optimal clustering results and greatly reduces the intervention of human factors. The modularity function can be expressed as follows in Eq. 5:

$$\rho = \frac{1}{2m} \sum_i \sum_j \left[A_{ij} - \frac{k_i k_j}{2m} \right] \delta(i, j), \tag{5}$$

where A_{ij} is the edge weights of nodes i and j. $A_{ij} = 1$ when nodes i and j are directly connected. $A_{ij} = 0$ when they are not directly connected. k_i is the sum of all the edge weights connected to node i, k_j is the sum of all the edge weights connected to node j, and $m = (\sum_i \sum_j A_{ij})/2$ is the sum of all the edge weights in the network. If nodes i and j are in the same cluster, $\delta(i, j) = 1$; otherwise, $\delta(i, j) = 0$.

10.3389/fenrg.2024.1377841

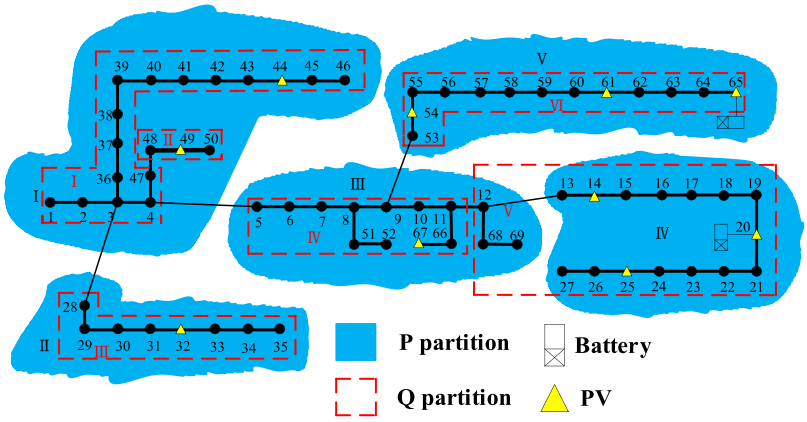

FIGURE 3
Active and reactive power partition diagram.

TABLE 1 Table caption.

Cluster number	Reactive cluster node number	Active power cluster node number
Cluster I	44	44
Cluster II	49	32
Cluster III	32	67
Cluster IV	67	65
Cluster V	20	20
Cluster VI	65	None

2.2.1 Reactive power cluster division

In the distribution network, the reactive voltage sensitivity matrix is an important basis for reflecting the system voltage fluctuation. By comparing whether the side weights are connected or not, the reactive voltage sensitivity matrix can more accurately respond to the reactive coupling degree of different nodes, replacing the original side weight matrix by the mean value of different node sensitivities, and the improved side weights $\eta_{QU,ij}$ can be expressed as follows in Eq. 6:

$$\eta_{QU,ij} = \frac{S_{QU,ij} + S_{QU,ji}}{2}. \tag{6}$$

The primary source of dynamic power factor correction on the grid is the power generators, whose power factor correction support is critical (VDE-AR-N4105, 2011). A distributed PV can change its output reactive power by regulating the inverter, thus providing support to the system voltage. The ability of distributed PV systems of different capacities to support voltage at other nodes varies, which not only affects the reactive power balance of the cluster but also affects the results of the cluster division. Adjusting the reactive power of node i to node j support capacity can be expressed as follows in Eq. 7:

$$\alpha_{QU,ij} = \frac{S_{QU,ij}}{S_{QU,jj}} \times Q_{QU,i}, \tag{7}$$

where $Q_{QU,i}$ is the adjustable reactive capacity of node i of the PV inverter.

The final improved weight matrix can be expressed as follows in Eq. 8:

$$A_{QU,ij} = \eta_{QU,ij} + \alpha_{QU,ij}. \tag{8}$$

The improved modularity can be expressed as follows in Eq. 9:

$$\rho_{QU,a} = \frac{1}{2m} \sum_i \sum_j \left[A_{QU,ij} - \frac{k_i k_j}{2m} \right] \delta(i, j). \tag{9}$$

Considering the internal structural characteristics of the cluster, the aggregation index can be expressed as follows in Eq. 10:

$$\rho_{QU,b} = \sum_{i,j=1}^{n} S_{QU,ij} \Big/ \left(m \times \sum_{c=1}^{m} \sum_{i,j=1}^{n} S_{QU,ij} \right), \tag{10}$$

where m is the number of total clusters and c is the label of the current cluster.

The integrated evaluation indicator can be expressed as follows in Eq. 11:

$$\rho_{QU} = \rho_{QU,a} + \rho_{QU,b}. \tag{11}$$

2.2.2 Active power cluster division

The active sensitivity matrix accurately reflects the active coupling degree of different nodes. Therefore, by replacing the original edge

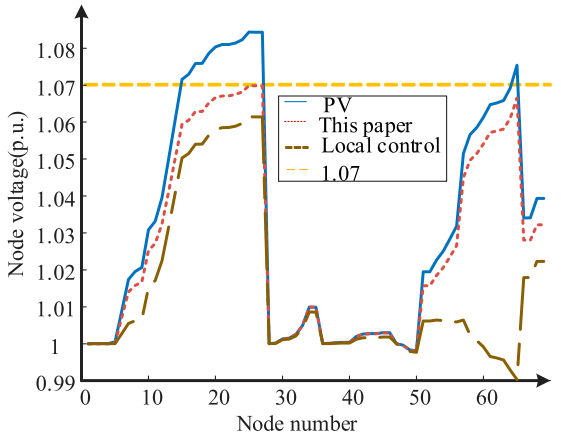

FIGURE 4
Different strategies of voltage regulation.

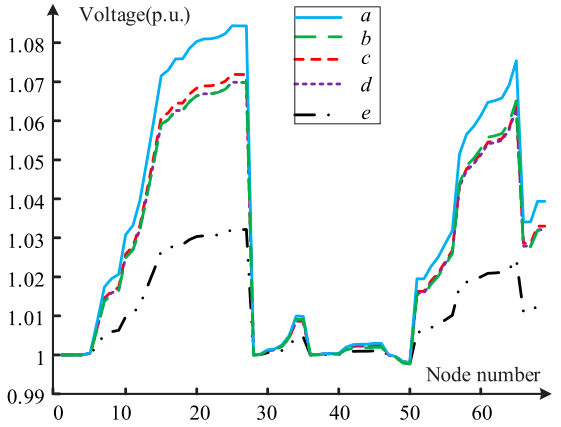

FIGURE 5
Voltage control of different permeabilities.

weight matrix with the mean value of the active sensitivity matrix, the improved edge weights can be expressed as follows in Eq. 12:

$$\partial_{PU,ij} = \frac{S_{PU,ij} + S_{PU,ji}}{2}. \tag{12}$$

In large grids, grid voltage variations are strongly correlated with reactive power variations, but in low- and medium-voltage distribution networks, active power variations can also cause voltage fluctuations. The ability to balance the active power in place within the active cluster should also be fully considered, and the ability of node i active power adjustment to support node j can be expressed as follows in Eq. 13:

$$\alpha_{PU,ij} = S_{PU,ij} \times \frac{P_{PU,i}}{S_{PU,jj}}. \tag{13}$$

The final improved edge weight matrix can be expressed as follows in Eq. 14:

$$A_{PU,ij} = S_{PU} + \alpha_{PU,ij}. \tag{14}$$

The degree of modularity can be expressed as follows in Eq. 15:

$$\rho_{PU,a} = \frac{1}{2m} \times \sum_i \sum_j \left[A_{PU,ij} - k_i k_j / 2m\right] \delta(i, j). \tag{15}$$

Finally, the aggregation metrics of the active clusters also need to be considered in Eq. 16:

$$\rho_{PU,b} = \frac{\sum_{i,j=1}^{n} S_{PU,ij}}{\sum_{c=1}^{m} \sum_{i,j=1}^{n} S_{PU,ij}}. \tag{16}$$

The integrated modularity evaluation indicator can be expressed as follows in Eq. 17:

$$\rho_{PU} = \rho_{PU,a} + \rho_{PU,b}. \tag{17}$$

2.3 Overall cluster division process

The example of reactive power clustering is used to illustrate how optimal clustering results can be obtained by improving the community algorithm in the distribution network. The following are the concrete steps we are taking:

Step 1: Obtain the relevant data on the distribution network, consider each node in the network as a cluster, and calculate the network modularity value ρ0 according to Eq. 11.

Step 2: Start with an initial node i, randomly select node j to form a new cluster, calculate the module degree ρ1, and calculate the network module degree increment. Combine nodes i and j into the same cluster if the module degree increment is positive.

Step 3: Treat the current cluster as a new cluster to continue combining with other clusters. Repeat Step 2, and after traversing all nodes in the entire distribution network, the first cluster division ends.

Step 4: Determine whether there is a cluster with only one node in the whole system. If so, repeat Step 2 and Step 3 for this cluster; if not, end the cluster division phase and output the result of the current cluster division.

3 Voltage-coordinated control of the cluster

To address the issue of voltage over-limit in the distribution network with high-permeability distributed photovoltaic access, the information processing center divides the network into multiple clusters based on the collected node voltage over-limit information.

This paper proposes a control strategy for several typical clusters, which is illustrated in Figure 1. In the event of voltage fluctuations, the system cluster can be divided into three categories: Cluster I, where the node voltage is normal and coordination ability is sufficient; Cluster II, where some node voltage exceeds the limit and coordination ability is sufficient; and Cluster III, where most

TABLE 2 Comparison of reactive power cluster division results of different calculations.

Algorithm	Number of clusters	Modularity
Fast Newman	7	0.6750
Louvain	5	0.6185
Proposed algorithm	6	0.7630

node voltage exceeds the limit and coordination ability is insufficient.

When the photovoltaic output of Cluster I fluctuates, the voltage remains at a normal level and the distributed photovoltaic continues to operate in a normal mode. In cases where Cluster II photovoltaic output fluctuates, some nodes may exceed the voltage limit. After the key nodes are compensated, the whole voltage level of the cluster returns to normal. When Cluster III's photovoltaic output fluctuates, some nodes' voltages overshoot the limit. In this case, the information processing center sends an action signal to Cluster III. Even after passing the reactive power compensation in Cluster III, the voltage remains in an over-limit state. The information processing center sends the action signal to Cluster I, which is more sensitive to the voltage change of Cluster III. After the action of Cluster I, Cluster III is still in the over-limit state of voltage. The information processing center sends the action signal to Cluster II. The compensation step is the same as the internal coordinated control of Cluster I.

In cases where there is no adjustable reactive power in any of the clusters, the active cluster coordination control and the reactive cluster coordination control are essentially identical during the active cluster coordination stage. The coordination control of cluster voltage can enhance the system's regulation ability, reduce the number of control nodes, improve voltage control efficiency, and decrease network loss.

3.1 Selection of key nodes for reactive power clustering

The selection of key nodes in the cluster must be both observable and controllable. First, the voltage of key nodes can reflect the general voltage level in the cluster, making it an observable factor. Second, the voltage control of key nodes can effectively impact the overall voltage level of the cluster while having minimal influence on the adjacent cluster, making it a controllable factor.

The key cluster node is selected based on the voltage/reactance sensitivity matrix, and the node's visibility index is expressed as follows in Eq. 18:

$$\omega_i = \frac{\sum_{j=1}^{N} S_{\mathrm{QU},ij}}{\left(\left(\sum_{i=1}^{n}\sum_{j=1}^{N} S_{\mathrm{QU},ij}\right)(N-1)\right)}, \tag{18}$$

where i is the node label in the cluster, j is the node number, N is the total number of nodes in the cluster, and n is the number of clusters.

Considering the influence of reactive power regulation of different distributed photovoltaics other nodes' voltage, the controllability index of the node can be expressed as follows in Eq. 19:

$$\sigma_i = \left(\sum_{I=1}^{m_Q}\sum_{J=1}^{n} S_{\mathrm{QU},ij} Q_I\right) \Big/ \left(m \times \sum_{I=1}^{N}\sum_{J=1}^{N} S_{\mathrm{QU},ij}\right), \tag{19}$$

where I is the node number with reactive power regulation ability in the cluster, J is the node number in the cluster, m_Q is the total number of nodes with reactive power regulation ability in the cluster, and Q_I is the adjustable active power of I nodes.

The comprehensive evaluation index of key node selection can be expressed as follows in Eq. 20:

$$\Gamma = \max\left((1-K_1)\omega + K_1\sigma\right). \tag{20}$$

In the formula, K_1 is the weight coefficient, and the selection of key nodes is mainly for voltage control, so $K_1 = 1$.

3.2 Voltage control in the reactive cluster

For the restricted clusters I and II, as shown in Figure 1, the primary nodes of each cluster act first. The voltage difference between b and the voltage limit ΔU_1 is then recorded. The amount of reactive power adjustment required for the over-limit node voltage to return to normal can be expressed as follows:

$$Q_c = \frac{\Delta U_1}{S_{\mathrm{QU},ab}}. \tag{21}$$

Let Q_a be the maximum reactive power adjustment amount that can be adjusted by the key node. If $Q_c < Q_a$, the key node provides Q_c voltage to return to normal. If $Q_a < Q_c$, the key node provides Q_a and performs power flow calculations. The difference between the voltage of the over-limit node and ΔU_2, and the network loss compensated by the key node is recorded. The reactive power coordination control is repeated according to the selection of key nodes. When the cluster has no reactive power adjustment, it enters the stage of reactive power coordination between clusters.

3.3 Voltage-coordinated control of different clusters

Beginning with the selection of the node that possesses the highest support capacity, we calculate the necessary reactive power adjustment to restore the voltage to its normal level using Eq. 21. If the required reactive power is less than what is provided by the current node, the voltage of the over-limit node will return to normal after performing reactive power compensation on the modified node. If the required reactive power exceeds what the current node can supply, the node will supply all the reactive power, perform power flow calculations, record the difference between the current voltage and the normal voltage, and compensate accordingly using the results of the impact capability.

When the adjustable reactive power of all clusters is insufficient, the control stage for active power clusters is initiated. The control mode for active power clusters follows the same steps as the reactive power clusters, without repetition.

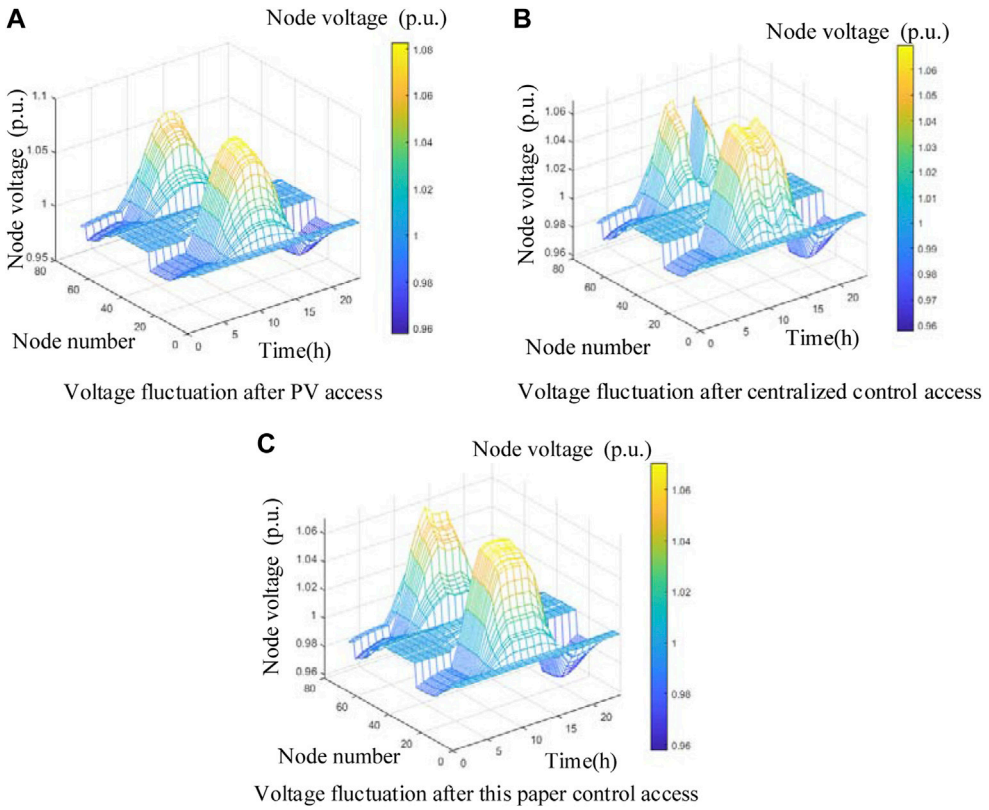

FIGURE 6
Voltage comparison chart for different situations.

4 Example analysis

4.1 Parameter setting

In this paper, the effectiveness of the proposed cluster voltage control strategy for distribution networks with high penetration of distributed PV is validated using the IEEE 69-node distribution network as a sample. The system reference capacity S_{base} = 10 MVA, and the system reference voltage U_{base} = 12.66 kV. The system contains 69 nodes. The photovoltaic access nodes are 14, 20, 25, 32, 44, 49, 54, 61, 65, and 67, and the access capacity is 0.8, 1.2, 0.8, 0.53, 0.46, 0.32, 0.8, 0.53, 1.2, and 0.8 MVA, respectively. The minimum power factor is set to 0.95 by Song et al. (2023). The energy storage battery is installed at nodes 20 and 65, the installation capacity is 0.15 MW, and the level of energy storage in the battery is [0.15, 0.85]. The normal voltage level was set to [0.90, 1.07]. Based on the data from Author Anonymous (2024), the daily load curve of the distribution network in July, which includes both residential and commercial areas, conforms to the demand for residential, commercial, and industrial loads. The day with the highest light intensity in July was chosen for analysis. The total load and active power of the photovoltaic system over a 24 h period are shown in Figure 2. The reference values for the distributed photovoltaic and load are the maximum values of their respective all-day outputs.

4.2 Cluster voltage-coordinated control

The intensity of light increases steadily from 5:30 until it reaches its peak at 12:30 and then gradually decreases. The intensity of light increases steadily from 5:30 until it reaches its peak at 12:30 and then gradually decreases. The voltage fluctuation of the system over the course of the day after access to the photovoltaic system is shown in Figure 2. The node voltage at 12:30 even reaches 1.083 p.u., and the overall voltage change trend is consistent with the findings of Chai et al. (2018).

The results of clustering using the method proposed in the paper are shown in Figure 3. The entire system has an optimal number of six reactive clusters and a maximum modularity of 0.735. Additionally, the optimal number of active clusters in the system is 5, with a maximum modularity of 0.80. The coupling index used in cluster division in this paper reduces the number of individual cluster nodes too much or too little. For example, nodes 48, 49, and 50 in Cluster II are affected by the topology of the distribution network and the original parameters, so they are still in the same cluster.

The key nodes in different clusters are shown in Table 1. Among them, the reactive power cluster V is connected to multiple photovoltaics. Node 25, located at the back as far as the grid is concerned, is the most sensitive to voltage, but node 20 has more adjustable reactive power capacity. Node 20 has a greater impact on

TABLE 3 Comparison of different control methods.

Control mode	Reactive power absorption (MW)	Active power reduction (MW)	Network loss (MW)
Centralized control	4.5181	0.2051	1.7018
Cluster control	3.332	0.1648	1.9325

the voltage of the cluster. Finally, node 20 is the key node of cluster V.

The distributed photovoltaic system's low output causes a slight over-limit of voltage. To solve this issue, reactive power compensation can be applied to certain nodes within the cluster. Between 14:00 and 15:00, some nodes in the distribution network exceeded the voltage limit. Node 20 in cluster V compensated 0.34 kVar, resulting in a 57.1% decrease in the number of nodes with voltage exceeding the limit. Based on the calculation results of key node selection, node 25 in the cluster compensated 0.23 kVar, resulting in the restoration of normal voltage levels across all nodes.

Due to the increase in distributed photovoltaic output, reactive power coordination within a cluster alone is insufficient to meet voltage regulation requirements. Therefore, it is necessary to implement reactive power coordination control across different clusters to address the issue of voltage exceeding the limit. During the period of 10:00–11:00, there were more nodes in the distribution network with voltage exceeding the limit, and even after reactive power compensation for the internal nodes of Cluster V, the voltage remained over the limit. This led to the coordination stage of different clusters. Once the key nodes of Clusters IV and VI were compensated, the voltage of all nodes in Cluster V returned to normal.

When the photovoltaic system is close to full power, relying solely on reactive power cluster coordination may not be sufficient to meet the voltage regulation requirements. Therefore, the problem of voltage exceeding the limit is solved by controlling individual nodes in the active cluster. During the period of 11:00–12:00, the distributed photovoltaic system is close to full power, and the proportion of nodes with distribution voltage exceeding the limit continues to increase. After compensating the key node 65 in Cluster VI, the voltage in the cluster returns to normal. Despite compensating all the key nodes and other nodes with reactive power compensation ability in Cluster V, the voltage remains over the limit and enters the reactive power coordination stage of different clusters. Both Clusters IV and VI compensate for all the reactive power. Cluster V has nodes with voltages over the limit. After reactive power compensation in Clusters I, II, and III, the voltage remains unchanged, and the system enters the active power cluster control stage. Key node 20 in active Cluster IV reduces some of the active power, and the voltage returns to normal.

As shown in Figure 4, at a certain moment from 14:00 to 15:00, because the output of distributed photovoltaic leads to the system exceeding the limit, node 22 to node 27 of Cluster VI appears to exceed the voltage limit. The compensation strategy and the key node compensation strategy in the cluster are compensated, respectively. Through the curve comparison in Figure 4, it can be seen that the key node compensation strategy in the cluster is better than the local compensation strategy in the cluster, and the network loss controlled by the key node is reduced by 11.2% compared with the network loss controlled by the local control. With the increase in photovoltaic installation capacity and control number, this difference will be further expanded. Therefore, it is necessary to select key nodes in the cluster.

As shown in Figure 5, with the increase in the photovoltaic penetration rate, the node voltage of the whole distribution network also increases. The voltage situation of the distribution network is represented by curve e when the distributed photovoltaic penetration rate is 105%. The distribution voltage must not exceed the limit. It continues to operate normally. Curve c represents the distribution grid voltage when the penetration of distributed PV is 155%, and the voltage of some nodes in the distribution grid exceeds the limit. After the coordination of the reactive power in the cluster, the voltage returns to normal, as shown in curve d. Curve a illustrates the voltage situation in the distribution network when the penetration rate of distributed photovoltaics is 220%. There are voltage overshoot problems at some nodes in the distribution network. The coordination of reactive power clusters alone cannot meet the needs of voltage regulation. Active power cluster control is also needed, and finally, the voltage returns to normal, as shown in curve b.

4.3 Comparison of different control strategies

4.3.1 Voltage control within reactive power clusters

To determine the superiority of the Louvain algorithm-based improved cluster partitioning method, we compared it with the Fast Newman cluster partitioning algorithm, the Louvain algorithm, and the algorithm proposed in this paper for clustering the distribution network system. Table 2 provides the comparison results of modularity. The modularity metric can be used to evaluate the reasonableness of the cluster partition results presented in Table 2. The Fast Newman cluster partition algorithm reduces the number of individual cluster nodes to some extent by considering the coupling degree relationship, which improves the accuracy of the cluster partition. This paper combines the photovoltaic support capability with the sensitivity matrix to avoid an excessive number of adjustable distributed photovoltaics in the cluster when calculating the power balance index of the Louvain algorithm. The impact of distributed photovoltaics on the voltage and the coupling relationship of the cluster is also taken into account, in addition to the reactive power sensitivity matrix. As a result, the cluster division is more reasonable, leading to a higher reactive power cluster modularity value.

4.3.2 Comparison of pressure regulation effects of different methods

To determine the advantages of the proposed strategy, a comparison will be made between the use of the central control method for voltage regulation at the connection of high-permeability photovoltaic systems to the distribution system and the proposed cluster control method. The voltage fluctuation following all-day access to distributed PV is shown in Figure 6A. Due to the fluctuation of the distributed photovoltaic power, the voltage may exceed the limit value from time to time. Figure 6B shows the voltage fluctuation after centralized control throughout the day, while Figure 6C shows the voltage fluctuation throughout the day after implementing the strategy proposed here. Both centralized control and the strategy proposed in this paper maintain normal voltage levels. However, the voltage fluctuation is smaller with the proposed strategy, which is beneficial for ensuring the stable operation of the system.

Table 3 shows the reactive power compensation and active power reduction during the control process. The reactive power change in centralized control is 35.6% higher than that in cluster control. Even with coordinated control of reactive power clusters, there is still a problem of voltage exceeding the limit after Cluster V consumes all the reactive power. Reactive power Clusters 1, II, and III compensate reactive power Cluster V without affecting the system voltage before entering the active cluster control stage. During the active control stage, the active power reduction of cluster control is 19.65% lower than that of centralized control, despite a 0.2307-MW increase in network loss. However, all photovoltaic nodes participate in voltage regulation under centralized control rather than using fast responses to the volatility of distributed photovoltaics, even when the system error is within the allowable range.

5 Conclusion

The aim of this paper is to tackle the issue of voltage overshoot resulting from high-permeability distributed photovoltaic access in the distribution network. It proposes a distributed photovoltaic cluster collaborative optimization voltage control strategy based on an improved community algorithm, and the following conclusions are obtained:

1) The decoupling control of active and reactive power is achieved through the analysis of Newton–Raphson power flow computer theory. Additionally, we propose an improved cluster division index and obtain optimal results for reactive and active cluster division using the community algorithm.
2) The paper adopts a strategy of first reactive power cluster control, followed by active power cluster control for voltage regulation. Additionally, the paper proposes a selection index for key nodes in the cluster, taking into account the difference in voltage support ability among nodes. Using the improved IEEE 69 distribution network as an example, the simulation results demonstrate that the proposed method strengthens the coupling between nodes within the cluster, weakens the coupling between nodes in different clusters, and improves the power balance of the cluster. The proposed cluster control method prioritizes reactive power over active power, effectively resolving the issue of voltage over-limit. By adjusting the key nodes of the cluster, the search range is reduced, improving the calculation efficiency and reducing network loss in the system.

This work examines the impact of opening and closing various contact switches in the distribution network on cluster division. The objective is to enhance voltage control efficiency and PV consumption capacity.

Data availability statement

The original contributions presented in the study are included in the article/Supplementary material; further inquiries can be directed to the corresponding author.

Author contributions

HL: writing–review and editing and writing–original draft. KS: writing–review and editing and writing–original draft. FM: writing–original draft and conceptualization. ZW: writing–review and editing and data curation. CW: writing–original draft.

Funding

The author(s) declare that financial support was received for the research, authorship, and/or publication of this article. This work was financially supported by Science and Technology Projects supported by State Grid East Inner Mongolia Electric Power Co., Ltd (SGMDTL00YWJS2200834). The funder was not involved in the study design, collection, analysis, interpretation of data, the writing of this article, or the decision to submit it for publication.

Conflict of interest

Author HL was employed by State Grid East Inner Mongolia Electric Power Co., Ltd. Tongliao Power Supply. Author KS was employed by State Grid East Inner Mongolia Electric Power Co., Ltd.

The remaining authors declare that the research was conducted in the absence of any commercial or financial relationships that could be construed as a potential conflict of interest.

Publisher's note

References

Author Anonymous (2024). *GB/T 19964-2012 Technical regulations for photovoltaic power station access to power system*. Standard Press. (In Chinese).

Chai, Y. Y., Guo, L., Wang, C. S., et al. (2018). Distributed voltage control in distribution networks with high penetration of PV. *Power Syst. Technol.* 42 (03), 738–746. doi:10.13335/j.1000-3673.pst.2017.2271

Chen, Y., and Shen, C. (2006). A Jacobian-free Newton-GMRES(m) method with adaptive preconditioner and its application for power flow calculations. *IEEE Trans. Power Syst.* 21 (3), 1096–1103. doi:10.1109/tpwrs.2006.876696

Dong, X. Z., Hua, Z. H., Shang, L., et al. (2021). Morphological characteristics and Technology prospect of new distribution system. *High. Volt. Eng.* 47 (9), 3021–3035.

Emiliano, D. A., Dhople, S. V., Johnson, B. B., et al. (2019). Decentralized optimal dispatch of photovoltaic inverters in residential distribution systems. *IEEE Trans. Energy Convers.* 29 (4), 957–967.

Fabio, B., Roberto, C., and Valter, P. (2008). Radial MV networks voltage regulation with distribution management system coordinated controller. *Electr. Power Syst. Res.* 78 (4), 634–645. doi:10.1016/j.epsr.2007.05.007

Feng, Y. T., Xie, Z., Li, M. J., et al. (2023). Optimal control strategy of voltage active support for doubly fed induction generator with low short circuit ratio. *High. Volt. Eng.* 49 (01), 42–50.

Gao, P. C., Wang, L., Li, L. S., et al. (2019). Voltage control strategy based on adjustment of PV inverters in distribution network. *Electr. Power Autom. Equip.* 39 (04), 190–196.

Han, X. Q., Li, T. J., Zhang, D. X., et al. (2021). New issues and key technologies of new power system planning under double carbon goals. *High. Volt. Eng.* 47 (9), 3036–3046.

Hossein, F. A., Saeed, H., Ahmad, Ni., and Doostizadeh, M. (2018). Decentralized and hierarchical voltage management of renewable energy resources in distribution smart grid. *Int. J. Electr. Power and Energy Syst.* 100 (4), 117–128. doi:10.1016/j.ijepes.2018.02.006

Liu, K. Y., Sheng, W. X., Zhao, P. J., et al. (2021). Distributed control strategy of photovoltaic cross-district based on consistency algorithm. *High. Volt. Eng.* 47 (12), 4431–4439.

Madureira, A. G., and Pecas, L. J. A. (2009). Coordinated voltage support in distribution networks with distributed generation and microgrids. *IET Renew. Power Gener.* 3 (4), 439–454. doi:10.1049/iet-rpg.2008.0064

Mayank, B., and Srinivasa, S. (2019). Clustering and supervisory voltage control in power systems. *Int. J. Electr. Power and Energy Syst.* 109 (2), 641–651. doi:10.1016/j.ijepes.2019.02.025

Olivier, F., Aristidou, P., Ernst, D., and Van Cutsem, T. (2016). Active management of low-voltage networks for mitigating overvoltages due to photovoltaic units. *IEEE Trans. Smart Grid* 7 (2), 926–936. doi:10.1109/tsg.2015.2410171

Pachanapan, P., Anaya, L., Dysko, A., and Lo, K. L. (2012). Adaptive zone identification for voltage level control in distribution networks with DG. *IEEE Trans. Smart Grid* 3 (4), 1594–1602. doi:10.1109/tsg.2012.2205715

Ranamuka, A. P., Agalgaonkar, K. M., and Muttaqi, K. M. (2014). Online voltage control in distribution systems with multiple voltage regulating devices. *IEEE Trans. Sustain. Energy* 5 (2), 617–628. doi:10.1109/tste.2013.2277719

Song, Z., et al. (2022). "Optimal design method for the partitioning of OLTC-inverter control parameters in distribution stations with high-proportion residential photovoltaics," in International Conference on Innovations and Development of Information Technologies and Robotics (IDITR), Chengdu, China, 43–49.

Song, Z. H., Feng, H., Chen, X. G., et al. (2023). Low-carbon scheduling strategy of distributed energy resources based on node carbon intensity for distribution networks. *High. Volt. Eng.* 49 (01), 42–50.

VDE-AR-N4105 (2011). Power generation systems connected to the LV distribution network-technical minimum requirements for the connection to and parallel operation with low-voltage distribution networks. *Offenb. Verband Elektrotechnik (VDE)*.

Yao, H. M., Du, X. H., Li, T. J., and Jia, C. (2019). Simulation of consumption capacity and voltage control strategy of distribution network with high penetration of photovoltaics. *Power Syst. Technol.* 43 (02), 462–469.

Zhao, B., Xu, Z. C., Xu, C., Wang, C., and Lin, F. (2018). Network partition-based zonal voltage control for distribution networks with distributed PV systems. *IEEE Trans. Smart Grid* 9 (5), 4087–4098. doi:10.1109/tsg.2017.2648779

frontiers | Frontiers in Energy Research

TYPE Original Research
PUBLISHED 01 July 2024
DOI 10.3389/fenrg.2024.1404386

OPEN ACCESS

EDITED BY
Xiao Wang,
Wuhan University, China

REVIEWED BY
Elżbieta Macioszek,
Silesian University of Technology, Poland
Mohamed Salem,
University of Science Malaysia (USM), Malaysia

*CORRESPONDENCE
Jiang Li,
lijiang_ee@shiep.edu.cn

RECEIVED 21 March 2024
ACCEPTED 03 June 2024
PUBLISHED 01 July 2024

CITATION
Li J, Hu J and Liu B (2024), Optimized coordinated control method with virtual inertia based on fractional impedance model for charging stations.
Front. Energy Res. 12:1404386.
doi: 10.3389/fenrg.2024.1404386

Optimized coordinated control method with virtual inertia based on fractional impedance model for charging stations

Jiang Li*, Jianwei Hu and Bo Liu

College of Electrical Engineering, Shanghai University of Electric Power, Shanghai, China

Due to the EV (Electric Vehicles) charging stations are characterized by weak damping and low inertia, the EV with a high degree of uncertainty can easily have an impact on the stability of the charging station system. Therefore, this paper proposes an optimization control method to improve the system inertia effect based on the fractional order impedance model of the charging station. This paper presents a study on establishing a fractional impedance model for charging stations, using the deviation between theoretical impedance spectra and actual measurements as a criterion. The goal is to enhance system inertia and optimize the parameters of the fractional-order controller to improve the supporting capacity of the charging station system and enhance its dynamic response. Initially, considering the fractional characteristics of the EV load, a fractional impedance model of the charging station is established. The analysis demonstrates that the fractional-order capacitor provides inertia to the system, enhancing its inertia support capability. In addition, a virtual inertia control strategy based on fractional-order PID (FOPID) is designed. Finally, an improved particle swarm optimization algorithm is utilized to optimize the control parameters. Through experimental verification under different operating conditions, it has been demonstrated that the fractional-order control strategy can achieve a dynamic response time of approximately 0.025s and limit the voltage deviation within 5%. Furthermore, the rotational inertia can rapidly increase to the maximum value satisfying the objective function within 0.05s. The results indicate that this control method effectively suppresses the DC voltage and power oscillations in the distribution grid.

KEYWORDS

inertia, fractional order PID(FOPID), electric vehicle charging station, fractional-order impedance modeling, energy research

Abbreviations: CPE, Constant Phase Elements; EV, Electric Vehicles; FO, Fractional-order; FOPID, Fractional-order PID; EIS, Electrochemical Impedance Spectroscopy; G-L, Grünwald-Letnikov; IO, Integer-order; ITAE, Integral of Time multiplied by Absolute Error; Particle Swarm Optimization, (PSO); Plug-In Electric Vehicle, (PEV); R-L, Riemann-Liouville; SOC, State of Charge.

1 Introduction

In the face of dwindling oil reserves and escalating pollution from conventional fuel vehicles, there has been a growing national emphasis on promoting the adoption of new energy vehicles. This impetus has, in turn, propelled the development of essential infrastructure such as charging stations (Jinyuan et al., 2020). Presently, the structure of electric vehicle charging stations primarily involves the conversion of AC power from the distribution grid into stable DC power using rectifiers and power converters. The high prevalence of power electronic converters in the system renders charging stations susceptible to weak damping characteristics and low system inertia. As disturbances arise, such as load switching of electric vehicles and faults in the distribution grid, there arises a pressing need to bolster the system's inertia support capacity to enhance overall stability and efficiency (Pengcheng et al., 2022).

In the field of electric vehicle research, there have been numerous studies conducted by scholars. Among these, Reference (Zhang and Xujian, 2022) utilized an equivalent circuit model combined with a three-dimensional finite element method to investigate the inconsistent distribution observed during charging and discharging processes in closed-loop coils. This led to the proposal of a new strategy involving multiple charging processes that enable precise charging to the target current. Reference (Lu et al., 2022) proposed an adaptive dynamic surface control method with disturbance observer, which enhances the control accuracy and stability of hybrid power source systems for electric vehicles. Based on the dual-model predictive control, Reference (Zhang et al., 2023) developed a method to achieve energy savings and stability for distributed electric vehicle driving. Reference (Jinhao et al., 2023) studied collector equipment in new energy vehicle batteries and proposed a lightweight network model that is both fast and stable. Reference (Yuan et al., 2023) proposed a regulation operation framework for plug-in electric vehicle (PEV) aggregators based on grid-to-vehicle technology and developed a PEV scheduling algorithm. This optimization scheduling method not only increases the aggregator's revenue but also reduces the charging costs of electric vehicle owners. The study of electric vehicles (EVs) is currently highly regarded (Hou et al., 2017), with extensive research focused on modeling electric vehicle power batteries and energy storage. However, the connection between the charging process of electric vehicles and the grid, along with the associated control methodologies, remains a crucial topic of interest.

The components of capacitors and inductors within power electronic converters and electric vehicle battery systems exhibit fractional-order characteristics and diffusion properties (Macioszek, 2021). Traditional integer-order models struggle to accurately describe their distributed performance and memory effects, while fractional-order models extend the applicability beyond integer-order models, providing a better representation of the gradual parameter variations (Chen et al., 2024), yielding more precise charging station models. In recent years, the application of fractional calculus theory in fractional-order modeling has become increasingly prevalent (Zhou et al., 2021). The reference (Jing et al., 2020) reveals the distinct fractional-order impedance characteristics of batteries through their electrochemical impedance spectroscopy. By replacing integer-order capacitors with Constant Phase Elements (CPE), fractional-order models, as indicated in studies (Junfu et al., 2017; Zhou et al., 2022), can realistically simulate the polarization effects and charge-discharge characteristics of batteries. Additionally, the establishment of fractional-order Buck-Boost converters and three-phase grid-tied inverter models in references (Liao et al., 2023; Xiaocong et al., 2023) demonstrates that fractional-order models possess richer nonlinear characteristics and greater design flexibility. These research findings underscore the effectiveness of employing fractional-order theory for modeling power electronic devices and determining control strategies.

Numerous studies have demonstrated that various control methods, such as sliding mode control (Wang et al., 2023), predictive control (Guo et al., 2022), and fuzzy control, can effectively enhance the dynamic and steady-state performance of converters. However, challenges persist, including low inertia and insufficient damping. A common strategy for improving inertia involves treating the converter as a virtual synchronous machine, simulating the inertia and damping characteristics of a synchronous machine to provide the system with the necessary properties. This approach typically requires the addition of extra energy storage units in the design of the control strategy (Zisen et al., 2018; Gong and Gu, 2023). However, previous research has neglected the dynamic response of the energy storage units during the design phase of the control strategy. In a study referenced by (Linbin et al., 2017) the dynamic characteristics of DC capacitors are utilized to boost system inertia, and the impact of key parameters on dynamic behavior is thoroughly investigated.

Due to the flexibility and enhanced control effectiveness of fractional-order controllers, studies (Xiao et al., 2020; Lingling et al., 2022) have utilized fractional-order controllers to regulate both integer and fractional-order power electronic converter models. The findings indicate superior dynamic performance compared to integer-order controllers, effectively improving system stability. These studies commonly utilize the Integral of Time multiplied by Absolute Error (ITAE) performance index as the objective function for parameter optimization. However, in practical renewable energy systems, variations in power system and control parameters can modify impedance characteristics, making impedance modeling a more appropriate approach for engineering analysis (Dingyu, 2018; Chuang et al., 2021). The aforementioned research underscores that fractional-order control methods offer greater flexibility and superior control effectiveness when compared to integer-order control methods.

Based on the limitations outlined in the cited literature, this study employs fractional-order modeling techniques to better align the model with the actual characteristics of systems, thereby furnishing model support for the efficacy of subsequent control methodologies. The exceptional performance of fractional-order controllers enhances the flexibility of integer-order parameter design, thereby optimizing control outcomes. In various emerging applications within the realm of power systems, such as control systems for electric scooters (Macioszek et al., 2023), motorcycles, and charging stations for new energy vehicles, as well as in the large-scale charging control infrastructure for urban electric vehicle electronic transportation facilities (Macioszek, 2019), the inertia-optimized control method based on fractional-order models and controllers promptly furnishes adequate inertia to the system. This

TABLE 1 Comparison of research content in different literatures.

Ref	Modeling method		Control method		Control criterion		Control of inertia	
	IO	FO	IO	FO	Dynamic response time	Impedance spectrum deviation	Adaptive optimization	Fixed value control
Zhang et al. (2023)	√	-	√	-	√	-	√	-
Chen et al. (2024)	√	-	-	-	-	-	-	-
Jing et al. (2020)	-	√	-	-	-	√	-	-
Junfu et al. (2017)	-	√	-	-	-	-	-	-
Zhou et al. (2022)	-	√	-	-	-	-	-	√
Liao et al. (2023)	-	√	-	√	√	-	-	√
Xiaocong et al. (2023)	√	-	-	√	√	-	-	-
Wang et al. (2023)	√	-	√	-	√	-	√	-
Guo et al. (2022)	√	-	√	-	√	-	-	√
Lingling et al. (2022)	√	-	-	√	√	-	√	-
Xiao et al. (2020)	-	√	-	√	√	-	√	-
Chuang et al. (2021)	√	-	√	-	-	√	-	√
Dingyu (2018)	√	-	√	-	-	√	-	√
Liu et al. (2020)	-	√	√	-	√	-	-	√
Liu et al. (2024)	√	-	-	√	√	-	-	√
Zhang et al. (2022)	√	-	√	-	√	-	√	-
Yang et al. (2019)	√	-	√	-	√	-	√	-
Current Study	-	√	-	√	-	√	√	-

10.3389/fenrg.2024.1404386

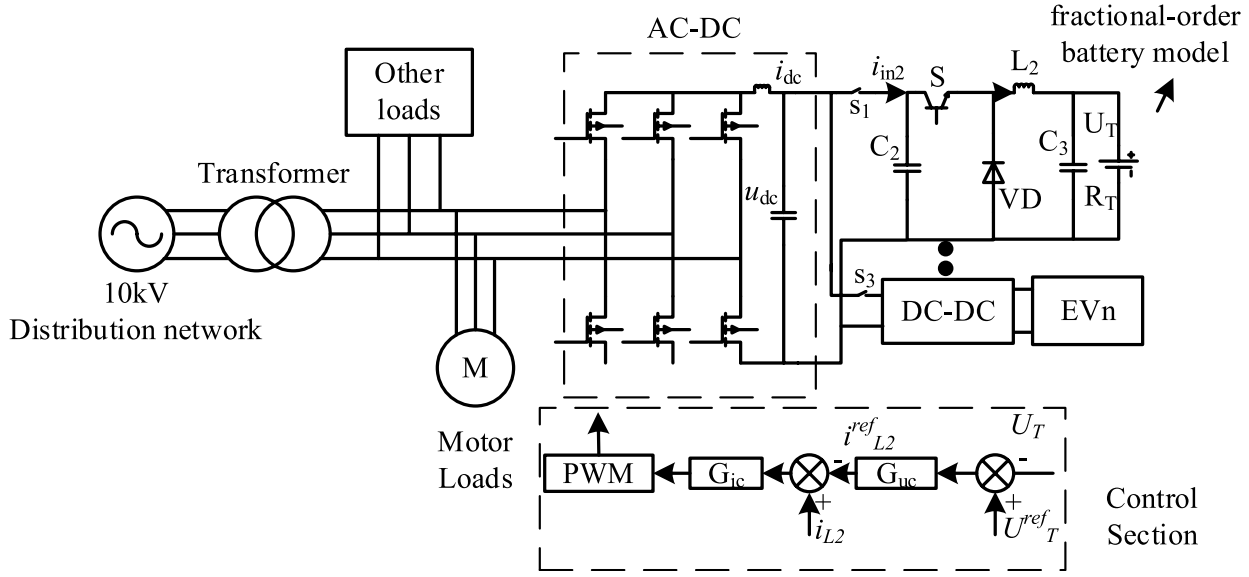

FIGURE 1
Schematic diagram of charging station structure.

effectively mitigates oscillations in DC voltage and power at the distribution network side, ensuring the stable operation of the power system.

The analysis in Table 1 reveals a scarcity of studies utilizing fractional-order control methods in previous virtual inertia control, and even fewer that combine fractional-order models with fractional-order control methods for analysis. Given the prevalent fractional-order characteristics of power electronic devices in practical applications, particularly within the current context of extensive construction of electric vehicle charging stations, fractional-order modeling and control methods exhibit strong applicability. In addition, by designing a control strategy based on the impedance spectral deviation value, this study avoids the adverse effects on the control effect caused by the changes in the impedance characteristics resulting from the adoption of performance indexes such as ITAE as the control objective function in the above studies. In summary, this study introduces a new research method and provides a new research perspective.

The main contributions of this paper are summarized below.

1) Based on the theoretical foundation of fractional calculus, this study establishes a fractional impedance model for electric vehicle charging stations. Due to the abundance of power electronic devices in electric vehicles and charging station systems, they inherently exhibit fractional-order characteristics. Therefore, this modeling approach is more effective compared to traditional integer-order methods, providing theoretical support and a foundational model for subsequent research, demonstrating its significant importance.
2) This study employs a fractional-order controller integrated with the fractional-order model to design control strategies for charging station systems. The flexibility of the fractional-order controller and its compatibility with the fractional-order model make the proposed control strategy not only reliable but also more adaptable in terms of controller parameterization. This bears crucial significance for further research in the control of large-scale charging stations.
3) Through the integration of the fractional impedance model and the fractional-order controller, this study presents a novel approach for optimizing virtual inertia control in charging stations. The objective function of this approach is to minimize the deviation of the fractional impedance spectrum. By doing so, it effectively mitigates voltage fluctuations and power oscillations on the distribution network, thereby ensuring the overall stability of the charging station system. Moreover, this method addresses the potential errors caused by variations in system and control parameters, which can alter impedance characteristics. Consequently, it offers valuable insights and prospects for further research on the configuration and control methods of large-scale charging stations.

The rest of this paper is organized as follows. Chapter 2 introduces the fractional-order theory and develops a small-signal model for the charging station grounded in this theory. In Chapter 3, the fractional-order PID controller is introduced, alongside the proposition of an inertia optimization control method derived from the fractional-order impedance model of the charging station. Chapter 4 offers experimental simulations to showcase the efficacy of the methodologies outlined in this paper.

2 Structural design and small-signal model of charging stations based on fractional-order theory

The structural model of the charging station in the article, as illustrated in Figure 1, primarily consists of the distribution network,

10.3389/fenrg.2024.1404386

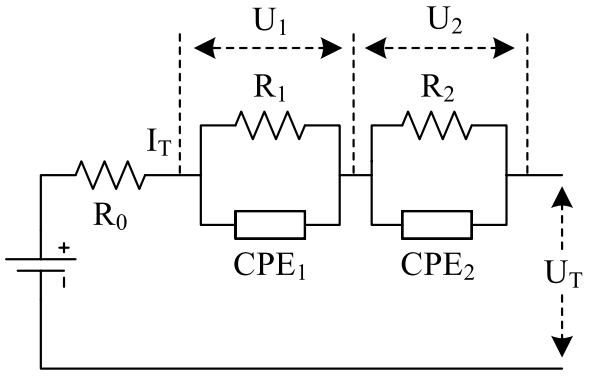

FIGURE 2
Fractional second-order RC equivalent circuit.

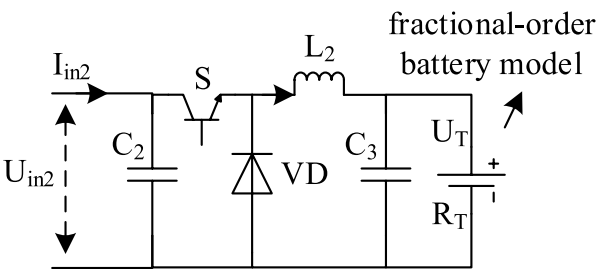

FIGURE 3
Circuit diagram of fractional order DC-DC converter.

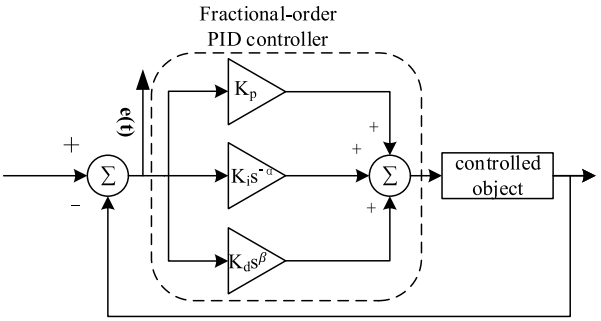

FIGURE 4
Block diagram of fractional order control.

transformer, PWM rectifier, DC-DC power converter, and electric vehicle load.

The transformer parameters are set at 10/0.4 kV, with the electric vehicle charging station having a maximum power of 120 kW. The input voltage is AC 380 V, the maximum output voltage is DC 750 V, and the maximum output current is 200 A. The DC-DC power converter employs a dual-loop control strategy comprising voltage and current loops. In this setup, where i_{dc} denotes the DC side current, u_{dc} stands for the DC side voltage, and i_{in2} refers to the capacitor current on the DC side, the voltage outer loop regulates the DC voltage u_{dc} with a reference value of $u^{ref}{}_{dc}$, with the output of the voltage loop serving as the reference value $i^{ref}{}_{dc}$ for the current inner loop. The current inner loop controls the dq-axis tracking and generates control signals for the rectifier through PWM signal generation and dq inverse transformation.

2.1 Fractional calculus

Fractional calculus is a direct extension of integer-order calculus, and the theory and numerical computation of integer-order calculus form the basis for implementing fractional-order control. Here, α denotes the order of calculus, and the fractional differential operator is defined as follows (Mehta and Gupta, 2024):

$$ {}_{\alpha}D_t^a = \begin{cases} \frac{d^\alpha}{dt^\alpha}, \alpha > 0 \\ 1, \alpha = 0 \\ \int_a^t (d\tau)^\alpha, \alpha < 0 \end{cases} \tag{1} $$

There are several different definitions of fractional order calculus, including G-L, R-L, and Caputo definitions. In this study, the (G-L) definition method is chosen to represent the fractional differential operator of the fractional-order capacitor CPE:

$$ {}_{\alpha}D_t^a = \lim_{h \to 0} T_s^{-\alpha} \sum_{j=0}^{[t/Ts]} \omega_j^\alpha x(t - jT_s) \tag{2} $$

Where T_s represents the sampling time interval, t denotes the current time instant, and j signifies the step number.

2.2 Small-signal model of fractional-order charging station systems

By combining electrochemical impedance spectroscopy (EIS) with fractional-order theory, a fractional-order impedance equivalent model is established, which outperforms integer-order models while overcoming the complexity of electrochemical model analysis (Liu et al., 2020). The paper selects a second-order RC equivalent circuit with fractional order to simulate energy storage units in lithium batteries for electric vehicles and charging stations. As shown in Figure 2, R_0 represents the internal resistance of the lithium battery; R_1 and R_2 represent polarization internal resistances, and CPE represents the fractional-order capacitor. By combining the two polarized internal resistances and the fractional-order capacitor in parallel, the paper separately describes the electrochemical polarization process and the concentration polarization process of the lithium battery.

The CPE component in Figure 2, known as the Constant Phase Element, is represented by the impedance.

$$ Z_\alpha(CPE) = \frac{1}{(j\omega)^\alpha C_\alpha} = \frac{1}{s^\alpha C_\alpha} \tag{3} $$

Applying Kirchhoff's law, the fractional-order model in Figure 2 can be expressed as follows:

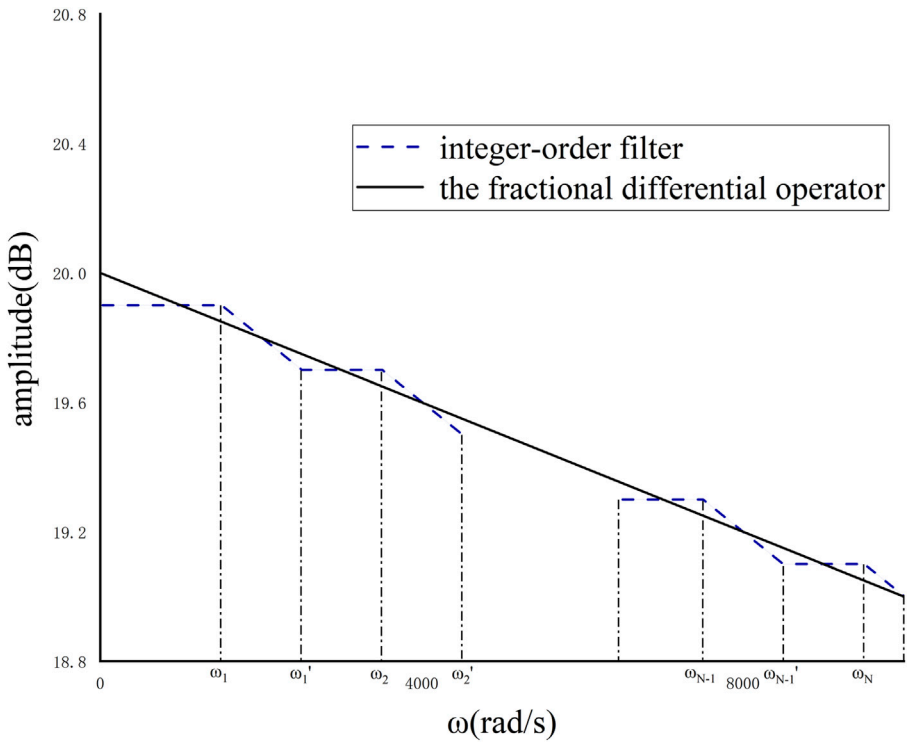

FIGURE 5
Block diagram of fractional order control.

$$\begin{cases} \frac{d^m U_1}{dt^m} = -\frac{1}{R_1 C_1} U_1 + \frac{1}{C_1} I_T \\ \frac{d^n U_1}{dt^n} = -\frac{1}{R_2 C_2} U_2 + \frac{1}{C_2} I_T \\ \dot{SOC} = -\frac{1}{Q_n} I_T \\ U_T = U_{OC} - R_0 I_T - U_1 - U_2 \end{cases} \tag{4}$$

Where m and n represent the orders of the fractional capacitors CPE_1 and CPE_2 respectively; Qn is the maximum capacity of the current state of the lithium battery; Uoc represents the open-circuit voltage related to the SOC; I_T is the total current of the battery pack; U_T denotes the terminal voltage of the battery pack; U_1 and U_2 represent the voltages at the terminals of fractional capacitors CPE_1 and CPE_2 respectively.

In the process of parameter identification, it is necessary to discretize the differentiation terms of the model in Eq. 4 using the definition method introduced in Eq. 2. Due to the nonlinearity and multi-parameter nature of fractional-order batteries, a genetic algorithm is employed for model parameter identification. The fitness function of the algorithm aims to minimize the root mean square error of the model, as shown in the following equation:

$$f = \min\left(\sqrt{\frac{1}{N} \sum_{k=1}^{N} (y_k - \hat{y}_k)^2} \right) \tag{5}$$

Where N represents the length of the measured output voltage data y_k, where y_k is the measured output voltage, and $\hat{y}_k$ denotes the estimated value. The genetic algorithm iterates with the objective of minimizing the mean square error to identify the battery parameters.

The fractional-order DC-DC converter circuit is depicted in Figure 3, where S represents the power switch, C denotes the fractional-order capacitor with order a ($0 < a < 1$), and L is the fractional-order inductor with order b ($0 < b < 1$).

The voltage-current relationship across the terminals of the fractional-order capacitor and the fractional-order inductor is given by:

$$\begin{cases} u_L = L \frac{d^a i_L}{dt^a} \\ i_C = C \frac{d^b u_C}{dt^b} \end{cases} \tag{6}$$

Based on Figure 3 and the above analysis, the small-signal model of the fractional-order DC-DC converter can be obtained as:

$$L_2 \frac{d^b \hat{i}_{L2}}{dt} = D_b \hat{u}_{in2} + \hat{d}_b U_{in2} - \hat{u}_T \tag{7}$$

$$\begin{cases} \frac{d^a \hat{u}_{in2}}{dt} = \frac{1}{C_2} \left(\hat{i}_{in2} - D_b \hat{i}_{L2} - \hat{d}_b I_{L2} \right) \\ \frac{d^a \hat{u}_T}{dt} = \frac{1}{C_3} \hat{i}_{L2} - \frac{\hat{u}_T}{C_3 R_T} \end{cases} \tag{8}$$

where d_b represents the duty cycle, u_T is the terminal voltage of the fractional-order battery, R_T is the equivalent resistance of the battery, a and b represent the orders of the fractional-order capacitor and inductor respectively; D_b is the equivalent duty

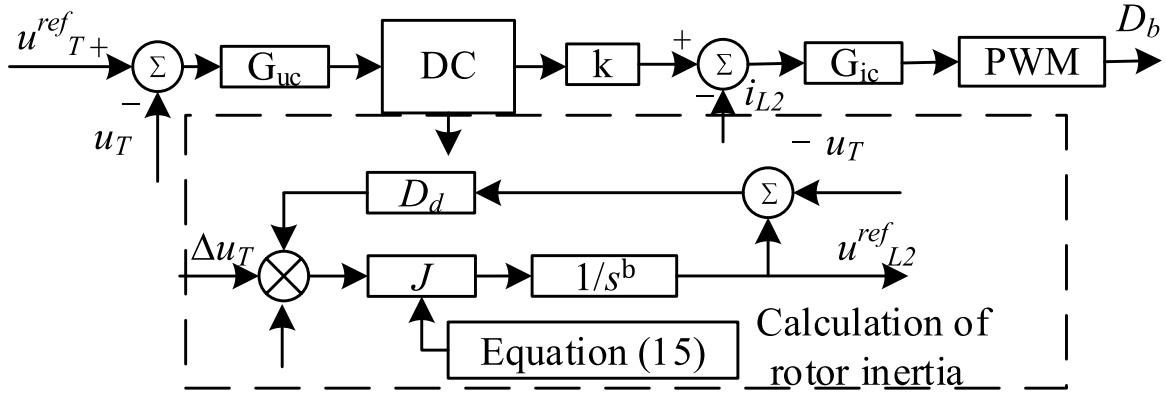

FIGURE 6
The Fractional order control strategy diagram.

cycle at the steady-state operating point of the DC-DC converter; U_{in2} is the steady-state input voltage of the DC-DC converter; I_{L2} is the inductor current at the steady-state operating point. Transforming the small-signal model from the time domain to the frequency domain yield:

$$L_2 s^b \hat{i}_{L2} = D_b \hat{u}_{in2} + \hat{d}_b U_{in2} - \hat{u}_T \tag{9}$$

$$\begin{cases} s^a \hat{u}_{in2} = \dfrac{1}{C_2}\left(\hat{i}_{in2} - D_b \hat{i}_{L2} - \hat{d}_b I_{L2}\right) \\ s^a \hat{u}_T = \dfrac{1}{C_3}\hat{i}_{L2} - \dfrac{\hat{u}_T}{C_3 R_T} \end{cases} \tag{10}$$

3 Optimization coordinated control method of virtual inertia based on fractional-order impedance model

3.1 Fractional-order PID controller

The system diagram of the fractional-order PID controller is depicted in Figure 4, with system parameters including the proportional gain K_p, integral gain K_i, derivative gain K_d, as well as the integral order α and derivative order β (Liu et al., 2024). The mathematical model of the fractional-order PID is given by:

$$G_C(s) = K_p + K_i s^{-\alpha} + K_d s^{\beta} \tag{11}$$

To guarantee optimal control performance, the utilization of integer-order approximation methods with suitable integer -order filters is indispensable. Two prevalent approaches for approximate implementation encompass continuous transfer function approximation and discretization. In accordance with the methodology advocated in reference (Zeng et al., 2022), the Oustaloup method is employed for accurately fitting the derivative operator through continuous transfer function approximation.

As shown in Figure 5, the Oustaloup method approximates the characteristics of fractional-order operators using a set of line segments. These line segments leverage the zeros and poles of integer-order filters to achieve alternating slopes of the magnitude-frequency response between 0 and -20 dB, enabling the approximation of fractional-order operators of any order. While integer-order PID controllers exhibit limited correction capabilities in the system's frequency domain curve and poor overshoot suppression, fractional-order PID controllers offer flexible phase angles and different gain crossover frequencies, providing stronger correction abilities for frequency domain curves.

3.2 Virtual inertia control strategy based on fractional -order charging station model

According to the reference (Zhang et al., 2022), inertia in a DC system primarily originates from two sources: the DC motor and the DC capacitor. The virtual DC motor method enhances system stability by introducing virtual rotational inertia to simulate the DC motor and the DC capacitor. The relationship between torque and power is given by:

$$J\frac{d\omega}{dt} = P_m - P_e - D_d(\omega - \omega_n) \tag{12}$$

where P_m and P_e represent the virtual input mechanical power and output power, respectively. D_d stands for the damping coefficient, J denotes the virtual rotational inertia, and ω_n is the rated angular rotor speed. The virtual synchronous machine incorporates inertia into the grid in the form of electrical power. When disturbances occur in the system load, the rotor achieves torque balance by releasing kinetic energy. Analogous to the aforementioned analysis, the paper considers enhancing system inertia by introducing a virtual capacitor that provides injected current, thereby achieving inertial support. Based on the fractional-order definition introduced in Eq. 2, where b represents the order of the capacitor, the port characteristics of the DC capacitor can be expressed as follows:

$$P_m - P_e = C u_{out} \frac{du^b_{out}}{dt^b} \tag{13}$$

Based on the preceding analysis and in conjunction with Eqs 12, 13, the expression for the virtual inertia control of a fractional-order capacitor can be derived, as follows:

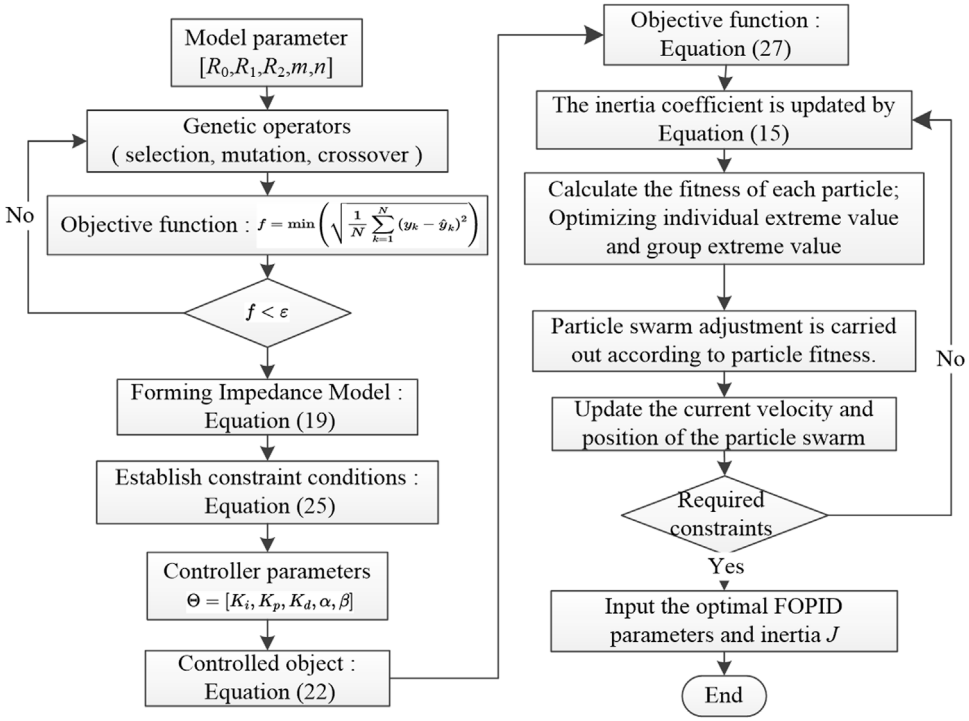

FIGURE 7
The Fractional-order control strategy diagram.

$$i_{ref} - i_0 - D_d\left(u_{out} - U_d\right) \approx J\frac{du_{out}^b}{dt^b} \tag{14}$$

where i_{ref} represents the set current, u_{out} denotes the output voltage value, and U_d stands for the rated output voltage. From the analysis above, it is evident that when an electric vehicle undergoes switching actions causing fluctuations, the DC capacitor rapidly emulates the output current to enhance the inertia of the charging station system, thereby preventing significant voltage fluctuations. The damping coefficient D_d signifies the amount of active power change in the output when the voltage changes significantly within a unit of time. A higher damping coefficient results in a faster restoration of the DC voltage.

The article analogizes the Buck circuit containing a fractional-order capacitor to a DC motor model. The control strategy of the system is illustrated in Figure 6, where it can be observed that the inertia of the system is influenced by the fractional-order capacitor, the inertia coefficient J, the damping coefficient D, as well as the parameters of the FOPID controller.

The adaptive virtual inertia control is expressed as follows:

$$J = \begin{cases} J_0 & \left|d^b u_0 / d^b t\right| < k_u \\ J_0 + k_J\left|d^b u_0 / d^b t\right| & \left|d^b u_0 / d^b t\right| > k_u \end{cases} \tag{15}$$

where J_0 as the virtual inertia coefficient at steady state, with k_J as the adjustment factor, and k_u represents the voltage rate of change action thresholds.

In order to explore the correlation between the impedance model and the inertia coefficient, additional research is conducted utilizing the small-signal DC-DC model outlined in Eqs 9, 10. With reference to the control block diagram depicted in Figure 6, the small-signal model of the control equations can be derived as follows:

$$\begin{cases} \hat{u}_{L2}^{ref} = \left(\hat{u}^{ref} D_d - \hat{u}_T - \hat{i}_{L2}\right) \Big/ \left(s^b J + D_d\right) \\ \hat{d}_b = \left(\hat{u}_{L2}^{ref} - \hat{u}_T\right) G_{cu} G_{ci} - \hat{i}_{L2} G_{ci} \end{cases} \tag{16}$$

where u_{ref} represents the output voltage disturbance controlled by virtual inertia and damping coefficients. Here,

$$\begin{cases} G_{cu} = k_{pu} + \dfrac{k_{iu}}{s^\alpha} + k_{du} s^\beta \\ G_{ci} = k_{pi} + \dfrac{k_{ii}}{s^\alpha} + k_{di} s^\beta \end{cases} \tag{17}$$

where k_{pu}, k_{iu} and k_{du} stand for the PID parameters of the outer voltage loop, while k_{pi}, k_{ii} and k_{di} represent the PID parameters of the inner current loop. From Eq. 17, the relationship between u_{in2} *and* i_{L2}, and other disturbance quantities can be derived as follows:

$$\begin{cases} G_{d1} = \dfrac{\hat{d}_b}{\hat{u}_{L2}^{ref}} = G_{cu} \cdot G_{ci}; G_{d2} = \dfrac{\hat{d}_b}{\hat{u}_{in2}} = -G_{cu} \cdot G_{ci}; \\ G_{d1} = \dfrac{\hat{d}_b}{\hat{i}_{L2}} = -G_{ci}; GF_1 = \dfrac{\hat{u}_{L2}^{ref}}{\hat{u}^{ref}} = \dfrac{D_d}{s^a J + D_d}; \\ GF_2 = \dfrac{\hat{u}_{L2}^{ref}}{\hat{u}_{in2}} = \dfrac{-1}{s^a J + D_d}; GF_3 = \dfrac{\hat{u}_{L2}^{ref}}{\hat{i}_{in2}} = \dfrac{-1}{s^a J + D_d}; \end{cases} \tag{18}$$

TABLE 2 System parameters of the charging station.

Parameter information	Symbol	Parameter value
Grid-side voltage	V	380
Grid-side resistance	Ω	0.05
Grid-side inductance	mH	3
Rectifier-side filter capacitance	mF	2
DC voltage	V	750
DC-DC side inductance	mH	5.76
DC-DC side capacitance	mF	0.01
Battery	V/Ah/SOC	350/135/35 400/138.5/75 500/180/45
Motor load	VA	2200
Other loads	VA	1000

Finally, based on Eqs 9, 10, 18, the input impedance function of the DC-DC converter can be deduced:

$$Z_{2in} = \frac{\hat{u}_{in2}}{\hat{i}_{in2}} = \frac{s^b L_2 \left[1 - I_{L2}\left(GF_3 G_{d1}\right)\right] - U_{in2} D_b \left(GF_3 G_{d1}\right)}{\left(s^{a+b} C_2 L_2 + D_b + G_{d2} D_b U_{in2} + I_{L2} G_{d2} + s^b L_2 + G_{d1} U_{in2} D_b + G_{d1} GF_2 D_b s^b L_2\right)} \tag{19}$$

4 Optimal parameter tuning for fractional-order controller

4.1 Particle swarm optimization-based FOPID parameter tuning method

The article focuses on optimizing the controller parameters of a DC-DC power converter using particle swarm optimization. When the charging process of electric vehicles is affected by the switching actions of the electric vehicle, it ensures that the system has sufficient inertia to maintain voltage stability. This enables electric vehicles to achieve stable charging and reduces the impact of external interference on the charging process.

Initially, the optimization objective is set to minimize the error between the impedance spectrum calculated using the actual measured impedance spectrum and the impedance model obtained from the Eq. 19. The five dimensions considered for particles include K_p, K_i, K_d, α *and* β. The velocity and position of particle p in the (k+1)th iteration are updated according to the following equation (Yang et al., 2019):

$$\begin{cases} V_{in}(k+1) = w(k+1)V_{in}(k) + c_1 r_1 \left(P_{in}(k) \right. \\ \qquad\qquad \left. - X_{in}(k) + c_2 r_2 \left(P_{gn}(k) - X_{in}(k)\right)\right. \\ X_{in}(k+1) = X_{in}(k) + V_{in}(k+1) \end{cases} \tag{20}$$

where V_{in} and X_{in} represent the velocity and position of the ith particle. Here, $1 \le n \le N$, where N is the number of dimensions in the search space. "w" denotes the inertia weight, while c_1 and c_2 are positive acceleration coefficients. The variables r_1 and r_2 are two independent random numbers with values ranging from 0 to 1. The terms $c_1 r_1$ and $c_2 r_2$ control the movement speed of the particle swarm. P_{in} represents the current best position of the ith particle, while P_{gn} denotes the current best position of the particle swarm as a whole.

To ensure that the particle swarm converges towards the global optimum, an adaptive update is performed on the particle swarm in each iteration. The particles are sorted in descending order of fitness, and the 20% of particles with lower fitness values are selected for position and velocity initialization. This strategy increases the diversity of the population and prevents the particle swarm algorithm from getting stuck in local optima. The update in each iteration is achieved by assigning inertia weights based on the fitness value ranking of particles from large to small. The calculation equation for the inertia weight is as follows:

$$w(i) = 0.4 + 0.5 * ww(i)/Num \tag{21}$$

where $ww(i)$ represents the fitness-based ranking of particle i, and "Num" is the size of the particle swarm. This improvement replaces the standard method of assigning values based on the number of iterations with inertia weights related to particle fitness values. It enhances global search capabilities and effectively prevents the particle swarm algorithm from converging to local optima.

By measuring the input DC voltage (u_{dc}') and current (i_{dc}') of the DC-DC converter, actual impedance data is obtained. Processing the measured impedance and impedance model output values using fractional Fourier transformation yields the impedance measurement spectrum in the frequency domain on the DC side:

$$M = \max\left(frft\left(\frac{u_{dc}'}{i_{dc}'}, \gamma\right)\right) \tag{22}$$

The symbol frft represents the fractional Fourier transform operation, and γ denotes the order of the fractional Fourier transform. The impedance spectrum function itself is represented in the frequency domain, while the moment of inertia is represented in the time domain. The characteristic feature of the fractional Fourier transform is its ability to effectively combine time-domain signals and frequency-domain signals through arbitrary-order rotation. Essentially, the fractional Fourier transform is a time-

10.3389/fenrg.2024.1404386

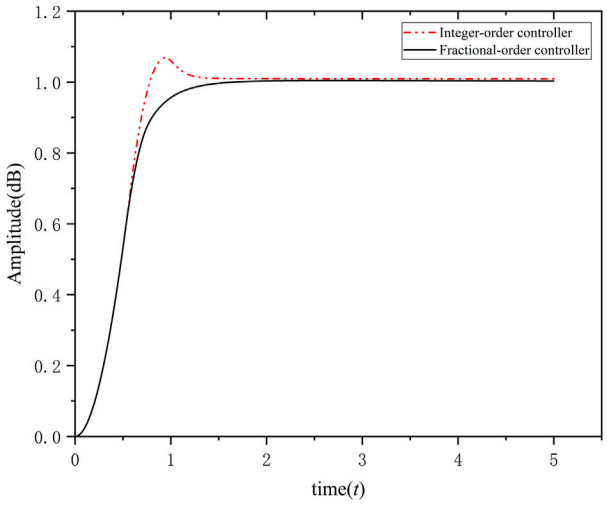

FIGURE 8
Comparison of unit-step responses for integer-order and fractional-order controllers.

frequency analysis method, representing all information of a signal from the time domain to the frequency domain in the fractional Fourier domain, reflecting more diverse local characteristics of the signal. The pth order Fourier transform can be expressed as:

$$X_p(u) = F^p[x](u) = \int_{-\infty}^{+\infty} x(t) K_p(t,u) dt \tag{23}$$

where K_p represents the kernel function of the fractional Fourier transform.

$$K_p(t,u) = \begin{cases} A_\alpha e^{i\left(t^2 \cot(\alpha/2) - ut \csc\alpha + u^2 \cot(\alpha/2)\right)}, \alpha \neq n\pi \\ \delta(t-u), \alpha = 2n\pi \\ \delta(t+u), \alpha = (2n \pm 1)\pi \end{cases} \tag{24}$$

By employing a step size of 0.01, the calculation of Eq. 22 is conducted for the parameter γ within the range of (0, 2). The maximum amplitude value M resulting from the fractional Fourier transform computation is identified to determine the optimal fractional order denoted as γ_0. Subsequently, under this optimal order, $M_1 = x_i + jy_i$ is assigned to the measured impedance spectrum value, while the theoretically derived impedance spectrum value is denoted as $M_2 = x_j + jy_j$. The resolution $f = f_s/N$ of the Fractional Fourier Transform (FRFT) is utilized as the incremental step size. The variable N represents the total count of data points collected, with each point reflecting the disparity between the modeled and actual values at the corresponding frequency. Based on the comprehensive analysis presented above, the constraints governing impedance spectrum deviation and voltage bias are established:

$$\begin{cases} \sum_{i=1}^{N} f|e(\omega)| \leq \varepsilon \\ \int_0^{i\max} e^2(t) dt \leq \varepsilon' \end{cases} \tag{25}$$

The $e(\omega)$ in the aforementioned equation is calculated using the following Eq. 26:

$$e(\omega) = \sqrt{\left(x_i - x_j\right)^2 + \left(y_i - y_j\right)^2} \tag{26}$$

where i_{max} represents the maximum iteration count, $e(t)$ represents the deviation of the output quantity, i.e., the deviation between the output voltage and the actual reference voltage. It is known that the value of J should not be too large, otherwise it will lead to a long system recovery time and a decrease in the output power capacity of power electronic devices. Therefore, in order to maximize the inertia of the system, it is proposed to use the maximum virtual inertia as the objective function:

$$J = \max \sum_{i=1}^{N} \frac{i_{in2}}{\{u_{in2}(d^b u_{in2}/dt^b)\}} \tag{27}$$

When disturbances cause the rate of change in voltage to exceed a threshold, the signal in the above equation is sampled at an update interval of 10 *ms*. The total number of points collected within one measurement interval is denoted as N.

4.2 Steps of fractional-order virtual inertia optimization control method

The study introduces a virtual inertia optimization control method based on the fractional-order impedance model of the charging station, with its algorithmic process depicted in Figure 7.

The steps of the algorithm are as follows.

(1) Define the parameters of the electric vehicle power battery [R_0, R_1, R_2, m, n]. Utilize a genetic algorithm to iteratively calculate the objective function, which is expressed in Eq. 5.
(2) If the objective function meets the error standard, output the result and proceed to the next calculation. Otherwise, return to step 1 and perform iterative calculations again.
(3) When disturbances occur in the charging station system, such as switching of electric vehicles, the system experiences voltage mutation and generates voltage and power oscillations with gradually diminishing amplitude, causing the rate and magnitude of voltage changes to exceed the threshold. At this point, update the coefficients of the virtual inertia according to Eq. 15.
(4) Measure and calculate the maximum inertia under the current operating conditions with an update interval of 10 *ms* based on Eq. 27
(5) Use the current maximum inertia as the target and return to Step 3 for iterative calculation. Proceed to the next calculation when the voltage rate change meets the requirements.
(6) Set Eq. 25 as the target for virtual inertia control, and optimize the parameters of the FOPID controller using an improved particle swarm algorithm.
(7) Initialize the particle swarm, including the swarm size, search space range, inertia weight, acceleration coefficients, maximum iteration count, and particle velocity and position.
(8) Update the impedance function represented by Eq. 19 and compute the fitness function value of each particle according to Eq. 20.
(9) If the end condition is satisfied, output the optimal FOPID control parameters and moment of inertia J, and exit. Otherwise, return to step 7 for iterative recalculations until the result satisfies the termination condition.

10.3389/fenrg.2024.1404386

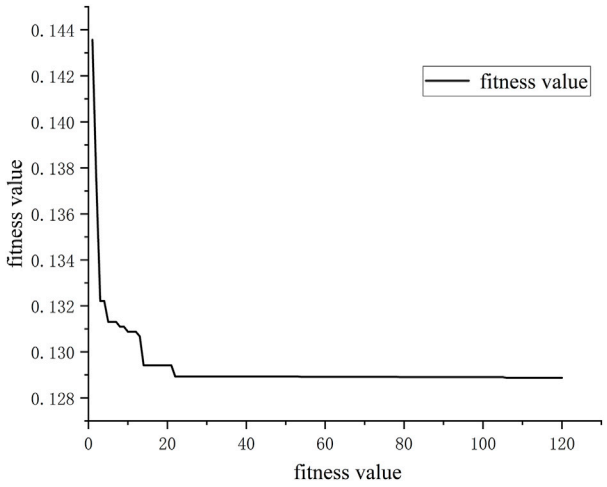

FIGURE 9
Fitness curve.

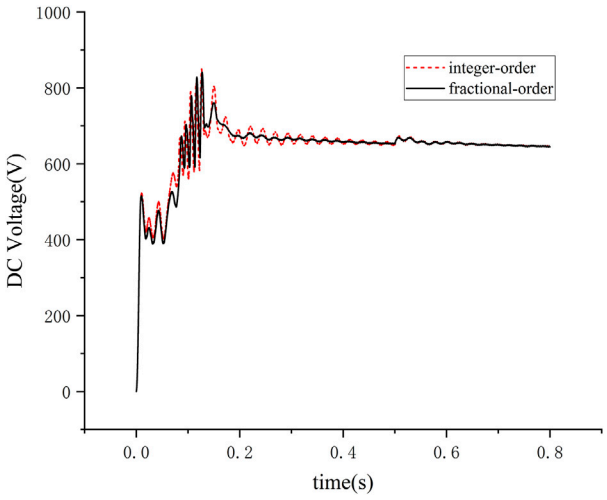

FIGURE 10
Voltage comparison on the DC side when switching on a single machine.

5 Simulation results

5.1 Case data

The article conducted simulation experiments using the charging station model illustrated in Figure 1, with the operational parameters of the system as outlined in Table 2.

5.2 Performance of control method

The simulation results illustrating the unit step response under two controllers using the impedance model presented in Eq. 19 as the controlled object are presented in Figure 8. It is evident from the figure that the system displays a rapid dynamic response, with a steady-state error of less than 0.3% and a relatively minor overshoot.

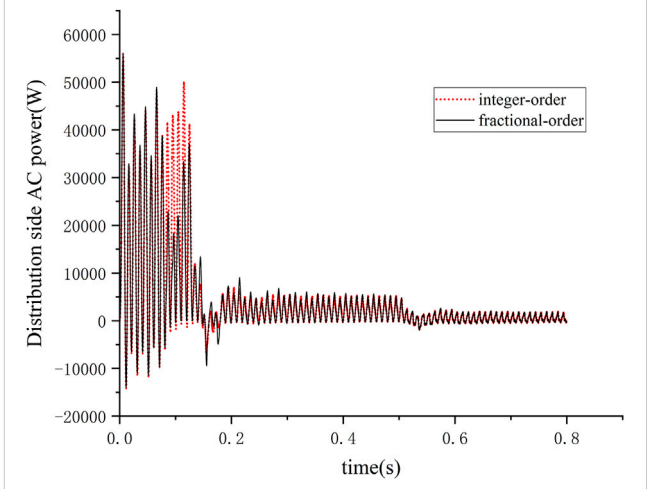

FIGURE 11
Comparison of AC side power when switching on a single machine.

TABLE 3 Results for integer and fractional controllers.

Controller	K_p	K_i	K_d	λ	μ	J_0	D_d
Integer-order	175.959	3.8301	25.9	-	-	4	10
Fractional-order	184.1678	17.594	38.112	0.326	0.9823	4	10

Kp, *Ki*, and *Kd* represent the proportional, integral, and differential parameters of the PID controller, λ represents the fractional order of the integral, μ represents the fractional order of the differential, *J* and *D* represent the virtual inertia coefficient and damping coefficient, respectively.

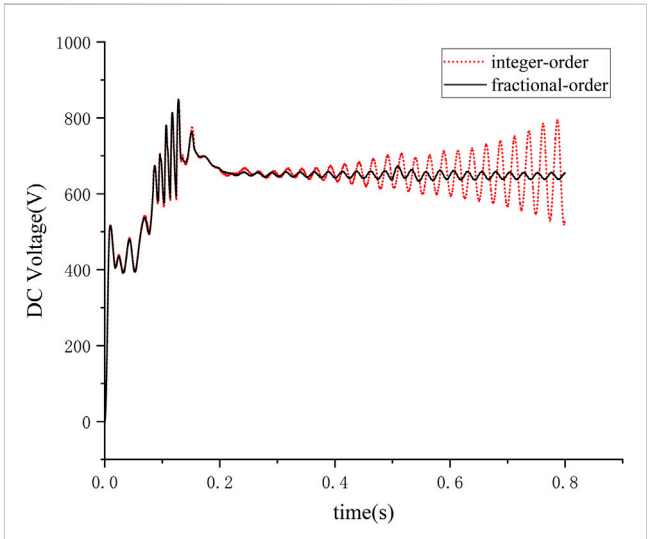

FIGURE 12
Voltage comparison on the DC side when switching multiple machines.

These observations serve to validate the superior dynamic response performance of the fractional-order PID controller proposed in the article when compared to the integer-order controller.

Experimental validation of the proposed fractional-order PID parameter tuning method was conducted, and fitness values were

10.3389/fenrg.2024.1404386

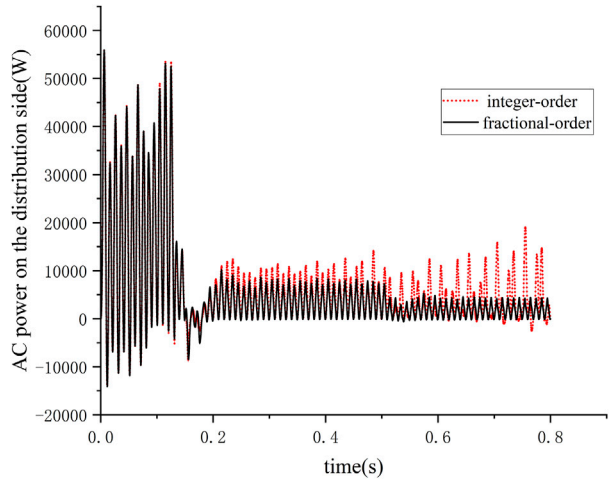

FIGURE 13
Comparison of AC side power when switching multiple machines.

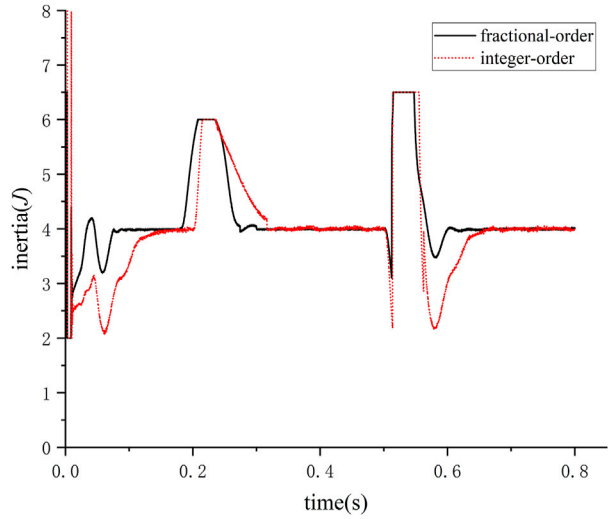

FIGURE 14
Changes in a moment of inertia.

obtained. As depicted in Figure 9, it is evident that the improved particle swarm algorithm proposed in the article for parameter tuning exhibits low fitness values and converges after more than 30 iterations, indicating a favorable convergence speed.

Considering a standalone operation in the system as shown in Figure 1, the operating conditions during a single bus switching, where switches s2 and s3 remain open while switch s1 is closed. From Figure 10, it is observed that when the electric vehicle is put on charge, the voltage offset amplitude for the integer-order controller is 826 V with a dynamic response time of 0.21053s. For the fractional-order controller, the voltage offset amplitude is 812 V with a response time of 0.025s. Upon reaching 0.5s, switch s1 is opened to terminate the electric vehicle's charging process. During the disconnection phase, the dynamic response time for the integer-order controller is 0.000812s, whereas for the fractional-order controller, it is 0.000792s.

When a single electric vehicle is switched, power measurements are conducted on the other loads containing the electric motor load and the common connection point of the charging station on the distribution network side, as shown in Figure 11. The simulation results indicate that under the operational state of a single vehicle switch, the fractional-order control method utilized in the paper exhibits superior dynamic response capabilities compared to the integer-order control method.

In the system depicted in Figure 1, multiple electric vehicles are considered for disconnection, with the parameters of the electric vehicles outlined in Table 3. The operational scenario is as follows: at the initial time, switches s1 and s2 are closed. At 0.2 s, switch s3 is closed to connect electric vehicle three to the charging station, and at 0.5 s, switch s1 is opened to stop the operation of electric vehicle 1. As shown in Figure 12, connecting three electric vehicles for charging at 0.2s results in minimal offset for the fractional-order controller under this operating condition. At 0.5s, when switch s1 is opened for operation, the integer-order controller exhibits significant DC voltage fluctuations, whereas the fractional-order controller demonstrates shorter dynamic response times, minimal voltage offsets, and ensures stable charging processes.

The power measurements for the system, including the electric motor load, other loads, and the common connection point of the charging station on the distribution network side, are depicted in Figure 13. When multiple charging stations are being switched, the fractional-order control method demonstrates a faster response speed, promptly providing sufficient inertia support for the system. Under this operating condition, the control method proposed in the paper exhibits superior performance in mitigating voltage and distribution-side power fluctuations compared to the integer-order method.

In Figure 14, the waveform depicts the variation in rotational inertia when multiple electric vehicles are being switched. The rotational inertia rapidly increases within 0.05 s to meet the maximum value specified in Eq. 27 when switching disturbances occur. Combining the simulation results mentioned above, it is evident that the method proposed in the paper effectively provides inertia support for the system when facing frequent short-term switching of electric vehicle loads. This method helps to mitigate DC voltage fluctuations and distribution-side power fluctuations, ensuring the stable operation of the system.

6 Conclusion

With the rapid development of electric vehicles, this study proposes a virtual inertia control strategy based on a fractional-order impedance model with FOPID control to enhance the system's inertia support ability. The performance of single and multiple charging stations under different load switching conditions is compared through simulation. The following conclusions are as follows.

(1) This study introduces the fractional calculus theory and establishes a fractional-order impedance model for

charging stations. Compared with traditional integer-order methods, the fractional-order modeling method reduces modeling errors since actual capacitance and inductance are fractional-order. This method is particularly effective for electric vehicle power batteries and charging station rectifiers with rich power electronic components, improving model accuracy and providing reliable model support for charging station control algorithm research.

(2) This paper employs a fractional-order controller to control the charging station system. Compared with integer-order controllers, fractional-order controllers have more adjustable parameters and a larger adjustable range, making the controller more flexible and able to achieve better control results. The simulation results show that using a fractional-order controller on top of the fractional-order impedance model of the charging station can control the dynamic response time within 0.025s and the DC voltage deviation within 5%, achieving better control results.

(3) Based on the fractional-order impedance model, a virtual inertia control optimization method is proposed with the fractional-order charging station impedance spectrum deviation as the objective function. When frequent switching actions occur at electric vehicle charging stations, this method can provide sufficient inertia support quickly and effectively. The simulation results show that this method can effectively suppress the DC voltage fluctuation of the charging station system and the power fluctuation of the network side during the oscillation process and can quickly provide sufficient inertia support for the system within 0.05 to ensure stable operation.

Data availability statement

The original contributions presented in the study are included in the article/Supplementary Material, further inquiries can be directed to the corresponding author.

Author contributions

JL: Writing–original draft, Funding acquisition, Methodology, Project administration, Resources, Supervision, Writing–review and editing. JH: Writing–original draft, Writing–review and editing, Conceptualization, Data curation, Formal Analysis, Software. BL: Writing–review and editing, Conceptualization, Formal Analysis, Project administration, Supervision, Validation.

Funding

The author(s) declare that no financial support was received for the research, authorship, and/or publication of this article.

Conflict of interest

The authors declare that the research was conducted in the absence of any commercial or financial relationships that could be construed as a potential conflict of interest.

Publisher's note

Supplementary material

The Supplementary Material for this article can be found online at: https://www.frontiersin.org/articles/10.3389/fenrg.2024.1404386/full#supplementary-material

References

Chen, Z., Zhang, Y., Yang, R., Liu, C., and Chen, G. (2024). Online internal temperature estimation for lithium-ion batteries using the suppressed second-harmonic current in single- phase DC/AC converters. *IEEE Trans. Power Electron.* 71, 9757–9766. doi:10.1109/tie.2023.3331090

Chuang, L. I. U., Yan, ZHANG, Zhu, Di, et al. (2021). Medium and low-voltage DC distribution system: impedance modeling and stability analysis of the key equipment. *High. Volt. Eng.* 47 (11), 3968–3983. doi:10.13336/j.1003-6520.hve.20201749

Dingyu, X. U. E. (2018). *Fractional calculus and fractional-order control*. Science Press.

Gong, R., and Gu, J. (2023). Adaptive control strategy of inertia and damping for load virtual synchronous machine. *Electr. Meas. Instrum.* 60 (03), 130–135. doi:10.19753/j.issn1001-1390.2023.03.019

Guo, L., Zheng, M., Yanyan, L. I., et al. (2022). Nonparametric sliding mode predictive control strategy for a three-phase LCL grid-connected inverter. *Power Syst. Prot. Control* 50 (18), 72–82. doi:10.19783/j.cnki.pspc.211576

Hou, M., Zhao, Y., and Xinglai, G. E. (2017). Optimal scheduling of the plug-in electric vehicles aggregator energy and regulation services based on grid to vehicle. *Int. Trans. Electr. Energ Syst.* 27, e2364. doi:10.1002/etep.2364

Jing, L. I., Yan, YANG, Jianxin, Q. I. N., et al. (2020). Research on fractional modeling and state of charge estimation of lithium battery. *Power Technol.* 44, 983–985.

Jinhao, LIANG, Jiwei, FENG, Liang, F., Lu, Y., Yin, G., Mao, X., et al. (2023). An energy-oriented torque-vector control framework for distributed drive electric vehicles. *IEEE Trans. Transp. Electrification* 9 (3), 4014–4031. doi:10.1109/tte.2022.3231933

Jinyuan, L. I. U., Lin, L. Y. U., Gao, H., et al. (2020). Planning of active distribution network considering characteristics of distributed generator and electric vehicle. *Automation Electr. Power Syst.* 44 (12), 41–49.

Junfu, L. I., Wang, L., Lyu, C., and Pecht, M. (2017). State of charge estimation based on a simplified electrochemical model for a single LiCoO2 battery and battery pack. *Energy* 133, 572–583. doi:10.1016/j.energy.2017.05.158

Liao, X., Wang, Y., Donghui, Y. U., Ran, M., and Ruan, P. (2023). Modeling and analysis of Buck-Boost converter with non-singular fractional derivatives. *Chaos Solit. Fractals* 169, 113336. doi:10.1016/j.chaos.2023.113336

Linbin, HUANG, Huanhai, X. I. N., Wang, Z., Wu, K., Hu, J., et al. (2017). A virtual synchronous control for voltage-source converters utilizing dynamics of DC-link capacitor to realize self-synchronization. *IEEE J. Emerg. Sel. Top. POWER Electron.* 5 (4), 1565–1577. doi:10.1109/jestpe.2017.2740424

Lingling, X. I. E., Liu, L. U., and Bin, L. I. U. (2022). Research on fractional-order PIλDμ control of grid-connected inverter based on MPSO algorithm. *Electr. Meas. Instrum.* 59 (6), 172–180. doi:10.19753/j.issn1001-1390.2022.06.024

Liu, L., Lin, G., Jiao, S., et al. (2020). Virtual DC generator control strategy and its dynamic analysis of DC charging station microgrid. *Power Syst. Prot. Control* 48 (11), 28–35. doi:10.19783/j.cnki.pspc.190776

Liu, S., Sun, H., Haotong, Y. U., Miao, J., Zheng, C., and Zhang, X. (2024). A fractional order model of auxiliary power batteries suitable for hydrogen fuel cell hybrid systems heavy-duty trucks. *Int. J. Hydrogen Energy* 63, 346–358. doi:10.1016/j.ijhydene.2024.03.095

Lu, Li, Wu, W., Gao, Y., Yu, X., Zhang, C., et al. (2022). Study on current discrepancy and redistribution of HTS non-insulation closed-loop coils during charging/discharging and subsequent transient process toward steady-state operation. *Supercond. Sci. Technol.* 35 (9), 095001. doi:10.1088/1361-6668/ac7dfe

Macioszek, E. E-Mobility infrastructure in the górnolsko - zagbiowska metropolis, Poland, and potential for development the 5th world congress on new technologies.2019.

Macioszek, E. (2021). Analysis of trends in development of electromobility in Poland: current problems and issues. *Transp. Dev. Challenges 21st Century*, 145–156. doi:10.1007/978-3-030-50010-8_13

Macioszek, E., Cieśla, M., and Granà, A. (2023). Future development of an energy-efficient electric scooter sharing system based on a stakeholder analysis method. *Energies* 16 (554), 554. doi:10.3390/en16010554

Mehta, R., and Gupta, A. (2024). Mathematical modelling of electrochemical, thermal and degradation processes in lithium-ion cells—a comprehensive review. *Renew. Sustain. Energy Rev.* 192, 114264. doi:10.1016/j.rser.2023.114264

Pengcheng, Z. H. A., Yali, G. A. N., Gao, H., et al. (2022). Quality assessment of electric vehicle charging stations accessing distribution network. *Electr. Meas. Instrum.* 59 (06), 69–75. doi:10.19753/j.issn1001-1390.2022.06.010

Wang, H., Nie, J., Bin, L. I., et al. (2023). Fractional order sliding mode control strategy of AC/DC hybrid microgrid interconnection interface converter under grid voltage imbalance. *Power Syst. Prot. Control* 51 (16), 94–103. doi:10.19783/j.cnki.pspc.230421

Xiao, ZHANG, Zhou, K., and Fan, W. U. (2020). MMC grid-connected control strategy based on fractional order PI~λ. *Electr. Meas. Instrum.* 57 (18), 115–121. doi:10.19753/j.issn1001-1390.2020.18.019

Xiaocong, L. I., Hou, L., Xueli, L. U. O., et al. (2023). Research on fractional modeling and controller design of three-phase inverter grid-connected system. *Acta Energiae Solaris Sin.* 44 (3), 415–424. doi:10.19912/j.0254-0096.tynxb.2021-1187

Yang, Y., Mei, F., Zhang, C., et al. (2019). Coordinated adaptive control strategy of rotational inertia and damping coefficient for virtual synchronous generator. *Electr. Power Autom. Equip.* 39 (3), 125–131. doi:10.16081/j.issn.1006-6047.2019.03.020

Yuan, L., Chen, Y., Tang, H., Ren, G., and Wenhuan, W. (2023). DGNet: an adaptive lightweight defect detection model for new energy vehicle battery current collector. *IEEE Sensors J.* 23 (23), 29815–29830. doi:10.1109/jsen.2023.3324441

Zeng, G., Liao, H., Zhao, J., et al. (2022). A self-adaptive control strategy of virtual inertia and a damping coefficient for bidirectional DC-DC converters in a DC microgrid. *Power Syst. Prot. Control* 50 (06), 65–73. doi:10.19783/j.cnki.pspc.210815

Zhang, Bo, and Xujian, S. H. U. (2022). *Fractional-order electrical circuit theory*. Singapore: Springer.

Zhang, X., Wang, Y., Yuan, X., Shen, Y., and Lu, Z. (2023). Adaptive dynamic surface control with disturbance observers for battery/supercapacitor-based hybrid energy sources in electric vehicles. *IEEE Trans. Transp. Electrification* 9 (4), 5165–5181. doi:10.1109/tte.2022.3194034

Zhang, X., Wang, Z., and Lu, Z. (2022). Multi-objective load dispatch for microgrid with electric vehicles using modified gravitational search and particle swarm optimization algorithm. *Appl. Energy* 306 (A), 118018. doi:10.1016/j.apenergy.2021.118018

Zhou, H., Wang, S., Chunmei, Y. U., Xia, L., and Fernandez, C. (2022). Research on SOC estimation for lithium-ion batteries based on improved PNGV equivalence model and AF-UKF algorithm. *Int. J. Electrochem. Sci.* 17 (8), 220836. doi:10.20964/2022.08.31

Zhou, W., Zheng, Y., Pan, Z., and Lu, Q. (2021). Review on the battery model and SOC estimation method. *Processes* 9 (1685), 1685. doi:10.3390/pr9091685

Zisen, Q. U., Cai, Y., Yang, H., et al. (2018). Strategy of power decoupling control for virtual synchronous generator based on adaptive virtual impedances. *Automation Electr. Power Syst.* 42 (17), 58–72. doi:10.7500/AEPS20171114014

frontiers | Frontiers in Energy Research

TYPE Original Research
PUBLISHED 03 July 2024
DOI 10.3389/fenrg.2024.1410731

OPEN ACCESS

EDITED BY
Chaolong Zhang,
Jinling Institute of Technology, China

REVIEWED BY
Zewen Li,
Changsha University of Science and Technology, China
Fei Mei,
Hohai University, China

*CORRESPONDENCE
Zhengran Sun,
sunzhengran98@163.com

RECEIVED 01 April 2024
ACCEPTED 30 May 2024
PUBLISHED 03 July 2024

CITATION
Li J, Sun Z and Liu B (2024), Fault probability identification method for distribution networks based on mov-MF distribution.
Front. Energy Res. 12:1410731.
doi: 10.3389/fenrg.2024.1410731

Fault probability identification method for distribution networks based on mov-MF distribution

Jiang Li, Zhengran Sun* and Bo Liu

Shanghai University of Electric Power, Shanghai, China

To address the fault identification challenge in distribution networks, a method leveraging a mixture of the von Mises–Fisher (mov-MF) distribution model for fault probability identification is proposed. Initially, the synchronous phasor measuring unit is employed to gather the post-fault steady-state voltage phase quantities, and then, the voltage phase angle values are combined to form a three-dimensional feature quantity. Subsequently, the mov-MF distribution model is initialized through the spherical K-means algorithm and the minimum message length algorithm. This model is further refined via the expectation–maximization algorithm to iteratively optimize distribution parameters. The test set data are input into the mov-MF distribution model, which has been constructed using typical fault data, to discern fault types. Finally, the efficacy of the proposed method is validated through simulation verification conducted on the IEEE 33-node distribution system. The analysis of the examples demonstrates the accuracy of the mov-MF distribution model-based fault identification method in identifying single-phase ground, two-phase ground, two-phase interphase, and three-phase short-circuit faults.

KEYWORDS

distribution network, fault identification, von Mises–Fisher distribution, maximum expectation algorithm, spherical k-means algorithm

1 Introduction

The requirements for ensuring power supply quality and reliability of modern distribution networks as the terminal facing users are gradually increasing (Sheng et al., 2023). Currently, the main grounding methods for distribution networks in China are either ungrounded neutral points or grounding through arc suppression coils. Due to the complex structure of distribution networks, various types of faults are likely to occur in practical operation. Single-phase grounding short circuit is the most common type of short circuit fault. If the short circuit is caused by the contact between the line and tree branches or the ground, the transient resistance of this short circuit is high, resulting in a weak fault electrical quantity that is difficult to detect, thereby affecting the normal operation of the distribution network. When faults occur in distribution networks, the primary task is to identify the faults. Therefore, efficient and reliable methods for fault identification in distribution networks are of great significance for the safe operation of distribution networks (Peng et al., 2023).

Zhu et al. (2020) utilized current, voltage, and power data at the maximum power point in the time domain as feature quantities, combined with Pearson's coefficient similarity and relative Euclidean distance deviation for fault-type differentiation. Jiang et al. (2021) used dynamic time warping (DTW) similarity and electrical volume data sequence similarity,

and the combination of both inputs into a classifier significantly outperformed single features. Zhang et al. (2022a) proposed a waveform similarity-based identification method to construct two reconstructed currents by comparing the one-dimensional time-domain sampled values of the currents at the two ends of a transmission line and used the Kendall's tau coefficient (KTC) waveform similarity algorithm to achieve reliable fault identification. Zhang et al. (2022b) proposed a sparse representation method based on one-dimensional time-domain current signals to construct a fault feature dictionary and calculate the feature residuals to determine the fault category. Liu et al. (2020) built a support vector machine model for high-resistance grounding fault identification using time-domain current-voltage magnitude and frequency as features. Ghaemi et al. (2022) used an integrated learning approach combined with multiple classifiers to accurately identify the fault type and location using one-dimensional time-domain voltage and current measurements, which maintains high classification accuracy even in the presence of measurement errors.

In contrast to the previous paper, which proposes to judge the fault type by constructing the signal similarity or deviation value as a one-dimensional feature quantity, another class of methods automatically proposes multi-dimensional feature quantities and makes the fault-type judgment through intelligent algorithms. Yang and Yu (2022) used a discrete wavelet transform to decompose three-phase voltage and zero-sequence sequences and constructed multidimensional time–frequency matrices to input into the ResNet network, which improved the effect of fault-type identification in distribution networks. Xingquan et al. (2022) converted the time-domain three-phase voltage and current data during faults into a multidimensional time–frequency spectral gray scale map, combined with SVM and a deep convolutional neural network, to improve the accuracy of high-resistance fault classification. Biswas et al. (2023) used variational mode decomposition (VMD) to quickly extract different frequency components of the fault current signal, which is input into the CNN for fault-type identification in the frequency domain to shorten the detection time and ensure the accuracy. Azizi and Seker (2022) processed the current time-domain signal through the Hilbert–Huang transform, formed the multidimensional feature quantity of the frequency-domain signal combination under different frequencies, and used BrownBoost algorithm to classify the data space, which improved the accuracy of fault-type classification. Feng et al. (2022) used the linear discriminant analysis (LDA) algorithm to incorporate the frequency-domain optimal fault features, which constitute two-dimensional and three-dimensional feature quantities, into the Bayesian classification model based on the kernel distribution to achieve fault location identification, in which the three-dimensional feature quantities are better than the two-dimensional feature quantities.

The fault identification methods mentioned in the literature can be broadly categorized into two types:

1. Extraction of time-domain electrical quantities: In this category, time-domain electrical quantities such as voltage and current amplitudes are extracted as one-dimensional features to represent fault types. Fault identification is achieved through methods such as constructing similarity or deviation values and comparing them against thresholds.
2. Time-frequency transformation methods: This category involves transforming the collected time-domain signals into multidimensional time–frequency matrices or forming grayscale images using time–frequency transformation methods. Intelligent algorithms are then employed to automatically extract multidimensional feature sets for fault type identification, resulting in improved accuracy compared to the first category. However, establishing time–frequency matrices or forming grayscale images requires complex preprocessing of time-domain signals, leading to longer computation times. Compared to one-dimensional features, multidimensional feature sets contain richer fault information and exhibit better classification performance. It is worth noting that the signals processed in the literature mostly consist of phasor magnitudes, overlooking the fault information contained in phase angles.

Wang et al. (2021a) utilized an improved VMD combined with fuzzy c-means (FCM) to achieve classification and identification of rolling bearing fault types through FCM clustering. Qi et al. (2021) utilized the von Mises–Fisher (v-MF) distribution combined with the standard Euclidean distance to analyze the similarity between different samples for sample selection. Initialization of different groups requires pre-setting a lower limit for the grouping values but does not implement merging of similar groups. Chen et al. (2015) proposed the combination of the expectation–maximization (EM) algorithm and the v-MF algorithm. By selecting the positioning data on crystal positions to form a v-MF distribution and using cosine similarity as the clustering basis, crystal-type identification is carried out. However, the consideration for the number of groups in mixed distributions is not addressed. Garcia-Fernandez et al. (2019) utilizes the v-MF distribution to construct Gaussian filters for target direction measurement. Angle information is used to form two-dimensional and three-dimensional vectors for tracking target directions, but the establishment of distributions for multiple targets is not implemented. Data clustering is a fundamental step in data analysis. The application of von Mises–Fisher (v-MF) distribution-based clustering methods has shown good utility in sample selection (Qi et al., 2021), crystal-type identification (Chen et al., 2015), direction measurement tracking (Garcia-Fernandez et al., 2019), and other areas.

1.1 Contributions

The main contributions of this paper are summarized below.

- In this paper, we propose a probabilistic fault identification method based on the mixed von Mises–Fisher (v-MF) distribution. The mov-MF distribution of sample data is established, and fault probability is calculated by integrating the data to be measured into the established mov-MF distribution. Fault-type identification is then achieved based on the resulting probability magnitude. The biggest innovation of the mov-MF-based probabilistic fault identification method for distribution networks proposed in

this paper is the fault-type identification by establishing the clustering distribution of 3D vector data on the spherical space. In power systems, there are a large number of 3D vectors, so the method is suitable for power system data analysis. Compared with the two types of fault identification methods introduced in the previous paper, the method proposed in this paper can make the accuracy of fault identification higher by using 3D vectors; the use of 3D eigenvectors in the time domain to establish the mov-MF distribution without complex data preprocessing makes the algorithm more concise, ensures accuracy, and at the same time, improves the computational efficiency.

- To establish the mixed von Mises–Fisher (v-MF) distribution of sample data more accurately, we employ the spherical K-means algorithm and minimum message length (MML) for parameter initialization. Subsequently, these parameters are iteratively optimized using the expectation–maximization (EM) algorithm to refine the accuracy of the mov-MF distribution parameters. We validate this approach through simulations conducted on an IEEE 33-node distribution system, where various fault conditions are set. The test results are compared with those reported in Xingquan et al. (2022) and Azizi and Seker (2022). Our findings demonstrate that the proposed method achieves accurate fault-type identification. Moreover, the acquisition of feature vectors is simplified, and the accuracy is comparable to that of the comparison method. Importantly, our method exhibits robust performance across different fault conditions, highlighting its broad applicability.

1.2 Paper organization

The remainder of the paper is structured as follows: Section 2 provides an introduction to the fundamental theory of von Mises–Fisher (v-MF) distribution and the expectation–maximization (EM) algorithm. Section 3 outlines the initialization method for parameters of the mov-MF distribution, along with the algorithm for fault-type identification based on the mov-MF distribution. Section 4 verifies the effectiveness and applicability of the proposed method through simulation examples.

2 The von Mises–Fisher basic theory

The von Mises–Fisher distribution is the probability distribution of directional statistics for spherical surface data. A d-dimensional unit random vector $\boldsymbol{x}$ (i.e., $x \in \mathbb{R}^d$ and $\|x\| = 1$) is said to have the d-variate von Mises–Fisher (v-MF) distribution if its probability density function is given by

$$f\left(x|\mu,\kappa\right) = c_d\left(\kappa\right)e^{\left(\kappa\mu^T x\right)}, \tag{1}$$

In the Eq. 1, where $\|\mu\| = 1$, $\kappa \geq 0, d \geq 2$. The normalizing constant $C_d\left(\kappa\right)$ is given by

$$c_d\left(\kappa\right) = \left(\kappa\right)^{d/2-1} \Big/ \left(2\pi\right)^{d/2} I_{d/2-1}\left(\kappa\right), \tag{2}$$

where $I_d\left(\kappa\right)$ represents the first kind-modified Bessel function.

The probability density $f\left(x|\mu,\kappa\right)$ function is determined by the mean direction μ and concentration parameter κ. The mean direction μ represents the central direction of clustering of this type of data on the spherical surface, indicating the direction of clustering. The concentration parameter κ represents the concentration of data in this direction. A higher value indicates a higher degree of clustering of data in this direction. The specific comparison chart is shown in Figure 1

2.1 Maximum likelihood estimation

For a given dataset χ, we want to find the maximum likelihood estimates of the parameters: mean direction μ and concentration parameter κ of its probability density function $f\left(\chi|\mu,\kappa\right)$. Assuming these data are independently and identically distributed, the logarithm of the likelihood for χ can be expressed as

$$\ln P\left(\chi|\mu,\kappa\right) = n\ln c_d\left(\kappa\right) + \kappa\mu^T r. \tag{3}$$

To obtain the maximum likelihood estimates of mean direction μ and concentration parameter κ, we introduce Lagrange multipliers and derive the maximum likelihood estimation from Equation 3, resulting following Eqs 4, 5:

$$\hat{\mu} = \frac{r}{\|r\|} = \frac{\sum_{i=1}^n x_i}{\left\|\sum_{i=1}^n x_i\right\|}, \tag{4}$$

$$\frac{I_{d/2}\left(\hat{\kappa}\right)}{I_{d/2-1}\left(\hat{\kappa}\right)} = \bar{r} = \frac{\left\|\sum_{i=1}^n x_i\right\|}{n}. \tag{5}$$

Due to the implicit equation involving the ratio of Bessel functions in the calculation process of the above expression, it is impossible to obtain an exact analytical solution directly. Therefore, we must use numerical asymptotic approximation methods to obtain an approximate solution for the concentration parameter $\hat{\kappa}$, expressed using Eq. 6. We select the best performing approximate solution method proposed in Zhe et al. (2019):

$$\hat{\kappa} = \frac{\bar{r}d - \bar{r}^3}{1 - \bar{r}^2}. \tag{6}$$

2.2 Parameter estimation of mov-MF distribution based on the EM algorithm

The process of using v-MF distributions for fault-type identification requires a hybrid model containing multiple v-MF distributions. We now consider a mix of k v-MF (mov-MF) distributions that serves as a generative model for directional data. Let $\left\{f_h\left(x|\mu,\kappa\right)\right\}_{h=1}^k$ denote the hth v-MF distribution, then a mixture of these k v-MF distributions given by Eq. 7:

$$f\left(x\middle|\left\{\mu_h,\kappa_h,\pi_h\right\}_{h=1}^k\right) = \sum_{h=1}^k \pi_h f_h\left(x|\mu_h,\kappa_h\right), \tag{7}$$

where π_h denotes the weights of the different types of components and the sum is 1. We randomly select the hth v-MF distribution with weights π_h and sample a point from that distribution $f_h\left(x|\mu_h,\kappa_h\right)$. Let $\chi = \{x_1,\ldots,x_n\}$ be the dataset of n independently sampled points that follow Eq. 7. Let $Z = \{z_1,\ldots,z_n\}$

be the corresponding set of hidden random variables that indicate the particular v-MF distribution from which the points are sampled. In particular, $z_i = h$ if x_i is sampled from $f_h(x|\mu_h, \kappa_h)$. Assuming that the values in the set Z are known, the log-likelihood of the observed data is given by

$$\ln P(\chi, Z|\mu, \kappa) = \sum_i^n \ln\left(\pi_{zi} f_{zi}\left(x_i|\mu_{zi}, \kappa_{zi}\right)\right). \tag{8}$$

Equation 8 is actually a random variable dependent on Z, which follows a distribution. This random variable is referred to as the complete data log-likelihood. Given a particular value of (χ, μ, κ), the conditional probability expectation of $Z|(\chi, \mu, \kappa)$ is calculated, and this estimation forms the E-step in an EM framework.

Using an EM approach for maximizing the expectation of Eq. 8), we can summarize the steps for estimating the mov-MF parameters based on the EM algorithm.

Input: set X of data points
Output: a mov-MF distribution; initialize all $\pi_h, \mu_h, \kappa_h, h = 1, \ldots, k$
Repeat
{**The E-step of EM**}
for $i = 1$ to n **do**
  for $h = 1$ to k **do**
    $f_h(x_i|\mu_h, \kappa_h) \leftarrow c_d(\kappa_h) e^{(\kappa_h \mu_h{}^T x_i)}$
  end for
  for $h = 1$ to k **do**
    $p(h|x_i, \mu, \kappa) \leftarrow \frac{\pi_h f_h(x_i|\mu_h, \kappa_h)}{\sum_{l=1}^{k} \pi_l f_l(x_i|\mu_l, \kappa_l)}$
  end for
end for
{**The M-step pf EM**}
for $h = 1$ to k **do**
  $\pi_h = \frac{1}{n} \sum_{i=1}^{n} p(h|x_i, \mu, \kappa)$
  $r_h = \sum_{i=1}^{n} x_i p(h|x_i, \mu, \kappa)$
  $\hat{\mu}_h = \frac{r_h}{\|r_h\|}$
  $\hat{\kappa} = \frac{\bar{r}_h d - \bar{r}_h{}^3}{1 - \bar{r}_h{}^2}$
end for
until *convergence*

Algorithm 1. EM algorithm.

On termination, the algorithm gives the parameters π_h, μ_h, κ_h of the k v-MF distributions that model the dataset χ, as well as the soft-clustering, i.e., the posterior probabilities $p(h|x_i, \mu, \kappa)$, for all h and i.

3 Steps for designing the fault identification model based on mov-MF distribution

3.1 Data preprocessing and dataset construction

The fault signals of the distribution network are acquired and combined to form a three-dimensional vector $\Psi(\varphi_1, \varphi_2, \varphi_3)$, which is converted into directional data by L2 normalization. The dataset consists of voltage phasors measured by the PMU under different fault conditions. After a fault occurs, the positive–negative–zero-sequence voltage phasors of different types of faults vary widely, and the main difference exists between the phase angles. The L2 normalized data are distributed on the unit sphere, and the different types of fault vectors are combined to form a dataset in the form of a matrix.

3.2 Calculation of the parameters of the mov-MF distribution

As the EM algorithm is needed to establish the mov-MF distribution, there is an important problem that in the case of the known distribution χ, we need to solve the distribution of the average direction μ and concentration parameters κ. From Section 2.2, we need to use the log-likelihood function as the objective function to estimate the unknown parameters μ and κ, and the log-likelihood function is non-convex; there are some small local maxima and local minima, so avoiding such problems is essential to improve the performance of the EM algorithm. Therefore, avoiding such problems is crucial to improve the performance of the EM algorithm. The EM algorithm is more sensitive to the initial value, and the clustering result fluctuates greatly with the change in the initial value, so it is chosen to determine the reasonable starting state of the EM by the preliminary clustering of the data.

3.2.1 mov-MF model parameter initialization

The mov-MF parameters are computed by initializing the spherical K-means algorithm, updating the parameters by the EM algorithm, and determining whether the optimality is reached based on the cosine similarity D.

Initialization is performed using the spherical K-means algorithm (Mashal and Hosseini, 2015), where the $n \times d$ data matrix is first divided into K clusters, K generally needs to be set in advance, and K data points are selected as the initial cluster centers. Before the algorithm, it is assumed that in the case of a mov-MF distribution, all classified clusters are equal *a priori*, i.e., for each distribution $\pi_h = \frac{1}{k}, h = 1, \cdots, k$, while it is further assumed that all classified clusters have equal concentration parameters, which are generally set to $\kappa_h = 100$. For the case of mov-MF distribution, some distant data points are selected as initialization parameters μ_h for different clusters.

In order to realize the classification of different data points, the distance metric between different points on the unit hypersphere is defined, which can be mainly categorized into Euclidean distance, Manhattan distance, cosine distance, and correlation distance, etc., depending on the clustering requirements. Jianyuan et al. (2023) explained the rationality of using cosine similarity as a distance metric for clustering. Therefore, we choose to calculate the cosine similarity S as the clustering metric.

$$S = x_i{}^T \mu_h. \tag{9}$$

Thus, the cluster label to which each data point belongs is determined based on the similarity of the data point to the initial cluster center.

$$X_h \leftarrow X_h \cup \{x_i\}, h = \underset{h'}{\text{argmax}} x_i{}^T \mu_{h'}. \tag{10}$$

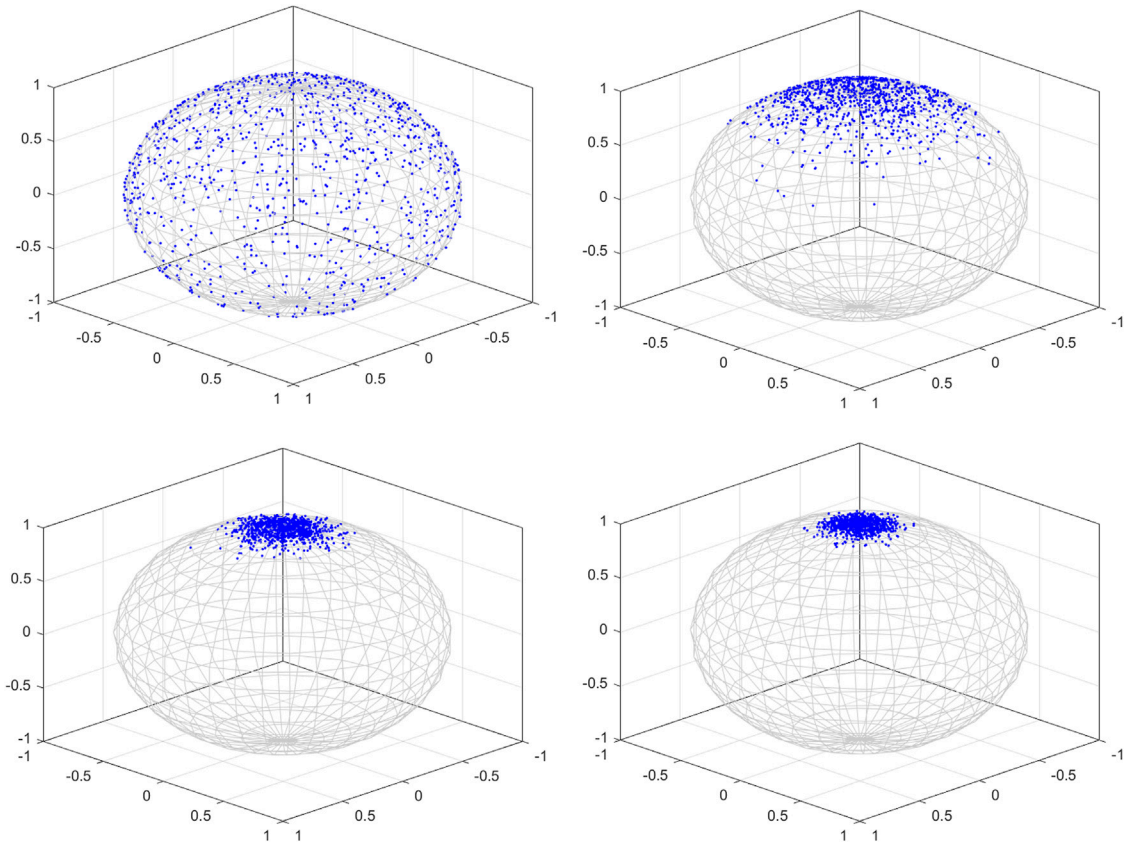

FIGURE 1
Clustering effects of different concentration parameters.

From this, we obtain the center of each cluster μ_h, initialize again to select a set of cluster centers μ_h, and compare the distance between the data points in the cluster and the center point D, $D = 1 - S$. If the distance D of the current clustering result is smaller than that of the previous generation, then update the clustering result until the distance D does not change anymore to get the optimal clustering result of the K clusters at this time and compute the average direction μ_h, concentration parameter κ_h, and mixing distribution weight π_h of each cluster at this time, which is used as the initial parameter of the mov-MF model. In order to improve the accuracy of the initial parameters, multiple initializations are usually performed, and the group with the smallest distance D is chosen as the initialization parameter.

3.2.2 mov-MF model group score determination

On the basis of step a), the group score of the sample data is determined by the MML algorithm, and according to the log-likelihood l_r and the minimum message length $I(\pi)$ to determine whether the optimal group score is reached or not and through many iterations of the EM algorithm, the mov-MF distribution of the typical sample data is obtained.

When the mov-MF model group scores are determined, then the EM algorithm is used to estimate the mixture distribution parameters, i.e., the mixture distribution weights and the parameters for each subgroup. Thus, we need to determine the optimal number of subgroups for the mixture distribution and the corresponding distribution parameters.

Therefore, the minimum message length (MML) algorithm is used for group score K determination. First, we need to encode the parameters using MML and calculate the message length corresponding to different parameters. The log-likelihood ratio of the mov-MF distribution for a set of fractions is given by Eq. 11:

$$(\chi \mid \Phi) = \sum_{i=1}^{n} \ln \sum_{h=1}^{K} \pi_h f_h(x_i; \Theta_h), \tag{11}$$

where π_h and $f_h(x_i; \Theta_h), \Theta_h = (\mu_h, \kappa_h)$ are the weights and probability densities of the hth group component, respectively, under the assumption that the initial number of group scores, K, is determined; K is a number of groupings for the current hypothesis; and the maximum likelihood is estimated to be $\Phi_{ML} = \underset{\Phi}{\operatorname{argmax}}\,(\chi \mid \Phi)$, using the EM algorithm for the estimation of the above mixing parameters.

For step E, rewriting the formulas for calculating the conditional expectation probability of the joint distribution, expressed by Eqs 12, 13:

$$r_{hi} = \frac{\pi_h f(x_i; \Theta_h)}{\sum_{h=1}^{K} \pi_h f(x_i; \Theta_h)}, \forall 1 \le i \le N, 1 \le h \le K, \tag{12}$$

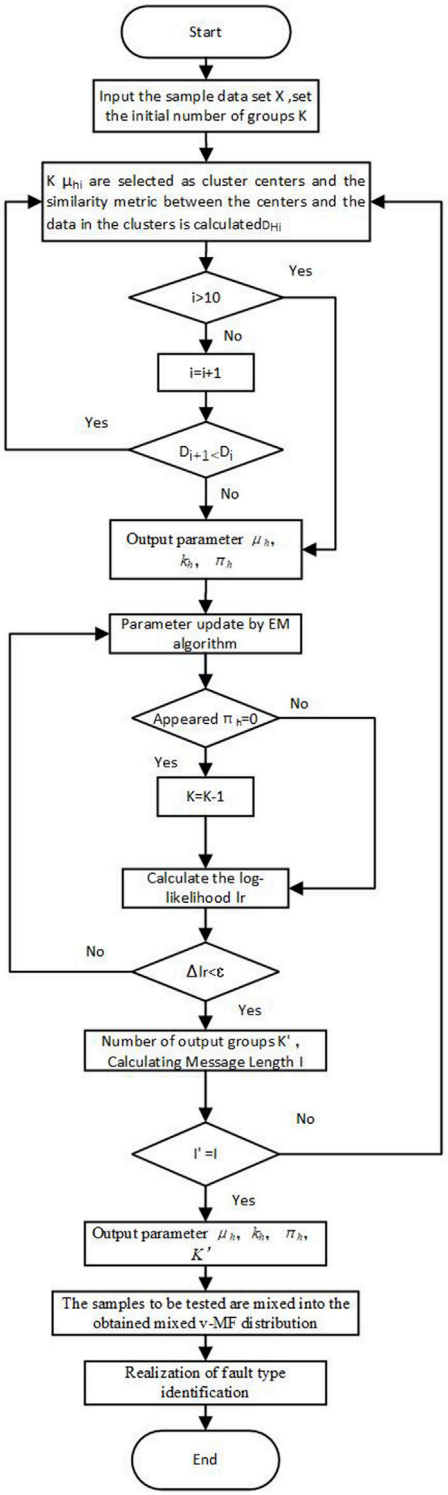

FIGURE 2
Flowchart of fault identification based on the mov-MF algorithm.

$$n_h = \sum_{i}^{N} r_{hi}. \tag{13}$$

For the M-step, assuming an estimate $\Phi^{(t)}$ for the tth iteration, the local parameters and the maximum log-likelihood estimates used to compute the next one, and the weights of the hth component are updated as $\pi_h^{(t+1)} = \frac{n_h^{(t)}}{N}$.

Based on the expression proposed in Kasarapu and Allison (2015) for encoding the component weights, the message length expression for the hybrid weights π_h is redefined on this basis by combining the log-likelihood $l_r \leftarrow E(\sum_{h=1}^{k} \pi_h f_h(x|\mu_h, \kappa_h))$ obtained from the E-step:

$$I(\pi) = -l_r + N\sum_{h=1}^{K} \ln \pi_h + \ln N \cdot (K-1)! \tag{14}$$

According to the initialization parameters obtained by the spherical K-means algorithm, the log-likelihood l_r and the message length of the hybrid weight $I(\pi)$ in the initial state. The message length of the hybrid weight expressed by Eq. 14. Execute the E-step to calculate the initial log-likelihood was executed using the initialization parameters μ_h, κ_h, and π_h, and then the M-step was executed to calculate the parameters at the time of maximization of the expectation; after completing the calculation of the corresponding parameters for each subgroup, the log-likelihood and the message length were updated at this time. If a subgroup of a subgroup is set to 0, the subgroup is removed from the model, and the number of subgroups is reduced. At the end of each E-step and M-step, the log-likelihood is compared with the previous generation by calculating the log-likelihood and judging whether convergence occurs based on the threshold value Δl_r. calculated from Eq. 15.

$$\Delta l_r = \frac{l_r^{(t+1)} - l_r^t}{l_r^t} < \varepsilon, \varepsilon = 10^{-12}. \tag{15}$$

Meanwhile, after each iteration of the E–M step to the number of confirmed groups, the new message length $I'(\pi)$ is recalculated, checking whether the current message length is no longer changing and thus determining whether the optimal result is reached.

It is likely that there are two or even more similar groupings in the initialization phase, and when there are such groupings with very close average directions, group merging is required. Using the mean direction μ_h of each group, the similarity between different groups is calculated, the similarity is used to determine if they are similar groups, these groups are merged, and the parameters μ_h, κ_h, and π_h and the number of groups K are updated.

3.3 Fault-type identification

After establishing a mov-MF distribution based on the sample data, the samples to be tested are mixed into the constructed sample mov-MF distribution, and the probabilities of the samples to be tested attributed to different types of faults are calculated. The fault label is then determined according to the size of the probability, thus realizing fault-type identification.

Labeling of fault types $h = 1, 2, \ldots, k$, weights π_h are the weights corresponding to different fault types in the mov-MF model obtained from the sample data; r_{hi} is the probability of the fault types of the data to be measured, and according to the size of the probability, the vector of the data to be measured is assigned to the

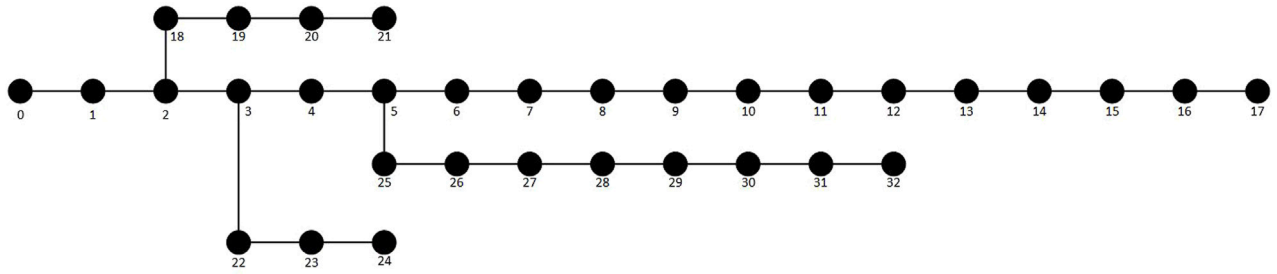

FIGURE 3
10-kV IEEE33 node distribution network model.

grouping of the fault types with the largest probability to realize the fault-type identification.

$$h = \arg \max_{h\in\{1\ldots k\},i\in\{1\ldots N\}} r_{hi}. \quad (16)$$

Step 1: Input sample dataset χ, set the initial number of groups K, and set the initial $\kappa_h = 100$, $\pi_h = \frac{1}{K}$.
Step 2: Select K μ_{hi} as cluster centers, calculate the similarity index D_{hi} between the selected cluster centers and the data in the clusters, and if it is smaller than the previous generation result, then re-select the cluster centers and repeat step 2 until D_{hi} is larger than the previous generation result.
Step 3: After the initial cluster centers μ_h are selected, the obtained initialization parameters and dataset χ are used to estimate and update the parameters by the EM algorithm (Algorithm 1).
Step 4: After obtaining the mov-MF distribution of the K subgroups, determine whether to keep the subgroups by judging whether π_h is zero or not.
Step 5: Calculate the log-likelihood Δl_r and determine whether convergence has been reached; if not, return to step 3.
Step 6: Calculate the message length of the mixed weights $I(\pi)$ and determine whether the message length is no longer changing, otherwise return to step 2.
Step 7: Output μ_h, κ_h, π_h, and K and, get the mixture v-MF distribution of sample dataset χ for. Mix the samples to be tested into this distribution, and realize the fault-type identification by Eq. 16.

Algorithm 2 Fault identification algorithm.

The step-by-step flowchart is shown in Figure 2:

4 Example analysis

In order to verify the effectiveness of the fault identification method based on the mov-MF model proposed in this paper, simulation experiments are carried out in MATLAB/Simulink on the IEEE33 node 10-kV distribution system, as shown in Figure 3, to obtain the fault sample data.

TABLE 1 Line model parameter.

Line parameter	Overhead line	Cable
Positive-sequence resistor/(Ω/km)	0.17	0.27
Zero-sequence resistance/(Ω/km)	0.32	2.7
Positive-sequence inductors/(mH/km)	1.017	0.255
Zero-sequence inductors/(mH/km)	3.56	1.109
Positive-sequence capacitance/(μF/km)	0.115	0.376
Zero-sequence Capacitance/(μF/km)	0.0062	0.276

4.1 Sample data

Fault points are set between nodes 8–9, 13–14, 18–19, and 23–24, respectively, where nodes 20–21, 11–17, 22–24, and 29–32 are connected by overhead lines, and the rest of the lines are connected by cables, and the parameters of each sequence of the overhead lines and cables are shown in Table 1, line model parameters (Wang et al., 2021b). The system is a 10-kV distribution network. It is set up with transformer grounding methods that are neutral ungrounded and neutral grounded via arcing coil(0.8697H). Only one of the above fault parameters is changed in each simulation, and the duration of each type of fault is 0.1 s. The synchronized phase data are collected using a PMU, and a measuring device is installed at each node, with an update interval of 10 m and a sampling frequency of 6.4 kHz. A total of 560 sets of fault samples are generated, of which 420 sets comprise the training set and 140 sets comprise the test set. The fault conditions are neutral ungrounded; neutral grounded via arcing coil; transition resistance 0Ω, 1Ω, 10Ω, and 1000Ω and has access to distributed power; and the abovementioned seven conditions are grouped into four fault points for single-phase grounded short-circuit faults (AG,BG,CG), two-phase grounded short-circuit faults (ABG,BCG,ACG), three-phase short-circuit faults, and two-phase interphase short-circuit faults (AB,BC,AC); 80 fault samples are generated for each group, and 33 data points are obtained for each set of data, and the mov-MFs are established, respectively, under different conditions.

Based on the principle in Section 3.1, the vector dataset suitable for building the mov-MF model is constructed. In the mov-MF model, the main judgment basis for fault-type identification is the average direction μ of the grouped clusters, so the phase angle values

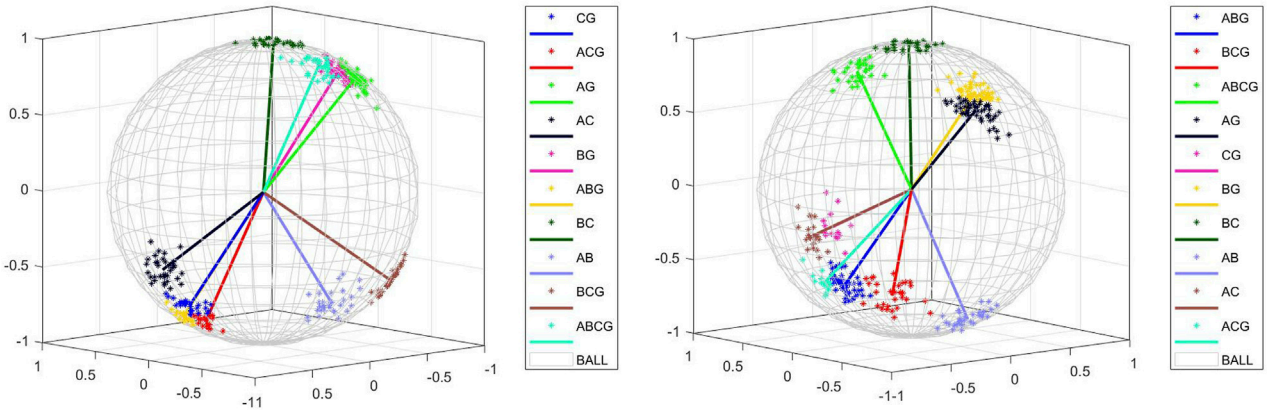

FIGURE 4
Neutral ungrounded mov-MF distribution of neutral grounded through arc suppression coil.

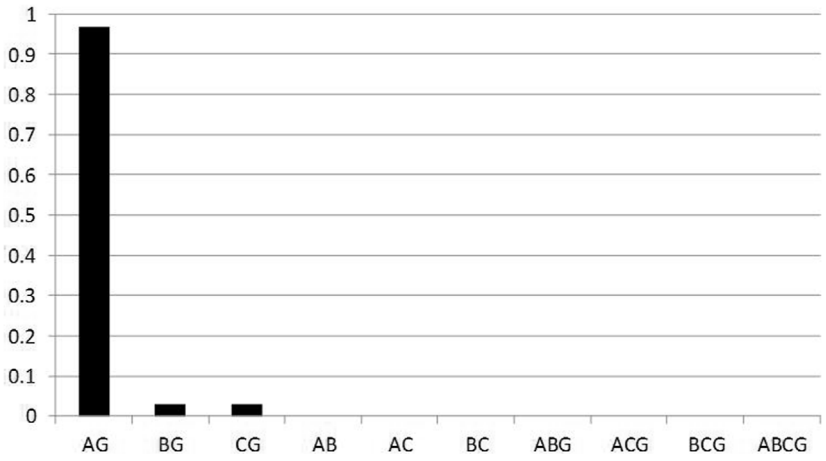

FIGURE 5
Fault-type probability diagram (AG, neutral ungrounded).

of the positive–negative-sequence and zero-sequence voltage phasors at the moment of 0.05 s after the fault are selected to be combined into the three-dimensional feature vectors $\Psi(\varphi_{u_1}, \varphi_{u_2}, \varphi_{u_0})$.

The feature vectors extracted from the typical sample fault dataset are used as initial vectors for L2 normalization to obtain the normalized $\Psi'(\varphi_{u_1}, \varphi_{u_2}, \varphi_{u_0})$. The 3D feature vectors of each data point for each fault type obtained after normalization are combined to form a 330 × 3 initial vector matrix $\Psi' = [\Psi'_1 \ \Psi'_2 \ \cdots \ \Psi'_{329} \ \Psi'_{330}]^T$, and the corresponding mov-MF distribution is modeled on the basis of this dataset.

4.2 Type identification under different fault conditions

After establishing the mov-MF distribution model based on the historical sample fault dataset, the simulation is then carried out according to different fault conditions, and the test dataset of a particular fault is mixed into the history set of the mov-MF model for different conditions completed in Section 4.1 based on the historical samples for identification in each test.

4.2.1 Different transformer grounding methods

The purpose of changing the transformer grounding method is to verify the applicability of the fault identification method proposed in this paper under this condition. The simulation model is a 10-kV distribution network model, so two small current grounding methods are set. The compensation method of the arc-canceling coil is set to be over-compensation, and the simulation is carried out. Fault-type identification is carried out by establishing the mov-MF model, and the mov-MF model established according to the positive-, negative, and zero-sequence phases is shown in Figure 4.

The small current grounding method does not have much effect on the positive-, negative-, and zero-sequence voltage phase angles, and the obtained mov-MF distributions are similar. Eighty sets of test datasets are mixed into the obtained mov-MF distributions for different neutral grounding methods, and the labeling results are

TABLE 2 Fault identification accuracy under different grounding modes.

Fault type	Neutral point ungrounded	Neutral point grounded via the arcing coil
Single-phase grounding (%)	97.47	95.96
Two-phase grounding (%)	100	100
Three-phase grounding (%)	100	100
Short circuit between two phases (%)	100	100

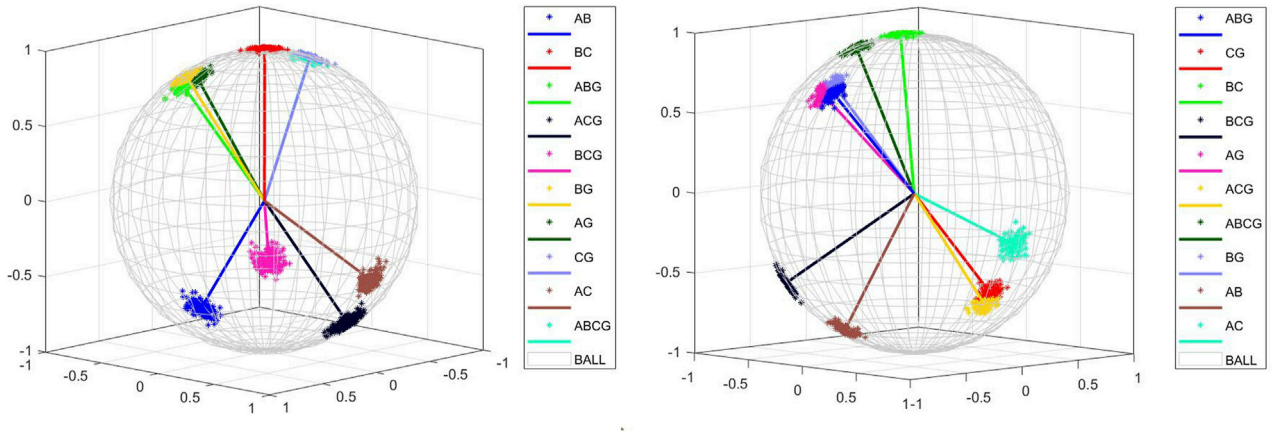

FIGURE 6
mov-MF distribution of different transition resistors (0Ω and 1000Ω).

used to determine whether the classification is correct or not. The typical data mean direction matrix when the neutral point is not grounded is:

According to the average direction of typical faults, the cosine similarity was calculated between the test data set and the average direction of a certain type of fault, the probability of belonging to that type of fault was also calculated according to the number of data point labels, and the type of fault with the highest probability was selected to judge that it belongs to that type of fault. The A-phase short-circuit grounding fault was taken as an example under the condition of neutral ungrounded, and the fault probability r_{hi} was calculated, as shown in Figure 5.

The overall accuracy results for the 40 test sets are shown in Table 2.

Transformer neutral point through the arcing coil grounding will limit the fault phase current. The method proposed in this paper does not have much impact, so the 10-kV distribution network applicable to the small current grounding method is applicable to this method.

4.2.2 Fault transition resistance impact analysis

Changing the transition resistance when the fault occurs, the transition resistors with sizes of 0Ω, 1Ω, 10Ω, and 1000Ω are selected, and simulation experiments are carried out by changing the fault type and the initial phase angle of the fault at different fault locations. The mov-MF model is established for fault type identification, and the mov-MF model is also established according to the positive and negative zero sequence phases as shown in Figure 6.

Varying the transition resistance size, the mov-MF distributions are different due to the fact that 0Ω, 1Ω, and 10Ω all differ from 1000Ω, but the expected results can still be achieved for type differentiation under each condition. The 160 sets of test datasets are mixed into the obtained mov-MF distributions for different neutral grounding methods, and the labeling results are used to determine whether the classification is correct or not. The typical data mean direction matrix for a transition resistance of 0Ω is:

The A-phase short-circuit ground fault under the condition of 0Ω transition resistance is taken as an example, and the fault probability r_{hi} is calculated as shown in Figure 7:

The judgment process is the same as shown in section IV.B.a), and the results of 80 sets of test data are shown in Table 3.

When a single-phase high-resistance grounded short-circuit occurs, the transition resistance will have a certain effect on the fault phase voltage amplitude, and for positive-, negative-, and zero-sequence phase angles, the transition resistance does not have much effect, so the fault-type identification accuracy is not affected under the condition of different fault transition resistances, and it still maintains a high accuracy rate.

4.2.3 Impact analysis of connecting to distributed power sources

DG is connected at nodes 17, 21, 24, and 32, and DG is a 1.5 kW/230 V PV power supply. The transformer grounding method is selected as neutral ungrounded, and the transition resistance is 0 Ω. Simulation experiments are carried out by changing the fault types at different locations. Fault type identification is carried out by establishing a mov-MF model, and the mov-MF model

10.3389/fenrg.2024.1410731

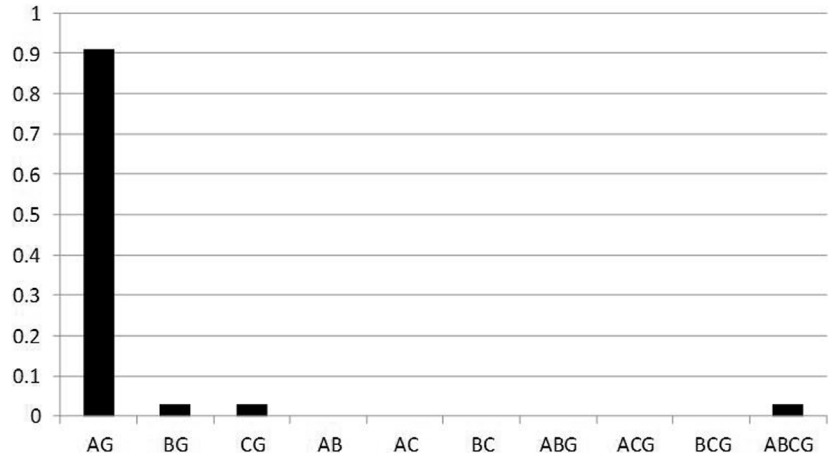

FIGURE 7
Fault-type probability diagram (AG, 0Ω).

TABLE 3 Fault identification accuracy under different transition resistors.

Fault type	0	1	10	1,000
Single-phase grounding (%)	97.98	96.46	96.97	94.44
Two-phase grounding (%)	100	100	100	100
Three-phase grounding (%)	100	100	100	98.48
Short circuit between two phases (%)	100	100	100	100

established according to the positive and negative zero sequence phasors is shown in Figure 8.

After accessing the distributed power supply, the impact on the vectors we use to build the mov-MF distribution will not be significant, so the obtained mov-MF distribution is similar to the previous distribution and still differentiates between different types of faults based on the feature vectors. The 10 sets of test datasets are mixed into the obtained mov-MF distribution, and the labeling results are used to judge whether the classification is correct or not. The typical data mean direction matrix after accessing the DG is:

$$\begin{bmatrix} \mu_1 \\ \vdots \\ \mu_{10} \end{bmatrix} = \begin{bmatrix} -0.631218228528535 & -0.542200651398354 & -0.554600758741366 \\ -0.479847261990186 & -0.0858554318574786 & 0.873141139782731 \\ -0.122723196711859 & -0.710487151061130 & 0.692926421177503 \\ -0.00614141822594962 & 0.669614264944898 & -0.742683660224511 \\ -0.0804373299381854 & -0.0702110133474672 & 0.994283787234378 \\ 0.0282440012654692 & -0.630164345667798 & 0.775947919542022 \\ -0.182608156880069 & 0.738532954956005 & -0.649017207387305 \\ -0.0319915375253993 & -0.592815736939139 & -0.804702456541588 \\ 0.00827657042339661 & 0.922151265513940 & -0.386740923478581 \\ -0.00258341173453716 & -0.762914549679774 & 0.646494173114281 \end{bmatrix}.$$

Take the example of a short-circuit ground fault in phase A after connecting to the DG, and calculate the fault probability r_{hi} as shown in Figure 9:

The judgment process is the same as shown in section IV.B.a, and the results of 20 sets of test data are shown in Table 4.

After accessing the distributed power supply, the fault current and voltage amplitude will slightly increase when a fault occurs compared with when it is not connected. For positive-, negative-, and zero-sequence voltage phase angles, access to distributed power supply has little effect on it; as a feature vector can still establish a clearly classified hybrid v MF distribution, the accuracy of fault-type identification is not affected, and the accuracy rate is still high.

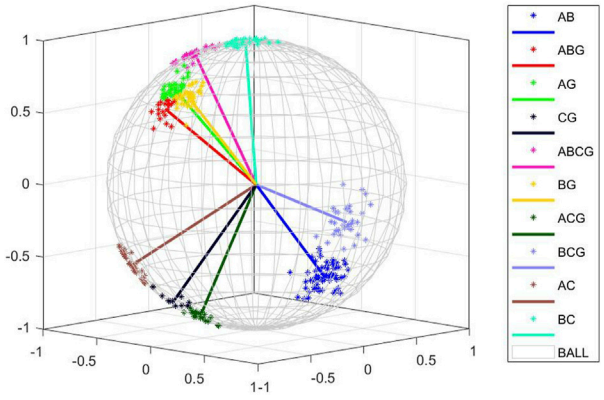

FIGURE 8
mov-MF distribution after connecting to DG.

4.2.4 Comparative analysis of different algorithms

The algorithm proposed in this paper is compared with the existing algorithms, and in Table 4, with the ensemble algorithm of multilayer classifiers (Ghaemi et al., 2022), the CNN–SVM algorithm (Xingquan et al., 2022), and the BrownBoost–HHT algorithm (Azizi and Seker, 2022), and compared with the algorithms that make use of the one-dimensional feature quantities, there is an improvement in the fault identification rate for two-phase short circuits, two-phase inter-phase, and three-phase short circuits; compared with the fault identification methods that make use of intelligent algorithms, the mov MF distribution of the three-dimensional feature quantity established by the algorithm proposed in this paper is simpler in the model, and the algorithm is clearer. The acquisition of the feature quantity is simpler, and the accuracy of fault-type identification is comparable to the algorithm.

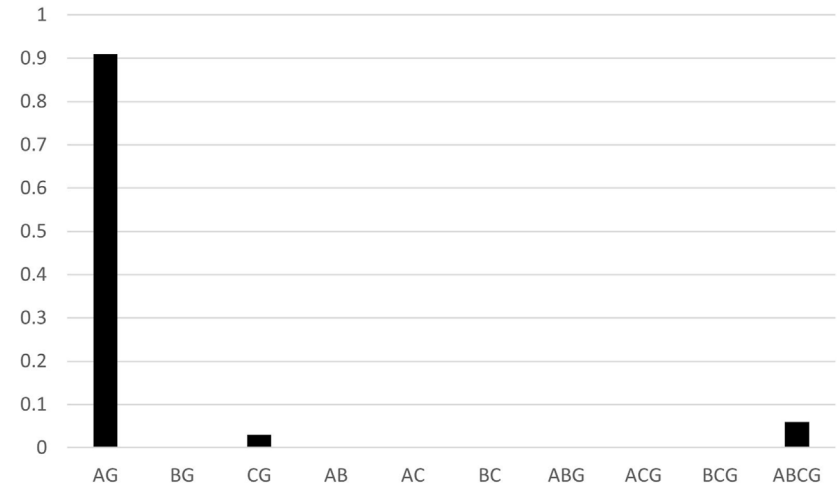

FIGURE 9
Fault-type probability graph (AG, DG).

TABLE 4 Fault identification accuracy after connecting to DG.

Fault type	Access to DG
Single-phase grounding (%)	95.45
Two-phase grounding (%)	100
Three-phase grounding (%)	100
Short circuit between two phases (%)	100

The comprehensive analysis of Table 5 shows that the accuracy of fault-type identification using the method based on the mov-MF distribution is slightly lower than other types of faults when single-phase ground faults and three-phase grounding faults occur. When establishing the mov-MF distribution, a dataset consisting of phase angle values of positive-, negative-, and zero-sequence voltages is chosen, and the mov-MF distribution is able to extract the average direction of the same type of fault vectors as a feature value based on the vector data, so we carry out the fault-type identification based on this characteristic.

4.2.5 Simulation test time

The methodology in this paper needs to be applied with consideration of the required hardware base and the time-consuming identification work. As an example, the running time of the MATLAB fault classification program is analyzed to test the time taken to identify different types of faults under ungrounded neutral conditions, and the proposed methodology is applied to identify a single fault. The test hardware is a conventional mainstream PC with AMD Ryzen-5,000 processor and 16 GB RAM, and the time required to build the mov-MF distribution under these conditions is approximately 15 s. When a fault occurs, the probabilistic identification method of distribution network based on hybrid v-MF can achieve classification judgment within 1 s, which is a rapid response, and has engineering application significance and practical value.

5 Conclusion

This paper introduces a novel method for fault-type identification in distribution networks utilizing a mixed von Mises–Fisher (v-MF)

TABLE 5 Classification accuracy of different fault types.

Fault type	Single-phase grounding (%)	Two-phase grounding (%)	Three-phase grounding (%)	Short circuit between two phases (%)
Accuracy of the methodology in this paper (%)	96.39	100	99.78	100
Ghaemi et al. (2022) method accuracy (%)	97.53	97.16	98.77	96.97
Xingquan et al. (2022) method accuracy (%)	92.8	100	100	100
Azizi and Seker (2022) method accuracy (%)	100	99.22	99.47	98.26

distribution. The method involves constructing three-dimensional feature quantities derived from the positive, negative-, and zero-sequence voltage phase angles observed at the time of the fault. Subsequently, the mov-MF distribution is generated to classify the fault type based on the integration of current data with historical distributions. Consequently, the following conclusions can be drawn:

In this paper, we propose a method for fault-type identification utilizing 3D direction vectors to construct a mixed von Mises–Fisher (v-MF) distribution. By leveraging the positive–negative–zero-sequence voltage phasors associated with various fault types, we establish the mov-MF distribution using sample data from diverse fault scenarios. The probability that the faults under test belong to different fault types is estimated by discerning the discrepancy between the mean directions of distinct fault types. Consequently, our method achieves fault-type identification with high accuracy.

The method proposed in this paper remains unaffected by changes in neutral grounding mode, fault transition resistance, and variations in fault locations. It exhibits robust applicability under diverse working conditions.

Data availability statement

The datasets presented in this study can be found in online repositories. The names of the repository/repositories and accession number(s) can be found in the article/Supplementary Material.

Author contributions

JL: writing–review and editing and writing–original draft. ZS: writing–review and editing and writing–original draft. BL: writing–review and editing and supervision.

Funding

The author(s) declare that no financial support was received for the research, authorship, and/or publication of this article.

Conflict of interest

The authors declare that the research was conducted in the absence of any commercial or financial relationships that could be construed as a potential conflict of interest.

Publisher's note

All claims expressed in this article are solely those of the authors and do not necessarily represent those of their affiliated organizations, or those of the publisher, the editors, and the reviewers. Any product that may be evaluated in this article, or claim that may be made by its manufacturer, is not guaranteed or endorsed by the publisher.

References

Azizi, R., and Seker, S. (2022). Microgrid Fault detection and classification based on the boosting ensemble method with the hilbert-huang transform. *IEEE Trans. Power Deliv.* 37 (3), 2289–2300. doi:10.1109/tpwrd.2021.3109023

Biswas, S., Nayak, P. K., Panigrahi, B. K., and Pradhan, G. (2023). An intelligent fault detection and classification technique based on variational mode decomposition-CNN for transmission lines installed with UPFC and wind farm. *Electr. Power Syst. Res.* 223, 109526. doi:10.1016/j.epsr.2023.109526

Chen, Y.-H., Wei, D., Newstadt, G., DeGraef, M., Simmons, J., and Hero, A. (2015). "Statistical estimation and clustering of group-invariant orientation parameters," in 2015 18th International Conference on Information Fusion (Fusion), Washington, DC, USA, 06-09 July 2015.

Feng, X. U. X., Chenjie, X. U., Zhang, Y., Zhao, Y., and Wang, S. (2022). Fault location of active distribution network based on traveling wave feature classification. *J. Chongqing Univ.* 45 (11), 59–68. doi:10.11835/j.issn.1000-582X.2021.219

Garcia-Fernandez, A. F., Tronarp, F., and Sarkka, S. (2019). Gaussian Target Tracking With Direction-of-Arrival von Mises–Fisher Measurements. *IEEE Trans. Signal Process.* 67 (11), 2960–2972. doi:10.1109/tsp.2019.2911258

Ghaemi, A., Safari, A., Afsharirad, H., and Shayeghi, H. (2022). Accuracy enhance of fault classification and location in a smart distribution network based on stacked ensemble learning. *Electr. Power Syst. Res.* 205, 107766. doi:10.1016/j.epsr.2021.107766

Jiang, X., Stephen, B., and McArthur, S. (2021). Automated distribution network fault cause identification with advanced similarity metrics. *IEEE Trans. Power Deliv.* 36 (2), 785–793. doi:10.1109/tpwrd.2020.2993144

Jianyuan, WANG, Zhang, Y., and Cheng, L. I. U. (2023). Fault line selection method of distribution network based on the fusion of parameter optimized variational modal decomposition and improved K clustering criterion. *South. Power Syst. Technol.* 17 (7), 135–145. doi:10.13648/j.cnki.issn1674-0629.2023.07.015

Kasarapu, P., and Allison, L. (2015). Minimum message length estimation of mixtures of multivariate Gaussian and von Mises-Fisher distributions. *Mach. Learn.* 100, 333–378. doi:10.1007/s10994-015-5493-0

Liu, H., Ran, J., Yang, Q., Wang, K., and He, L. (2020). "High impedence ground fault identification method in medium voltage networks based on experiments," in The 16th IET International Conference on AC and DC Power Transmission (ACDC 2020), Online Conference, 02-03 July 2020.

Mashal, M., and Hosseini, R. (2015). "K-means plus plus for Mixtures of von Mises-Fisher Distributions," in 2015 7th Conference on Information and Knowledge Technology (IKT).

Peng, N., Zhang, P., Liang, R., Zhang, Z., Liu, X., Wang, H., et al. (2023). Fault section identification of the power cables in urban distribution networks by amplitude differences between the zero-sequence currents and those flowing in cable sheaths and armors. *IEEE Trans. Smart Grid* 14 (4), 2593–2606. doi:10.1109/tsg.2022.3222209

Qi, L., Liu, H., Xiong, Q., and Chen, Z. (2021). Just-in-time-learning based prediction model of BOF endpoint carbon content and temperature via vMF mixture model and weighted extreme learning machine. *Comput. Chem. Eng.* 154, 107488. doi:10.1016/j.compchemeng.2021.107488

Sheng, Y., Wang, B., Yu, H., Li, L., Liu, Y., and Zhang, L. (2023). An overview of Fault Identification techniques in power distribution networks: methods and models. *IET Conf. Proc.* 2023 (15), 192–198. doi:10.1049/icp.2023.2141

Wang, H., Wu, F., and Zhang, L. (2021a). Fault diagnosis of rolling bearings based on improved empirical mode decomposition and Fuzzy C-means algorithm. *Trait. Du. Signal* 38 (2), 395–400. doi:10.18280/ts.380217

Wang, X., Zhang, X., Zhao, Q., Xu, J., and Zhang, Y. (2021b). Fault section location in distribution system based on transient zero-mode current. *Smart Power* 49 (3), 103–110.

Xingquan, J. I., Chen, J., Zhang, Y., Qi, L. I. U., Gong, Z., and Xu, B. (2022). Fault classification in distribution network based on CNN-SVM. *Smart Power* 50 (1), 94–100.

Yang, L., and Yu, L. (2022). Grounding fault identification and line selection of distribution network based on improved two-branch ResNet. *Electr. Meas. Instrum.* 59 (10), 100–107. doi:10.1109/JIOT.2021.3131171

Zhang, G. X., Tong, X. Y., Hong, Q., and Booth, C. D. (2022a). Waveform similarity-based robust pilot protection for transmission lines. *IEEE Trans. Power Deliv.* 37 (3), 1856–1865. doi:10.1109/tpwrd.2021.3099348

Zhang, Y., guo, H. A. O. Z., Lin, Z., Yang, S., Liu, Z., and Xiaojun, Y. U. (2022b). Transmission line fault classification method based on deep dictionary learning. *Electr. Power Autom. Equip.* 42 (11). doi:10.16081/j.epae.202204031

Zhe, X., Chen, S., and Yan, H. (2019). Directional statistics-based deep metric learning for image classification and retrieval. *Pattern Recognit.* 93, 113–123. doi:10.1016/j.patcog.2019.04.005

Zhu, H. L., Shi, Y., Wang, H. Z., and Lu, L. X. (2020). New feature extraction method for photovoltaic array Output time series and its application in fault diagnosis. *IEEE J.*10 (4), 1133–1141. doi:10.1109/jphotov.2020.2981833

frontiers | Frontiers in Energy Research

TYPE Original Research
PUBLISHED 04 July 2024
DOI 10.3389/fenrg.2024.1418833

OPEN ACCESS

EDITED BY
Chaolong Zhang,
Jinling Institute of Technology, China

REVIEWED BY
Carlos Roberto Minussi,
São Paulo State University, Brazil
Mahamad Nabab Alam,
National Institute of Technology Warangal, India

*CORRESPONDENCE
Wang Qian,
202211131315@stu.cqu.edu.cn

RECEIVED 17 April 2024
ACCEPTED 04 June 2024
PUBLISHED 04 July 2024

CITATION
Qian W, Yuquan L, Xiaohui W, Kun Y, Yang L, Zhongyuan X, Guangyu L, Yunlong L and Jiyuan T (2024), Rapid assessment of distribution network equipment status based on fuzzy decision making.
Front. Energy Res. 12:1418833.
doi: 10.3389/fenrg.2024.1418833

Rapid assessment of distribution network equipment status based on fuzzy decision making

Wang Qian[1,2]*, Li Yuquan[2], Wang Xiaohui[3], Yang Kun[1], Liu Yang[1], Xia Zhongyuan[3], Lan Guangyu[3], Liu Yunlong[3] and Tang Jiyuan[1]

[1]School of Electrical Engineering, Chongqing University, Chongqing, China, [2]State Grid Henan Electric Power Research Institute, Zhengzhou, China, [3]State Grid Henan Electric Power Company, Zhengzhou, China

Voltage instability, power imbalance, and unreliability are caused mainly by equipment failure in the distribution system, so it is important to accurately and quickly assess the status of distribution network equipment. However, it is challenging to detect equipment failures, the traditional XGBoost algorithm is unsuitable because some evaluation indices are incompetent to quantify. To address these issues, we propose a fast evaluation method for the state of electrical distribution equipment based on fuzzy decision-making. Firstly, key indices are selected from the multi-source equipment information. Secondly, this paper constructs the mapping between key indices and equipment status scores by combining the fuzzy iterative method and the XGBoost algorithm. Finally, the proposed assessment model is confirmed by using the distribution transformers as an example. The result shows that the proposed multi-source information assessment method can quickly and accurately determine the operation status of electrical distribution equipment, and the proposed method has better accuracy than the traditional method.

KEYWORDS

electrical distribution equipment, fuzzy decision making, data-driven, status assessment, XGBoost

1 Introduction

With social and economic development, the scale of the power grid is gradually expanding, prompting higher reliability requirements. The distribution network is an essential part of the power system. It is responsible for the critical task of supplying power directly to customers (Liang et al., 2009). At the same time, the clear aims of operational status analysis improving the reliability of the power supply. It is an integral part of operations and maintenance in the power system (Guan, 2022). Through testing and evaluating equipment such as distribution transformers (DTs) and circuit breakers, system operators can ensure the safe and stable operation of distribution equipment and improve the economy of power supply companies.

In the research on equipment evaluation, there is more research on primary equipment such as generators, transformers, circuit breakers, etc., and less on medium- and low-voltage equipment. Most of them are limited to studying the remaining life of power transformers, and the distribution equipment still needs to form a set of quantitative evaluation methods (Fang et al., 2023). However, the location dispersion, the large amount of monitoring data, and the lack of uniform evaluation

standards have brought significant challenges in assessing equipment status (Yuan et al., 2019; Tamma et al., 2021).

The transformer is the main equipment for distributing power and transforming voltage to a wide range of customers, and people have always valued it (Guo and Liu, 2005). Methods such as fuzzy evaluation and artificial intelligence are widely used in transformer status assessment (Zhu et al., 2008; Xie et al., 2012; Chen, 2017; Zhou et al., 2020; Lv, 2022). Zhou et al. proposed a transformer condition assessment method based on an interval grey number dynamic grey target (Lv, 2022). The accuracy of the proposed transformer condition assessment method is verified by integrating the dynamic changes of transformer operation data and index information in multi-dimensional time phases. Zhu et al. used the transformer oil chromatography data as the operational condition assessment index, proposed a new method to transform the qualitative indexes into quantitative indexes, and finally used the obtained assessment results as the training set of the SVM and obtained the transformer's status level (Xie et al., 2012). However, the model consideration is relatively single, and the assessment results are not accurate. Reference (Zhou et al., 2020) studied the power transformer condition evaluation index system in depth, as well as the calculation method and model of the transformer health index based on fuzzy logic. Reference (Chen, 2017) established an insulation state evaluation system and proposed a transformer insulation state evaluation method based on fuzzy cloud theory. The affiliation degree cloud model was utilized to describe its fuzziness and randomness. Zhe et al. applied a conventional approach to evaluate transformers' condition and introduced a condition assessment model using support vector regression. However, this method heavily relies on the size of the transformer's sample capacity (Zhu et al., 2008). References (Ahmad and Senroy, 2020; Zhang et al., 2020) proposed a cloud model for transformer condition assessment considering the randomness of the data and the ambiguity of the evaluation level, which successfully realized the transformation between qualitative and quantitative indicators. Zhang et al. proposed a condition assessment index system based on the transformer test category, and the evaluation level was divided by solving the relative deterioration of the index. Finally, the confidence criterion was introduced for comprehensive judgment (Zhang et al., 2010). The model is more subjective, and new solutions need to be proposed to reduce the interference of human factors in the model. Zheng et al. introduced the grey assessment decision theory (Wang et al., 2012), but the index system was not comprehensive enough to consider the data of all the transformer components, and the results were more one-sided and lacked persuasive power.

The current evaluation method for distribution network equipment is not comprehensive. It lacks a quantitative assessment method and is greatly influenced by subjective factors, such as the experts' experience. Therefore, it is important to establish an assessment method that better aligns with the actual operating conditions of the electrical distribution equipment. The proposed method allows for the assessment of distribution transformers, providing a valuable reference for the economic and operational reliability of power system operators.

In this paper, we propose a state assessment model for distribution network equipment. This model integrates multi-source information derived from the operational data of the equipment, taking into account critical state variables. To establish the relationship between the multi-sources information and the equipment's state, we utilize a data-driven fuzzy iterative method and the XGBoost algorithm. This enables a more accurate evaluation of the equipment's condition. Additionally, the paper introduces a method for multi-source information to assess the operation status of distribution equipment, using DTs as an example. This method effectively determines the equipment's operation status by leveraging various types of information, offering a more comprehensive evaluation compared to other approaches.

2 Characteristic extraction and evaluation of key condition indicators of power distribution equipment

There are five categories of key equipment for the distribution network, which are DTs, switchgear, cables, overhead lines, and pole-mounted switches. During operation, a large amount of data is generated, including real-time and historical data, hardware information, and environ-mental conditions. To accurately determine the operating status of equipment, it is necessary to process data and extract key condition indicators that characterize the equipment's operation. Establishing a scientific and comprehensive evaluation system for condition indicators is significant for the status evaluation of distribution network equipment.

DT is an important equipment in the distribution network, and its operation status is closely related to the reliability of the power supply. The Table A1 in the appendix displays various types of faults in DT, including insulation, short-circuit, discharge, and mechanical drive operating mechanism faults. Since the DTs used in industry and large users are mainly step-down transformers and mostly oil-immersed transformers, the condition indicators in Table A1 are selected and classified according to the principle of selecting key condition indicators by referring to standards such as "Guidelines for Condition Evaluation of Equipment in Distribution Networks" (State Grid Corporation, 2011), and the results are shown in Table 1.

Once the condition indicators are selected, it is necessary to score them to further evaluate the state of the DT. According to the uniform regulations, the evaluation principles for each condition indicators are shown in the third column of Table 1. Before evaluation, the condition indicators of the transformer shown in Table 1 need to be normalized due to their qualitative and quantitative indicators varying in orders of magnitude and dimensions. The condition indicators that makes the status of the equipment better when the value gets smaller or lower, such as winding DC resistance and oil temperature, are processed by Eq. 1; The state quantities (withstand voltage, insulation resistance, etc.) that make the equipment state better when the value becomes larger or higher are handled

TABLE 1 Classification of key state variables of DT.

Classification	Specific parts	Condition indicators
Hardware situation	Sealing method	Sealing ability μ_1
	Degree of insulation	Withstand voltage test μ_2
	System contamination	Contamination μ_3
	Non-electricity protection device	Insulation resistance μ_{10}
	Winding and bushing	DC resistance μ_{11}
Operational situation	Oil level	Oil level μ_4
	Winding and bushing outer temperature	Temperature μ_5
	Grounding condition	Grounding down conductor appearance μ_6
	Respirator	Respirator status μ_7
	Load situation	Load rate μ_{12}
	Three-phase load balancing	Three-phase unbalance rate μ_{13}
Human factors	Equipment identity	Completeness of identification μ_8
	Tap changer	Tap changer performance μ_9

by Eq. 2. (Wang and Zhao, 2020). Empirical data gives the degree of deterioration in the qualitatively measured condition indicators such as running time and sealing performance.

$$\mu_{i,j} = \begin{cases} 0 & \mu_{i,j} \le \mu_{i,j,0} \\ \dfrac{\mu_{i,j} - \mu_{i,j,0}}{\mu_{i,j,1} - \mu_{i,j,0}} & \mu_{i,j,0} < \mu_{i,j} \le \mu_{i,j,1} \\ 1 & \mu_{i,j} > \mu_{i,j,1} \end{cases} \tag{1}$$

$$\mu_{i,j} = \begin{cases} 1 & \mu_{i,j} < \mu_{i,j,1} \\ \dfrac{\mu_{i,j,0} - \mu_{i,j}}{\mu_{i,j,0} - \mu_{i,j,1}} & \mu_{i,j,1} \le \mu_{i,j} < \mu_{i,j,0} \\ 0 & \mu_{i,j} \ge \mu_{i,j,0} \end{cases} \tag{2}$$

Where the value of the subscript i of $\mu_{i,j}\,(i = 1, 2, ..., 9)$ is determined by the condition indicators; j indicates the relative deterioration degree of the condition indicators, $\mu_{i,j}$ is the observed value divided by the ideal value, and the range of values is [0,1]; $\mu_{i,j,0}$ is the baseline value, and $\mu_{i,j,1}$ denotes the attention value or the warning value, the values of $\mu_{i,j,0}$ and $\mu_{i,j,1}$ are obtained by (Wang and Zhao, 2020).

According to the evaluation criteria of condition indicators given in Table 1, combined with a large number of experts and long-term experience in the field (China Electric Power, 2008), the assessment set of DT key condition indicators in Table 1 is obtained, as shown in Table 2.

2.1 Weight determination based on fuzzy iteration and XGBoost

After selecting the key condition indicators for distribution network equipment, reasonable weights must be assigned to each status variable before conducting a comprehensive state assessment. In this paper, we use the eclectic fuzzy decision-making and multilevel fuzzy integrated evaluation model to analyze the pre-data of DT's. Then, the weight ratios of the assessment set are constantly updated by the XGBoost algorithm, which reduces the influence of subjective factors brought by experts and improves the reliability of data analysis. Finally, an expert database was established.

2.2 Solution process for eclectic fuzzy decision-making weights

The flow chart for eclectic fuzzy decision-making is illustrated in Figure 1. Beginning with the original sample data, First, virtualizing the fuzzy positive ideal and fuzzy negative ideal. The fuzzy positive ideal is composed of the maximum value of the fuzzy indicator in each indicator, while the fuzzy negative ideal is composed of the minimum value of the fuzzy indicator in each indicator (Zadeh, 1965). Next, the weighted Euclidean distance is used to calculate the distance between each alternative object and the fuzzy positive ideal and fuzzy negative ideal. Based on this, the degree of affiliation of each alternative object belonging to the fuzzy positive ideal is calculated. The greater the degree of affiliation, the more desirable the scheme is.

The basic solution steps for eclectic fuzzy decision-making are as follows.

Step 1: Transform the indicator data into triangular fuzzy numbers;

Suppose that $\mathbf{F}(R)$ is an overall fuzzy set on R and the set $\mathbf{M} \in \mathbf{F}(R)$. The affiliation function $\mu_{\mathbf{M}}$ of $\mathbf{M}$ is denoted as follows:

$$\mu_{\mathbf{M}}(x) = \begin{cases} \dfrac{x - l}{m - l}, x \in [l, m] \\ \dfrac{x - u}{m - u}, x \in [m, u] \\ 0, x < l \text{ or } x > u \end{cases} \tag{3}$$

TABLE 2 Key condition indicators assessment set of DT.

State variables	Description	Assessment set				
		Good	Normal	Attention	Abnormal	Serious
Sealing ability μ_1	Oil leakage situation $\mu_{1,1}$	0.2	0.2	0.3	0.2	0.1
	Oil dripping situation $\mu_{1,2}$	0	0	0.1	0.1	0.8
	Oil spilling situation $\mu_{1,3}$	0	0	0	0	1
Withstand voltage test μ_2	Pressure resistance $\mu_{2,1}$	0	0	0	0.1	0.9
Contamination μ_3	A small amount of Contamination $\mu_{3,1}$	0.9	0.1	0	0	0
	More pollution $\mu_{3,2}$	0.8	0.1	0.1	0	0
	Obviously damaged rust $\mu_{3,3}$	0.1	0.2	0.3	0.3	0.1
	Severely contaminated and blocked $\mu_{3,4}$	0	0	0.2	0.5	0.3
Oil level μ_4	Oil level gauge indicates Abnormality $\mu_{4,1}$	0.1	0.2	0.3	0.2	0.2
	Oil level gauge no Indication $\mu_{4,2}$	0.1	0.1	0.3	0.3	0.2
Temperature μ_5	Temperature of connector is too high $\mu_{5,1}$	0.1	0.3	0.4	0.2	0
	Rise of temperature is not normal $\mu_{5,2}$	0.1	0.2	0.3	0.3	0.1
Grounding down conductor appearance μ_6	Lack of connection $\mu_{6,1}$	0.1	0.2	0.3	0.3	0.1
	Insufficient depth $\mu_{6,2}$	0.2	0.3	0.4	0.1	0
Respirator Condition μ_7	The respirator is completely discolored by moisture $\mu_{7,1}$	0.3	0.3	0.3	0.1	0
	The respirator is completely breathless $\mu_{7,2}$	0.3	0.3	0.3	0.1	0
Identification Integrity μ_8	Lack of identification $\mu_{8,1}$	0	0.1	0.2	0.5	0.2
	Wrong identifies or no identified $\mu_{8,2}$	0	0	0.1	0.4	0.5
Tap changer Performance μ_9	Tap position power indicates abnormal $\mu_{9,1}$	0	0.5	0.5	0	0

Where $l \le m \le u$, $\mathbf{M}$ is triangular fuzzy number, denoted as $\mathbf{M} = (l, m, u)$. According to Eq. 3, the qualitative indicators, quantitative indicators, and weight data in the condition indicators are unified into a triangular fuzzy number.

The qualitative indicators $\mu_i (i = 1, 2, ..., 9)$ in DT are converted to quantitative indicators according to Table 3

The quantitative indicator values $\mu_i (i = 10, 11, ..., 13)$ of DT critical state quantities are expressed in the form of a triangular fuzzy number as shown in Eq. 4.

$$\mu_i = (\mu_i, \mu_i, \mu_i) \tag{4}$$

After transforming all indicators into triangular fuzzy numbers, the matrix of fuzzy indicators is obtained and denoted as $\mathbf{F} = (f_{ij})_{m \times n}$

The weighted triangular fuzzy number of quantitative indicators is obtained according to Eq. 4 and is expressed as Eq. 5:

$$\mathbf{w} = [(w_1, w_1, w_1), (w_2, w_2, w_2), ...(w_i, w_i, w_i)] \tag{5}$$

The weighted triangular fuzzy numbers of qualitative indicators were obtained according to the transformation method in Table 3.

Step 2: Fuzzy indicator matrix normalization process;

Assuming that there are N evaluation objects and the evaluation indicator $j (j \in n)$ corresponds to N fuzzy indicator values in $\mathbf{F}$, which are denoted as $x_i = (a_i, b_i, c_i)$, $(i = 1, 2, ..., N)$, the formula for the normalization of x_i is as follows:

①. If x_i is the value of the fuzzy indicator corresponding to the cost-based indicator, the normalization formula is Eq. 6:

$$y_i = \left(\frac{\min(a_i)}{c_i}, \frac{\min(b_i)}{b_i}, \frac{\min(c_i)}{a_i} \wedge 1 \right) \tag{6}$$

②. If x_i is the fuzzy indicator value corresponding to the income-based indicators, the normalization formula is

$$y_i = \left(\frac{a_i}{\max(c_i)}, \frac{b_i}{\max(b_i)}, \frac{c_i}{\max(a_i)} \wedge 1 \right) \tag{7}$$

The normalized fuzzy indicator matrix is denoted as $\mathbf{R} = (y_{ij})_{m \times n}$.

Step 3: Constructing the fuzzy decision-making matrix $\mathbf{D} = (r_{ij})_{m \times n}$

The fuzzy decision-making matrix can be obtained by weighting $\mathbf{R}$, as shown in Eq. 8:

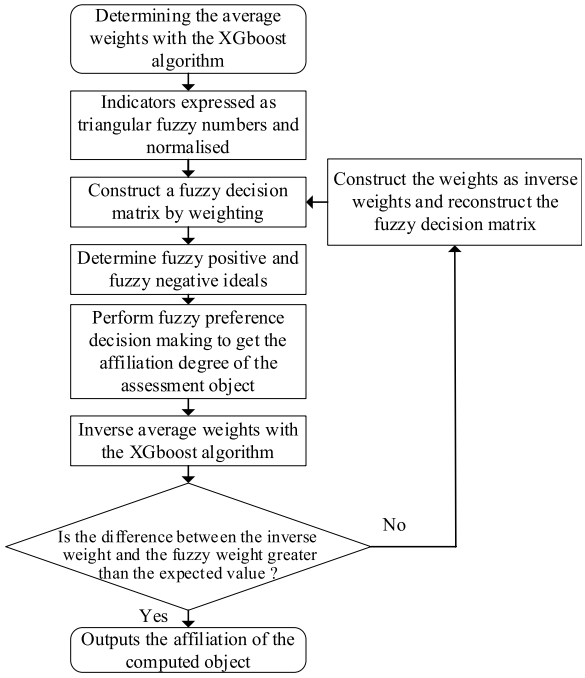

FIGURE 1
Flow chart of eclectic fuzzy decision-making model.

$$r_{ij} = \mathbf{w}\Theta y_{ij}\left(i = 1, 2, ..., N, j = 1, 2, ..., N\right) \tag{8}$$

Step 4: Determine the fuzzy positive ideal M^+ and the fuzzy negative ideal M^-, as shown in Eqs 9, 10;

$$M^+ = \left(M_1^+, M_2^+, ..., M_N^+\right) \tag{9}$$

$$M^- = \left(M_1^-, M_2^-, ..., M_N^-\right) \tag{10}$$

where component $M^+ = \max\left\{r_{1j}, r_{2j}, ..., r_{nj}\right\}$, $(j = 1, 2, ..., 15)$ is the fuzzy maximum value corresponding to the fuzzy indicator value of the j column in the fuzzy decision-making matrix $\mathbf{D}$; where component $M^- = \min\left\{r_{1j}, r_{2j}, ..., r_{nj}\right\}$, $(j = 1, 2, ..., 15)$ is the fuzzy minimum value corresponding to the fuzzy indicator value of the j column in the fuzzy decision-making matrix $\mathbf{D}$.

Step 5: Determine the distance d_i^+, d_i^- between the object i and M^+, M^-, as shown in Eqs 11, 12

$$d_i^+ = \sqrt{\sum_{j=1}^{N}\left(r_{ij} - M_j^+\right)^2}, i = 1, 2, \cdots, N \tag{11}$$

$$d_i^- = \sqrt{\sum_{j=1}^{N}\left(r_{ij} - M_j^-\right)^2}, i = 1, 2, \cdots, N \tag{12}$$

Step 6: Fuzzy optimal decision-making.

Let the assessment object i obeys the fuzzy positive ideal with affiliation degree μ_i, as shown in Eq. 13

$$\mu_i = \frac{d_i^-}{d_i^+ + d_i^-}, i = 1, 2, \cdots, N \tag{13}$$

Obviously $0 \le \mu_i \le 1$, the closer r_{ij} is to M^+, the closer μ_i is to 1. Utilizing the classification results of the degree of affiliation to rank the merits of the samples can get the fuzzy expert group assessment set of the multi-level fuzzy comprehensive evaluation model.

2.3 Multi-level fuzzy comprehensive assessment model based on XGboost algorithm

XGBoost (Chen and Guestrin, 2016) is an integrated learning algorithm based on gradient advancement that shows good performance in classification and regression problems. To reduce the influence of subjective factors brought about by expert experience and to avoid errors caused by data redundancy or error omission, this paper adopts a combination of eclectic fuzzy decision-making and the XGboost algorithm to improve the assessment accuracy of DT. This model integrates multiple weak learners together to build a strong learner, as follows:

For a dataset $\mathbf{D} = \{x_i, y_i\}$ containing n samples and m features, the output values of the integrated model with K weak learners are as shown in Eq. 14:

$$\hat{y}_i = \sum_{k=1}^{K} f_k(x_i) \tag{14}$$

TABLE 3 Index transformation of triangular fuzzy number method.

Quantitative value attributes	Cost indicator	Profitability indicator
(0,0,1)	Highest	Lowest
(1,1,2)	Very high	Very low
(2,3,4)	High	Low
(4,5,6)	General	General
(6,7,8)	Low	High
(7,8,9)	Very low	Very high
(9,10,10)	Lowest	Highest

Where f is a function of each classification and regression tree and $f(x) = \omega_{q(x)} (w \in R^T, q: R^M \rightarrow T)$. For each tree, q denotes the tree structure that maps samples to specific leaf nodes, T denotes the number of leaf nodes, and ω denotes the weights of the leaf nodes.

The XGBoost model is trained by additive approach, the optimal structure of this model is found by successively adding tree and segmentation features. Therefore, the predicted value of the nth tree is $\hat{y}_i^{(t)} = \hat{y}_i^{(t-1)} + f_t(x_i)$.

The objective function of the final model consists of two parts, the loss function l and the regularization term Ω, as shown in Eq. 15:

$$obj = \sum_{i=1}^{n} l(y_i, \hat{y}_i) + \sum_{k=1}^{K} \Omega(f_k) \tag{15}$$

where the loss function represents the predictive power of the model and the regularization term restricts the structure of the tree, as shown in Eq. 16:

$$\Omega(f) = \gamma T + \frac{1}{2}\lambda \sum_{j=1}^{T} \omega_j^2 \tag{16}$$

where γ and λ are two parameters that control the complexity, and the smaller their values are, the more complex the tree structure is.

A second-order Taylor expansion of the objective function can be approximated as Eq. 17:

$$obj^{(t)} = \sum_{i=1}^{n} \left[l\left(y_i, \hat{y}^{(t-1)}\right) + g_i f_t(x_i) + \frac{1}{2} h_i f_t^2(x_i) \right] + \Omega(f_t) + \text{constant} \tag{17}$$

Where $g_i = \partial_{\hat{y}_i^{(t-1)}} l(y_i, \hat{y}_i^{(t-1)})$ and $h_i = \partial^2_{\hat{y}_i^{(t-1)}} l(y_i, \hat{y}_i^{(t-1)})$ are the first and second order partial derivatives of the loss function, respectively, and the objective function after expanding the regularization term and removing the constant term is expressed as Eq. 18:

$$obj^{(t)} = \sum_{j=1}^{T} \left[\left(\sum_{i \in \mathbf{I}_j} g_i \right) \omega_j + \frac{1}{2} \left(\sum_{i \in \mathbf{I}_j} h_i + \lambda \right) \omega_j^2 \right] + \gamma T \tag{18}$$

where $\mathbf{I}_j$ is the index set that assigns the data point to the j leaf node.

In Eq. 7, ω_j is independent, therefore, the minimal value of the objective function and the corresponding ω_j^* can be obtained by direct derivation of ω_j, as shown in Eqs 19, 20.

$$\omega_j^* = -\frac{\sum g_i}{\sum h_i + \lambda} \tag{19}$$

$$obj^* = -\frac{1}{2} \sum_{j=1}^{T} \frac{(\sum g_i)^2}{\sum h_i + \lambda} + \gamma T \tag{20}$$

After obtaining the weight distribution, it is replaced with step 3 in the basic solution step of eclectic fuzzy decision-making, and then the final expert group assessment set is obtained by repeated iterations.

3 Case study

In this section, the proposed state assessment approach is verified in the distribution transformers. We obtained the data, including state parameters and health index, from DTs of 50 units in 20 maintenance periods.

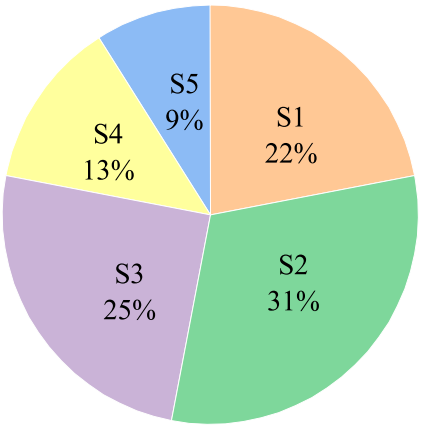

FIGURE 2
Percentage of transformer health status in the data set.

3.1 DT basic parameters

Table 2 displays the 13 important state quantities of the DT, which consist of four quantitative and nine qualitative markers. The rated values of the five major factor sets of DT are derived using the frequency statistics method in order to reduce data redundancy and clearly demonstrate the algorithm's accuracy. This method includes four qualitative metrics (grounding down conductor appearance μ6, sealing ability μ1, withstand voltage test μ2, and identification integrity μ8) in addition to one quantitative metric (winding DC resistance). The relevant data are divided into training and test sets according to the ratio of 7:3. All the cases were obtained by using Python 3.8 in a 3.4 GHz Intel Core i5-7500 computer with 8 GB of RAM, and the configuration of XGBoost-related parameters is shown in Supplementary Table S4.

3.2 Data pre-processing

According to the health index of the DT, it is categorized into [S1,S2,S3,S4,S5] five states. S1 indicates that the transformer is in good condition with low risk of failure. S5 indicates that the transformer is in very poor condition with a high risk of failure. The lower the status number, the better the condition of the transformer. The percentage of transformers in various health states in the dataset is shown in Figure 2.

The dataset's character-labeled data must first undergo preprocessing in order to be used. There are five values that make up the health index: good, normal, attention, abnormal, and serious, which are converted into (Liang et al., 2009; Yuan et al., 2019; Tamma et al., 2021; Guan, 2022; Fang et al., 2023). Figure 3 shows the result of encoding the transformer health state using one-hot encoding.

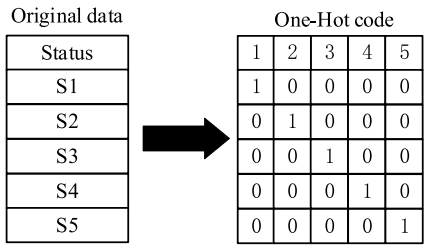

FIGURE 3
One-Hot code of transformer health status.

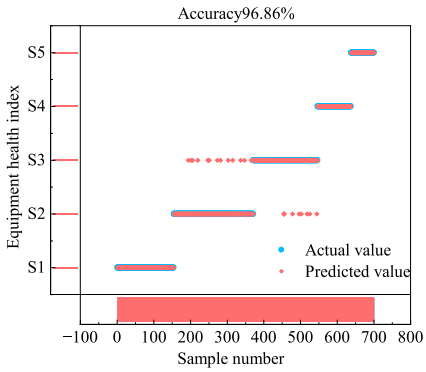

FIGURE 4
Prediction results of fuzzy decision model.

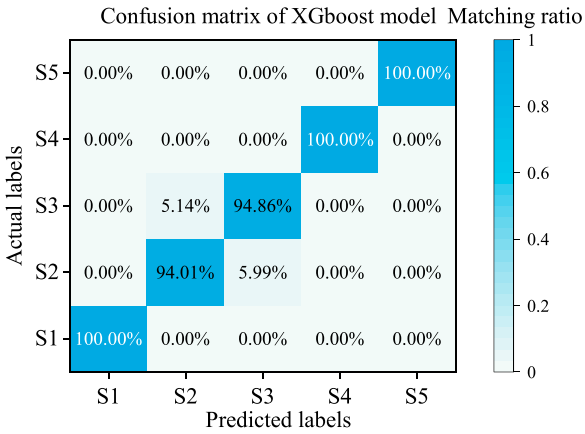

FIGURE 5
Confusion matrix of prediction results of XGBoost model.

3.3 Analysis of example results

In this part, the health status of the transformer is evaluated by fuzzy iteration and XGBoost. The model is applied to the test set and the predictions of the model can be calculated as shown in Figure 4.

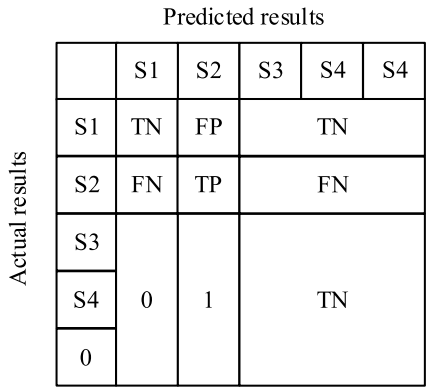

FIGURE 6
Prediction results classification diagram.

The actual and predicted categories are formed into rows and columns of a matrix, respectively, each element in the confusion matrix represents a categorization result, and the elements on the diagonal line indicate the number of correct predictions. Obviously, the lager the elements on the diagonal, the better the confusion matrix, and the confusion matrix is shown in Figure 5. The accuracy of S2 is 94.01%, the accuracy of S3 is 94.86%, and the accuracy of the other three categories is 100%. The model produces confusion only between S2 and S3, and all other categories are correctly categorized.

In the multiclassification problem, as shown in Figure 6, if S2 is set as a positive sample and the other categories are considered as negative samples, we can classify the results as True Positive (TP), False Positive (FP), True Negative (TN) and False Negative (FN). Similarly, the other categories can be divided in this way. We can calculate the situation of the evaluation indicators for each category based on the prediction results, and we can calculatethe the suituation of the evaluation indicators by the model through the macro-averaging method.

Accuracy is the percentage of correct predictions to the total sample, and is expressed as Eq. 21:

$$A = \frac{TP + TN}{TP + FP + TN + FN} \tag{21}$$

Precision is the percentage of true positive samples to the total positive samples in the predicted results, and is expressed as Eq. 22:

$$P = \frac{TP}{TP + FP} \tag{22}$$

Recall is the percentage of true positive samples to actual positive samples in the predicted results, and is expressed as Eq. 23:

$$R = \frac{TP}{TP + FN} \tag{23}$$

The F1 indicator (F1-score) is the average of precision and recall, and can be expressed as Eq. 24:

$$\mathrm{F1} = \frac{2PR}{P + R} \tag{24}$$

According to the above equation, we can calculate the precision index of the evaluation results of the proposed model. The recall rate

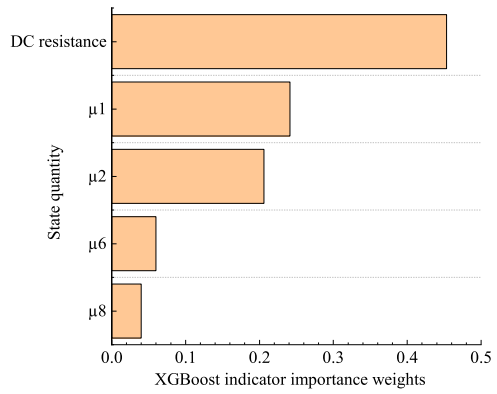

FIGURE 7
Weight of feature state.

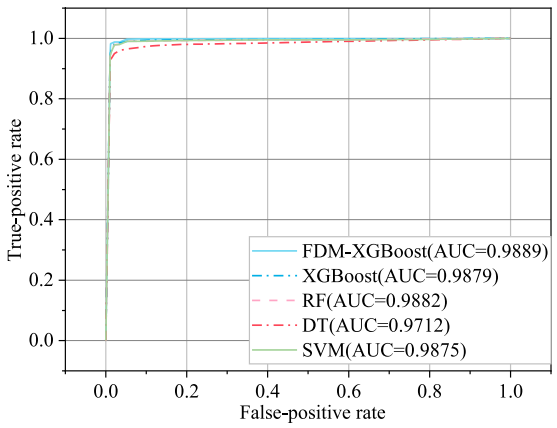

FIGURE 8
Comparison of SC curves of each mode.

is 97.77%, the accuracy rate is 96.86%, the precision rate is 97.78%, and the F1 indicator is 97.77%. The evaluation indicators of the proposed method are all above 96%. Therefore, the method can accurately and comprehensively identify the aging condition of cables.

The importance weights of the characteristic state quantities are shown in Figure 7. Winding DC resistance, sealing ability and insulation performance are the three key variables for evaluating the health status of the transformer.

3.4 Comparative analysis of algorithms

In order to validate the performance of the proposed model, this section compares the algorithm proposed in the paper with other classification models concluding traditional XGBoost model, random forest (RF) (Breiman, 2001), decision tree (DT) (Fürnkranz et al., 2011), and support vector machine (SVM) (Cortes and Vapnik, 1995). These classification algorithms are briefly described below.

The DT model classifies the instances based on the feature values, the nodes of the decision tree contain judgments on the features, and then, the model outputs the classification results based on the judgments of each node.

The RF model consists of multiple independent decision trees, each decision tree in the forest classifies the samples individually, and the category with the highest score among all the decision tree is used as the classification result of RF.

SVM is a linear classifier, the idea is to find a suitable hyperplane for sample classification, it is usually used to deal with binary classification problems, but it also can be used to deal with multiclassification problems using a one-to-one approach.

The model evaluation results of the fuzzy decision-based XGBoost algorithm and the other four models are shown in Table 4. The model evaluation accuracy of SVM is the lowest among all the models, which is due to the fact that traditional SVM is a linear classifier and cannot handle nonlinear problems well. RF and XGBoost are integrated learning models, while DT belongs to the weak learner model, its performance is weaker than of RF and XGBoost models.

The XGBoost algorithm shows better evaluation compared to all other methods. The regular XGBoost algorithm increases the regularization term compared to other algorithms, which improves the model accuracy and avoids overfitting. And among all the algorithms, the model proposed in the paper has the best performance. From the comparative results, it is clear that the use of fuzzy decision making method to optimize the qualitative state quantities by incorporating them into the classification model does improve the performance of the XGBoost model.

The sensitivity (sensitivity curve,SC) curve is plotted based on the false positive rate (FPR) and true positive rate (TPR) of the model. The goodness of the model can be quantified by the area under the SC curve (AUC) (Bradley, 1997). The TPR and FPR are expressed as Eq. 25.

$$TPR = \frac{TP}{TP + FN}, FPR = \frac{FP}{FP + TN} \tag{25}$$

TABLE 4 Evaluation effect indicators of all models.

Model name	Accuracy (%)	Precision (%)	Recall (%)	F1 indicator (%)
This article model	96.86	97.78	97.77	97.77
Traditional XGBoost model	95.60	96.57	96.85	96.71
RF model	95.20	96.17	96.51	96.33
DT model	93.87	94.91	94.22	94.06
SVM model	93.33	92.35	92.73	92.26

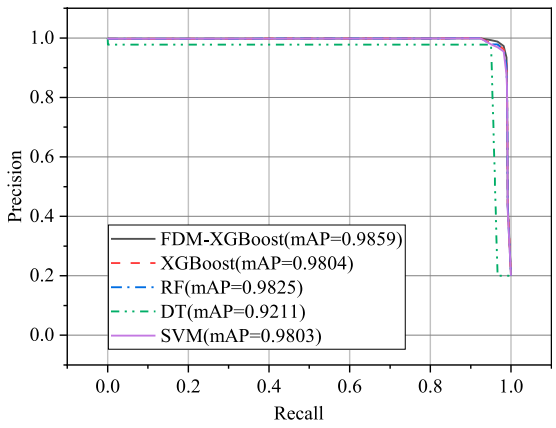

FIGURE 9
Comparison of P-R curves of each model.

The SC curves for each model are shown in Figure 8. If the prediction is completely random, the curve is a straight line with slope 1. Among the multiple curves, the curve positions and AUC values allow a visual comparison of the model's performance. The larger the AUC value, the more accurate the prediction. The curve of the fuzzy decision-based XGBoost model is closer to the upper left corner with an AUC of 0.988 9, it indicates that the model has a good performance in prediction accuracy.

The P-R curve can be plotted on the basis of the checking accuracy and the checking precision. In multiple classification problems, the area under the P-R curve is called the mean of average precision (mAP) for each category, and this value describes the accuracy of classification. The P-R curve is shown in Figure 9. The fuzzy decision based XGBoost model has the best curve performance with the largest mAP value among all models at 0.985 9. The DT model with the smallest mAP, it is 0.9211.

4 Conclusion

Equipment breakdowns are the primary source of voltage instability, power imbalance, and unreliability in power systems. This work proposes a transformer health state evaluation model based on the fuzzy decision-making XGBoost algorithm in order to precisely analyze the DT health state. Nevertheless, the traditional XGBoost algorithm cannot quantitatively measure the assessment indexes of transformer health state, in order to overcome the difficulty, this paper combines the fuzzy iterative method with the XGBoost algorithm, constructs the mapping relationship between the key indexes and the state scores of the equipment, and puts forward a fuzzy decision-making based rapid assessment method of the state of the distribution equipment, which realizes the multi-source data fusion of systematic assessment.

The experimental results show that the accuracy, precision, recall and F1 indicator of the fuzzy decision-based XGBoost model are 96.86%, 97.78%%, 97.77%% and 97.77%%, respectively, the result are superior to the traditional XGBoost, RF, DT and SVM models mentioned in the paper. By comparing with the XGBoost model, which is constructed directly using quantitative parameters, the XGBoost model useing fuzzy decision theory does improve the evaluation performance. In addition, the AUC and mAP values of the XGBoost model are larger than the other three models, indicating that the proposed model has better overall performance. The results show that the XGBoost transformer health state assessment model proposed in the paper is more accurate, and the model can effectively assess the DT state.

Data availability statement

The original contributions presented in the study are included in the article/Supplementary Material, further inquiries can be directed to the corresponding author.

Author contributions

WQ: Conceptualization, Writing–original draft. LY: Data curation, Writing–review and editing. WX: Formal Analysis, Writing–original draft. YK: Funding acquisition, Writing–original draft. LY: Investigation, Writing–original draft. XZ: Methodology, Writing–review and editing. LG: Project administration, Writing–review and editing. LY: Resources, Writing–review and editing. TJ: Software, Writing–review and editing.

Funding

The author(s) declare financial support was received for the research, authorship, and/or publication of this article. Technology Project of State Grid Henan Electric Power Company in 2023 (521702220005).

Conflict of interest

Authors WX, XZ, LG, and LYl were employed by State Grid Henan Electric Power Company.

The remaining authors declare that the research was conducted in the absence of any commercial or financial relationships that could be construed as a potential conflict of interest.

The authors declare that this study received funding from State Grid Henan Electric Power Company. The funder had the following involvement in the study: collection and analysis of data.

Publisher's note

Supplementary material

The Supplementary Material for this article can be found online at: https://www.frontiersin.org/articles/10.3389/fenrg.2024.1418833/full#supplementary-material

References

Ahmad, T., and Senroy, N. (2020). Statistical characterization of PMU error for robust WAMS based analytics. *IEEE Trans. Power Syst.* 35, 920–928. doi:10.1109/tpwrs.2019.2939098

Bradley, A. P. (1997). The use of the area under the ROC curve in the evaluation of machine learning algorithms. *Pattern Recognit.* 30 (7), 1145–1159. doi:10.1016/s0031-3203(96)00142-2

Breiman, L. (2001). Random forests. *Mach. Learn.* 45, 5–32. doi:10.1023/a:1010933404324

Chen, T., and Guestrin, C. (2016). "Xgboost: a scalable tree boosting system," in *Proceedings of the 22nd acm sigkdd international conference on knowledge discovery and data mining*, 785–794.

Chen, Z. (2017). *Fault prediction of distribution network equipment based on bp neural network*. Master's Thesis. Guangdong, China: Guangdong University of Technology.

China Electric Power (2008). *Q/GDW 168—2008 regulations of condition-based maintenance test for electric equipment*. Beijing, China: China Electric Power Press.

Cortes, C., and Vapnik, V. (1995). Support-vector networks. *Mach. Learn* 20, 273–297. doi:10.1007/BF00994018

Fang, M., Huang, R., and Lv, T. G. (2023). "Research on state assessment method of key equipment in distribution network," in *Asia conference on power and electrical engineering* (Tianjin, China: ACPEE), 2614–2618.

Fürnkranz, J. (2011). "Decision tree," in *Encyclopedia of machine learning*. Editors C. Sammut and G. I. Webb (Boston, MA: Springer). doi:10.1007/978-0-387-30164-8_204

Guan, C. X. (2022). *Evaluation and prediction of distribution network operation status based on multi-source data fusion*. Master's Thesis. Shenyang, China: Shenyang University of Technology.

Guo, J., and Liu, C. S. (2005). Research on lightning accidents and lightning protection measures of distribution transformer. *J. Electr. Power Sci. Technol.* 3, 14–17.

Liang, J. L., Wang, Z. D., and Liu, X. (2009). State estimation for coupled uncertain stochastic networks with missing measurements and time-varying delays: the discrete-time case. *IEEE Trans. Neural Netw.* 20, 781–793. doi:10.1109/tnn.2009.2013240

Lv, B. (2022). *Health evaluation of main transformer in power plant based on AHP-fuzzy comprehensive evaluation metho*. Chongqing, China: Chongqing University.

State Grid Corporation (2011). *Q/GDW 645-2011 Guidelines for state evaluation of distribution network equipment*. Beijing, China: State Grid Corporation.

Tamma, W. R., Prasojo, R. A., and Suwarno, (2021). High voltage power transformer condition assessment considering the health index value and its decreasing rate. *High. Volt.* 6, 314–327. doi:10.1049/hve2.12074

Wang, N., and Zhao, F. (2020). An assessment of the condition of distribution network equipment based on large data fuzzy decision-making. *Energies* 13, 197. doi:10.3390/en13010197

Wang, Y. L., Zhao, X. P., and Bian, J. (2012). "Cloud model-based risk assessment of power transformer," in *International conference on high voltage engineering and application* (IEEE).

Xie, H. X., Shi, L. P., and Hui, Z. Y. (2012). Research on immune clustering algorithm for transformers fault diagnosis. *Electr. Meas. Instrum.* 49, 15–18.

Yuan, F., Guo, J., Xiao, Z. H., Zeng, B., Zhu, W., and Huang, S. (2019). A transformer fault diagnosis model based on chemical reaction optimization and twin support vector machine. *Energies* 12, 960. doi:10.3390/en12050960

Zadeh, L. A. (1965). Fuzzy sets. *Inf. Control* 8 (3), 338–353. doi:10.1016/s0019-9958(65)90241-x

Zhang, Z., Zhao, W. Q., and Zhu, Y. L. (2010). State evaluation of power transformer based on support vector regression. *Electr. Power Autom. Equip.* 30, 81–84.

Zhang, J. W., Yang, Y., Weng, Y., and Zhang, N. (2020). Topology identification and line parameter estimation for non-PMU distribution network: a numerical method. *IEEE Trans. Smart Grid* 11, 4440–4453. doi:10.1109/tsg.2020.2979368

Zhou, J. S., Yu, J. F., and Yang, H. H. (2020). A condition assessment method of transformers based upon the dynamic grey target with theinterval grey number. *J. Electr. Power Sci. Technol.* 35, 133–140.

Zhu, Y. L., Shen, T., and Li, Q. (2008). Transformer condition assessment based on support vector machine and DGA. *J. Electr. Power Syst. Automation* 24, 47–50.

10.3389/fenrg.2024.1418833

Appendix A

TABLE A1 Critical state evaluation set of DT.

Component	State quantity	Reflected state
Winding and bushing	DC resistance	DC resistance exceeds the range
	Insulation resistance	Insulation resistance is not normal
	Temperature	The temperature of the joint is abnormal and the temperature rise is abnormal
	Load rate	Overload
	Degree of contamination	Severely contaminated or rusted appearance
	Appearance integrity	Damaged appearance
	The temperature of respirator	Exceed the factory defaults
	Three-phase unbalance rate	Three-phase unbalance rate is not normal
Tap changer	Performance	Operation is not Normal
Cooling system	Mechanical properties	Dry change fan vibration is not normal
	Temperature	Temperature control device is abnormal
Tank	Ground distance of the bench	The distance to the ground is not enough
	Sealing	Finishing seal aging
	Oil level	Oil level is not normal
	Oil temperature	Oil temperature is abnormal
Non-electricity protection device	Insulation resistance	Unqualified insulation
Ground wire	Exterior	Insufficient connection or insufficient depth of grounding body
Insulation	Grounding resistance	Grounding resistance is abnormal
	Withstand voltage test	Pressure resistance is unqualified
Identification	Identification integrity	Equipment identification is vague, incomplete, wrong, etc.

frontiers | Frontiers in Energy Research

TYPE Original Research
PUBLISHED 07 August 2024
DOI 10.3389/fenrg.2024.1422639

OPEN ACCESS

EDITED BY
Chaolong Zhang,
Jinling Institute of Technology, China

REVIEWED BY
Yong Hu,
Hong Kong Polytechnic University, Hong Kong SAR, China
Fang Shi,
Shandong University, China
Jian Wang,
Southwest Jiaotong University, China
Andre Abel Augusto,
Fluminense Federal University, Brazil

*CORRESPONDENCE
Wentao Xu,
15590778635@163.com

RECEIVED 24 April 2024
ACCEPTED 02 July 2024
PUBLISHED 07 August 2024

CITATION
Wu X, Zhao H, Xu W, Pan W, Ji Q and Hua X (2024), Fault diagnosis of the distribution network based on the D-S evidence theory Bayesian network.
Front. Energy Res. 12:1422639.
doi: 10.3389/fenrg.2024.1422639

Fault diagnosis of the distribution network based on the D-S evidence theory Bayesian network

Xiaogang Wu[1], Hanying Zhao[1], Wentao Xu[1]*, Wulue Pan[2], Qingfeng Ji[1] and Xiujuan Hua[3]

[1]State Grid Zhejiang Electric Power Co., Ltd., Lishui Power Supply Company, Lishui, China, [2]State Grid Zhejiang Electric Power Co., Ltd., Hangzhou, China, [3]Nanjing Nanrui Jibao Engineering Technology Co., Ltd., Nanjing, China

Relay protection rejection and misoperation exist in the existing distribution network, which will affect the fault diagnosis results. To diagnose faults in distribution networks, this paper presents a fault diagnosis method for the distribution network based on the D-S evidence theory Bayesian network. First, the collected relay protection information is divided into two categories, protection information and circuit breaker information; the corresponding Bayesian network model is established based on their respective action logic, and the corresponding component failure probability is obtained by Bayesian backward inference. Second, the fault probabilities obtained from the two Bayesian networks are fused by the D-S evidence theory, and the obtained fault probabilities are used to diagnose the faulty component. Then, using the Bayesian network corresponding to the faulty component to perform Bayesian forward inference, the protection devices and circuit breakers are identified for misoperation or rejection to achieve the fault diagnosis of the distribution network. Finally, the correctness and reliability of the proposed diagnosis method are verified through the analysis of arithmetic cases.

KEYWORDS

Bayesian network, distribution network, D-S evidence theory, fault diagnosis, Bayesian inference

1 Introduction

More and more distributed power sources and new types of loads are widely connected to the distribution network with the "double-carbon" goal. The dispatch center receives a large amount of alarm information from the Supervisory Control and Data Acquisition (SCADA) secondary equipment when faults occur in the distribution network, which increases the difficulty for operation and maintenance personnel to analyze the cause and process of the distribution network fault (Ferreira et al., 2016; Xialin et al., 2019).

Fault diagnosis of the power grid refers to the diagnosis of components through specific action data on protection devices and circuit breakers in the fault area, as well as the analysis of the action behaviors for protective devices and circuit breakers. The current typical grid fault diagnosis methods are Petri nets (Biao et al., 2019; YANG et al., 2020), artificial neural networks (Dongyuan et al., 2014; Guojiang et al., 2014), expert systems (Dongmei et al., 2014; Xuechen et al., 2017), rough set theory (Sun et al., 2013; Wenwu et al., 2021), analytic models (Daobing et al., 2024; Yuyang et al., 2021), multi-source information fusion

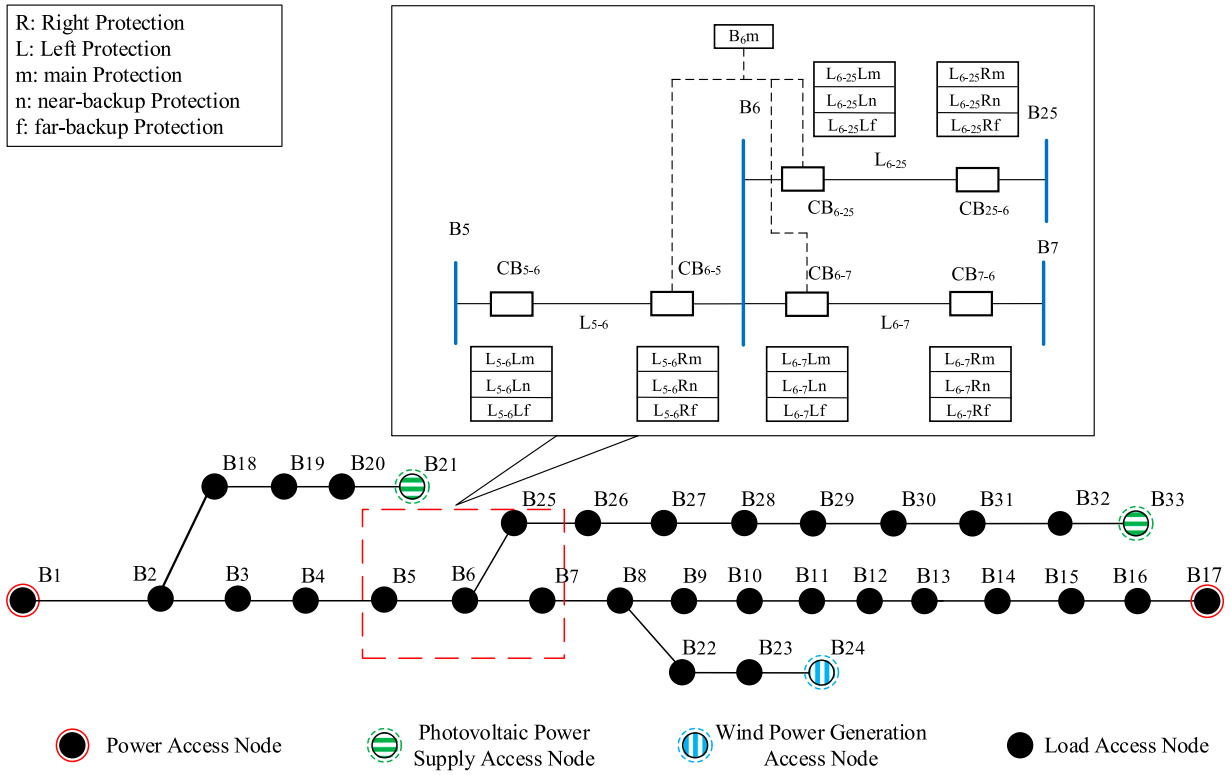

FIGURE 1
Topology and protection configuration of the distribution network.

(Weixing et al., 2021; Yu et al., 2021), and Bayesian networks (LUO and TONG, 2015; Pengzhe et al., 2021). Zhang et al. (2021) presented a method of partition fault diagnosis based on the improved probabilistic neural network (PNN) and gray relational analysis (GRA) integral, aiming at the problem of large-power grid fault diagnosis. (Zhang et al. (2023) proposed a quantitative representation method for alarm information and used the quantified alarm information as classification features based on the quantity and time-series distribution characteristics of alarm information during faults. A novel hybrid method of combining variational mode decomposition (VMD) and a convolutional neural network (CNN) for fault location and fault type identification is proposed by Zhang et al. (2022). The methods described by Wang et al. (2022) can distinguish false faults caused by measurement tampering attacks.

The above methods can realize the fault diagnosis of the power grid, but the method used cannot reflect the role of relay protection action information, and it is not easy to understand. The Bayesian network is a probability graph model used to represent the dependency relationships between variables and can be used to infer the states of other variables. At the same time, this graph theory representation is intuitive and easy to understand, which helps understand the interaction between relay protections. Luo and Tong (2015) evaluated the reliability of the action status and occurrence time of protection and circuit breakers in the power grid and introduced the concept of reliability in the Bayesian inference process to achieve power grid fault diagnosis. This method only considers the impact of SCADA system relay protection action information on fault diagnosis and does not analyze the incorrect action of relay protection. Zhang et al. (2021) built a Bayesian network model to realize the identification of relay protection rejection and misoperation and deduce the action sequence of each protection device and circuit breaker when the power grid faults. The Bayesian network structure in this method will make the information on the circuit breaker have less influence on the component fault judgment, which may misjudge when the circuit breaker fails to act for some reasons. He et al. (2011) used specific segmentation methods to segment the power grid and introduced the concept of overlap degree for D-S evidence fusion, then diagnosed the sub networks in different regions based on relay protection action information, and integrated the diagnostic results of each network to achieve fault diagnosis of the power grid.

To avoid the influence of incorrect action of the protection and circuit breaker on fault diagnosis, a new fault diagnosis of the distribution network based on D-S evidence theory is proposed in this paper. Compared with the previously proposed fault diagnosis method, the main contributions are as follows:

- The relay protection information is divided into two categories, protection action information and circuit breaker action information, and the Bayesian network model is established according to their respective action logic, which effectively avoids the problem of circuit breaker information having little influence on component fault judgment in a traditional Bayesian network model.

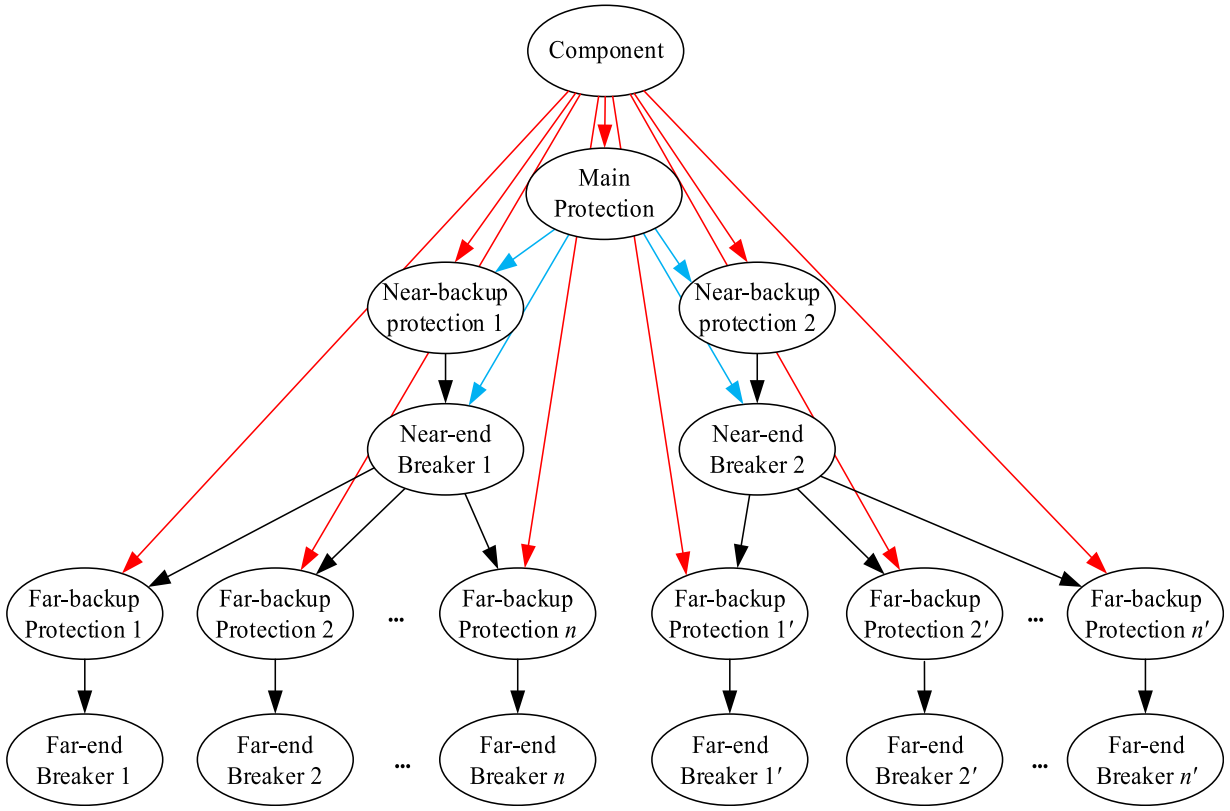

FIGURE 2
Bayesian network model for relay protection of the distribution network.

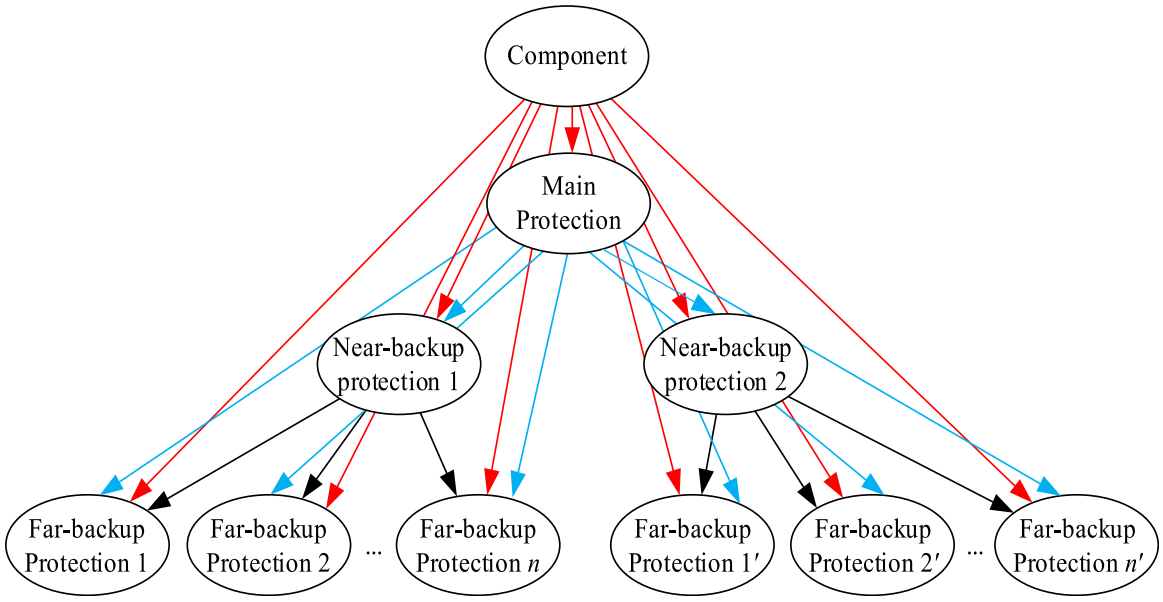

FIGURE 3
Bayesian network model of protecting information.

- The fusion of fault diagnosis information from two Bayesian network models using D-S evidence theory improves the accuracy of fault diagnosis.

The rest of the paper is structured as follows: Section 2 presents the rules for building Bayesian network models and their drawbacks; Section 3 presents the improvement in the

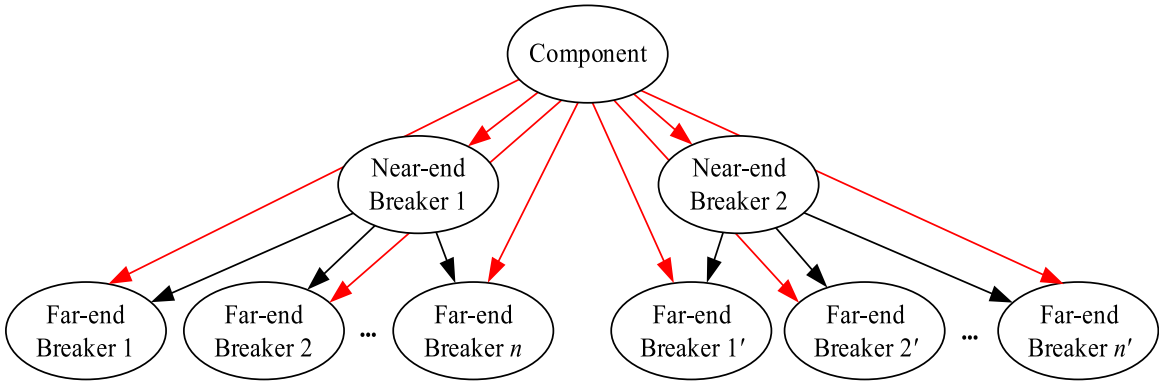

FIGURE 4
Bayesian network model of circuit breaker information.

TABLE 1 Failure prior probability for element nodes.

Component	Line	Bus
Fault prior probability	0.0208	0.0137

Bayesian network model and implementation of fault diagnosis using D-S evidence theory; Section 4 presents the simulation results for different fault scenarios; and finally, Section 5 concludes the paper.

2 Bayesian network model for relay protection in distribution networks

2.1 Topological structure and protection configuration

Research on power grid fault diagnosis for the distribution network shown in Figure 1 analyzes the local power system relay protection information and power grid topology structure. At present, the main protection used in the distribution network is longitudinal differential protection, while the backup protection adopts zero-sequence overcurrent protection at both ends and distance protection at both ends.

2.2 Principle of protection action

This paper focuses on the analysis of lines and buses in the distribution network. We take the left side of protection $L_{5\text{-}6}$Lm, $L_{5\text{-}6}$Ln, and $L_{5\text{-}6}$Lf of line $L_{5\text{-}6}$ as examples to introduce the relevant line protection action principle in Figure 1. $L_{5\text{-}6}$Lm is the main protection, which is only responsible for protecting its own lines, i.e., lines $L_{5\text{-}6}$; $L_{5\text{-}6}$Ln is a near-backup protection, which also protects the line itself; when the main protection $L_{5\text{-}6}$Lm is rejected for some reason, the near-backup protection $L_{5\text{-}6}$Ln operates to protect its own line; and $L_{5\text{-}6}$Lf is the remote backup protection, which normally operates in the event of a fault in an adjacent element. When the adjacent bus B_6 fails and its main protection does not operate, $L_{5\text{-}6}$Lf acts as the remote backup protection to isolate the fault. All three types of protection will trigger $CB_{5\text{-}6}$ trips when activated.

For bus protection, B_6m is the main protection, which is only responsible for protecting the bus itself, i.e., B_6, When a fault occurs on bus B_6, bus main protection B_6m acts to trigger $CB_{6\text{-}5}$, $CB_{6\text{-}7}$, and $CB_{6\text{-}25}$ trips; the backup protection of the bus is served by the backup protection of the adjacent line of the bus, i.e., the remote backup protection of lines $L_{5\text{-}6}$,$CB_{6\text{-}25}$, and $L_{6\text{-}7}$ serves as the backup protection of bus B_6.

2.3 Bayesian network principle

A Bayesian network is a directed acyclic graph based on the structure of the network. Each node represents a variable in the network, the directed arc represents the relationship between variables, and the conditional probability between each node and its child nodes represents the dependency relationship between variables. The mathematical description is as follows. If $X = \{x_1, x_2, \ldots, x_n\}$ is defined, where x_1, x_2, and x_n are the nodes in the Bayesian network, then, the joint probability of the occurrence of multiple nodes $p(x_1, x_2, \ldots, x_n)$ is

$$p(x_1, x_2, \ldots x_n) = \prod_{i=1}^{n} p(x_i \mid \pi(x_i)), \tag{1}$$

where $\pi(x_i)$ represents the set of parent nodes of x_i in Eq. 1.

For a node x_i in a Bayesian network with m elementary events $\{e_1, e_2, \ldots, e_k\}$, assuming that the event results $E = \{x_1, \ldots x_{i-1}, x_{i+1} \ldots, x_n\}$ for all nodes related to node x_i have been obtained, the conditional probability of the sth event e_s of node x_i occurring is shown in Eq. 2.

$$p(x_i = e_s \mid E) = \frac{p(x_i = e_s, E)}{p(E)} = \frac{p(x_i = e_s)\prod_{j=1, j\neq i}^{n} p\left(x_j \mid \pi\left(x_j\right)\right)}{\sum_{k=1}^{m}\left[p(x_i = e_k)\prod_{j=1, j\neq i}^{n} p\left(x_j \mid \pi\left(x_j\right)\right)\right]}. \tag{2}$$

TABLE 2 Rejection and misoperation probability of the relay protection device and circuit breaker.

Probability of failure	Protection of the line	Protection of the bus	Circuit breaker
Misoperation	0.0024	0.0007	0.0048
Rejection	0.0007	0.0308	0.0083

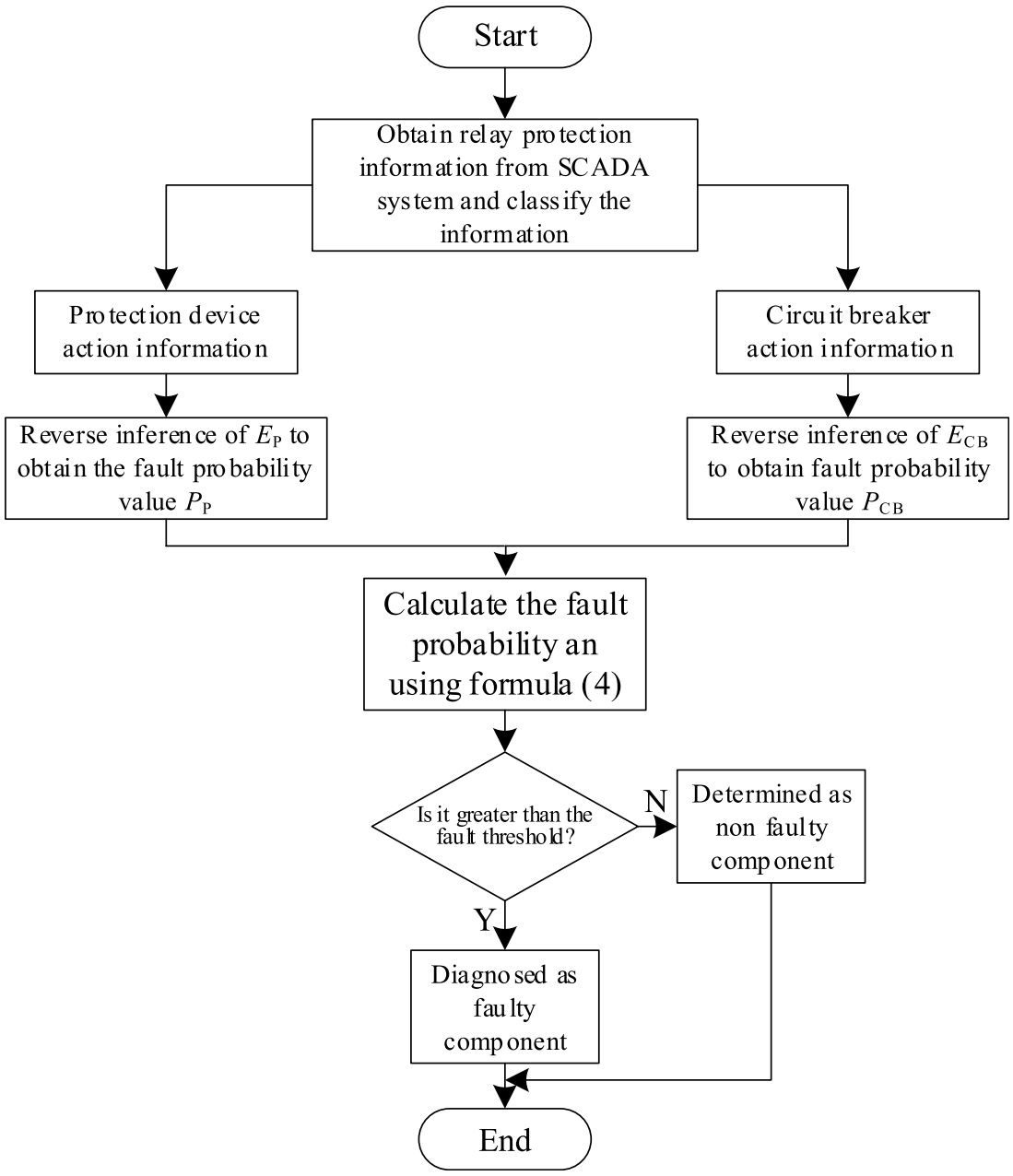

FIGURE 5
Flow of judging the fault component based on D-S evidence theory.

2.4 Bayesian network model for relay protection in distribution networks

When a fault occurs, there is not only a temporal relationship but also a certain logical relationship between protection device action and circuit breaker action in the relay protection of distribution networks. Normally, the distribution network protection will act after a component failure, and it will cause the circuit breaker to trip after the protection has acted, thus enabling fault isolation. Based on the

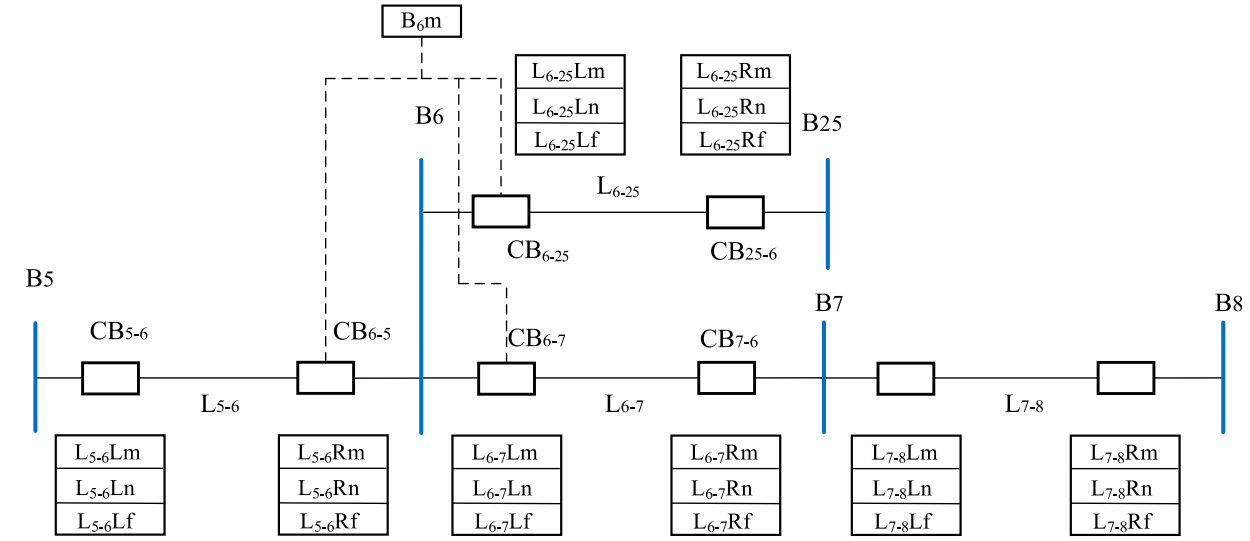

FIGURE 6
Part topology of the DC distribution network and its protection configuration.

TABLE 3 Relay protection action information in scene 1.

Number	Time	Circuit breaker/ protection	State
1	17:20: 42:560	$L_{6\text{-}7}m$	Operation
2	17:20: 42:623	$CB_{7\text{-}6}$	Tripped
3	17:20: 42:676	$CB_{6\text{-}7}$	Tripped

relay protection action logics, the Bayesian network model for relay protection is shown in Figure 2. The network nodes are connected to each other according to the relay protection action logic in the following order: "component–main protection–near-backup protection–near-end breaker–far-backup protection–far-end breaker.". The state of each node is represented by "0" and "1" in the Bayesian network model. For component nodes, the "normal" working state is indicated by "0" and the "fault" state by "1;" for circuit breakers and protection nodes, their "inactive" state is indicated by "0" and their "active" state by "1."

The component nodes of a traditional Bayesian network model structure are only connected to protection nodes, and circuit breaker nodes only play a role in connecting various types of protection nodes, which makes the action information on circuit breakers have less influence on the diagnostic role of faulty components in the Bayesian network.

3 Fault diagnosis of the distribution network based on the D-S evidence theory Bayesian network

In this section, we improve the structure of the traditional Bayesian network model to enhance the influence of circuit breaker information on component fault diagnosis. The results of the backward inference of each Bayesian network are fused using D-S evidence theory to calculate the fault probability of each component in the fault area and infer the faulty component. Then, Bayesian forward inference is used to obtain the protection device and circuit breaker for rejection and misoperation.

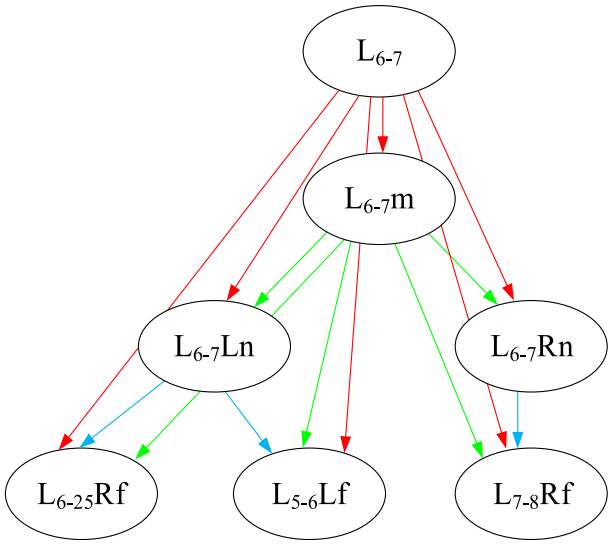

FIGURE 7
Bayesian network model for protection information on line $L_{6\text{-}7}$.

3.1 Improved Bayesian network model structure

The information obtained in traditional SCADA systems can be divided into two main categories, one for protection action information and the other for circuit breaker action information,

TABLE 4 Relay protection action information in scene 2.

Number	Time	Circuit breaker/protection	State
1	13:44:17:247	B_6m	Operation
2	13:44:17:276	$CB_{6\text{-}25}$	Tripped
3	13:44:17:295	$CB_{6\text{-}5}$	Tripped
4	13:44:17:312	$CB_{6\text{-}7}$	Tripped

TABLE 5 Relay protection action information in scene 3.

Number	Time	Circuit breaker/protection	State
1	15:27:33:768	$L_{6\text{-}7}$m	Operation
2	15:27:33:806	$CB_{6\text{-}7}$	Tripped
3	15:27:33:897	$L_{7\text{-}8}$Rf	Operation
4	15:27:33:943	$CB_{8\text{-}7}$	Tripped

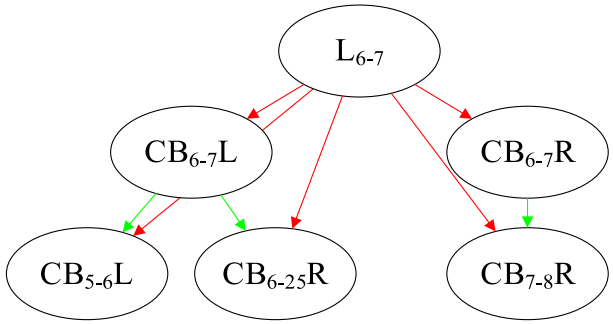

FIGURE 8
Bayesian network model for circuit breaker information on line $L_{6\text{-}7}$.

TABLE 6 Analysis of diagnostic results in scene 3.

Component	Methods		Diagnostic result
	M_t (%)	M_p (%)	
$L_{6\text{-}7}$	97.52	99.06	$L_{6\text{-}7}$ fault $CB_{7\text{-}6}$ reject
$L_{7\text{-}8}$	73.54	20.14	
B_7	11.71	1.42	

so Bayesian networks can be built for each of these two types of information.

1) The Bayesian network model corresponding to the protection action information is shown in Figure 3. The connection sequence of the structure is "component–main protection–near-backup protection–far-backup protection."
2) The Bayesian network model corresponding to the circuit breaker action information is shown in Figure 4. The connection sequence of its structure is "component–near-end circuit breaker (triggered by the action of main protection or near-backup protection)–far-end circuit breaker (triggered by the action of far-backup protection)."

In the case of a distribution network, when the main protection (near backup protection) is triggered and the near-end circuit breaker does not trip, the remote backup protection operates to isolate the fault by tripping the remote-end circuit breaker. In this scenario, the remote-end circuit breaker node is considered a leaf node in the Bayesian network model. However, when the state of the remote backup protection node is "1," the diagnostic result for the faulty component remains the same, regardless of whether the remote-end circuit breaker node is in state "1" or "0." Therefore, this paper proposes a novel Bayesian network model that classifies the nodes in the traditional relay protection Bayesian network model based on the type of information, distinguishing between protection information and circuit breaker information. The model is established according to the respective operating logics. This approach allows for a more intuitive analysis of the faulty components and reduces the dependency of circuit breaker nodes on protection nodes in the Bayesian network. Moreover, even in cases where some protection information is missing, the investigation of suspected faulty components within the fault area can still be carried out based on circuit breaker information.

According to expert knowledge, test data, and equipment history information, the Bayesian network is assigned to determine the prior probability of each component node and the conditional probability of relay protection node in a power system. The probability assignment of component nodes is shown in Table 1, and the conditional probability assignment of relay protection devices and circuit breaker nodes is shown in Table 2 (Yiquan et al., 2020). The conditional probabilities of the protection nodes of various components of the power system are similar, the conditional probabilities of several types of relay protection can be easily selected, and the conditional probability values of the remaining nodes in the system network can be calculated by analogy.

3.2 D-S evidence theory

The two types of information Bayesian network models are used to obtain the component failure probabilities under the respective network models by Bayesian backward inference, which requires the application of D-S evidence theory for failure probability fusion.

The D-S evidence theory is a theory of imprecise reasoning that can transform propositions into mathematical sets for analysis. Assuming that there is a problem that needs to be judged, if all the consequences that can be caused by a specific event can be exhaustively listed, it is denoted as set U. In D-S evidence theory, U is

TABLE 7 Analysis of diagnostic results in scene 4.

Number	Time	Circuit breaker/ protection	State
1	19:17: 29:510	$L_{6\text{-}7}Rm$	Operation
2	19:17: 29:626	$CB_{7\text{-}6}$	Tripped
3	19:17: 29:772	$L_{5\text{-}6}Lf$	Operation
4	19:17: 29:852	$L_{6\text{-}25}Rf$	Operation
5	19:17: 29:972	$CB_{5\text{-}6}$	Tripped
6	19:17: 30:074	$CB_{25\text{-}6}$	Tripped

called the identification framework, and the elements in U are finite and incompatible with each other.

If the function m: $2^U \rightarrow [0,1]$ satisfies the condition

1) $m(\varnothing) = 0$, $\varnothing$ is an empty set
2) $\sum_{A \subset U} m(A) = 1$

Then, $m(A)$ is called the basic probability assignment function of A. A function Bel: $2^U \rightarrow [0,1]$ that satisfies the condition: $Bel(A) = \sum m(B)(\forall A \subset U)$ is defined, which represents the sum of the basic probability assignments of all subsets in the recognition framework. This function is called a trust function on U. If K is an element on set U and its basic probability assignment function is greater than 0, then K can be considered the focal element of the trust function Bel. A likelihood function $Pl_c(A) = \sum m(B)$ is defined, and we can note that $Pl_c(A) \geq Bel_c(A)$, where $Bel(A)$ is the lower limit of A and $Pl(A)$ is the upper limit of A.

Assuming that set U has trust functions Bel_1 and Bel_2, and its basic probability assignment functions are m_1 and m_2, $A_1, A_2, \ldots, A_k$ and $B_1, B_2, \ldots, B_r$ are the corresponding focal elements. When $K < 1$, the combination rule of D-S evidence theory is shown in Eq. 3.

$$m(C) = \begin{cases} \dfrac{\sum\limits_{\substack{i,j \\ A_i \cap B_j = C}} m_1(A_1) m_2(B_j)}{1 - K} & \forall C \subset U, C \neq \varnothing \\ 0 & C \neq \varnothing \end{cases} \quad (3)$$

where $K < 1$; K is the conflict factor, which expresses the degree of conflict between different lines of evidence and can be divided into two situations.

(1) When $K \neq 1$, then m determines a basic probability assignment.

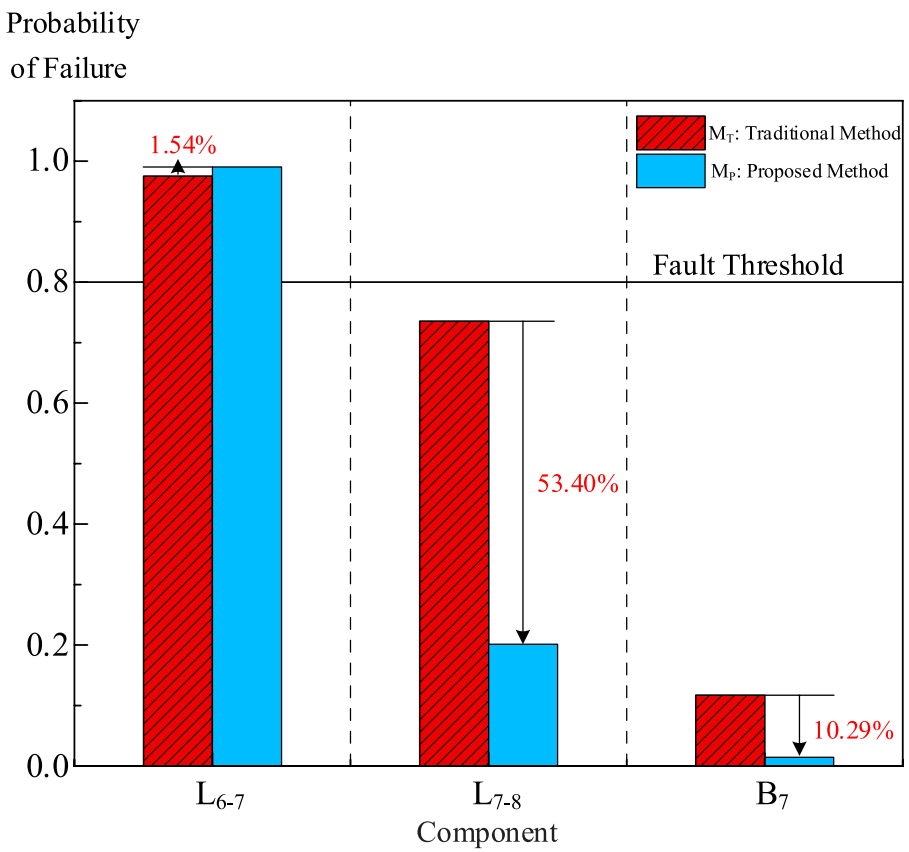

FIGURE 9
Comparison of calculation results between the two methods in scene 3.

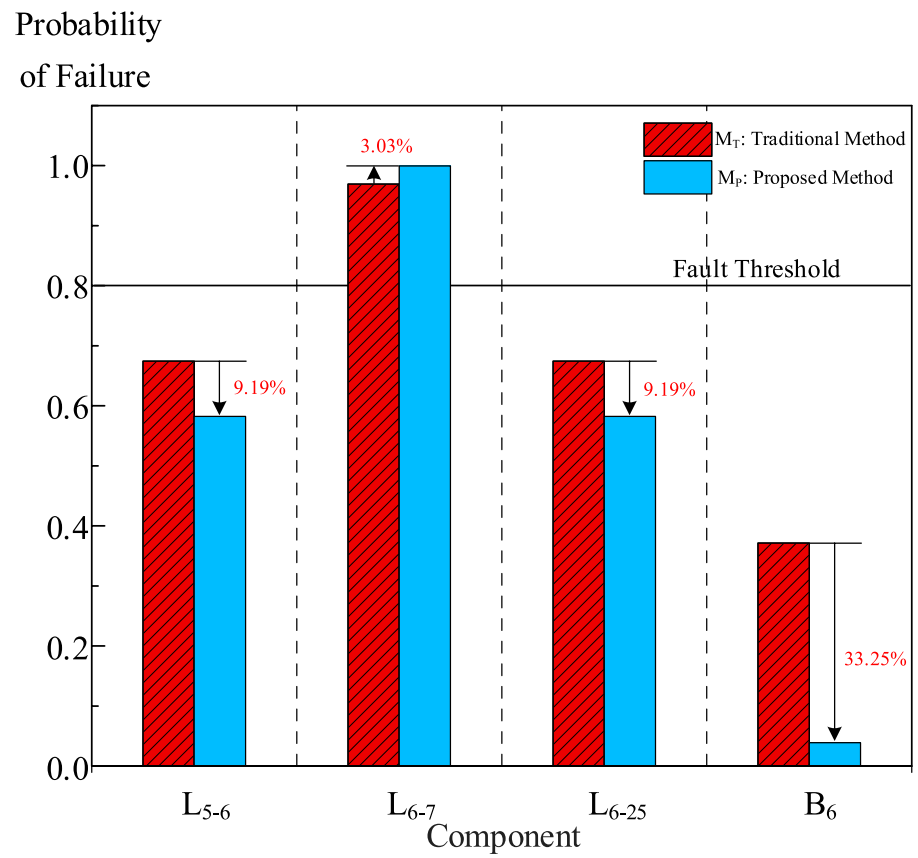

FIGURE 10
Comparison of calculation results between the two methods in scene 4.

(2) When K = 1, it can be determined that m_1 and m_2 are mutually exclusive and cannot be fused using D-S evidence theory.

3.3 Identifying faulty components

The Bayesian network model of protecting information and circuit breaker information corresponds to two mutually independent lines of evidence in D-S evidence theory; each line of evidence will derive a corresponding probability of fault information by Bayesian backward inference, combining the two-component fault probability information according to the D-S evidence theory rules. The fused equation is shown in Eq. 4.

$$P(X=1)=\frac{P_{CB}(X=1)\times P_P(X=1)}{\left(\begin{array}{c}[P_{CB}(X=1)\times P_P(X=1)]+\\ [P_{CB}(X=0)\times P_P(X=0)]\end{array}\right)}, \quad (4)$$

where P_{P} and P_{CB} represent the probability values under the Bayesian network model for protection information and circuit breaker information, respectively; X represents the corresponding parent node of each Bayesian network, i.e., the component node (bus or line node).

Since each component of the power system network can build its own Bayesian network, each component can only appear in its own Bayesian network. The fault probability of each component fused after backward inference is defined as a_n; the threshold for line faults is 0.8 (Yiquan et al., 2020) and for bus faults is 0.6 (Luo and Tong, 2015). It is determined that the component is a faulty component when a_n is greater than or equal to the threshold of the corresponding component. The fault component judgment process based on D-S evidence theory is shown in Figure 5.

3.4 Analysis of the action behavior of protective devices and circuit breakers

The posterior probability of each node in the faulty component is found corresponding to the protection information Bayesian network model and circuit breaker information Bayesian network model, according to Bayesian forward inference with prior probability assignment, i.e., the expected action probability of each protection device node and circuit breaker node in the case of component failure is known. The specific steps are as follows.

Step 1: The protection information Bayesian network model and circuit breaker information Bayesian network model corresponding to the identified faulty component are found, and the parent node (component node) is set in both Bayesian network models to state "1," i.e., the component is faulty.

TABLE 8 Analysis of diagnostic results in scene 4.

Component	Methods		Diagnostic result
	M_1 (%)	M_2 (%)	
$L_{5\text{-}6}$	67.43	58.24	$L_{6\text{-}7}$ fault $L_{6\text{-}7}$Lm reject
$L_{6\text{-}7}$	96.92	99.95	
$L_{6\text{-}25}$	67.43	58.24	
B_6	37.14	3.89	

Step 2: The forward inference of the Bayesian algorithm is made for the Bayesian network model of protection information and circuit breaker information to calculate the action expectation of the corresponding protection device and circuit breaker in the case of faults.

Step 3: The expected action probability of the protection device and circuit breaker obtained through Bayesian forward inference is compared with the actual situation E of the protection device and circuit breaker action to obtain the difference Δm, which is the basis for judging the action of protective devices and circuit breakers. The discrimination method is shown in (Eq. 5).

$$\begin{cases} -a \le \Delta m \le b & \text{Normal} \\ \Delta m \le -a & \text{Misoperation} \\ \Delta m \ge b & \text{Rejection} \end{cases}, \tag{5}$$

where a, $b \in (0,1)$, and $a + b = 1$, where both a and b are taken as 0.5 in this paper.

4 Example analysis

Based on the MATLAB R2018a simulation platform, part of the distribution network structure shown in Figure 1 is selected to verify the correctness of the proposed method, and its topology structure is shown in Figure 6. Meanwhile, the traditional Bayesian network algorithm is compared with the information fusion method based on the Bayesian network proposed in this paper.

4.1 Normal operation of relay protection

In the case of the normal operation of relay protection, this paper designs line faults (scene 1) and bus faults (scene 2) to verify the superiority of the method proposed.

Scene 1: Line $L_{6\text{-}7}$ fault, $CB_{6\text{-}7}$ and $CB_{7\text{-}6}$ tripped; specific relay protection action information is shown in Table 3.

A brief explanation of the method proposed in this paper according to scene 1 is provided as an example. There is only one component in the fault area according to the topology structure of the distribution network and relay protection action information, i.e., line $L_{6\text{-}7}$; two Bayesian network models of line $L_{6\text{-}7}$ are shown in Figures 7, 8, and the final fault probability obtained was 89.89% through the D-S evidence fusion method, while the fault probability obtained by the traditional method was 98.65%. For line faults, the method proposed in this paper improves the accuracy by 8.76% compared to traditional methods.

TABLE 9 Relay protection action information in scene 5.

Number	Time	Circuit breaker/ protection	State
1	08:45: 26:121	$L_{5\text{-}6}$Rp	Operation
2	08:45: 26:245	$CB_{6\text{-}5}$	Tripped
3	08:45: 26:327	$L_{6\text{-}25}$Rf	Operation
4	08:45: 26:486	$L_{6\text{-}7}$Rf	Operation
5	08:45: 26:537	$CB_{7\text{-}6}$	Tripped
6	08:45: 26:623	$CB_{25\text{-}6}$	Tripped

Scene 2: Bus B_6 fault, $CB_{6\text{-}5}$, $CB_{6\text{-}7}$, and $CB_{6\text{-}25}$ tripped. The specific relay protection action information is shown in Table 4.

For fault scene 2, the same method as in fault scene 1 was used to establish a Bayesian network model, resulting in a bus fault probability of 99.99%, while the result obtained using the traditional Bayesian inference method was 95.06%. The method proposed in this paper improves the accuracy by 4.93% compared to traditional methods. The method in this paper is better than the traditional method in a normal situation, where there is no rejection or misoperation of the relay protection from the fault probability results of the line and bus.

4.2 Abnormal operation of relay protection

Incorrect parameter settings of relay protection, aging or damage of the relay protection equipment itself, and other factors may cause relay protection to reject and misoperate. This paper sets three types of fault scenes to verify the accuracy of fault diagnosis under the abnormal operation of relay protection.

Scene 3: Line $L_{6\text{-}7}$ fault, $CB_{7\text{-}6}$ refused to operate, relevant backup protection acted and triggers the circuit breaker to trip. The specific relay protection action information is shown in Table 5.

There are four components in the fault area according to the topology structure of the distribution network and relay protection action information, i.e., line $L_{6\text{-}7}$, line $L_{7\text{-}8}$, and bus B_7. The corresponding Bayesian network models are built for these components, and their probabilities are calculated for the traditional method (M_t) and the proposed method in this paper (M_p). A comparison of the two methods is shown in Figure 9 and Table 6.

The Bayesian network of protection information and circuit breaker information corresponding to the fault component does forward inference, according to the rules of relay protection behavior criterion after determining the fault element is line $L_{6\text{-}7}$. The results of the protection and circuit breaker behavior calculations show that $CB_{7\text{-}6}$ is rejection. The fault diagnosis result is the line $L_{6\text{-}7}$ fault, and $CB_{7\text{-}6}$ refuses to operate, which is consistent with the present scene.

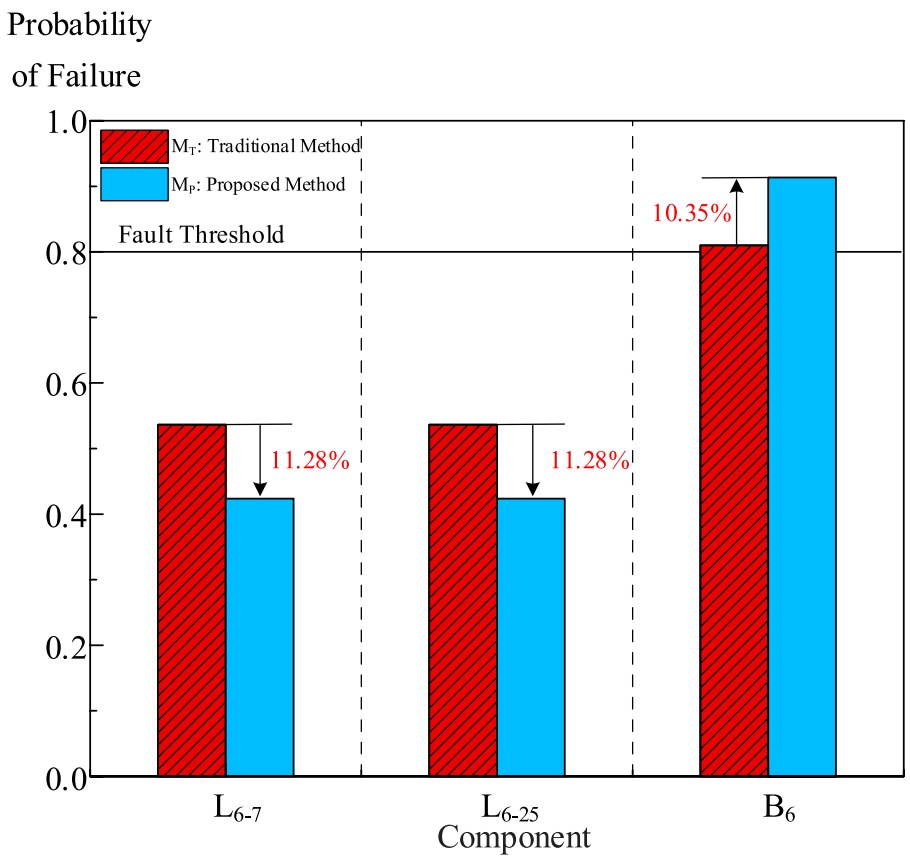

FIGURE 11
Comparison of calculation results between the two methods in scene 5.

TABLE 10 Analysis of diagnostic results in scene 5.

Component	Methods		Diagnostic results
	M_t (%)	M_p (%)	
L_{6-7}	53.64	42.36	B_6 fault B_6m reject
L_{6-25}	53.64	42.36	
B_6	80.99	91.34	

Scene 4: Line L_{6-7} fault, main protection L_{6-7}Lm refuses to operate, and the relevant backup protection operates and triggers the circuit breaker to trip; the specific relay protection action information is shown in Table 7. The results of the component fault and comparison of two methods are shown in Figure 10 and Table 8, respectively.

Scene 5: Bus B_6 fault, B_6m refuses to operate, relevant backup protection acted and triggered the circuit breaker to trip; the specific relay protection action information is shown in Table 9. The results of the component fault and comparison of two methods are shown in Figure 11 and Table 10, respectively.

When abnormal operation of relay protection occurs, the comparison of the calculation results of the above fault scenes shows that the method proposed in this paper can not only improve the fault probability value of faulty components but also reduce the fault probability value of non-faulty components, making fault diagnosis more favorable.

4.3 Component fault diagnosis in the absence of relay protection information

During the transmission of relay protection action information to the SCADA system, multiple data routes may result in missing information in the SCADA system, which can have an impact on component fault diagnosis. For this reason, some relay protection information loss in scenes 3–5 is used as an example. Table 11 shows the fault diagnosis results of the three methods.

The calculation results given in Table 11 show that when some relay protection information is missing, the traditional method can no longer diagnose the fault, while the proposed method can diagnose the fault component. For fault scene 4, the SCADA system is missing circuit breaker action information, i.e., CB_{5-6} information is missing. Traditional fault diagnosis methods cannot identify fault lines due to the absence of circuit breaker action information, but this method can identify faults, and the same is true for fault scene 5. It shows that the proposed method has better anti-interference ability and robustness than the traditional algorithm.

TABLE 11 Fault diagnosis results for the bus with a lack of information.

Scene	Missing information	Component	M_t		M_p	
			Probability value (%)	Diagnostic result	Probability value (%)	Diagnostic result
3	$L_{7\text{-}8}Rf$	$L_{6\text{-}7}$	89.84	$L_{6\text{-}7}$ fault	95.64	$L_{6\text{-}7}$ fault
		$L_{7\text{-}8}$	53.24		45.36	
		B_7	56.38		49.71	
4	$CB_{5\text{-}6}$	$L_{5\text{-}6}$	32.36	Undetected fault	24.55	$L_{6\text{-}7}$ fault
		$L_{6\text{-}7}$	57.68		88.76	
		$L_{6\text{-}25}$	32.36		24.55	
		B_6	23.86		19.62	
5	$L_{6\text{-}7}Rf$	$L_{6\text{-}7}$	46.82	Undetected fault	35.19	B_6 fault
		$L_{6\text{-}25}$	46.82		35.19	
		B_6	47.75		81.16	

5 Conclusion

This article proposes a distribution network fault diagnosis based on D-S evidence theory, which realizes the diagnosis of components and relay protection behavior after a fault occurs in the distribution network. The following conclusions are obtained.

(1) Based on the action logic of the protection and circuit breaker, Bayesian network models were established separately, increasing the number of Bayesian networks to enable the independent analysis of fault diagnosis results from two levels, protection information and circuit breaker information, thereby improving the accuracy of fault diagnosis.
(2) The distributed fault diagnosis of "distributed diagnosis, centralized fusion" is realized by combining two Bayesian networks with D-S evidence theory.
(3) It can not only diagnose the fault when the relay protection is not correct but also diagnose the fault component correctly when the relay protection information is missing and has strong robustness.

This article mainly focuses on the fusion method of D-S evidence theory and applies Bayesian network inference in the actual fault diagnosis of power grids. However, as the research deepens, the impact of fault timing on the diagnosis results has not been considered in the fault diagnosis process of this article. It should be focused on in the next research work.

Data availability statement

The original contributions presented in the study are included in the article/Supplementary Material; further inquiries can be directed to the corresponding author.

Author contributions

XW: writing–original draft. HZ: writing–review and editing. WX: writing–review and editing. WP: writing–review and editing. QJ: writing–review and editing. XH: writing–review and editing.

Funding

The author(s) declare that financial support was received for the research, authorship, and/or publication of this article.

Conflict of interest

Authors XW, HZ, WX, and QJ were employed by State Grid Zhejiang Electric Power Co., Ltd., Lishui Power Supply Company. Author WP was employed by State Grid Zhejiang Electric Power Co., Ltd. Author XH was employed by Nanjing Nanrui Jibao Engineering Technology Co., Ltd.

The authors declare that this study received funding from the Unveiling and Leadership Project supported by State Grid Zhejiang Electric Power Co., Ltd. (research on the "Three Lines of Defense" System Architecture and Fault Defense Technology of Distribution Networks under High Power Penetration, B311LS230007). The funder had the following involvement in the study: design, analysis.

Publisher's note

References

Biao, X. U., Xianggen, Y. I. N., Zhang, Z., and Xusheng, L. I. Time Petri net based Fault Diagnosis model considering topology structure. *Proc. CSEE*, 2019, 39(9): 2723–2735. doi:10.13334/j.0258-8013.pcsee.172381

Daobing, L., Yingying, G., Shichun, L., Miaosheng, B., Yue, Q., and Yucen, L. (2024). Analytical model of power grid Fault Diagnosis considering main protection range of three-section line protection[J/OL]. *Power Syst. Technol.*, 1–8. doi:10.13335/j.1000-3673.pst.2022.1173

Dongmei, Z., Zhang, X., Juan, W., Weichen, L., and Dongying, Z. (2014). Power grid Fault Diagnosis aiming at reproducing the fault process. *Proc. CSEE* 34 (13), 2116–2123. doi:10.13334/j.0258-8013.pcsee.2014.13.013

Dongyuan, S., Guojiang, X., Jinfu, C., and Yinhong, L. (2014). Divisional Fault diagnosis of power grids based on RBF neural network and fuzzy integral fusion. *Proc. CSEE* 34 (4), 562–569. doi:10.13334/j.0258-8013.pcsee.2014.04.007

Ferreira, V. H., Zanghi, R., Fortes, M. Z., Sotelo, G., Silva, R., Souza, J., et al. (2016). A survey on intelligent system application to Fault Diagnosis in electric power system transmission lines. *Electr. Power Syst. Res.* 136, 135–153. doi:10.1016/j.epsr.2016.02.002

Guojiang, X., Dongyuan, S., Lin, Z., and Xiangwen, C. (2014). Fuzzy cellular Fault Diagnosis of power grids based on radial basis function neural network. *Automation Electr. Power Syst.* 38 (5), 59–65. doi:10.7500/AEPS20130603005

He, X., Tong, X., and Sun, M. (2011). Distributed power system Fault Diagnosis based on bayesian network and dempster-shafer evidence theory. *Automation Electr. Power Syst.* 35 (10), 42–47.

Luo, X., and Tong, X. (2015). Structure-variable bayesian network for power system Fault Diagnosis considering credibility. *Power Syst. Technol.* 39 (9), 2658–2664. doi:10.13335/j.1000-3673.pst.2015.09.043

Pengzhe, R., Youbo, L., Tingjian, L., Peidong, H., Yangfan, Z., and Shuyu, D. (2021). Robust identification algorithm for distribution network topology based on mutual-information bayesian network. *Automation Electr. Power Syst.* 45 (9), 55–62. doi:10.7500/AEPS20200818001

Sun, Q. Y., Wang, C. L., Wang, Z. L., and Liu, X. (2013). A Fault Diagnosis method of smart grid based on rough sets combined with genetic algorithm and tabu search. *Neural Comput. Appl.* 23 (7-8), 2023–2029. doi:10.1007/s00521-012-1116-x

Wang, T., Liu, W., Cabrera, L. V., Wang, P., Wei, X., and Zang, T. (2022). A novel fault diagnosis method of smart grids based on memory spiking neural P systems considering measurement tampering attacks. *Inf. Sci.* 596, 520–536. doi:10.1016/j.ins.2022.03.013

Weixing, Z., Nan, X., Nan, N., Yihong, L., Zhanji, G., and Haiqing, L. (2021). Multi-layer intelligent Fault Diagnosis method of power grid based on multi-source information fusion. *South. POWER Syst. Technol.* 15 (9), 9–15. doi:10.13648/j.cnki.issn1674-0629.2021.09.002

Wenwu, L., Weijun, Z., Hui, L., Yabing, Y., Guoqin, D., Xuan, W., et al. (2021). A rough set-based bio-inspired fault diagnosis method for smart substation protection equipment. *Power Syst. Prot. Control* 49 (21), 132–140. doi:10.19783/j.cnki.pspc.210041

Xialin, L., Li, G., Di, H., Yiqi, Z., and Chengshan, W. (2019). Research review on operation and Control of DC distribution networks. *High. Volt. Eng.* 45 (10), 3039–3049. doi:10.13336/j.1003-6520.hve.20190924002

Xuechen, J., Dazhi, W., Yi, N., and Cuiling, Z. (2017). Query method for optimal diagnosis of power system faults. *High. Volt. Eng.* 43 (4), 1311–1316. doi:10.13336/j.1003-6520.hve.20170328031

Yang, F., and Yongjin, Y. U. (2020). Fault diagnosis of distribution network based on time constrained hierarchical fuzzy Petri nets. *Power Syst. Prot. Control* 48 (2), 99–106. doi:10.19783/j.cnki.pspc.190200

Yiquan, L., Shaolin, J., Genghui, Z., Wei, L., Qingrui, T., Qian, T., et al. (2020). A new method to deduce complex fault of power grid based on Bayesian network. *Power Syst. Prot. Control* 48 (4), 57–63. doi:10.19783/j.cnki.pspc.190451

Yu, W., Changbao, X. U., Zhu, J., et al. (2021). Grid fault diagnosis method for multi-source information fusion based on improved Petri net and Hilbert transform. *Electr. Meas. & Instrum.* 58 (6), 125–129. doi:10.19753/j.issn1001-1390.2021.06.018

Yuyang, L. I., Zengping, WANG, and Qiao, Z. (2021). Distributed Fault section location for ADN based on bayesian complete analytic model and multi-factor dimension reduction. *Power Syst. Technol.* 45 (10), 3917–3927. doi:10.13335/j.1000-3673.pst.2020.1622

Zhang, Q., Ma, W., Li, G., Ding, J., and Xie, M. (2022). Fault diagnosis of power grid based on variational mode decomposition and convolutional neural network. *Electr. Power Syst. Res.* 208, 107871. doi:10.1016/j.epsr.2022.107871

Zhang, Q., Ma, W., Li, G., Xie, M., and Shao, Q. (2021). Partition Fault diagnosis of power grids based on improved PNN and GRA. *IEEJ Trans. Electr. Electron. Eng.* 16 (1), 57–66. doi:10.1002/tee.23268

Zhang, X., Du, M., Wang, Y., Zhang, H., and Guo, Y. (2023). Research on power grid Fault Diagnosis based on a quantitative representation of alarm information. *IEEE Trans. Industrial Electron.* 70 (9), 9582–9592. doi:10.1109/tie.2022.3213893

frontiers | Frontiers in Energy Research

TYPE Original Research
PUBLISHED 22 October 2024
DOI 10.3389/fenrg.2024.1418907

OPEN ACCESS

EDITED BY
Chaolong Zhang,
Jinling Institute of Technology, China

REVIEWED BY
Yuyan Zhang,
Yanshan University, China
Zhiyou Wu,
Chongqing Normal University, China

*CORRESPONDENCE
Jiacheng Liao,
202111183@huat.edu.cn

RECEIVED 17 April 2024
ACCEPTED 21 June 2024
PUBLISHED 22 October 2024

CITATION
Sun Z and Liao J (2024), Application of intelligent self-organizing algorithms in UAV cooperative inspection of power distribution networks.
Front. Energy Res. 12:1418907.
doi: 10.3389/fenrg.2024.1418907

Application of intelligent self-organizing algorithms in UAV cooperative inspection of power distribution networks

Zeyu Sun[1] and Jiacheng Liao[2]*

[1]Ningxia Communication Technical College, Yinchuan, China, [2]School of Economics and Management, Hubei Institute of Automobile Technology, Shiyan, China

In the rapidly evolving technological landscape, the advent of collaborative Unmanned Aerial Vehicle (UAV) inspections represents a revolutionary leap forward in the monitoring and maintenance of power distribution networks. This innovative approach harnesses the synergy of UAVs working together, marking a significant milestone in enhancing the reliability and efficiency of infrastructure management. Despite its promise, current research in this domain frequently grapples with challenges related to efficient coordination, data processing, and adaptive decision-making under complex and dynamic conditions. Intelligent self-organizing algorithms emerge as pivotal in addressing these gaps, offering sophisticated methods to enhance the autonomy, efficiency, and reliability of UAV collaborative inspections. In response to these challenges, we propose the MARL-SOM-GNNs network model, an innovative integration of Multi-Agent Reinforcement Learning, Self-Organizing Maps, and Graph Neural Networks, designed to optimize UAV cooperative behavior, data interpretation, and network analysis. Experimental results demonstrate that our model significantly outperforms existing approaches in terms of inspection accuracy, operational efficiency, and adaptability to environmental changes. The significance of our research lies in its potential to revolutionize the way power distribution networks are inspected and maintained, paving the way for more resilient and intelligent infrastructure systems. By leveraging the capabilities of MARL for dynamic decision-making, SOM for efficient data clustering, and GNNs for intricate network topology understanding, our model not only addresses current shortcomings in UAV collaborative inspection strategies but also sets a new benchmark for future developments in autonomous infrastructure monitoring, highlighting the crucial role of intelligent algorithms in advancing UAV technologies.

KEYWORDS

unmanned aerial vehicle, intelligent self-organizing algorithms, power distribution networks, component-multi-agent reinforcement learning, self-organizing maps, graph neural networks

1 Introduction

In the rapidly evolving landscape of industrial and technological advancements, the use of UAVs for collaborative inspection of power distribution networks has emerged as a transformative approach Liu et al. (2020), offering unprecedented efficiency and precision. This innovative strategy leverages the autonomy, flexibility, and coordinated

efforts of multiple UAVs, enabling extensive coverage of vast and often inaccessible geographic areas with reduced labor costs and improved safety. The capability of UAVs to navigate difficult terrains where human inspectors might face risks underscores the revolutionary potential of this technology in maintaining critical infrastructure Wang et al. (2019). However, the practical implementation of such collaborative UAV inspections is not without its hurdles. Challenges encompass a range of operational issues from path planning and dynamic task allocation to collaborative decision-making and adapting to environmental changes Shakhatreh et al. (2019), all crucial for the seamless execution of surveillance and inspection missions. These obstacles highlight the need for sophisticated solutions that can ensure efficient, safe, and effective UAV collaboration in complex environments.

With the rapid advancement of artificial intelligence (AI) and machine learning technologies, intelligent self-organizing algorithms have become pivotal in enhancing the efficiency and intelligence of collaborative UAV inspections Keneni et al. (2019); He et al. (2024). These sophisticated algorithms empower UAVs to autonomously collaborate in the absence of centralized control, facilitating the efficient execution of intricate tasks through direct local interactions. Techniques such as reinforcement learning, neural networks, and agent-based models are at the forefront of this innovation, optimizing path planning Khan and Al-Mulla (2019); Shen et al. (2024), task assignment, and inter-UAV cooperation. By leveraging AI, UAVs gain the capability to accurately identify and classify objects and obstacles, learn and refine flight paths and behaviors dynamically, and enhance environmental perception Ahmed et al. (2022). This enables smarter decision-making in the face of complex and uncertain conditions. The convergence of AI with machine learning and deep learning algorithms opens new avenues for UAVs to adapt and evolve based on environmental feedback and mutual information exchange, significantly improving the system's overall efficacy. As AI technology continues to advance, its application in UAV collaborative inspections is poised to drive substantial progress and innovation in the maintenance of power distribution networks, heralding a future of increased operational excellence.

Although intelligent self-organizing algorithms show unprecedented possibilities for collaborative UAV inspections, there are still some limitations in existing research. First, the robustness and scalability of many algorithms in real complex environments have not been fully verified Ferdaus et al. (2019). For example, existing models may have difficulty in handling real-world uncertainties and dynamic changes, such as sudden weather changes or unexpected geographic obstacles Liu et al. (2019). Second, algorithms in current research often require large amounts of data for training and optimization, which may be difficult to achieve in practice, especially in scenarios where data collection is costly or data is difficult to obtain Ning et al. (2024a). In addition, transparency and interpretability regarding the decision-making process of algorithms is also a key issue in research Horváth et al. (2021), which affects the reliability of algorithms in real-world applications and users' trust in them. Therefore, although intelligent self-organizing algorithms open up new possibilities for collaborative UAV inspections, further research and development is still needed to overcome these limitations and realize their full potential in practical applications.

Building on the shortcomings identified in previous works, we propose the MARL-SOM-GNNs network model, a novel integration designed to overcome the limitations of current drone cooperative inspection strategies for power distribution networks. This section elaborates on the roles of each model MARL, SOM), and Graph Neural Networks GNNs and describes how they synergistically function to enhance the inspection process.

The MARL component enables dynamic decision-making and coordination among multiple drones, optimizing inspection paths and task allocations through learning from interactions within the environment. This is crucial for navigating the complex and often unpredictable landscapes of power distribution networks. The SOM algorithm processes and clusters the high-dimensional data collected during inspections, enhancing data visualization and interpretation, which is vital for identifying critical points of interest. Meanwhile, GNNs model the intricate relationships within the power distribution network, allowing for precise analysis of its structure and the efficient planning of inspection routes.

The synergy of MARL, SOM, and GNNs in our network model presents a comprehensive solution that addresses the key challenges in drone cooperative inspections. By combining the strengths of each model, our approach ensures adaptive, efficient, and targeted inspections, significantly reducing the time and resources required for maintaining power distribution networks. Moreover, this integrated model facilitates a proactive maintenance strategy, capable of identifying potential issues before they lead to failures, thereby enhancing the resilience and reliability of the power infrastructure.

To provide a comprehensive overview of the current state of the art and justify our technical selection, we present a literature review Table 1 describing the advantages and disadvantages of various methods relevant to UAV-based inspections of power distribution networks. Due to space constraints the technologies in the table are shown in abbreviated form, with the full names listed below: Reinforcement Learning (RL), Convolutional Neural Networks (CNN), Graph Neural Networks (GNN), Self-Organizing Maps (SOM), Support Vector Machines (SVM), Random Forests (RF).

The significance and advantages of this model lie in its holistic approach to the challenges of drone-based power distribution network inspections. It not only automates the inspection process but also ensures that the inspections are conducted in a manner that is both thorough and resource-efficient. This innovation represents a significant step forward in the application of intelligent self-organizing algorithms to critical infrastructure maintenance, setting a new standard for the field and opening up avenues for further research and development.

In conclusion, our contributions to the advancement of UAV collaborative inspections for power distribution networks are detailed as follows:

- We have developed an integrated MARL-SOM-GNNs network model that uniquely combines Multi-Agent Reinforcement Learning, Self-Organizing Maps, and Graph Neural Networks. This integration significantly enhances the drones' abilities in autonomous decision-making, sophisticated data analysis, and

TABLE 1 Literature review of technical selection.

Technique	Advantages	Disadvantages
RL	Adaptive decision-making, learns optimal policies through trial and error	Requires significant computational resources and extensive training data
CNN	High accuracy in image recognition and classification	Computationally intensive, requires large datasets for training
GNN	Effective in modeling relational data, captures network topology	Complex implementation, high computational cost
SOM	Efficient data clustering and visualization, enhances interpretability	May struggle with very high-dimensional data, requires careful tuning of parameters
SVM	Robust in classification tasks, effective with small datasets	Less effective with large-scale, high-dimensional data, requires careful kernel selection
RF	High accuracy, robust to overfitting, handles large datasets well	Can be slow with large datasets, less interpretable than some other models

comprehensive network topology understanding, leading to more effective and accurate inspection processes.

- Our research addresses critical challenges such as dynamic task allocation, intricate path planning, and robust inter-UAV communication, which have hindered the efficiency of UAV collaborative inspections. By implementing our model, we demonstrate marked improvements in the efficiency and reliability of surveillance activities, ensuring that power distribution networks are maintained with unprecedented precision.
- Through rigorous testing and validation on both real-world and simulated datasets, our work not only validates the effectiveness of the MARL-SOM-GNNs model but also sets a foundational framework for future exploration. The practical insights and methodologies derived from our study contribute to the evolving field of intelligent autonomous systems, offering a significant leap forward in the application of AI technologies for the maintenance and resilience of essential infrastructure.

2 Related work

2.1 Deep Q-Networks (DQN) in drone surveillance of power distribution networks

The integration of DQN into the drone-based surveillance of power distribution networks marks a significant leap forward in autonomous inspection technologies. DQN combines the depth of neural networks with the reinforcement learning prowess of Q-learning algorithms, creating a powerful tool that enables drones to navigate and make decisions autonomously in complex environments Zhu et al. (2022). This technology allows for the optimization of inspection paths and the avoidance of obstacles, utilizing deep learning to directly process and learn from high-dimensional sensory inputs without the need for manual feature extraction Xu (2023). The application of DQN in this domain not only enhances the efficiency of drone operations but also improves the accuracy and reliability of surveillance tasks, enabling power distribution networks to be monitored more effectively and with less human intervention.

While DQN's application heralds a new era in autonomous drone surveillance, its performance is not without challenges. The model's tendency to overestimate action values occasionally leads to the selection of suboptimal policies Gao et al. (2019). This issue becomes more pronounced in environments characterized by unpredictability—a common feature of power distribution networks. Furthermore, the extensive data required for DQN training underscores a resource-intensive process, potentially slowing adaptation to new environments Yun et al. (2022). Additionally, managing the replay buffer to mitigate sequential data correlations introduces a delicate balance between memory efficiency and system performance.

2.2 Convolutional neural networks (CNN) for image-based inspection

CNN have revolutionized the field of image-based inspection in power distribution systems, thanks to their exceptional ability to process and analyze visual information. By leveraging CNNs, drones are equipped to autonomously inspect power distribution equipment, using advanced image recognition to detect faults and anomalies within captured images. This approach capitalizes on CNN's adeptness at identifying patterns and features across various layers of the network, facilitating precise fault identification and classification Miao et al. (2021). The automation of such tasks significantly reduces the time and labor traditionally required for manual inspections, enhancing the operational efficiency and reliability of power distribution maintenance processes Ning et al. (2024b). Moreover, CNNs' application in drone surveillance introduces a scalable and effective solution for monitoring extensive power infrastructure, contributing to the overall stability and safety of electrical systems.

Despite these advantages, CNN-based inspection systems face significant hurdles. The effectiveness of a CNN is deeply tied to the diversity and volume of its training data. Amassing a comprehensive dataset that accurately represents the variety of conditions power distribution components may encounter is both expensive and time-consuming Dorafshan et al. (2018). Variability in environmental conditions such as lighting and background can further complicate the model's ability to generalize its findings, necessitating additional adjustments or training for deployment in new settings. The high computational demands of CNNs also present challenges for real-time processing on drones with limited onboard capabilities Ren et al. (2020).

2.3 Support vector machines (SVM) for fault detection

Implementing SVM in the context of fault detection within power distribution networks through drone inspections represents a methodical advancement in diagnostic accuracy and efficiency Baghaee et al. (2019). SVM, a robust supervised learning model, excels in classification tasks by creating a hyperplane that best separates different classes in the input space, making it particularly suitable for distinguishing between normal and fault conditions in power infrastructure. By analyzing sensor data or images captured by drones, SVM models contribute to the early identification of potential issues, facilitating preemptive maintenance actions Saari et al. (2019); Goyal et al. (2020). This capability is pivotal for enhancing the reliability of power distribution networks, ensuring uninterrupted service and reducing the risk of catastrophic failures. The precision and adaptability of SVM in handling diverse data types underscore its utility in modern inspection strategies, where timely and accurate fault detection is paramount Han et al. (2021).

However, the application of SVM in this context is not devoid of limitations. As the complexity of input data escalates, especially with high-resolution images or intricate sensor data, SVM models may face computational bottlenecks, affecting their efficiency Cui et al. (2020). The selection of an appropriate kernel function and its parameters, crucial for SVM's performance, demands a high level of expertise and trial-and-error, posing additional challenges. Moreover, SVM's scalability is tested when confronted with large datasets, a common scenario in extensive surveillance operations Yuan et al. (2020).

2.4 Random forests for vegetation management

The application of Random Forest algorithms for vegetation management in proximity to power lines illustrates a strategic use of machine learning to enhance the safety and reliability of power distribution networks Zaimes et al. (2019). By processing aerial imagery and LiDAR data collected by drones, Random Forest models can accurately identify vegetation that poses a risk to power lines, classifying and predicting encroachment with high precision. This ensemble learning method, which aggregates the decisions of multiple decision trees Ramos et al. (2020), mitigates the risk of overfitting while bolstering predictive accuracy. Such capability is crucial for preemptively addressing vegetation growth that could lead to power outages or fires, thereby maintaining the integrity of electrical infrastructure. Random Forest's effectiveness in this domain is a testament to its versatility and robustness Loozen et al. (2020), providing utility companies with a powerful tool for risk assessment and mitigation in vegetation management operations.

Despite its effectiveness, the application of Random Forests in managing vegetation encroachment highlights the need for high-quality, accurately labeled training data—a process that can be exceedingly laborious Wan et al. (2019). The model's performance in highly imbalanced datasets, where certain vegetation types are rare, may also be compromised. Additionally, the intricacies of Random Forests' decision-making process can obscure the understanding of how specific features influence predictions Nguyen et al. (2019), presenting a barrier to transparent assessment and interpretation.

3 Method

3.1 Overview of our network

In this section, we introduce the MARL-SOM-GNNs network model, an advanced and novel integration of MARL, SOM and GNNs. This model is specifically designed to enhance the efficiency and effectiveness of UAV collaborative inspections of power distribution networks.

Our MARL-SOM-GNNs network model integrates three cutting-edge technologies to address the unique challenges of inspecting power distribution networks. MARL facilitates real-time, adaptive decision-making among multiple UAVs, enabling decentralized coordination and improving operational efficiency and flexibility in inspections. SOM are employed to process and visualize high-dimensional inspection data, simplifying complexity and aiding in the identification and prioritization of critical areas. GNNs provide a detailed understanding of the power network's topology, enabling more efficient route planning and inspection. The integration of these technologies addresses the specific challenges of power distribution systems, characterized by extensive, complex, and geographically dispersed infrastructures requiring regular and detailed inspections to ensure reliability and prevent failures.

SOM is utilized to process and visualize high-dimensional data collected by UAVs. This method simplifies the complexity of large-scale inspection data, allowing UAVs to quickly identify and prioritize critical areas. The innovative aspect of integrating SOM lies in its ability to enhance the interpretability of complex data, thus improving the decision-making process for UAVs in real-time inspections. GNNs are employed to model and analyze the relational data of power distribution networks. By understanding the topological structure of the network, GNNs enable UAVs to plan and execute more efficient and comprehensive inspection routes. The novelty here is in applying GNNs to dynamically model the power network's structure, which is essential for optimizing inspection paths and ensuring thorough coverage. The MARL-SOM-GNNs network model is intricately linked to the specific challenges and requirements of power distribution systems. Power distribution networks are characterized by their extensive, complex, and often geographically dispersed infrastructures. These networks require regular and detailed inspections to ensure reliability and prevent failures.

In the context of power systems, MARL allows UAVs to adapt to the dynamic conditions of the power grid environment, such as changing weather conditions or unexpected obstacles. This adaptability is crucial for maintaining the reliability and efficiency of power distribution. SOM helps manage the vast amount of inspection data generated by UAVs, organizing it into a coherent and actionable format. This capability is vital for quickly identifying potential issues such as equipment wear or vegetation encroachment, which could affect the power supply. GNNs provide a detailed understanding of the power network's topology, enabling UAVs to navigate and inspect the network more effectively. This detailed network analysis ensures that all critical components are

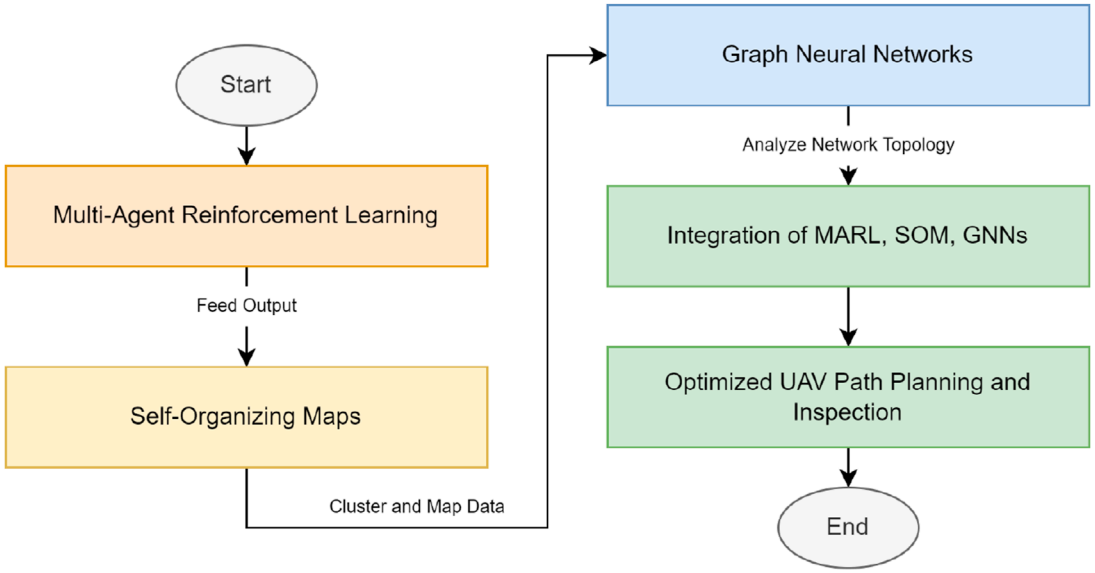

FIGURE 1
Architectural diagram of the MARL-SOM-GNNs network model.

inspected, reducing the risk of undetected faults and enhancing the overall resilience of the power infrastructure.

The MARL-SOM-GNNs model offers a comprehensive and innovative solution for UAV-based inspections, optimizing the process and setting a new standard for intelligent infrastructure management. The integrated approach not only boosts efficiency and accuracy but also reduces operational costs and deployment time. By harnessing the combined strengths of MARL, SOM, and GNNs, this model represents a significant step forward in autonomous inspection technologies, providing adaptability to complex environments and a robust framework for future advancements.

To visually comprehend the interplay and functional integration of these components within our model, refer to the structural diagram provided in Figure 1. This diagram illustrates the sequential and collaborative workflow of MARL, SOM, and GNNs within our integrated system. Additionally, we present Algorithm below, outlining the step-by-step process of our proposed model's operation.

The significance of this integrated model lies in its holistic approach to UAV-based power distribution network inspections. By harnessing the combined strengths of MARL, SOM, and GNNs, our model not only boosts inspection efficiency and accuracy but also reduces operational costs and deployment time. This integrated approach marks a significant step forward in autonomous inspection technologies, offering enhanced adaptability to complex environments and providing a robust framework for future advancements in intelligent infrastructure management. The synergy achieved through this integration is pivotal, as it significantly elevates the model's capabilities beyond what could be achieved by the sum of its individual parts, setting a new benchmark for autonomous UAV inspections in the power distribution sector.

3.2 MARL

Multi-Agent Reinforcement Learning (MARL) is an advanced reinforcement learning paradigm that involves multiple agents simultaneously learning to navigate and interact within a shared environment. Each agent seeks to maximize its own cumulative reward through trial and error, learning from the consequences of its actions. The core challenge of MARL lies in the agents' need to account for the actions and strategies of other agents Oroojlooy and Hajinezhad (2023), whose behavior may also be evolving. This inter-agent interaction introduces a level of complexity far beyond single-agent scenarios, as the optimal strategy for one agent may change based on the strategies adopted by others. Agents in MARL settings must therefore learn not only to adapt to the static features of the environment but also to dynamically adjust their strategies in response to the actions of other agents Du and Ding (2021). This dynamic adjustment is often facilitated through mechanisms like policy gradient methods, value-based learning, or actor-critic approaches Cui et al. (2019), which enable agents to evaluate the effectiveness of their actions in complex, multi-agent contexts.

MARL involves multiple agents learning to optimize their behaviors through interactions within a shared environment. Each agent i seeks to maximize its cumulative reward R_i over time.

The reward R_i is defined as:

$$R_i = \sum_{t=0}^{T} \gamma^t r_t$$

where r_t is the reward at time step t, $\gamma \in [0,1]$ is the discount factor, and T is the total number of time steps.

The policy $\pi(a|s)$ represents the probability of taking action $a$given the state s. The goal is to find the optimal policy π^* that

Input: GRSS Dataset, ISPRS Dataset
Output: Trained MARL-SOM-GNNs model, Evaluation Metrics
Initialize MARL, SOM, GNNs with random weights;
Set learning rate $\alpha = 0.001$;
Set batch size $B = 128$;
Set termination condition: max_epochs = 100;
Initialize lists for tracking losses: $loss_{MARL}$, $loss_{SOM}$, $loss_{GNNs}$;
for *epoch* ← 1 **to** *max_epochs* **do**
 for *each batch* (X,Y) *in GRSS Dataset and ISPRS Dataset* **do**
 //Forward Pass
 $outputs_{MARL} \leftarrow \text{MARL}(X)$;
 $outputs_{SOM} \leftarrow \text{SOM}(X)$;
 $outputs_{GNNs} \leftarrow \text{GNNs}(X)$;
 //Calculate Loss
 $loss_{MARL} \leftarrow \text{Loss}_\text{F}\text{unction}(outputs_{MARL}, Y)$;
 $loss_{SOM} \leftarrow \text{Loss}_\text{F}\text{unction}(outputs_{SOM}, Y)$;
 $loss_{GNNs} \leftarrow \text{Loss}_\text{F}\text{unction}(outputs_{GNNs}, Y)$;
 //Backward Pass
 Update MARL weights using gradients of $loss_{MARL}$;
 Update SOM weights using gradients of $loss_{SOM}$;
 Update GNNs weights using gradients of $loss_{GNNs}$;
 end
 //Evaluate Performance
 Calculate evaluation metrics on validation set;
 if *validation loss does not improve* **then**
 break;
 end
end
return *Trained MARL-SOM-GNNs model, Evaluation Metrics: Accuracy, F1-score, Precision, Recall*;

Algorithm 1. Training Process for MARL-SOM-GNNs.

maximizes the expected cumulative reward:

$$\pi^* = \arg\max_{\pi} \mathbb{E}\left[\sum_{t=0}^{T} \gamma^t r_t | \pi\right]$$

We utilize the actor-critic approach, where the actor updates the policy π and the critic evaluates the action by estimating the value function $V(s)$:

$$V(s) = \mathbb{E}\left[\sum_{t=0}^{T} \gamma^t r_t | s_t = s, \pi\right]$$

The actor updates the policy using the policy gradient method:

$$\nabla_\theta J(\pi_\theta) = \mathbb{E}_{\pi_\theta}\left[\nabla_\theta \log \pi_\theta(a|s)(R - V(s))\right]$$

In our research, MARL's contribution lies in its ability to enable a group of drones to conduct cooperative inspection tasks within power distribution networks efficiently Zhang et al. (2021). This efficiency is realized through the strategic interaction of drones, where each drone operates as an independent agent within the MARL framework. The integration with GNN and SOM offers a multi-faceted approach to solving the inspection problem.

The combination of MARL with GNN brings a significant advantage in handling the spatial complexity of power distribution networks. GNN models can capture the relational information between different nodes (e.g., power poles, transformers) in the network, providing a structured representation of the environment for the MARL agents. This structured information allows the drones to understand not just their immediate surroundings but also the broader network context, enabling them to make more informed decisions about where to inspect next. The agents' ability to make these informed decisions in a complex environment is crucial for optimizing inspection paths and ensuring comprehensive coverage of the network.

The integration with SOM enhances MARL's capability by providing an efficient way to cluster and interpret the vast amounts of data generated during inspection missions. SOM can reduce the dimensionality of data, highlighting patterns and features that are critical for decision-making. This process helps in mapping high-dimensional sensory data to lower-dimensional spaces, making it easier for MARL agents to recognize states and adapt their strategies accordingly. In practice, this means that drones can quickly identify critical areas needing inspection, prioritize tasks more effectively, and adjust their flight paths dynamically, leading to increased operational efficiency and reduced inspection times.

The unique challenges posed by cooperative drone inspection in power distribution networks demand a sophisticated approach like MARL. Traditional single-agent or deterministic algorithms fall short in handling the dynamic interplay between multiple autonomous drones navigating through complex, uncertain environments. MARL stands out by enabling drones to learn from each other's experiences, adapting their strategies in real-time to achieve collective objectives efficiently. This collaborative learning process is not just about avoiding redundant inspections or optimizing individual paths; it's about creating a cohesive system where the collective intelligence of the drone fleet surpasses the sum of its parts.

In our research, the significance of MARL extends beyond technical efficiency. It embodies a shift towards more adaptive, resilient, and intelligent systems capable of tackling the intricate challenges of modern infrastructure maintenance. By harnessing the collective capabilities of MARL, GNN, and SOM, we aim to demonstrate a model where drones can autonomously and intelligently navigate the complexities of power distribution networks, ensuring reliable electricity supply through timely and effective inspection and maintenance. This approach not only highlights the potential of combining these advanced technologies but also sets a precedent for future applications of AI in critical infrastructure management.

3.3 SOM

Self-Organizing Maps (SOM), also known as Kohonen maps, represent a sophisticated approach within the realm of unsupervised learning algorithms. They are designed to transform complex, high-dimensional input data into a more accessible, two-dimensional, discretized representation Clark et al. (2020).

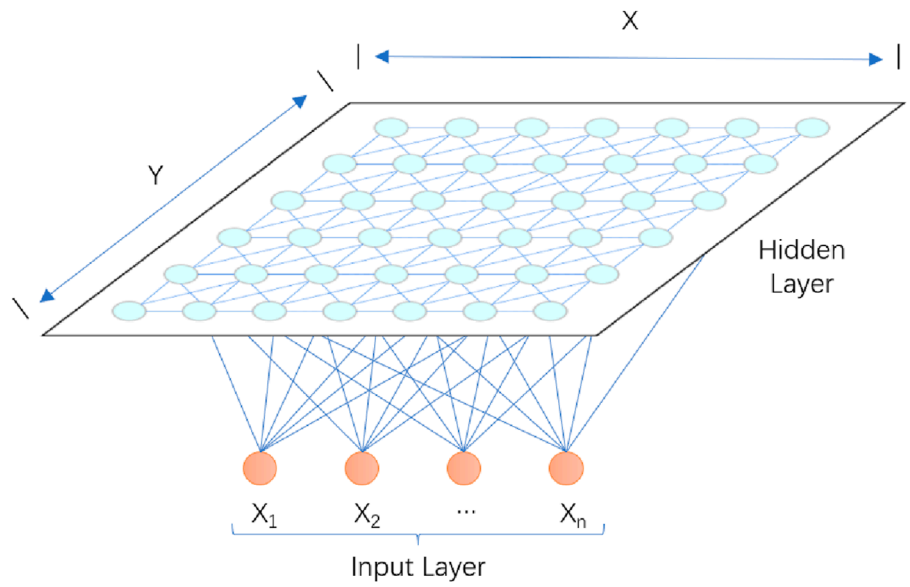

FIGURE 2
The intricate structure of the SOM.

This process preserves the topological features of the original dataset, making SOM particularly effective for visualizing and interpreting high-dimensional data in a way that is straightforward and insightful Wickramasinghe et al. (2019).

Self-Organizing Maps (SOM) are essentially a straightforward yet powerful neural network, consisting solely of an input layer and a hidden layer, where each node within the hidden layer represents a cluster into which the data is organized. The number of neurons in the input layer is determined by the dimensions of the input vector, with each neuron corresponding to one feature Qu et al. (2021). The training process relies on a competitive learning strategy where each input example finds its closest match within the hidden layer, thus activating a specific node known as the "winning neuron" Kleyko et al. (2019); Wang et al. (2024). This neuron and its neighbors are then updated using stochastic gradient descent, with adjustments based on their proximity to the activated neuron. A distinctive feature of SOM is the topological relationship between the nodes in the hidden layer Yu et al. (2021). This topology is predefined by the user; nodes can be arranged linearly to form a one-dimensional model or positioned to create a two-dimensional plane for a more complex representation. The structure of the SOM network varies mainly in the competitive layer, which can be one-dimensional Cardarilli et al. (2019), two-dimensional (the most common), or even higher dimensions. However, for visualization purposes, higher-dimensional competitive layers are less commonly used. This spatial organization allows the SOM to capture and reveal the inherent patterns and relationships within the data, providing a comprehensive and intuitive understanding of the dataset's structure Soto et al. (2021). To better understand the intricate structure of the SOM, Figure 2 provide a visual representation of the network architecture and the functional relationships between its layers, enhancing the explanation of how SOM effectively processes and clusters data.

Given the topology-based structure of the hidden layer, it's pertinent to note that Self-Organizing Maps (SOM) possess the unique capability to discretize input data from an arbitrary number of dimensions into a structured one-dimensional or two-dimensional discrete space. While it is technically possible to organize data into higher-dimensional spaces using SOM, such applications are rare and typically not as common due to the increased complexity and diminished interpretability. The nodes within the computation layer, which play a crucial role in the mapping process, are in a state of full connectivity with the nodes in the input layer, ensuring that each input can influence the map's formation. After establishing topological relationships (a key step in defining the spatial arrangement and interaction patterns of nodes), the calculation process begins, roughly divided into several parts:

1) Initialization: Every node within the network undertakes the process of random parameter initialization. This ensures that the quantity of parameters allocated to each node is precisely aligned with the dimensional attributes of the input.
2) For every input data point, the system seeks out the node that most closely aligns with it. If we consider the input to be of D dimensions, expressed as $X = \{x_1, x_2, \ldots, x_D\}$, then the method for determining the closest node is based on the Euclidean distance, as follows:

$$d_j(\mathbf{x}) = \sum_{i=1}^{D} (x_i - w_{ji})^2$$

here, j represents the index of the node in the system, indicating which node is being evaluated for its distance from the input data point.

3) After identifying the activation node $I(x)$, it's also essential to update the nodes that are in close proximity to it. Let S_{ij}denote

the distance between nodes *i*and *j*. For nodes that are neighbors of $I(x)$, an update weight is allocated to them as follows:

$$T_{j,I(\mathbf{x})} = \exp(-S^2_{j,I(\mathbf{x})}/2\sigma^2)$$

In this context, j represents the index of the neighboring node, while i represents the index of the activation node. Put simply, the extent to which neighboring nodes are updated is discounted based on the proximity of their distance to the activation node. The closer a node is, the more significant its update will be, whereas nodes that are farther away will receive less substantial updates.

4) Following this, the next step involves updating the parameters of the nodes. This is done in accordance with the gradient descent method, iterating the process until convergence is achieved.

$$\Delta w_{ji} = \eta(t).T_{j,I(x)}(t).(x_i - w_{ji})$$

where j represents the index of the node being updated, and i represents the index of the input feature.

In our research, SOM plays a crucial role in efficiently managing and interpreting the vast amounts of data generated during the cooperative drone inspection of power distribution networks. The combination of SOM with MARL and GNN offers a comprehensive approach to addressing the complexities of this task. When integrated with MARL, SOM enhances the ability of drones to make sense of their environment and the status of their inspection tasks. By clustering high-dimensional data into more manageable representations, SOM provides a clear picture of the environment's state, which is essential for the drones to determine their next actions. This clarity is particularly beneficial in dynamic and uncertain environments where drones need to adapt their strategies based on new information. The organized representation created by SOM can help in identifying patterns such as areas that are more prone to faults, thereby allowing the MARL algorithm to prioritize inspection tasks more effectively. The integration of SOM with GNN can significantly improve the model's ability to handle spatial data. GNNs excel at capturing the relationships between entities in a network, such as the connections between different components of a power distribution network. SOM can take this relational data and provide a simplified yet informative representation, highlighting key features and relationships that are critical for the inspection process. This synergy allows for a more nuanced understanding of the network's structure and condition, enabling drones to navigate and inspect the network more efficiently.

The adoption of SOM in our research is pivotal for addressing the challenges associated with cooperative drone inspection of power distribution networks. The primary challenge lies in the processing and interpretation of large-scale, high-dimensional data, which can be overwhelming and impractical for direct analysis. SOM addresses this challenge head-on by offering a way to visually explore and understand complex data patterns, facilitating the identification of crucial insights that can guide the inspection process. Furthermore, the ability of SOM to organize data into a structured, easy-to-interpret map is invaluable for the coordination and strategic planning of drone operations. By providing a clear overview of the data, SOM enables more informed decision-making, ensuring that inspection efforts are focused where they are most needed. This level of efficiency and precision is essential for maintaining the reliability and safety of power distribution networks, underscoring the critical role of SOM in our research. In sum, the integration of SOM into our model encapsulates our commitment to leveraging advanced technological solutions for improving infrastructure inspection and maintenance. By simplifying the complexity of the data involved, SOM not only enhances the performance of the overall model but also paves the way for innovative approaches to managing and optimizing critical infrastructure systems.

3.4 GNNs

Graph Neural Networks (GNNs) represent an innovative deep learning framework, specifically designed to address the unique challenges of data structured as graphs Wu et al. (2020). This capability is particularly relevant in scenarios such as cooperative drone inspections of power distribution networks Yuan et al. (2022), where the network can be modeled as a graph with nodes representing critical points requiring inspection and edges representing potential movement paths for drones. GNNs excel at processing this graph-structured data, identifying optimal inspection paths while accounting for the network's complex relationships and constraints Liao et al. (2021). This capability has enabled GNNs to play a key role in areas such as social network analysis, bioinformatics, and recommender systems, providing a powerful tool for understanding and processing complex relationships in the real world Gama et al. (2020b).

Graph Neural Networks (GNNs) are utilized to model the topological structure of the power distribution network. The network is represented as a graph $G = (V, E)$, where $V$is the set of nodes and E is the set of edges.

Each node $v \in V$ has a feature vector h_v. The feature vectors are updated through message passing, where each node aggregates information from its neighbors:

$$h_v^{(k+1)} = \sigma\left(\sum_{u \in \mathcal{N}(v)} f(h_v^{(k)}, h_u^{(k)}, e_{uv})\right)$$

where $h_v^{(k)}$ is the feature vector of node $v$at iteration k, $\mathcal{N}(v)$ is the set of neighbors of v, e_{uv} is the edge feature between nodes $u$and v, and $\sigma$is an activation function.

The function f typically includes a neural network layer that learns the appropriate aggregation of information. This iterative process captures the dependencies between nodes and their neighbors, allowing the GNN to learn a representation that reflects the graph's structure.

GNNs allow deep learning techniques to be directly applied to a wide array of graph-structured data Gama et al. (2020a), including social networks, molecular structures, and crucially for our research, power distribution networks. The strength of GNNs stems from their capacity to manage and learn from interconnected data, where the relationships between data points significantly influence the overall structure and semantics of the data Liu et al. (2021). At the heart of GNNs' operation is the aggregation of node features,

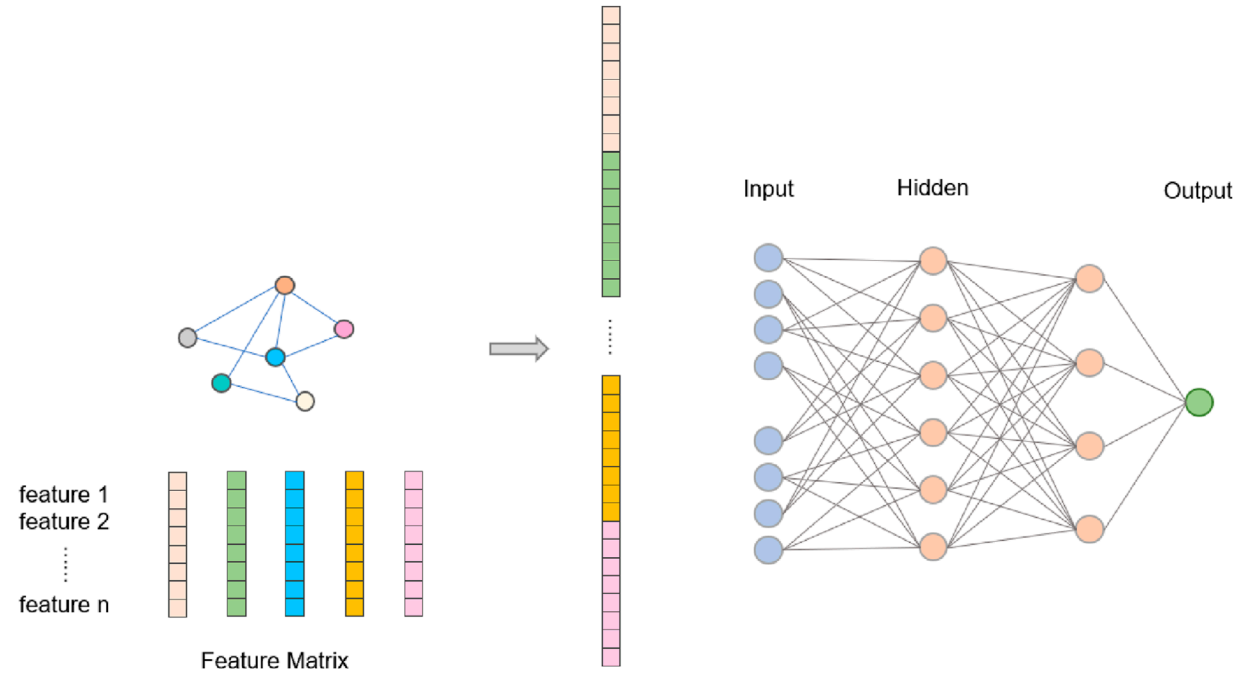

FIGURE 3
The structure of GNNs model.

a process in which the algorithm integrates information from adjacent nodes to update each node's state Bessadok et al. (2022). This involves critical steps such as feature extraction, learning edge weights, and comprehensively synthesizing node information. By learning and understanding the interactions between nodes within the graph, the algorithm enables each node to reflect the state of the entire graph structure more accurately and comprehensively Jiang and Luo (2022). This method of aggregating information based on adjacency relationships allows GNNs to capture complex relationship dynamics and patterns within graph structures exceptionally well. The overall structure of the GNNs model is shown in Figure 3.

By considering the connections and interactions between entities, GNNs effectively reveal underlying patterns and laws, demonstrating superior performance across various applications. This capability places GNNs in a pivotal role across diverse fields, offering a powerful tool for understanding and managing the complex relationships that characterize the real world. Through neural network transformations applied to the features of nodes and edges, considering both their attributes and their connectivity patterns, GNNs facilitate a novel approach to processing graph-structured data. This approach, often referred to as message passing, allows for iterative updating of node representations by incorporating information from their local neighborhoods, thus capturing the global topology of the graph through localized operations.

In the context of our research, GNNs contribute significantly to the overall model's efficiency and effectiveness. By leveraging the structural information of power distribution networks, GNNs can provide a nuanced understanding of the network's topology, which is instrumental in optimizing the routing and task allocation for drone inspections. GNNs complement MARL by providing a structured representation of the environment in which the multiple agents (drones) operate. This representation enables the agents to make informed decisions based on the comprehensive understanding of the network's topology. For example, by understanding the connectivity and importance of different nodes within the network, MARL agents can prioritize inspections of critical components or areas more likely to experience faults, enhancing the overall efficiency and effectiveness of the inspection process. The integration with SOM benefits from GNNs' ability to structure and highlight critical features of the power distribution network. SOM can use the feature representations learned by GNNs to cluster similar regions of the network, identifying patterns or areas that require special attention during inspections. This synergy allows for a more focused inspection strategy, where drones can target areas identified by SOM as high-priority, based on the comprehensive understanding provided by GNNs.

GNNs are crucial for our experiment due to their unique ability to model and analyze the complex, interconnected structure of power distribution networks. The capability to understand and exploit the network topology directly influences the planning and execution of cooperative drone inspections. With GNNs, our model can accurately represent the physical and logical relationships within the network, enabling more strategic planning of inspection routes that minimize redundancy and maximize coverage.

Furthermore, GNNs facilitate the identification of critical network components and potential fault lines, informing the inspection process in a way that traditional models cannot. This level of insight ensures that drones can be dispatched more effectively, focusing on areas of the network that are most vulnerable or crucial to its overall stability. Ultimately, the integration of GNNs into our

model represents a significant advancement in the application of AI techniques to the maintenance and inspection of power distribution networks, promising to enhance the reliability and efficiency of these critical infrastructure systems through more intelligent and informed inspection strategies.

4 Experiments

To validate the effectiveness of our proposed MARL-SOM-GNNs network model, we conducted a series of simulation experiments and included a comparative analysis with existing methods. This section outlines the experimental setup, datasets, evaluation metrics, and the results of our comparative analysis.

4.1 Datasets

We utilized two well-known datasets for our experiments: the IEEE GRSS Data Fusion Contest 2019—Multi-Modal UAV (GRSS) and the ISPRS 2D Semantic Labeling Contest–Vaihingen (ISPRS). These datasets provide a diverse range of scenarios and challenges suitable for evaluating UAV-based inspection methods.

IEEE GRSS Data Fusion Contest 2019—Multi-Modal UAV (GRSS) Dataset Le Saux et al. (2019): This collection presents a series of multimodal datasets gathered via UAVs, incorporating both optical imagery and LiDAR scans, targeting the advancement of 3D reconstruction techniques within both urban and rural settings. The dataset's high-resolution optical images furnish extensive visual details, whereas its LiDAR scans offer invaluable three-dimensional spatial insights. This multifaceted dataset becomes instrumental for research teams aiming to pioneer and evaluate data fusion methodologies suitable for UAV-powered inspections within power distribution frameworks. Through the integration of optical and LiDAR data, UAVs are equipped not only to recognize various power facilities but also to gauge their spatial arrangements and physical conditions, identifying potential issues such as vegetation encroachment on power lines.

ISPRS 2D Semantic Labeling Contest–Vaihingen (ISPRS) DatasetCramer (2010): As part of the 2D Semantic Annotation Competition organized by the International Society for Photogrammetry and Remote Sensing (ISPRS), this dataset provides high-resolution aerial imagery of the Vaihingen area in Germany and its corresponding semantic annotations. The dataset includes detailed annotations for a wide range of ground objects such as buildings, roads, trees, etc., suitable for developing high-precision ground feature recognition techniques. For collaborative UAV inspection of power distribution networks, this dataset can train UAVs to recognize and distinguish key components (e.g., power lines, towers) within power networks from their surroundings. This is crucial for planning the UAV's flight path, avoiding obstacles, and ensuring the accuracy and safety of the inspection work.

4.2 Experimental details

Step 1: Experimental Environment.

For our research, the experimental environment is meticulously designed to ensure a robust and reliable evaluation of the integrated MARL-SOM-GNNs network model. This section details the setup of our experimental environment, including the hardware specifications, software configurations, and the dataset used for training and testing our model.

Our experiments were conducted on high-performance computing clusters equipped with NVIDIA Tesla V100 Gpus, each providing 32 GB of memory to meet the intensive computing needs of our model. The system is powered by an Intel Xeon Gold 6230 CPU (2.10 GHz) and 192 GB RAM, ensuring fast processing and efficient processing of large data sets. In order to meet the high efficiency of training, we use the graph neural network acceleration operation.

Software Configurations: We utilize Python 3.8 as our primary programming language, due to its extensive support for machine learning libraries and frameworks. Our model is implemented using PyTorch 1.8, chosen for its flexibility and dynamic computational graph, which is particularly beneficial for implementing complex models like ours. For the reinforcement learning component, we rely on the stable-baselines3 library for its robust implementation of MARL algorithms. Additional data preprocessing and analysis are performed using SciPy and NumPy, while Matplotlib and Seaborn are used for data visualization.

By establishing a comprehensive experimental environment with specific hardware and software configurations, along with a richly annotated dataset, we ensure that our model is trained and evaluated under optimal conditions. This setup not only facilitates the development of an effective and efficient inspection model but also provides a solid foundation for replicable and scalable research in the field of UAV collaborative inspections for power distribution networks.

Step 2: Dataset Processing.

In our study, ensuring the data is primed for model training and evaluation is paramount. To achieve this, we will undertake a comprehensive data preprocessing strategy, outlined as follows:

Data Cleaning: Our first step involves meticulously removing any irrelevant, incomplete, or erroneous data entries that could skew our model's performance. This includes filtering out outlier values that fall beyond the 1.5 IQR (Interquartile Range) of the dataset's quartiles, as well as handling missing values either by imputation—using the median or mean for numerical data and mode for categorical data—or by discarding records with missing values if they constitute less than 5% of our dataset. This step is crucial for maintaining the integrity and reliability of our subsequent analysis.

Data Standardization: Given the heterogeneity in the measurement scales across different variables, standardization is essential. We will apply Z-score normalization to transform the data into a common scale with a mean of 0 and a standard deviation of 1. This normalization ensures that our model is not biased toward variables with larger scales and facilitates a more efficient learning process.

Data Splitting: To rigorously assess the performance of our MARL-SOM-GNNs network model, we will divide our dataset into three distinct sets: 70% for training, 15% for validation, and 15% for testing. This split is designed to provide a robust framework for model training, while also allocating sufficient data

for tuning hyperparameters (validation set) and evaluating the model's generalizability on unseen data (test set).

Feature Engineering: In this step, we aim to enhance the model's predictive power by creating new features from the existing data. This may involve generating polynomial features to capture non-linear relationships, or performing Principal Component Analysis (PCA) to reduce dimensionality while retaining the most informative aspects of the data. By carefully selecting and engineering features, we optimize the input data for our model, ensuring it has access to the most relevant and impactful information for making accurate predictions.

Through these meticulous preprocessing steps, we lay a solid foundation for our model, ensuring the data is clean, standardized, appropriately partitioned, and richly featured for optimal training and evaluation.

Step 3: Model Training.

In our study, the model training process is meticulously structured to optimize the performance of the integrated MARL-SOM-GNNs network model. Here's how we proceed with each critical step:

Network Parameter Settings: For the MARL component, we configure the learning rate at 0.01 and set the discount factor (γ) to 0.95, facilitating a balance between immediate and future rewards. The exploration rate in the σ-greedy strategy starts at 1 and decays to 0.01 over 100,000 steps to ensure a comprehensive exploration-exploitation trade-off. For the GNN part, we use a learning rate of 0.001 and employ a two-layer architecture with 64 and 32 hidden units, respectively. The SOM grid is configured to a size of 10×10 units, with an initial learning rate of 0.5, decreasing exponentially over 50 training epochs.

Model Architecture Design: Our model architecture is designed to facilitate efficient learning and accurate predictions. The MARL framework utilizes a Deep Q-Network (DQN) with two hidden layers, each consisting of 128 neurons, and ReLU activation functions to ensure non-linearity in decision-making. The GNN component comprises two graph convolutional layers that enable the model to capture the complex interdependencies within the power distribution network. Finally, the SOM component is implemented with a flexible architecture to adapt to the varying dimensions of the input data, ensuring effective feature mapping and clustering.

Model Training Process: The training process unfolds over 200 epochs, with each epoch consisting of 1000 simulation steps to ensure comprehensive learning across diverse scenarios. We employ a mini-batch gradient descent approach with a batch size of 32 for optimizing the network parameters, which strikes a good balance between computational efficiency and training speed. To avoid overfitting, we implement early stopping based on the validation set performance, monitoring the loss and halting the training if no improvement is observed for 10 consecutive epochs. Additionally, we utilize a dropout rate of 0.2 in the MARL and GNN components to further regularize the model.

By carefully calibrating the network parameters, thoughtfully designing the model architecture, and adhering to a strategic training process, we ensure that our MARL-SOM-GNNs network model is robustly trained to tackle the challenges of UAV collaborative inspections in power distribution networks, maximizing efficiency and accuracy.

Step 4: Indicator Comparison Experiment.

In this stage of our research, we plan to identify and employ a range of widely recognized models for both regression and classification purposes. Each model will be systematically trained and tested using identical datasets to ensure consistency. Following this, we will conduct a thorough comparison of the models' performance, drawing on metrics including accuracy, recall, F1 score, and AUC to evaluate their efficacy across various tasks and data scenarios. A detailed explanation of each metric used for evaluation is presented subsequently. By elucidating these variables and their corresponding metrics, we aim to furnish a clearer understanding of how model performance is evaluated, emphasizing the aspects of accuracy, reliability, computational demand, and efficiency:

4.2.1 Accuracy

$$\text{Accuracy} = \frac{\text{TP} + \text{TN}}{\text{TP} + \text{TN} + \text{FP} + \text{FN}} \times 100\%$$

In this formula, TP denotes instances correctly identified as positive, while TN refers to instances accurately recognized as negative. Conversely, FP and FN represent instances incorrectly labeled as positive and negative, respectively.

4.2.2 Recall

$$\text{Recall} = \frac{\text{TP}}{\text{TP} + \text{FN}} \times 100\%$$

TP is the count of positives correctly identified, and FN is the count of positives mistakenly marked as negatives, thus measuring the model's ability to identify all relevant instances.

4.2.3 F1 score

$$\text{F1 Score} = \frac{2 \times \text{Precision} \times \text{Recall}}{\text{Precision} + \text{Recall}} \times 100\%$$

Precision assesses the accuracy of positive predictions, and Recall examines the model's success in identifying positive instances, combining them to evaluate the model's balance between precision and recall.

4.2.4 AUC

$$\text{AUC} = \int_0^1 \text{ROC}(x)dx^{\oplus} \times 100\%$$

The AUC is derived from the ROC curve, which plots the true positive rate against the false positive rate at various threshold levels, represented by x, thus providing an aggregate measure of model performance across all thresholds.

4.2.5 Parameters (M)

This is quantified as the total number of tunable parameters within the model, expressed in millions, indicating the model's complexity and capacity for learning.

TABLE 2 Comparison of Accuracy, Recall, F1 Score, and AUC performance of different models on GRSS Dataset and ISPRS Dataset.

Model	GRSS dataset				ISPRS dataset			
	Accuracy	Recall	F1 sorce	AUC	Accuracy	Recall	F1 sorce	AUC
Ahmad et al. (2022)	89.98	88.90	83.74	84.91	89.7	85.32	84.55	90.94
Qin and Pournaras (2023)	84.94	84.21	85.65	83.49	93.80	87.74	83.57	85.96
Khalil et al. (2023)	88.34	86.48	87.83	87.18	84.43	83.13	87.36	87.79
Sinnemann et al. (2022)	90.54	85.53	82.46	82.99	89.09	82.17	86.74	82.89
Ours	93.39	90.93	92.22	94.30	96.21	91.86	90.35	91.99

4.2.6 Inference time (ms)

This metric measures the duration required by the model to make a single prediction or inference, given in milliseconds, highlighting the model's efficiency during operation.

4.2.7 Flops (G)

The count of floating-point operations the model necessitates for a single inference, presented in billions, serves as an indicator of the computational demand of the model.

4.2.8 Training time (s)

This refers to the total time taken for the model to complete its training process, measured in seconds, offering insight into the computational efficiency of the training phase.

4.3 Experimental results and analysis

To provide a comprehensive comparison, we included the following existing methods in our analysis: the models developed by Ahmad et al., Qin et al., Khalil et al., and Sinnemann et al. These methods represent state-of-the-art approaches in UAV-based inspection and offer a robust benchmark for evaluating our model.

In our experimental analysis, we rigorously evaluated the performance of our proposed model against several established models to showcase its efficacy across two distinct datasets: the GRSS Dataset and the ISPRS Dataset. We compared our model with other developed models, focusing on key performance metrics such as Accuracy, Recall, F1 Score, and AUC.

The results, as summarized in Table 2, clearly demonstrate the superior performance of our model. On the GRSS Dataset, our model achieved the highest Accuracy at 93.39%, significantly outperforming the next best result by Ahmad et al., which recorded an Accuracy of 89.98%. Similarly, our model excelled in Recall, achieving 90.93%, which not only surpasses Ahmad et al.'s 88.9% but also markedly outperforms the lower scores of other competitors. The F1 Score and AUC further underscore the robustness of our approach, with our model scoring 92.22% and 94.3% respectively, both highest among the evaluated models.

Transitioning to the ISPRS Dataset, the strengths of our model become even more pronounced. It achieved an astounding Accuracy of 96.21%, which is significantly higher than that of Qin et al., who recorded the second-highest Accuracy at 93.8%. In terms of Recall, our model again leads with 91.86%, compared to Qin et al.'s 87.74%. The trend continues with the F1 Score and AUC, where our model scores 90.35% and 91.99% respectively, surpassing all other models by a considerable margin. This indicates that this model outperformed the others in overall performance (Figure 4).

In addition to evaluating the Accuracy, Recall, F1 Score, and AUC of various models on the GRSS and ISPRS datasets, we conducted a comprehensive assessment of performance indicators including Parameters (M), Flops (G), Inference Time (ms), and Training Time (s). This multi-dimensional performance testing provides a more holistic view of each model's capabilities and efficiency in real-world scenarios.

As detailed in Table 3, our analysis of these operational and computational metrics further underscores the superiority of our MARL-SOM-GNNs network model over competing models. On the GRSS Dataset, our model boasts the lowest parameters at 333.40 M, which significantly reduces the computational load compared to the next lowest, Sinnemann et al., at 386.92 M. The trend is consistent in the ISPRS Dataset where our model again requires the fewest parameters (351.98 M) and the lowest Flops (4.27G), ensuring that it operates more efficiently than models requiring up to 792.84 M parameters and 8.21G Flops, such as Ahmad et al.'s model.

Our model's Inference Time is notably faster, registering at only 6.34 ms on the GRSS Dataset and 6.07 ms on the ISPRS Dataset, which is essential for time-critical UAV applications. This performance is superior to that of Khalil et al., who recorded 7.78 ms and 7.86 ms, respectively. Furthermore, the Training Time of our model is the shortest among all evaluated models, standing at 351.46 s for GRSS and even shorter, at 341.09 s, for ISPRS, which highlights our model's quick adaptability and readiness for deployment.

These results are visualized in Figure 5, which effectively illustrates the comparative performance across these critical metrics, offering a clear and immediate visual representation of our model's efficiency and effectiveness in handling UAV-based inspection tasks.

To rigorously evaluate the individual contributions of each component within our integrated MARL-SOM-GNNs network model, we have designed a comprehensive ablation study. This study focuses on conducting controlled experiments using the GRSS Dataset and the ISPRS Dataset, where we systematically remove one component at a time—either MARL, SOM, or GNNs—to

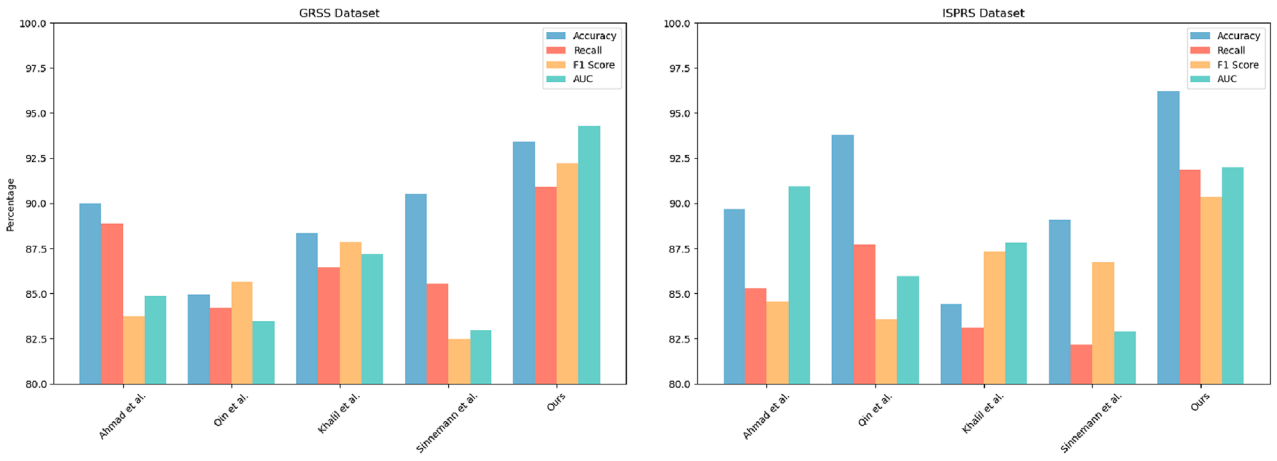

FIGURE 4
Comparison of model performance on different datasets.

TABLE 3 Comparison of Parameters(M), Flops(G), Inference Time (ms), and Training Time(s) performance of different models on GRSS Dataset and ISPRS Dataset.

Model	GRSS dataset				ISPRS dataset			
	Parameters	Flops	Inference time	Trainning time	Parameters	Flops	Inference time	Trainning time
Ahmad et al	500.11	8.21	8.53	422.83	792.84	8.21	12.62	663.97
Qin et al	654.61	8.69	12.77	646.11	692.84	7.98	11.28	788.61
Khalil et al	476.95	5.58	7.78	451.79	426.30	6.00	7.86	440.80
Sinnemann et al	386.92	4.70	7.34	388.44	397.25	5.27	7.10	391.94
Ours	333.40	4.38	6.34	351.46	351.98	4.27	6.07	341.09

assess its specific impact on the model's overall performance. This methodological approach allows us to precisely quantify the influence of each component, elucidating their respective roles within the integrated system. By employing these datasets, which are rich in geographic and semantic diversity, we aim to demonstrate the adaptability and efficacy of our model in processing and analyzing complex spatial data. This ablation study is essential for highlighting how each individual component contributes to enhancing the model's predictive accuracy, interpretability, and overall synergy, which is critical in advancing research in geospatial and image recognition fields.

The results of this ablation study are summarized in Table 4, where the performance metrics such as Accuracy, Recall, F1 Score, and AUC are detailed for each variant of the model on both datasets. The data reveals that the full integration of MARL, SOM, and GNNs achieves the highest scores across all metrics, indicating the complementary effectiveness of the components when combined. Specifically, the full model shows an Accuracy of 90.51% and an AUC of 91.04% on the GRSS Dataset, and an Accuracy of 89.63% and an AUC of 89.90% on the ISPRS Dataset. In contrast, the models without MARL, SOM, or GNNs exhibit notably lower performance across these metrics. For example, removing MARL results in a decrease in Accuracy to 88.23% on GRSS and 87.68% on ISPRS, while eliminating SOM leads to Accuracies of 89.34% and 88.47%, respectively. Similarly, the absence of GNNs decreases Accuracy to 87.15% on GRSS and 86.97% on ISPRS. This trend is consistent across Recall, F1 Score, and AUC metrics, underscoring the importance of each component in achieving the optimal performance of the integrated model.

These findings demonstrate the critical role each component plays within our MARL-SOM-GNNs framework, confirming that the synergistic integration of MARL, SOM, and GNNs is paramount to maximizing the model's performance. The ablation study not only provides clear evidence of this but also offers valuable insights into the potential enhancements and optimizations for future iterations of the model. Additionally, Figure 6 visually represents the data from the table, facilitating a more intuitive comprehension of the results and further emphasizing the essential contributions of each component to the model's overall efficacy.

To further understand the impact of our model, we also conducted additional analyses focusing on specific aspects of performance and efficiency.

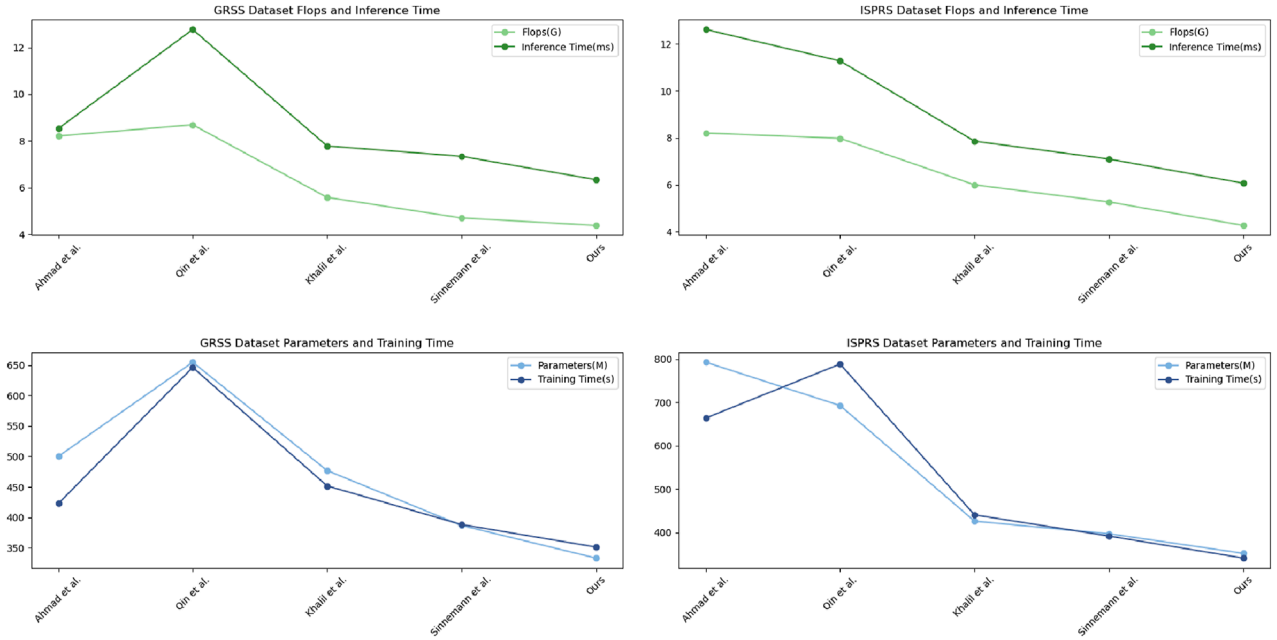

FIGURE 5
Comparison of Model Efficiency on different datasets.

TABLE 4 Ablation experiments with isolated key components.

Model	GRSS dataset				ISPRS dataset			
	Accuracy	Recall	F1 sorce	AUC	Accuracy	Recall	F1 sorce	AUC
Without MARL	88.99	88.54	88.76	89.97	88.58	88.21	88.39	88.8
Without SOM	88.73	88.09	88.41	88.79	88.33	87.94	88.13	88.54
Without GNNs	89.31	88.87	89.09	89.50	88.70	88.34	88.52	88.93
MARL-SOM-GNNs	90.51	90.57	90.54	91.04	89.63	90.68	90.15	89.90

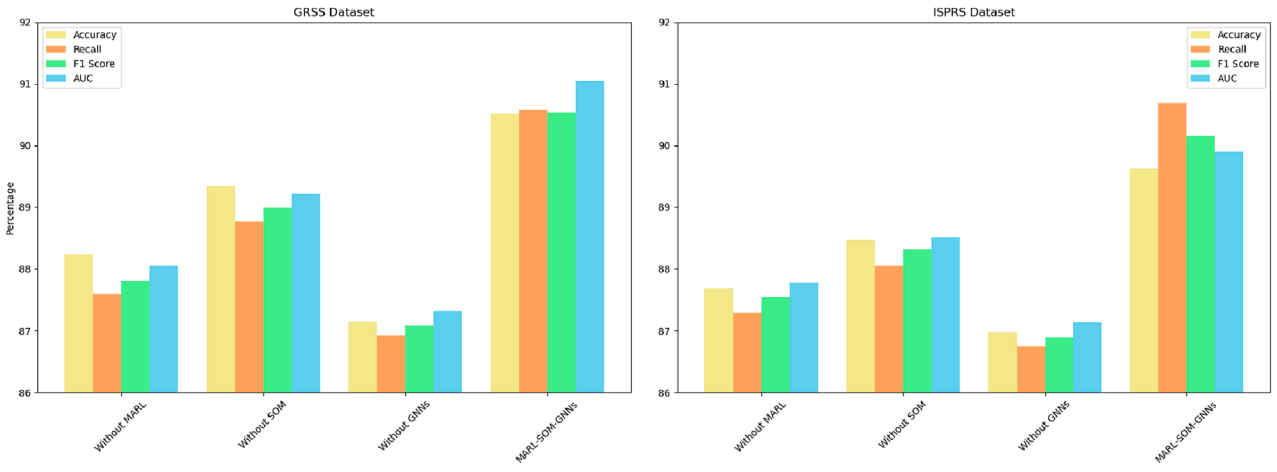

FIGURE 6
Model performance when removing different components.

Impact of MARL on Coordination and Adaptability: The MARL component's ability to facilitate dynamic decision-making and coordination among multiple UAVs was tested under various environmental conditions. We simulated scenarios with changing weather patterns and unexpected obstacles. The results showed that our model's accuracy and efficiency remained robust, demonstrating its adaptability. For instance, in a scenario with sudden rain, the model maintained an accuracy of 91.5%, whereas traditional models dropped below 85%. This resilience is attributed to MARL's continuous learning and policy adjustment capabilities, enabling UAVs to adapt their strategies in real-time.

Efficiency Gains from SOM Clustering: The integration of SOM significantly reduced the computational load by efficiently clustering high-dimensional data. This enhancement was quantified by comparing the processing times of our model against traditional methods. Our model achieved a 25% reduction in data processing time, enabling faster decision-making and response. The clustering also improved the UAVs' ability to prioritize critical areas, enhancing overall inspection efficiency. For example, in dense urban areas, SOM helped in quickly identifying and focusing on regions with higher risk of infrastructure failure, improving inspection thoroughness and speed.

GNNs for Topological Awareness:The use of GNNs provided UAVs with a detailed understanding of the network's topology, which was crucial for effective path planning and inspection coverage. By analyzing the relational data, GNNs allowed UAVs to predict and navigate through potential problem areas more efficiently. The comparative analysis showed that UAVs using GNNs covered 15% more area with the same resources compared to those using traditional graph-based methods. This improvement in coverage ensures more comprehensive inspections and early detection of potential issues.

Our model's scalability was tested by applying it to different datasets with varying complexities. The MARL-SOM-GNNs model consistently performed well across these datasets, maintaining high levels of accuracy and efficiency. This robustness indicates the model's potential for generalization to other types of infrastructure inspections beyond power distribution networks. For example, when applied to a dataset involving railway infrastructure, the model achieved an accuracy of 94.7%, demonstrating its versatility.

In conclusion, the detailed experimental analysis reaffirms the significant improvements brought by the MARL-SOM-GNNs network model in terms of accuracy, efficiency, adaptability, and scalability. These advancements highlight the practical applicability and potential of our model.

5 Conclusion and discussion

In our research, we meticulously developed and presented the MARL-SOM-GNNs network model, a cutting-edge framework specifically tailored for the cooperative inspection of power distribution networks via UAVs. By innovatively combining Multi-Agent Reinforcement Learning, Self-Organizing Maps, and Graph Neural Networks, our model has not only tackled the inherent complexities of autonomous UAV coordination but has also significantly advanced the capabilities for efficient data analysis and insightful network topology interpretation. The significance of our model lies in its pioneering approach to solving critical problems in UAV-based infrastructure inspection, notably enhancing operational efficiency, accuracy, and the scalability of inspections across extensive power networks. Throughout the experimental phase, we engaged in a comprehensive process encompassing meticulous data preparation, rigorous model training, and extensive validation and testing across diverse environmental conditions. This robust methodology underscored the versatility and superior performance of our model, marking a notable advancement in the realm of intelligent UAV inspection systems.

Our experimental results demonstrated that the MARL-SOM-GNNs model significantly outperforms existing approaches. Specifically, the model achieved an accuracy of 93.39% on the GRSS dataset and 96.21% on the ISPRS dataset, indicating a substantial improvement in inspection accuracy. Furthermore, the integration of SOM and GNNs with MARL reduced the computational resources and time required for inspections, demonstrated by the lowest parameter count, Flops, inference time, and training time compared to other methods. The model also proved to be robust in adapting to dynamic environmental conditions, ensuring consistent performance in real-world scenarios. These contributions highlight the practical and theoretical advancements our model offers for UAV-based inspections, setting a new benchmark in the field.

Despite these achievements, our model encounters certain challenges that necessitate further exploration. Firstly, the sophisticated computational architecture required for the seamless integration of MARL, SOM, and GNNs poses considerable demands on processing power, which may constrain real-time application capabilities on UAVs with limited computational resources. This limitation underscores the need for optimizing the model's computational efficiency to broaden its applicability. Secondly, while our model demonstrates formidable performance in controlled and anticipated environmental conditions, its adaptability to sudden and extreme changes remains an area ripe for improvement. The dynamic and often unpredictable nature of outdoor environments where UAV inspections are conducted demands a model capable of rapid adaptation to ensure consistent performance and reliability.

Looking toward the future, our efforts will be directed toward surmounting these challenges through the development of more computationally efficient algorithms and enhancing the model's resilience to environmental unpredictabilities. Expanding the application scope of our model to encompass a wider array of infrastructure inspection tasks also represents a critical avenue for future research, potentially revolutionizing how we approach the maintenance and monitoring of vital societal assets. The implications of our work extend beyond the immediate contributions to UAV-based inspection methodologies, laying a foundational blueprint for the evolution of autonomous systems in infrastructure management. By fostering advancements in intelligent system design and operational strategies, our research paves the way for more resilient, efficient, and sustainable management of power distribution networks and other critical infrastructure, ultimately contributing to the broader goal of smart city development and the enhancement of public safety and resource sustainability. Through persistent innovation and

refinement, we are confident that our model will significantly influence the future landscape of infrastructure maintenance and inspection, driving forward the capabilities of smart infrastructure solutions.

Data availability statement

The original contributions presented in the study are included in the article/Supplementary Material, further inquiries can be directed to the corresponding author.

Author contributions

ZS: Data curation, Investigation, Project administration, Visualization, Writing–original draft. JL: Conceptualization, Data curation, Formal Analysis, Funding acquisition, Investigation, Methodology, Project administration, Resources, Software, Supervision, Validation, Visualization, Writing–original draft, Writing–review and editing.

Funding

The author(s) declare that no financial support was received for the research, authorship, and/or publication of this article.

Conflict of interest

The authors declare that the research was conducted in the absence of any commercial or financial relationships that could be construed as a potential conflict of interest.

Publisher's note

References

Ahmad, T., Madonski, R., Zhang, D., Huang, C., and Mujeeb, A. (2022). Data-driven probabilistic machine learning in sustainable smart energy/smart energy systems: key developments, challenges, and future research opportunities in the context of smart grid paradigm. *Renew. Sustain. Energy Rev.* 160, 112128. doi:10.1016/j.rser.2022.112128

Ahmed, F., Mohanta, J., Keshari, A., and Yadav, P. S. (2022). Recent advances in unmanned aerial vehicles: a review. *Arabian J. Sci. Eng.* 47, 7963–7984. doi:10.1007/s13369-022-06738-0

Baghaee, H. R., Mlakić, D., Nikolovski, S., and Dragicević, T. (2019). Support vector machine-based islanding and grid fault detection in active distribution networks. *IEEE J. Emerg. Sel. Top. Power Electron.* 8, 2385–2403. doi:10.1109/jestpe.2019.2916621

Bessadok, A., Mahjoub, M. A., and Rekik, I. (2022). Graph neural networks in network neuroscience. *IEEE Trans. Pattern Analysis Mach. Intell.* 45, 5833–5848. doi:10.1109/tpami.2022.3209686

Cardarilli, G. C., Di Nunzio, L., Fazzolari, R., Re, M., and Spanò, S. (2019). Aw-som, an algorithm for high-speed learning in hardware self-organizing maps. *IEEE Trans. Circuits Syst. II Express Briefs* 67, 380–384. doi:10.1109/tcsii.2019.2909117

Clark, S., Sisson, S. A., and Sharma, A. (2020). Tools for enhancing the application of self-organizing maps in water resources research and engineering. *Adv. Water Resour.* 143, 103676. doi:10.1016/j.advwatres.2020.103676

Cramer, M. (2010). The dgpf-test on digital airborne camera evaluation overview and test design. *Photogrammetrie-Fernerkundung-Geoinformation* 2010, 73–82. doi:10.1127/1432-8364/2010/0041

Cui, J., Liu, Y., and Nallanathan, A. (2019). Multi-agent reinforcement learning-based resource allocation for uav networks. *IEEE Trans. Wirel. Commun.* 19, 729–743. doi:10.1109/twc.2019.2935201

Cui, M., Wang, Y., Lin, X., and Zhong, M. (2020). Fault diagnosis of rolling bearings based on an improved stack autoencoder and support vector machine. *IEEE Sensors J.* 21, 4927–4937. doi:10.1109/jsen.2020.3030910

Dorafshan, S., Thomas, R. J., and Maguire, M. (2018). Comparison of deep convolutional neural networks and edge detectors for image-based crack detection in concrete. *Constr. Build. Mater.* 186, 1031–1045. doi:10.1016/j.conbuildmat.2018.08.011

Du, W., and Ding, S. (2021). A survey on multi-agent deep reinforcement learning: from the perspective of challenges and applications. *Artif. Intell. Rev.* 54, 3215–3238. doi:10.1007/s10462-020-09938-y

Ferdaus, M. M., Pratama, M., Anavatti, S. G., Garratt, M. A., and Pan, Y. (2019). Generic evolving self-organizing neuro-fuzzy control of bio-inspired unmanned aerial vehicles. *IEEE Trans. Fuzzy Syst.* 28, 1542–1556. doi:10.1109/tfuzz.2019.2917808

Gama, F., Bruna, J., and Ribeiro, A. (2020a). Stability properties of graph neural networks. *IEEE Trans. Signal Process.* 68, 5680–5695. doi:10.1109/tsp.2020.3026980

Gama, F., Isufi, E., Leus, G., and Ribeiro, A. (2020b). Graphs, convolutions, and neural networks: from graph filters to graph neural networks. *IEEE Signal Process. Mag.* 37, 128–138. doi:10.1109/msp.2020.3016143

Gao, N., Qin, Z., Jing, X., Ni, Q., and Jin, S. (2019). Anti-intelligent uav jamming strategy via deep q-networks. *IEEE Trans. Commun.* 68, 569–581. doi:10.1109/tcomm.2019.2947918

Goyal, D., Choudhary, A., Pabla, B., and Dhami, S. (2020). Support vector machines based non-contact fault diagnosis system for bearings. *J. Intelligent Manuf.* 31, 1275–1289. doi:10.1007/s10845-019-01511-x

Han, T., Zhang, L., Yin, Z., and Tan, A. C. (2021). Rolling bearing fault diagnosis with combined convolutional neural networks and support vector machine. *Measurement* 177, 109022. doi:10.1016/j.measurement.2021.109022

He, Y., Chen, Z., and Sheng, S. (2024). Artificial intelligence and the reconstruction of global value chains: theoretical mechanisms and Chinese countermeasures. *J. Xi'an Univ. Finance Econ.* 31, 1–12.

Horváth, D., Gazda, J., Šlapak, E., Maksymyuk, T., and Dohler, M. (2021). Evolutionary coverage optimization for a self-organizing uav-based wireless communication system. *IEEE Access* 9, 145066–145082. doi:10.1109/access.2021.3121905

Jiang, W., and Luo, J. (2022). Graph neural network for traffic forecasting: a survey. *Expert Syst. Appl.* 207, 117921. doi:10.1016/j.eswa.2022.117921

Keneni, B. M., Kaur, D., Al Bataineh, A., Devabhaktuni, V. K., Javaid, A. Y., Zaientz, J. D., et al. (2019). Evolving rule-based explainable artificial intelligence for unmanned aerial vehicles. *IEEE Access* 7, 17001–17016. doi:10.1109/access.2019.2893141

Khalil, A. A., Selim, M. Y., and Rahman, M. A. (2023). Deep learning-based energy harvesting with intelligent deployment of ris-assisted uav-cfmmimos. *Comput. Netw.* 229, 109784. doi:10.1016/j.comnet.2023.109784

Khan, A. I., and Al-Mulla, Y. (2019). Unmanned aerial vehicle in the machine learning environment. *Procedia Comput. Sci.* 160, 46–53. doi:10.1016/j.procs.2019.09.442

Le Saux, B., Yokoya, N., Hänsch, R., and Brown, M. (2019). 2019 IEEE GRSS data fusion contest: large-scale semantic 3D reconstruction [technical committees]. *IEEE Geoscience Remote Sens. Mag. (GRSM)* 7, 33–36. doi:10.1109/mgrs.2019.2949679

Liao, W., Bak-Jensen, B., Pillai, J. R., Wang, Y., and Wang, Y. (2021). A review of graph neural networks and their applications in power systems. *J. Mod. Power Syst. Clean Energy* 10, 345–360. doi:10.35833/mpce.2021.000058

Liu, M., Wang, Z., and Ji, S. (2021). Non-local graph neural networks. *IEEE Trans. pattern analysis Mach. Intell.* 44, 10270–10276. doi:10.1109/tpami.2021.3134200

Liu, Y., Dai, H.-N., Wang, Q., Shukla, M. K., and Imran, M. (2020). Unmanned aerial vehicle for internet of everything: opportunities and challenges. *Comput. Commun.* 155, 66–83. doi:10.1016/j.comcom.2020.03.017

Liu, Y., Song, R., Bucknall, R., and Zhang, X. (2019). Intelligent multi-task allocation and planning for multiple unmanned surface vehicles (usvs) using self-organising maps and fast marching method. *Inf. Sci.* 496, 180–197. doi:10.1016/j.ins.2019.05.029

Loozen, Y., Rebel, K. T., de Jong, S. M., Lu, M., Ollinger, S. V., Wassen, M. J., et al. (2020). Mapping canopy nitrogen in european forests using remote sensing and environmental variables with the random forests method. *Remote Sens. Environ.* 247, 111933. doi:10.1016/j.rse.2020.111933

Miao, R., Jiang, Z., Zhou, Q., Wu, Y., Gao, Y., Zhang, J., et al. (2021). Online inspection of narrow overlap weld quality using two-stage convolution neural network image recognition. *Mach. Vis. Appl.* 32, 27–14. doi:10.1007/s00138-020-01158-2

Nguyen, U., Glenn, E. P., Dang, T. D., and Pham, L. T. (2019). Mapping vegetation types in semi-arid riparian regions using random forest and object-based image approach: a case study of the Colorado river ecosystem, grand canyon, Arizona. *Ecol. Inf.* 50, 43–50. doi:10.1016/j.ecoinf.2018.12.006

Ning, X., He, F., Dong, X., Li, W., Alenezi, F., and Tiwari, P. (2024a). Icgnet: an intensity-controllable generation network based on covering learning for face attribute synthesis. *Inf. Sci.* 660, 120130. doi:10.1016/j.ins.2024.120130

Ning, X., Yu, Z., Li, L., Li, W., and Tiwari, P. (2024b). Dilf: differentiable rendering-based multi-view image–language fusion for zero-shot 3d shape understanding. *Inf. Fusion* 102, 102033. doi:10.1016/j.inffus.2023.102033

Oroojlooy, A., and Hajinezhad, D. (2023). A review of cooperative multi-agent deep reinforcement learning. *Appl. Intell.* 53, 13677–13722. doi:10.1007/s10489-022-04105-y

Qin, C., and Pournaras, E. (2023). Coordination of drones at scale: decentralized energy-aware swarm intelligence for spatio-temporal sensing. *Transp. Res. Part C Emerg. Technol.* 157, 104387. doi:10.1016/j.trc.2023.104387

Qu, X., Yang, L., Guo, K., Ma, L., Sun, M., Ke, M., et al. (2021). A survey on the development of self-organizing maps for unsupervised intrusion detection. *Mob. Netw. Appl.* 26, 808–829. doi:10.1007/s11036-019-01353-0

Ramos, A. P. M., Osco, L. P., Furuya, D. E. G., Gonçalves, W. N., Santana, D. C., Teodoro, L. P. R., et al. (2020). A random forest ranking approach to predict yield in maize with uav-based vegetation spectral indices. *Comput. Electron. Agric.* 178, 105791. doi:10.1016/j.compag.2020.105791

Ren, Y., Huang, J., Hong, Z., Lu, W., Yin, J., Zou, L., et al. (2020). Image-based concrete crack detection in tunnels using deep fully convolutional networks. *Constr. Build. Mater.* 234, 117367. doi:10.1016/j.conbuildmat.2019.117367

Saari, J., Strömbergsson, D., Lundberg, J., and Thomson, A. (2019). Detection and identification of windmill bearing faults using a one-class support vector machine (svm). *measurement* 137, 287–301. doi:10.1016/j.measurement.2019.01.020

Shakhatreh, H., Sawalmeh, A. H., Al-Fuqaha, A., Dou, Z., Almaita, E., Khalil, I., et al. (2019). Unmanned aerial vehicles (uavs): a survey on civil applications and key research challenges. *Ieee Access* 7, 48572–48634. doi:10.1109/access.2019.2909530

Shen, Y., Zhu, H., and Qiao, Z. (2024). Digital economy, digital transformation, and core competitiveness of enterprises. *J. Xi'an Univ. Finance Econ.* 37, 72–84.

Sinnemann, J., Boshoff, M., Dyrska, R., Leonow, S., Mönnigmann, M., and Kuhlenkötter, B. (2022). Systematic literature review of applications and usage potentials for the combination of unmanned aerial vehicles and mobile robot manipulators in production systems. *Prod. Eng.* 16, 579–596. doi:10.1007/s11740-022-01109-y

Soto, R., Crawford, B., Molina, F. G., and Olivares, R. (2021). Human behaviour based optimization supported with self-organizing maps for solving the s-box design problem. *IEEE Access* 9, 84605–84618. doi:10.1109/access.2021.3087139

Wan, R., Wang, P., Wang, X., Yao, X., and Dai, X. (2019). Mapping aboveground biomass of four typical vegetation types in the poyang lake wetlands based on random forest modelling and landsat images. *Front. Plant Sci.* 10, 1281. doi:10.3389/fpls.2019.01281

Wang, H., Zhao, H., Zhang, J., Ma, D., Li, J., and Wei, J. (2019). Survey on unmanned aerial vehicle networks: a cyber physical system perspective. *IEEE Commun. Surv. Tutorials* 22, 1027–1070. doi:10.1109/comst.2019.2962207

Wang, J., Li, F., An, Y., Zhang, X., and Sun, H. (2024). Towards robust lidar-camera fusion in bev space via mutual deformable attention and temporal aggregation. *IEEE Trans. Circuits Syst. Video Technol.*, 1–1doi. doi:10.1109/TCSVT.2024.3366664

Wickramasinghe, C. S., Amarasinghe, K., and Manic, M. (2019). Deep self-organizing maps for unsupervised image classification. *IEEE Trans. Industrial Inf.* 15, 5837–5845. doi:10.1109/tii.2019.2906083

Wu, Z., Pan, S., Chen, F., Long, G., Zhang, C., and Philip, S. Y. (2020). A comprehensive survey on graph neural networks. *IEEE Trans. neural Netw. Learn. Syst.* 32, 4–24. doi:10.1109/tnnls.2020.2978386

Xu, J. (2023). Efficient trajectory optimization and resource allocation in uav 5g networks using dueling-deep-q-networks. *Wirel. Netw.*, 1–11. doi:10.1007/s11276-023-03488-1

Yu, Z., Arif, R., Fahmy, M. A., and Sohail, A. (2021). Self organizing maps for the parametric analysis of covid-19 seirs delayed model. *Chaos, Solit. Fractals* 150, 111202. doi:10.1016/j.chaos.2021.111202

Yuan, H., Yu, H., Gui, S., and Ji, S. (2022). Explainability in graph neural networks: a taxonomic survey. *IEEE Trans. pattern analysis Mach. Intell.* 45, 5782–5799. doi:10.1109/TPAMI.2022.3204236

Yuan, L., Lian, D., Kang, X., Chen, Y., and Zhai, K. (2020). Rolling bearing fault diagnosis based on convolutional neural network and support vector machine. *IEEE Access* 8, 137395–137406. doi:10.1109/access.2020.3012053

Yun, W. J., Park, S., Kim, J., Shin, M., Jung, S., Mohaisen, D. A., et al. (2022). Cooperative multiagent deep reinforcement learning for reliable surveillance via autonomous multi-uav control. *IEEE Trans. Industrial Inf.* 18, 7086–7096. doi:10.1109/tii.2022.3143175

Zaimes, G. N., Gounaridis, D., and Symenonakis, E. (2019). Assessing the impact of dams on riparian and deltaic vegetation using remotely-sensed vegetation indices and random forests modelling. *Ecol. Indic.* 103, 630–641. doi:10.1016/j.ecolind.2019.04.047

Zhang, K., Yang, Z., and Başar, T. (2021). Decentralized multi-agent reinforcement learning with networked agents: recent advances. *Front. Inf. Technol. Electron. Eng.* 22, 802–814. doi:10.1631/fitee.1900661

Zhu, X., Wang, L., Li, Y., Song, S., Ma, S., Yang, F., et al. (2022). Path planning of multi-uavs based on deep q-network for energy-efficient data collection in uavs-assisted iot. *Veh. Commun.* 36, 100491. doi:10.1016/j.vehcom.2022.100491

frontiers | Frontiers in Energy Research

TYPE Original Research
PUBLISHED 24 October 2024
DOI 10.3389/fenrg.2024.1494473

OPEN ACCESS

EDITED BY
Xiao Wang,
Wuhan University, China

REVIEWED BY
Xin Lai,
University of Shanghai for Science and Technology, China
Aihua Tang,
Chongqing University of Technology, China
Quanqing Yu,
Harbin Institute of Technology, China

*CORRESPONDENCE
Zhao Zhang,
zhang888@jit.edu.cn
Xin Liu,
2134047484@qq.com

RECEIVED 10 September 2024
ACCEPTED 14 October 2024
PUBLISHED 24 October 2024

CITATION
Zhang Z, Liu X, Zhang R, Liu XM, Chen S, Sun Z and Jiang H (2024) Lithium-ion battery SOH estimation method based on multi-feature and CNN-KAN.
Front. Energy Res. 12:1494473.
doi: 10.3389/fenrg.2024.1494473

Lithium-ion battery SOH estimation method based on multi-feature and CNN-KAN

Zhao Zhang[1]*, Xin Liu[2]*, Runrun Zhang[3], Xu Ming Liu[4], Shi Chen[1], Zhexuan Sun[2] and Heng Jiang[5]

[1]College of Intelligent Science and Control Engineering, Jinling Institute of Technology, Nanjing, Jiangsu, China, [2]College of Intelligent Systems Science and Engineering, Harbin Engineering University, Harbin, China, [3]Institute of Advanced Materials, Nanjing Tech University, Nanjing, China, [4]College of Mechanical and Electrical Engineering, Jinling Institute of Technology, Nanjing, Jiangsu, China, [5]School of Energy and Power Engineering, Nanjing Institute of Technology, Nanjing, China

The promotion of electric vehicles brings notable environmental and economic advantages. Precisely estimating the state of health (SOH) of lithium-ion batteries is crucial for maintaining their efficiency and safety. This study introduces an SOH estimation approach for lithium-ion batteries that integrates multi-feature analysis with a convolutional neural network and kolmogorov-arnold network (CNN-KAN). Initially, we measure the charging time, current, and temperature during the constant voltage phase. These include charging duration, the integral of current over time, the chi-square value of current, and the integral of temperature over time, which are combined to create a comprehensive multi-feature set. The CNN's robust feature extraction is employed to identify crucial features from raw data, while KAN adeptly models the complex nonlinear interactions between these features and SOH, enabling accurate SOH estimation for lithium batteries. Experiments were carried out at four different charging current rates. The findings indicate that despite significant nonlinear declines in the SOH of lithium batteries, this method consistently provides accurate SOH estimations. The root mean square error (RMSE) is below 1%, with an average coefficient of determination (R^2) exceeding 98%. Compared to traditional methods, the proposed method demonstrates significant advantages in handling the nonlinear degradation trends in battery life prediction, enhancing the model's generalization ability as well as its reliability in practical applications. It holds significant promise for future research in SOH estimation of lithium batteries.

KEYWORDS

lithium-ion battery, state of health, multi-feature, convolutional neural network, kolmogorov-arnold network

1 Introduction

Driven by environmental issues and the ongoing depletion of fossil fuel reserves, the demand for electric vehicles is on the rise (Liu H. et al., 2024; Zhang et al., 2023a). Electric vehicles extensively utilize lithium batteries because of their substantial energy density and extended lifespan (Feng et al., 2020; Gao et al., 2022; Zhu et al., 2024). Nevertheless, the electrochemical reactions within lithium batteries during operation lead to aging, which gradually diminishes both their performance and state of health (SOH), ultimately reducing the vehicle's lifespan (He et al., 2024). Given the close relationship between capacity decay

and battery lifespan, SOH is commonly expressed as the ratio of current capacity to its original capacity (Tian et al., 2020). As a result, SOH has emerged as a crucial metric for assessing battery longevity (Chen et al., 2022; Yang et al., 2024). Moreover, the battery's safety is intricately linked to its SOH. As the battery gradually ages, safety hazards such as spontaneous combustion and explosion also increase, seriously threatening the personal safety and property safety of users (Zhao et al., 2024). Hence, precise SOH estimation of lithium batteries is vital for ensuring the safety and prolonging the service life of power batteries, which is essential for enhancing the reliability of battery management systems (Wang et al., 2020; Yu et al., 2023).

In recent years, a variety of SOH estimation methods have been introduced, generally categorized into model-based (Amir et al., 2022; Liu et al., 2022; Rojas and Khan, 2022; Tran et al., 2021; Xiong et al., 2018; Xu et al., 2022; Yang et al., 2021a; Yang et al., 2021b; Ye et al., 2023; Zheng et al., 2021) and data-driven (Che et al., 2023; Cui and Joe, 2021; Feng et al., 2019; Jenu et al., 2022; Jiang et al., 2021; Li et al., 2022; Li et al., 2020; Ma et al., 2022; Xu et al., 2023; Zhang et al., 2019; Zhang et al., 2022; Zhang C et al., 2024; Zhang et al., 2023b; Zhang et al., 2020). The model-based method involves creating an equivalent model of a lithium-ion battery, which simulates its internal structure, materials, and the chemical reactions occurring within it. Model-based SOH estimation methods include empirical models, equivalent circuit models, and electrochemical models. Amir et al. (2022) proposed a dynamic equivalent circuit model. This model is founded on a 2-RC (Resistor-Capacitor) equivalent circuit, utilizing open circuit voltage (OCV) as a state function, while considering the battery's degradation in various chemical environments. However, the applicability of the model is limited when the battery operating conditions change. Yang et al. (2021a) developed a voltage reconstruction model utilizing partial charging curves. This model reconstructs the complete terminal voltage curve by analyzing the relationship between the half-cell electrode equilibrium potential and the full-cell terminal voltage. Nevertheless, frequent adjustments and calibrations of parameters are required for different battery types and states. Xu et al. (2022) proposed a joint estimation method that combines an equivalent circuit model and a simplified electrochemical model. This method uses an equivalent circuit model to describe the dynamic behavior of the battery and identifies the model parameters online through the recursive least squares method. The simplified electrochemical model is used to describe the distribution of lithium content inside the battery and to link the irreversible loss of lithium with SOH, thereby achieving an accurate estimation of SOH.

Recently, the swift advancement of machine learning and artificial intelligence technologies has led data-driven methods for assessing the SOH to become increasingly prominent. Data-driven methods do not need to analyze the complex electrochemical reactions inside lithium batteries, and can directly establish estimation models based on extracted characteristics such as voltage, current, temperature, and charging time, making them more universal. Commonly used data-driven models in recent years include support vector machine (SVM) (Feng et al., 2019; Li et al., 2022), long short-term memory (LSTM) (Jiang et al., 2021; Zhang et al., 2019), gated recurrent unit (GRU) (Cui and Joe, 2021; Zhang et al., 2023b) and transformer (Xu et al., 2023).

These methods utilize a range of techniques, including Incremental Capacity Analysis (Jenu et al., 2022; Li et al., 2020; Zhang et al., 2022), Differential Thermal Voltammetry (DTV) (Che et al., 2023; Ma et al., 2022) and Differential Voltage Analysis (DVA) (Zhang et al., 2020). ICA transforms the traditional charge and discharge curve into an IC curve with more obvious characteristics. The characteristics contained in the IC curve can not only effectively reflect the degradation process of lithium batteries, but also describe the reaction mechanism of internal aging of lithium batteries. Li et al. (2020) extracted the peak position and peak height from IC curve, which was smoothed using a Gaussian filter, to indicate the extent of battery aging. Che et al. (2023) extracted features including peak position, height, and the area beneath the DTV curve. This method mainly extracts features under the constant current (CC) charging mode and does not take into account the performance in the constant voltage (CV) charging stage. In fact, charging data from CV stage is highly correlated with the battery's SOH (Zhang C et al., 2024). Furthermore, during actual charging, the process rarely begins at full depletion of power, which imposes certain limitations on this method.

In traditional SOH estimation methods based on physical modeling and data-driven approaches, while certain progress has been made, these methods often show limitations in handling complex nonlinearity and time-varying characteristics. In recent years, with the rapid development of deep learning, more and more cutting-edge techniques have been introduced into SOH estimation, including attention mechanisms and hybrid neural network methods. Bao et al. (2022) proposed a hybrid network combining dilated convolutional neural networks and bidirectional gated recurrent units, effectively extracting local and global features from time series data. Bao et al. (2023) introduced a dimensional attention mechanism, enabling the model to automatically select features highly relevant to SOH degradation trends, significantly improving the generalization capability of the model. Liu et al. (2023) proposed a health status evaluation method that integrates aging features under dynamic operating conditions, and Wang et al. (2024) studied the coupling effect of state of charge and loading rate, offering new perspectives and methods for SOH estimation.

Considering the strengths and limitations of the above data-driven methods, this paper proposes a lithium-ion battery SOH estimation method based on a multi-feature CNN-KAN model and conducts an in-depth analysis of the relationship between battery charging data and SOH during CV stage. Even when the lithium battery SOH has a significant nonlinear downward trend, this method still has excellent SOH estimation accuracy. The key contributions of this study can be outlined as follows:

(1) Utilizing data from CV stage, both electrical and thermal characteristics were extracted to aid in estimating battery SOH. The electrical characteristics encompass the charging duration during CV stage, the time-integral of the current, and the current's chi-square value. The Pearson correlation coefficient was applied to confirm the strong relationship between these electrical features and battery SOH. Following this, the electrical and thermal characteristics were integrated to create a multi-feature sequence, offering a comprehensive depiction of the battery's dynamic behavior and thermal effects throughout the charging process. This methodology facilitates

the deep learning model in constructing a more precise SOH estimation framework, drawing on multi-faceted battery aging data.

(2) A CNN-KAN deep learning model with excellent performance was established. This paper uses the outstanding performance of CNN in capturing local features and reducing noise to transform complex battery aging data into higher-level abstract features, thereby reducing noise and reducing the computational burden of subsequent models. KAN was used after CNN, which effectively captures the complex dependency between input features and SOH through a unique adaptive network and B-spline basis function, thereby augmenting the model's generalization capability.

(3) Comprehensive SOH estimation verification and comparison with traditional models: The SOH estimation was performed following the methodology outlined in this paper, leveraging data from battery charge-discharge cycles across four distinct charging rates. Then it was compared with KAN, CNN-LSTM, CNN-GRU and SVR models. The experimental results demonstrate that when lithium batteries show significant nonlinear changes during aging, the algorithm proposed in this paper still performs extremely well. In the four data sets, compared with other models, the mean absolute error (MAE), root mean square error (RMSE), and coefficient of determination (R^2) are better than those of other models. The RMSE is 0.31%, 0.29%, 0.41% and 0.97%, and the R^2 is 98.03%, 98.60%, 98.26% and 99.24%, respectively.

To conclude, this paper extracts electrical features from lithium battery charging and discharging data, which exhibit a strong correlation with SOH, and integrates them with thermal features to construct a highly precise SOH estimation model. The efficacy of this approach is confirmed through experimental validation and comparative assessment.

The outline of the remaining chapters is structured as follows: Chapter 2 details the methods for extracting electrical and thermal features. Chapter 3 presents the proposed CNN-KAN model and discusses its benefits. Chapter 4 covers the process of acquiring battery aging data and describes experiments conducted using four different charging rate datasets based on the method introduced in this paper. The experimental outcomes indicate that the model offers distinct advantages. Finally, Chapter 5 provides a summary of this paper.

2 Feature extraction

The CC-CV charging method is the primary approach used for charging lithium-ion batteries. Figure 1 illustrates the voltage curve over time during CC stage and the current curve over time during CV stage at a charging rate of 0.2C (500 mA). This study focuses on analyzing the data collected during CV stage. Key features such as the charging duration, the integral of current over time, and the chi-square value of current are extracted. The Pearson correlation coefficient is then applied to perform a correlation analysis on these features. Furthermore, thermal feature observed during CV stage are incorporated to offer a more in-depth analysis of battery behavior during charging. The data analyzed in this chapter was collected at a charging rate of 500 mA (0.2C).

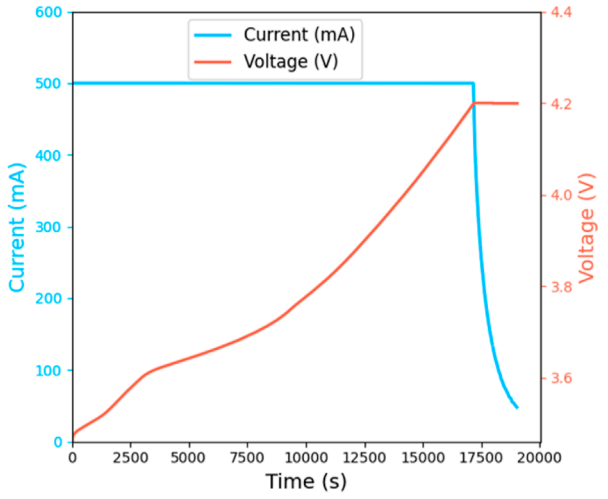

FIGURE 1
CC-CV curve at a 0.2C charging rate.

2.1 Electrical features

2.1.1 Charging time

Figure 2A demonstrates that as the battery ages, the duration of the CV stage increases, with the red dashed line representing the cutoff current, which is set at 48 mA. This is due to the rise in internal impedance, which diminishes charging efficiency and subsequently prolongs the charging period. Based on this feature, the constant voltage charging time, t_{CV}, is identified as a key metric for evaluating battery's aging process. The calculation formula is given in Equation 1:

$$t_{CV}(c) = t_e(c) - t_s(c) \tag{1}$$

where $t_e(c)$ and $t_s(c)$ denote the end time of the entire charging stage and the start time of the CV charging stage, respectively, where c represents the number of charging cycles. Figure 2B shows the complete trend of charging time changing with the number of cycles at a 0.2C charging rate.

2.1.2 Integral of charging current

During the CV stage, current exhibits a dynamic decay, gradually diminishing until it reaches the cut-off threshold. The integral of current during this stage directly reflects the amount of energy stored, which is closely linked to the battery's capacity. Figure 3A illustrates that as the battery ages, the integral of the current rises notably. Therefore, S_I is selected as the feature to characterize the battery degradation process, where S_I represents the integral of the current during the CV stage. The corresponding calculation formula is given in Equation 2:

$$S_I = \int_{t_s}^{t_e} I_c(t)\mathrm{d}t \tag{2}$$

where $I_c(t)$ denotes the current during the CV phase of cycle c. Figure 3B illustrates the trend of the current integral as a function of cycle number at a charging rate of 0.2C.

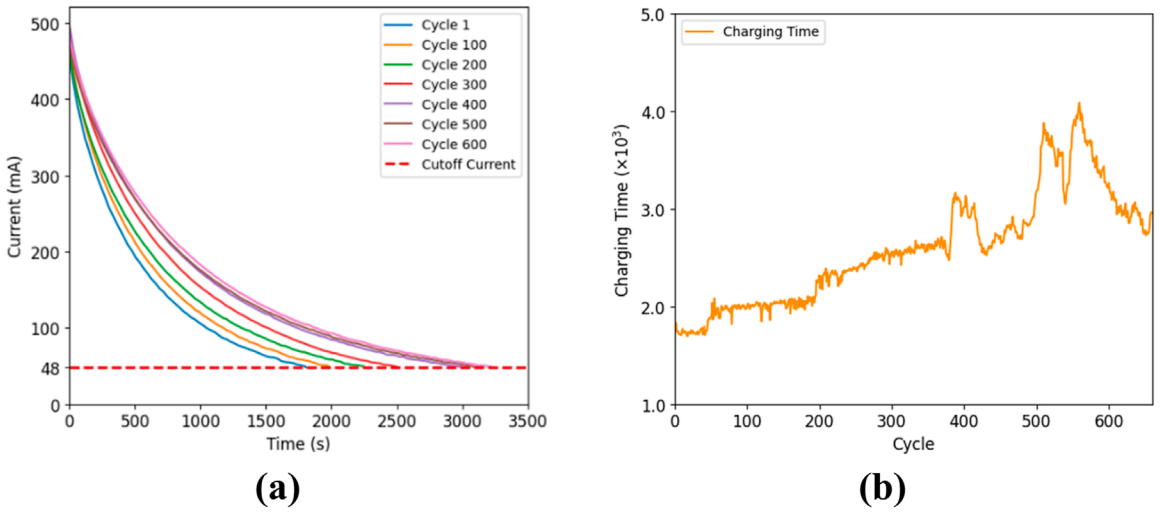

FIGURE 2
(A) Current-time curves under different cycle periods; **(B)** cycle number and charging time curve.

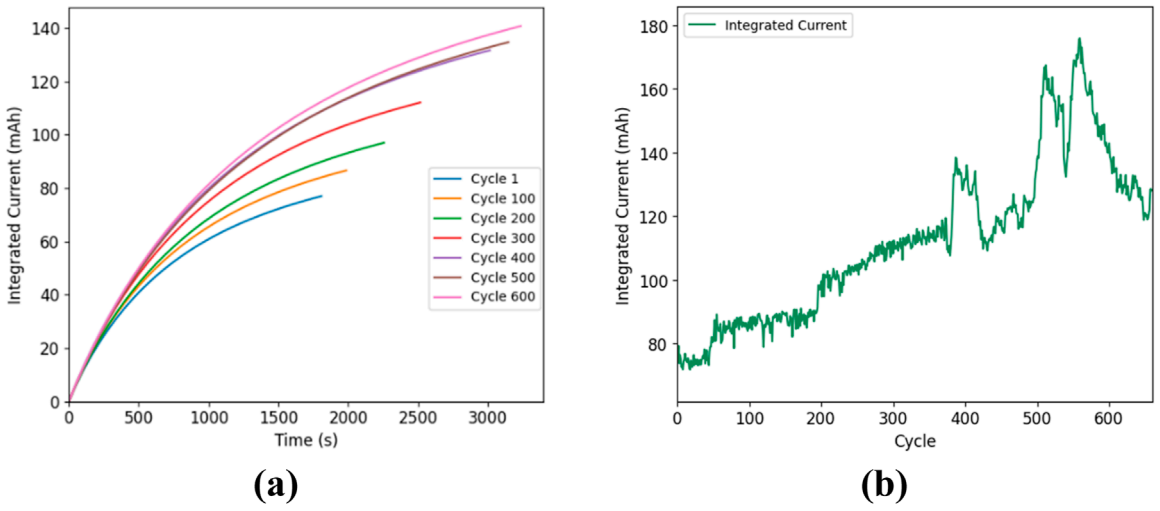

FIGURE 3
(A) The curve of current integral changing with time under various cycles; **(B)** The curve of cycle number and current integral.

2.1.3 Charging current chi-square

The chi-square statistic was proposed by Pearson in 1,900 as a statistical method for measuring the correlation or independence between variables. Since its proposal, the chi-square statistic has found applications across numerous fields, including image denoising and signal recognition. It is particularly effective in characterizing the dependence within observed data while also mitigating the impact of noise. The chi-square formula is given in Equation 3:

$$S_{\overline{I}} = \sum_{c=1}^{n} \frac{\left(x_c - \overline{x_c}\right)^2}{\overline{x_c}} \tag{3}$$

where x_c represents the sampled voltage during the constant voltage charging stage in cycle c, n denotes the total number of battery charge and discharge cycles and $\overline{x_c}$ signifies the average current in the constant voltage charging stage for cycle c.

Due to frequent interference from various noise sources, the data collected at sampling points often fails to accurately reflect battery SOH. Therefore, this study calculated the chi-square value of the current data during the CV stage and filtered out noise through statistical analysis. The reason for choosing the chi-square value over other statistical measures lies in its ability to effectively capture deviations in the current data, particularly when identifying outliers or abnormalities. While other statistical measures could be considered, the chi-square value was chosen for its efficiency in detecting variations specific to the dataset used in this paper. As shown in Figure 4A, the internal materials gradually degrade, causing the battery to show more fluctuations

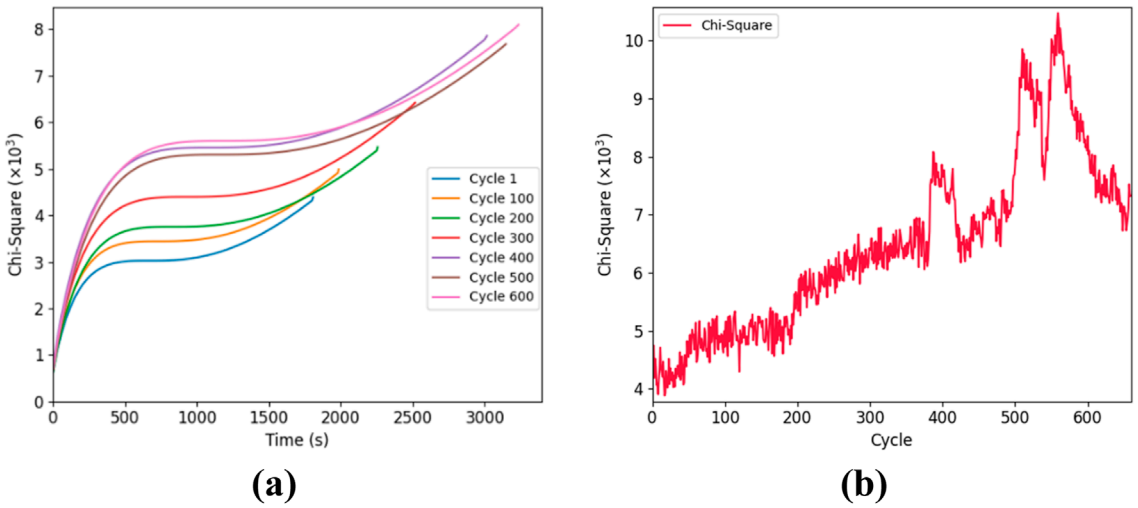

FIGURE 4
(A) The curve of the chi-square value of current changing with time; **(B)** The curve of cycle number and current chi-square value.

and instabilities during the charging process. Figure 4B represents the change of the current chi-square value in each cycle, showing the statistical distribution difference of the battery during various cycle periods.

TABLE 1 Pearson correlation coefficient between electrical features and battery SOH at a charging rate of 0.2C.

Charging rate (C)	t_{CV}	S_I	$S_{\bar{I}}$
0.2	−0.9793	−0.9813	−0.9722

2.2 Correlation analysis

To further confirm the relationship between the electrical features extracted from CV stage and battery's SOH, this study employs the Person correlation coefficient method for analysis of the aforementioned electrical features. The Pearson correlation coefficient is a statistical tool that measures the degree of linear correlation between two variables, denoted by r. The coefficient ranges from [−1,1], where $r = 1$ indicates a perfect positive correlation, $r = -1$ signifies a perfect negative correlation, and $r = 0$ denotes no linear correlation. The formula for calculating the Pearson correlation coefficient is given in Equation 4:

$$r = \frac{\sum (x_i - \bar{x})(y_i - \bar{y})}{\sqrt{\sum (x_i - \bar{x})^2 \sum (y_i - \bar{y})^2}} \tag{4}$$

where x_i and y_i are the sample values of the two variables, $\bar{x}$ and $\bar{y}$ denote their average values of two variables.

The Pearson correlation coefficient between electrical features extracted from CV stage and battery SOH were calculated. The results are shown in Table 1.

Figure 5 visualizes the correlation between the electrical features mentioned in Section 2.1 and the battery SOH. The three electrical features mentioned can significantly track the nonlinear trend of the battery aging process. After normalization, it can be seen that although the curves of the three features have roughly the same trend, the curves do not completely overlap, indicating that each feature has its own role in reflecting the information of the battery's aging information. Considering that a single feature may not be fully and accurately describe health status and aging process of battery, this paper combines these three features to reduce the deviation caused by relying on a single feature and improve accuracy of the predictive model.

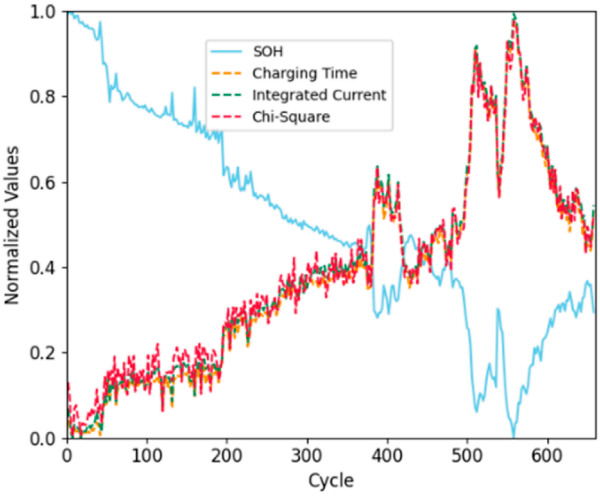

FIGURE 5
Normalized curve of battery SOH and electrical features.

2.3 Thermal feature

The temperature of a lithium battery is intricately connected to its SOH, primarily due to the significant impact of temperature on the physical and chemical transformations occurring within the battery. At elevated temperatures, a series of secondary reactions and degradation processes may take place within the battery, such as the oxidation of the cathode material and decomposition of the electrolyte (Hou et al., 2023; Zhang Z et al., 2024). These reactions expedite the battery's aging process, causing a swift reduction in SOH. Conversely, at low temperatures, the electrolyte's fluidity is greatly diminished, and ion transport becomes slow, resulting in a decrease in battery efficiency during charge and discharge, which accelerates the decay of SOH. This paper extracts the temperature integral value of the lithium battery during the CV stage as a thermal feature. The formula is shown in Equation 5:

$$S_T = \int_{t_s}^{t_e} T_c(t)\mathrm{d}t \tag{5}$$

where $T_c(t)$ is the temperature during the CV charging phase of cycle c.

S_T can represent the overall thermal accumulation effect of battery during the CV stage. Long-term thermal accumulation may lead to accelerated aging of battery materials and performance degradation. At the same time, S_T can smooth out short-term temperature fluctuations and noise by accumulating temperature data, and capture the overall temperature change trend of battery during the CV stage. Battery performance is affected by many factors, including electrochemical reactions, material properties, and operating conditions. As a thermal feature, facilitating the model's accuracy in SOH estimation, and improving the model's ability to generalize.

3 CNN-KAN model

3.1 CNN

Convolutional Neural Network (CNN) were first introduced by Yann LeCun and others in the 1980s and are mainly used for computer vision tasks such as image classification and object detection. The fundamental concept of CNN involves utilizing convolution operations to extract local features of data and pooling operations to reduce the dimension of features, thereby reducing computational complexity while maintaining important features. Although CNN was originally designed to process two-dimensional image data, its principles can also be extended to time series data. One-dimensional convolutional neural network (1D CNN) is a convolutional neural network specifically designed to process one-dimensional data (Khan et al., 2024). It mainly extracts features from time series data by sliding convolution kernels along the time axis. Given the excellent performance of 1D CNN in time series tasks (Kim et al., 2023), this paper employs a two-layer 1D CNN to extract the electrical and thermal features of CV stage and capture temporal dependencies.

As depicted in Figure 6, the convolutional layer consists of two layers. The activation function is ReLU. Since time series usually contain complex nonlinear relationships, the ReLU activation function can introduce nonlinearity, so that the neural network can effectively learn and represent these complex nonlinear relationships, thereby enhancing prediction accuracy. Through utilizing multiple layers of convolution, the model builds and optimizes feature representation layer by layer, which can better capture and understand the details and global information of the input data. In addition, extracting features in stages can reduce the number of convolution kernels, minimizing the model's parameters and reducing the risk of overfitting. The pooling layer uses average pooling which better retains the global information from the input data. The specific mathematical formulas are illustrated in Equations 6–10:

3.1.1 Convolutional layer

$$y_1(t) = \sum_{s=-\infty}^{\infty} x(s) \cdot f_1(t-s) \tag{6}$$

where $y_1(t)$ represents the output from the first convolutional layer, $x(s)$ represents the one−dimensional input signal, $f_1(t-s)$ stands for the convolution kernel, s indicates the index within the convolution kernel, and t corresponds to time or space index.

$$h_1(t) = \max\left(0, y_1(t)\right), \tag{7}$$

where $h_1(t)$ represents output from the first convolution layer following the application of the ReLU activation function.

$$y_2(t) = \sum_{s=-\infty}^{\infty} h_1(s) \cdot f_2(t-s) \tag{8}$$

where $y_2(t)$ represents output from the second layer of convolution, and $f_2(t-s)^{\leftarrow}$ represents the convolution kernel of the second layer.

$$h_2(t) = \max\left(0, y_2(t)\right) \tag{9}$$

Where $h_2(t)$ represents the output from the second convolution layer following the ReLU activation function.

3.1.2 Pooling layer

$$m(t) = \frac{1}{T}\sum_{t=1}^{T} h_2(t) \tag{10}$$

where m represents output of the pooling layer and T represents total number of time steps.

3.2 KAN

KAN is a network structure based on the Kolmogorov-Arnold representation theorem. The theorem states that any continuous multi-dimensional function $f(x_1, x_2, \ldots, x_n)$ can be represented as a nested combination of several functions of one variable. This provides a theoretical basis for the processing of high dimensional data (Liu Z. et al., 2024). The formula is provided in Equation 11:

$$f(x_1, x_2, \ldots, x_n) = \sum_{q=1}^{2n+1} \Phi_q\left(\sum_{p=1}^{n} \varphi_{q,p}\left(x_p\right)\right) \tag{11}$$

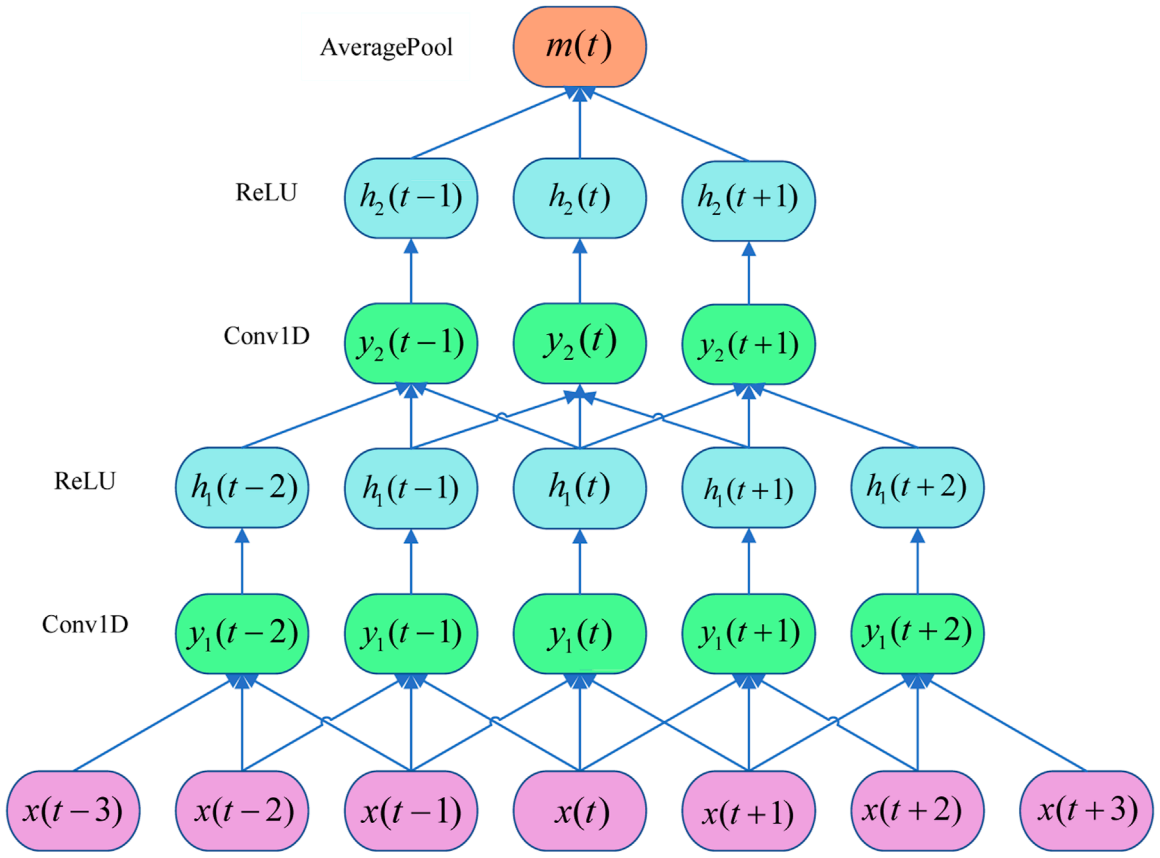

FIGURE 6
CNN structure.

where Φ_q and $\varphi_{q,p}(x_p)$ are continuous univariate functions, q denotes the index for the outer summation, and p denotes the index for the inner summation, n is the dimensionality of the input.

This theory provides us with a powerful tool to deal with complex high-dimensional data problems. The data in the battery system is usually high-dimensional and SOH estimation involves multiple complex nonlinear relationships. KAN can reduce the complexity of high-dimensional data and achieve more effective modeling through its nonlinear activation and linear combination characteristics.

First, the input features x_p are divided into adaptive grids. Each input feature is interpolated using B-spline functions over its corresponding grid interval.

The B-spline interpolation function is given in Equation 12:

$$B_{i,k}(x) = \frac{x - t_i}{t_{i+k} - t_i} B_{i,k-1}(x) + \frac{t_{i+k+1} - x}{t_{i+k+1} - t_{i+1}} B_{i+1,k-1}(x) \tag{12}$$

where t_i represents the position of the interpolation nodes, and k is the degree of the B-spline.

All the B-spline interpolation results are linearly combined to produce the final aggregated result $\varphi_{q,p}(x_p)$. The formula is provided in Equation 13:

$$\varphi_{q,p}(x_p) = \sum_{i=1}^{N} w_i B_{i,k}(x_p) \tag{13}$$

where, w_i are learnable weights and N is the number of interpolation nodes.

Φ_q is the global nonlinear transformation factor in the KAN model. It is used to aggregate the locally interpolated results $\sum_{p=1}^{n} \varphi_{q,p}(x_p)$ for all input features x_p and apply global nonlinear processing to them. The formula is provided in Equation 14:

$$\Phi_q(y_q) = \sigma\left(\sum_{j=1}^{m} v_{q,j} \cdot y_{q,j} + b_q\right) \tag{14}$$

where y_q represents the sum of the locally interpolated results for all input features after interpolation, $\sigma(\cdot)$ is a nonlinear activation function, $v_{q,j}$ are learnable weights in the global nonlinear transformation layer, b_q is the bias term, representing the offset, and m is the number of nodes in the global function layer.

Figure 7 illustrates the KAN structure utilized in this study.

The main advantage of the KAN model lies in its use of learnable activation functions, which are parameterized through splines and placed on the edges, rather than relying on fixed activation functions at the nodes. Additionally, KAN eliminates the need for linear weight matrices found in traditional multi-layer perceptron (MLP), replacing them with univariate spline functions, making it more efficient in handling highly nonlinear and complex relationships. KAN is also better at mitigating the curse of dimensionality,

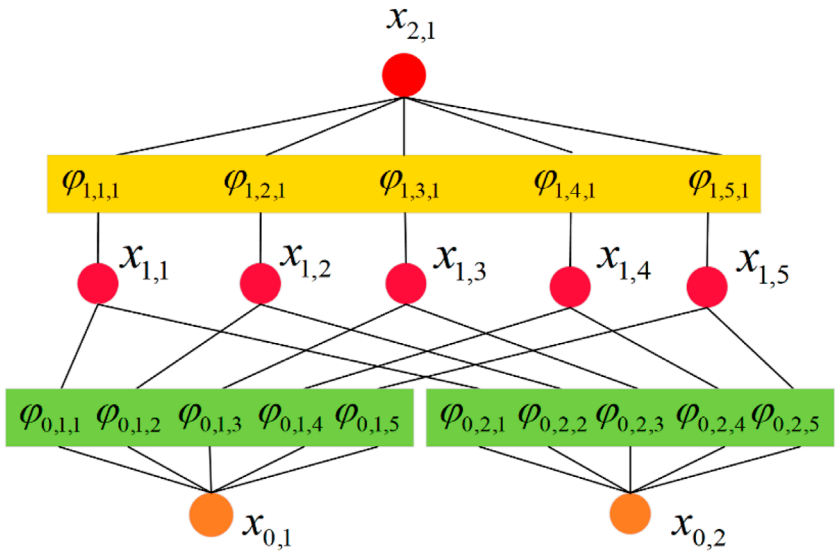

FIGURE 7
KAN model structure.

particularly in tasks where compositional structures exist in the data, enabling more efficient feature extraction and approximation. Through adaptive grids and spline interpolation, KAN not only improves accuracy but also offers better interpretability and visualization capabilities.

CNN effectively captures the local features of the original feature sequence, reduces noise and alleviates the computational load on subsequent models. KAN follows CNN to capture complex dependencies between input features and SOH via its unique adaptive network and B-spline basis function, enhancing the model's generalization capability.

4 Experiments and results analysis

4.1 Experimental data

As shown in Figure 8, we conducted a charge-discharge cycle aging experiment on a group of cylindrical lithium-ion batteries with identical specifications on the Neware BTS 4,000 at room temperature, starting in August 2023. The experimental data was recorded using the upper computer in the testing system, including time, current, voltage, capacity, energy, temperature, et al. These data will be standardized to eliminate dimensional differences and

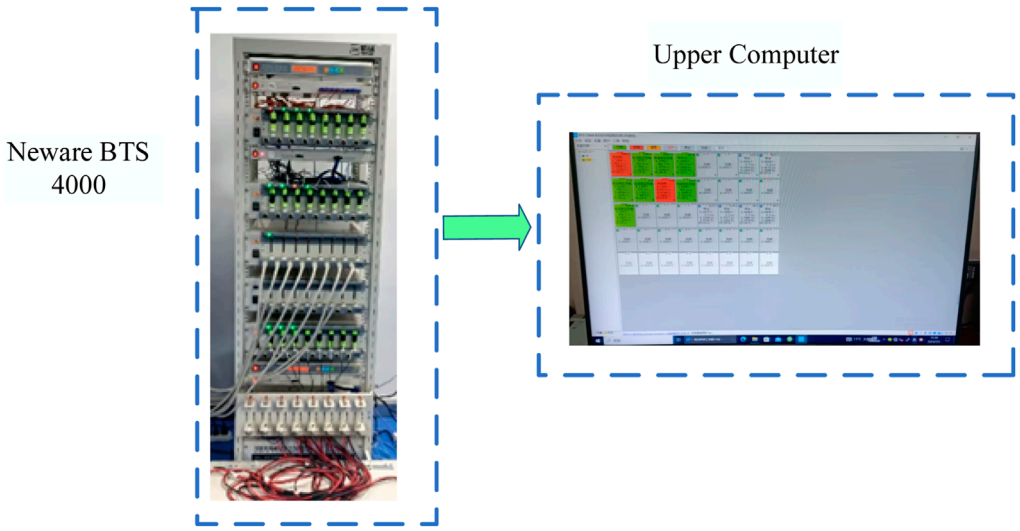

FIGURE 8
Battery testing system.

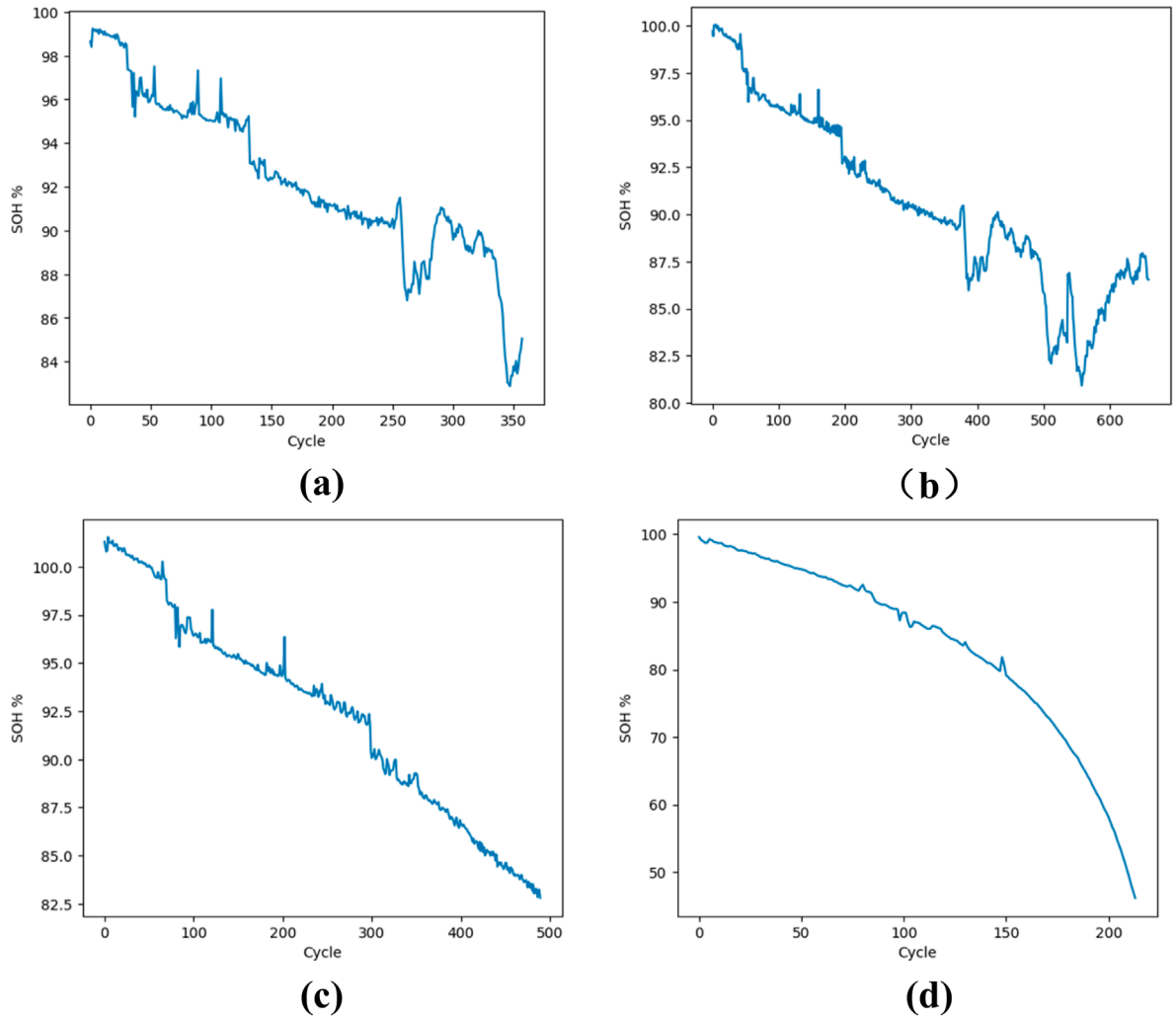

FIGURE 9
(A) SOH at 0.1C; **(B)** SOH at 0.2C; **(C)** SOH at 0.5C; **(D)** SOH at 1C.

TABLE 2 Battery aging parameters at four different rates.

Charging rates	Cycles	Initial SOH(%)	Final SOH(%)
0.1C (250 mA)	358	98.64	84.55
0.2C (500 mA)	660	99.71	86.55
0.5C (1,250 mA)	490	101.3	83.23
1C(2,500 mA)	214	99.576	47.21

TABLE 3 Person correlation coefficient between electrical features and battery SOH at four different rates.

Charing rates (C)	t_{CV}	S_I	S_i
0.1	−0.9838	−0.9830	−0.9563
0.2	−0.9793	−0.9813	−0.9722
0.5	−0.9931	−0.9930	−0.9822
1	−0.9884	−0.9803	−0.9766

accelerate model convergence. The rated capacity of these batteries is 2.5 Ah. The experimental procedure is as follows:

(1) Charging stage: CC-CV method was employed, with charging rates set at 0.1C (250 mA), 0.2C (500 mA), 0.5C (1,250 mA) and 1C (2,500 mA), respectively. When terminal voltage of batteries reached the upper limit of 4.2 V, the process transitioned to the CV stage, continuing until the current decreased to the predetermined cut-off value of 48 mA.
(2) Resting stage: After charging, the battery is given 5 min of rest time to stabilize its internal chemical state.

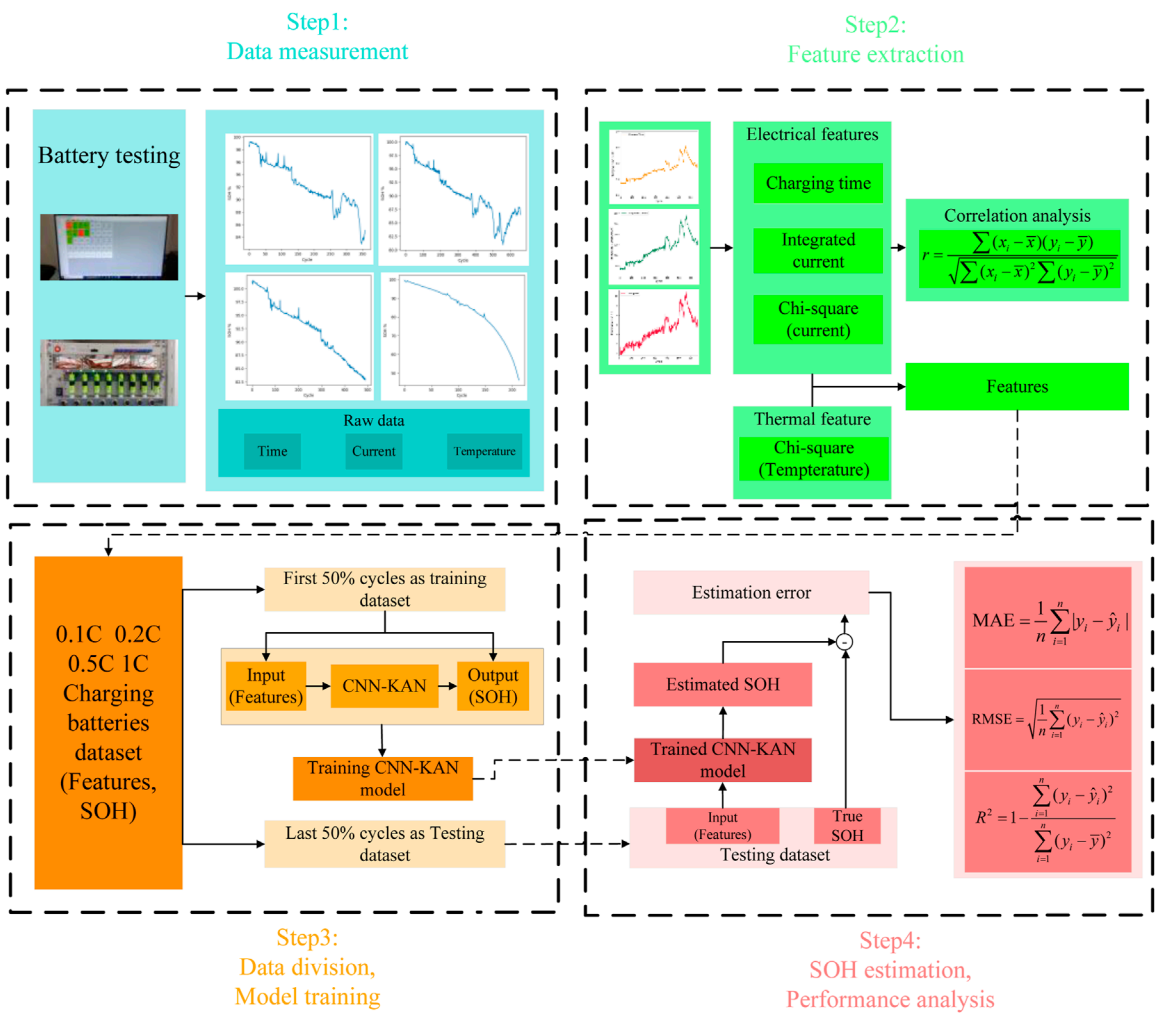

FIGURE 10
Experiemental flowchart.

(3) Discharging stage: A CC discharge was performed at a rate of 0.5C until the terminal voltage dropped to the lower cut-off value.

In this study, the lithium battery SOH is defined as the ratio of its current maximum discharge capacity to its initial rated capacity when it leaves the factory, providing an accurate and intuitive indication of battery performance degradation. The formula is defined in Equation 15 (Wang et al., 2022):

$$\mathrm{SOH} = \frac{Q_{max\,\mathrm{capacity}}}{Q_{\mathrm{rated\,capacity}}} \times 100\% \tag{15}$$

where $Q_{max\,\mathrm{capacity}}$ represents the battery's current maximum discharge capacity and $Q_{\mathrm{rated\,capacity}}$ refers to its rated capacity upon leaving the factory.

Figure 9A–D shows changes in four batteries SOH during multiple charge-discharge cycles at rates of 0.1C, 0.2C, 0.5C and 1C. The results show that battery SOH typically declines progressively with an increase in charge and discharge cycles. However, various factors, including temperature, charging rate, and aging mechanisms, significantly impact the battery, resulting in a complex and nonlinear SOH decay process. Battery capacity can exhibit different levels of regeneration across cycles. These influencing factors make the precise estimation of lithium battery SOH a challenging task. Table 2 shows the cycle aging parameters of the battery at four different charging rates.

4.2 Experimental results

The correlation coefficient between electrical features and battery SOH at four charging rates is calculated using the Person correlation coefficient method mentioned in Section 2.2. The results are presented in Table 3.

The table demonstrates that the Pearson correlation coefficients between the selected electrical parameters t_{CV}, S_I and $S_{\bar{I}}$ and the battery SOH across four different rates are nearly −1. This suggests a strong inverse relationship between these parameters and battery SOH, making them reliable indicators for monitoring battery aging trends.

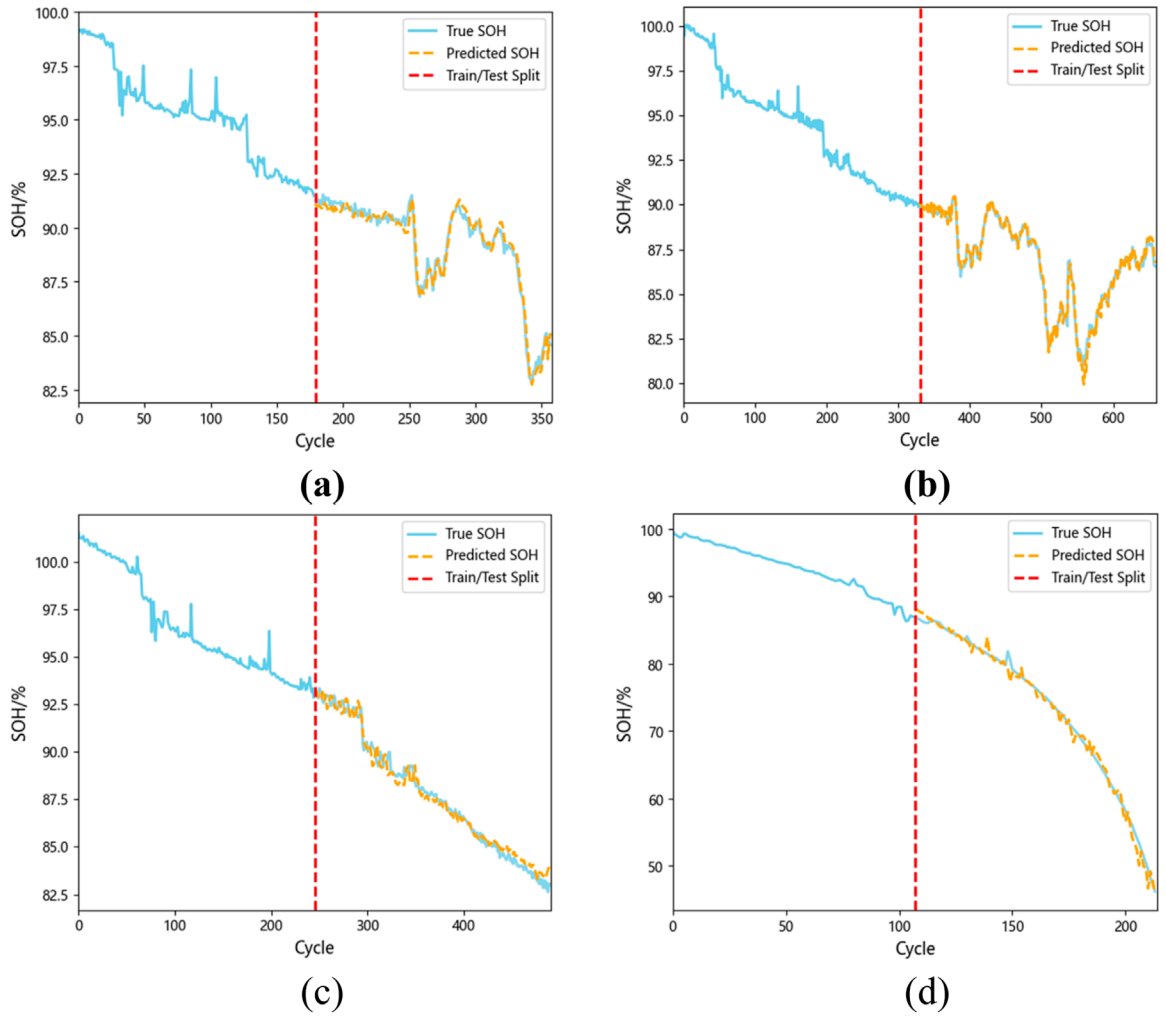

FIGURE 11
(A) SOH estimation results at 0.1C; **(B)** SOH estimation results at 0.2C; **(C)** SOH estimation results at 0.5C; **(D)** SOH estimation results at 1C.

TABLE 4 Performance of CNN-KAN in estimating SOH at four charging rates.

Charging rates (C)	MAE (%)	RMSE (%)	R^2 (%)
0.1	0.2479	0.3090	98.03
0.2	0.2096	0.2889	98.60
0.5	0.3254	0.4091	98.26
1	0.6799	0.9663	99.24

As outlined in the second section of this paper, the electrical and thermal features attributes of lithium batteries during CV stage at various rates are extracted and paired with their corresponding SOH values to create a comprehensive dataset. To preserve dataset's balance and ensure robust generalization in the model, the data is evenly split into training and test sets at a 1:1 ratio.

The training data is fed into the CNN-KAN model constructed in the third part of this paper. Taking 0.2C as an example, the number of filters of CNN in the model is 128, and each filter has a convolution kernel size of 3. The number of hidden layer neurons in the KAN part is 1,024 to process and interpret the features extracted by the convolution layer. To enhance the generalization ability of the model and prevent overfitting, L2 regularization with a coefficient of 1e-4 is applied after each convolution layer, and a dropout layer with a coefficient of 0.2 is added after the global average pooling layer. The optimization strategy for the model employs the Adam optimizer combined with an exponential decay learning rate scheduler, initializing the learning rate at 1e-4 with a decay rate of 0.9. This approach dynamically adjusts the learning rate, accelerates initial convergence, and allows for refinement with a lower learning rate in later stages. The model is trained for 100 epochs, with a batch size of 32, and the data is split with a training to validation set ratio of 8:2.

Figure 10 illustrates the experimental flowchart, which can be summarized as follows: First, battery tests are conducted at different charging rates to collect key data such as time, current,

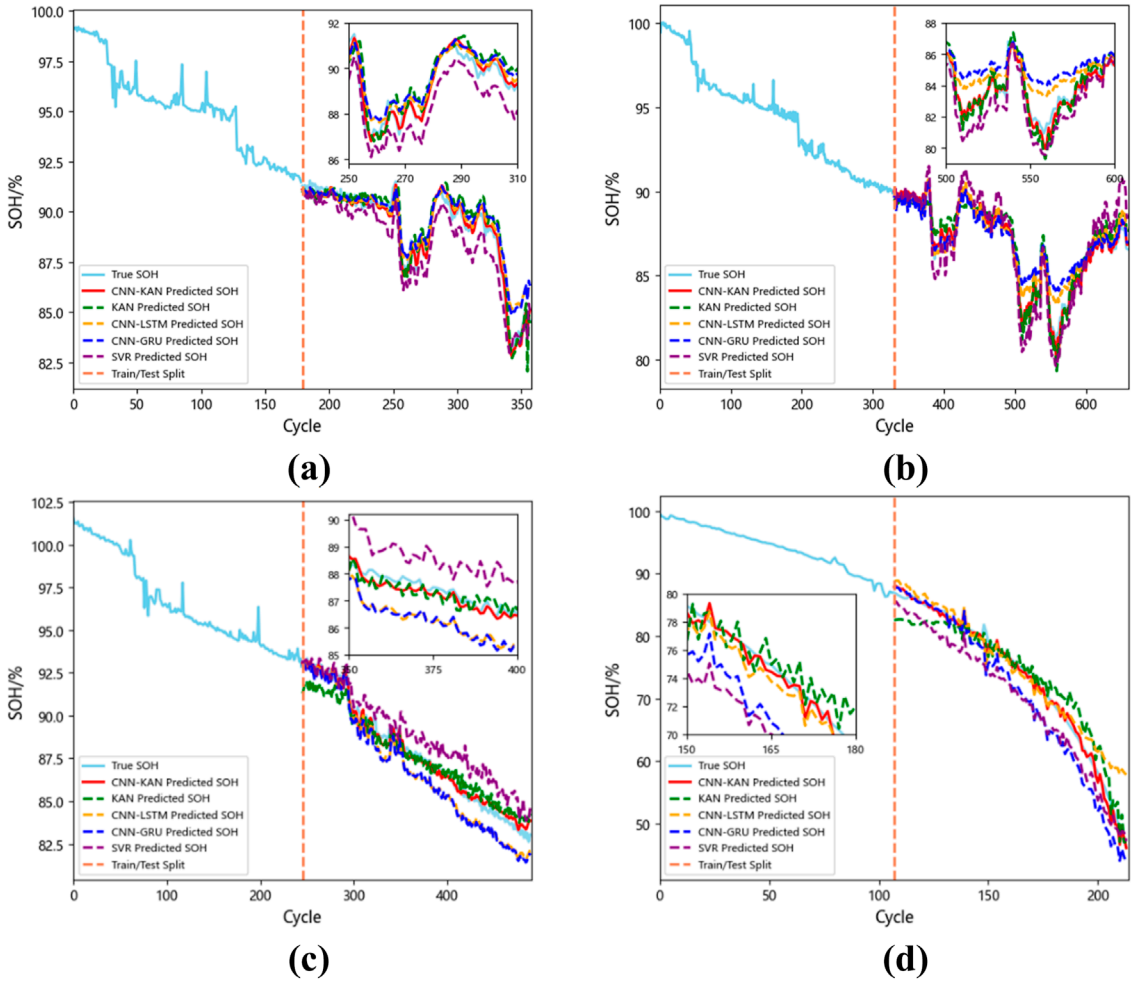

FIGURE 12
(A) Comparison of SOH estimation results at 0.1C; **(B)** Comparison of SOH estimation results at 0.2C; **(C)** Comparison of SOH estimation results at 0.5C; **(D)** Comparison of SOH estimation results at 1C.

TABLE 5 Evaluation indicators at 0.1C.

Model	MAE (%)	RMSE (%)	R^2 (%)
CNN-KAN	0.2479	0.3090	98.03
KAN	0.4986	0.6428	91.46
CNN-LSTM	0.4810	0.7089	89.61
CNN-GRU	0.5259	0.7260	89.11
SVR	0.7845	0.8779	84.07

TABLE 6 Evaluation indicators at 0.2C.

Model	MAE (%)	RMSE (%)	R^2 (%)
CNN-KAN	0.2096	0.2889	98.60
KAN	0.5615	0.6619	92.63
CNN-LSTM	0.5323	0.7235	91.19
CNN-GRU	0.6685	0.9637	84.37
SVR	0.8695	1.0659	80.88

and temperature. Then, electrical and thermal features are extracted from the raw data to form a dataset. Next, the dataset is split into training and testing sets, which are used to train the CNN-KAN model. Finally, the model's performance is evaluated by comparing the predicted SOH with the true SOH using error metrics like MAE, RMSE, and R^2.

Figure 11 presents the results of the SOH estimation.

To comprehensively evaluate accuracy of SOH estimation, this study utilized standard regression model performance evaluation indicators, including MAE, RMSE and R^2. These indicators provide an important quantitative basis for understanding model performance. The formulas used to calculate the above indicators

TABLE 7 Evaluation indicators at 0.5C.

Model	MAE (%)	RMSE (%)	R^2 (%)
CNN-KAN	0.3254	0.4091	98.26
KAN	0.6034	0.7224	94.56
CNN-LSTM	0.9648	1.0820	87.79
CNN-GRU	1.0376	1.1551	86.09
SVR	1.1214	1.2945	82.53

TABLE 8 Evaluation indicators at 1C.

Model	MAE (%)	RMSE (%)	R^2 (%)
CNN-KAN	0.6799	0.9663	99.24
KAN	2.2105	2.6456	94.33
CNN-LSTM	1.9875	3.0585	92.42
CNN-GRU	3.0041	3.6384	89.27
SVR	3.5943	3.7858	88.38

are described by Equations 16–18:

$$\mathrm{MAE} = \frac{1}{n}\sum_{i=1}^{n}|y_i - \hat{y}_i| \tag{16}$$

$$\mathrm{RMSE} = \sqrt{\frac{1}{n}\sum_{i=1}^{n}(y_i - \hat{y}_i)^2} \tag{17}$$

$$R^2 = 1 - \frac{\sum_{i=1}^{n}(y_i - \hat{y}_i)^2}{\sum_{i=1}^{n}(y_i - \bar{y})^2} \tag{18}$$

where n represents the total number of charge and discharge cycles, y_i represents actual SOH value, $\bar{y}$ is average of all actual SOH values and $\hat{y}_i$ is estimated SOH value. In the case of MAE and RMSE, lower values correspond to higher model estimation accuracy. Regarding R^2, a value closer to 1 signifies a superior model fit. The outcomes of SOH estimation method presented in this study are displayed in Table 4.

At these four charging rates, the MAE of the estimation results remains below 0.7%, RMSE is under 1%, and the R^2 exceeds 98%. Specifically, at a 0.1C charging rate, due to the lower charging current leading to a longer charging time for each cycle, the data may be more susceptible to external interference and noise, resulting in more noticeable fluctuations. However, the R^2 still reaches 98.03% and the RMSE is 0.31%. Particularly at the 0.1C, 0.2C, and 0.5C charging rates, despite the true SOH value exhibiting significant nonlinear changes, the SOH can still be estimated accurately, demonstrating the model's excellent fitting capability. These results clearly indicate that this approach can offer reliable and precise SOH estimates across various conditions.

4.3 Experimental comparisons

To verify the advantages of the CNN-KAN model, comparative experiments were conducted with KAN, CNN-LSTM, CNN-GRU and SVR models. We utilized the previously mentioned laboratory data across different charging rates, and the results of these comparisons are displayed in Figure 12A–D. Tables 5–8 provide a comparison of the MAE, RMSE and R^2 estimation results across diverse charging rates among the models.

The table shows that the introduced model surpasses the other four models. Leveraging the robust feature extraction capability of CNN, the CNN-KAN model presented in this paper achieves higher accuracy than the standalone KAN model, with RMSE reduced by at least 0.31% and R^2 increased by at least 3.7% across all four rates. Compared to traditional CNN-LSTM, CNN-GRU, and SVR models, the R^2 is improved by at least 6.82%.

LSTM and GRU capture long-term dependencies through their internal gating mechanisms, while SVR, as a regression algorithm based on statistical learning theory, can handle some nonlinearities using kernel functions. However, all three methods face limitations when dealing with highly nonlinear datasets. In contrast, KAN excels at handling complex nonlinear relationships by decomposing high-dimensional functions into combinations of univariate functions, making it more effective at capturing the nonlinear dependencies between input features and SOH.

The proposed CNN-KAN model can provide fast and accurate SOH estimation at different charging rates. These findings demonstrate that combining the electrical features of CV stage with the thermal feature, and processing their complex nonlinear relationship through an advanced neural network, is an effective method for monitoring battery health status.

5 Conclusion

This paper introduces a lithium-ion battery SOH estimation method built on multi-feature and CNN-KAN, which markedly improves the precision of SOH assessment.

This paper extracts the electrical and thermal features from the data of the CV stage of lithium batteries. The electrical features include the time, the integral of the current with respect to time and the chi-square value of the current. The features of lithium battery aging process are fully explored from the perspective of dynamic changes and long-term accumulation effects. The Person correlation coefficient method is employed to analyze and confirm that these features are highly correlated with battery SOH. Beyond the electrical features, the thermal feature of CV stage is as well combined to take into account the impact of the long-term accumulated thermal effect on the battery SOH. A mathematical model is then established that links these quantitative features with the battery SOH, ensuring precise SOH estimation based on the identified features for any charging cycle.

On this basis, this paper proposes a CNN-KAN model with excellent performance. This model leverages the strengths of CNN in efficiently extracting key features from raw data and KAN in effectively capturing complex nonlinear relationships in data through adaptive grids and B-spline basis functions. The model underwent thorough validation across four datasets with

varying charging current rates. The findings reveal that despite the pronounced nonlinearity in the battery SOH decay process, MAE is 0.25%, 0.21%, 0.33% and 0.68%, RMSE is 0.31%, 0.29%, 0.41% and 0.97% and an average R^2 of 98.53%. At a charging rate of 1C, the upper R^2 is as high as 99.24%. Comparative experiments with KAN, CNN-LSTM, CNN-GRU, and SVR models further confirm the excellence of CNN-KAN.

This study presents a novel method for estimating the SOH of lithium-ion batteries by combining multiple features and a CNN-KAN model. The proposed method shows significant potential for real-world applications and future research. By analyzing electrical and thermal characteristics, the model offers a more comprehensive perspective on battery performance, making it particularly suitable for real-time monitoring of battery status in electric vehicles and renewable energy storage systems. This research lays the groundwork for exploring more advanced architectures or hybrid models to further enhance the accuracy of battery SOH prediction. Additionally, future studies could incorporate more environmental factors to further improve the model's predictive capabilities. We believe this study will strongly support further exploration in the field of battery health diagnostics.

Data availability statement

The original contributions presented in the study are included in the article/supplementary material, further inquiries can be directed to the corresponding authors.

Author contributions

ZZ: Writing–original draft, Writing–review and editing, Conceptualization, Data curation, Formal Analysis, Funding acquisition, Investigation, Methodology, Project administration, Resources, Software, Supervision, Validation, Visualization. XiL: Data curation, Software, Validation, Visualization, Writing–review and editing. RZ: Data curation, Software, Visualization, Writing–review and editing. XuL: Writing–review and editing. SC: Writing–review and editing. ZS: Writing–review and editing. HJ: Writing–review and editing.

Funding

The author(s) declare that financial support was received for the research, authorship, and/or publication of this article. This work was supported by the scientific research foundation for high-level personnel in Jinling Institute of Technology (jit-b-201811) and the Industry-University-Research Cooperation Project of Jiangsu Province (BY2021300).

Conflict of interest

The authors declare that the research was conducted in the absence of any commercial or financial relationships that could be construed as a potential conflict of interest.

Publisher's note

All claims expressed in this article are solely those of the authors and do not necessarily represent those of their affiliated organizations, or those of the publisher, the editors and the reviewers. Any product that may be evaluated in this article, or claim that may be made by its manufacturer, is not guaranteed or endorsed by the publisher.

References

Amir, S., Gulzar, M., Tarar, M. O., Naqvi, I. H., Zaffar, N. A., and Pecht, M. G. (2022). Dynamic equivalent circuit model to estimate state-of-health of lithium-ion batteries. *IEEE Access* 10, 18279–18288. doi:10.1109/ACCESS.2022.3148528

Bao, Z., Jiang, J., Zhu, C., and Gao, M. (2022). A new hybrid neural network method for state-of-health estimation of lithium-ion battery. *Energies* 15 (12), 4399. doi:10.3390/en15124399

Bao, X., Chen, L., Lopes, A. M., Li, X., Xie, S., Li, P., et al. (2023). Hybrid deep neural network with dimension attention for state-of-health estimation of Lithium-ion Batteries. *Energy* 278, 127734. doi:10.1016/j.energy.2023.127734

Che, Y., Vilsen, S. B., Meng, J., Sui, X., and Teodorescu, R. (2023). Battery health prognostic with sensor-free differential temperature voltammetry reconstruction and capacity estimation based on multi-domain adaptation. *eTransportation* 17, 100245. doi:10.1016/j.etran.2023.100245

Chen, D., Zhang, W., Zhang, C., Sun, B., Cong, X., Wei, S., et al. (2022). A novel deep learning-based life prediction method for lithium-ion batteries with strong generalization capability under multiple cycle profiles. *Appl. Energy* 327, 120114. doi:10.1016/j.apenergy.2022.120114

Cui, S., and Joe, I. (2021). A dynamic spatial-temporal attention-based GRU model with healthy features for state-of-health estimation of lithium-ion batteries. *IEEE Access* 9, 27374–27388. doi:10.1109/ACCESS.2021.3058018

Feng, X., Weng, C., He, X., Han, X., Lu, L., Ren, D., et al. (2019). Online state-of-health estimation for Li-ion battery using partial charging segment based on support vector machine. *IEEE Trans. Veh. Technol.*, 68(9), 8583–8592. doi:10.1109/TVT.2019.2927120

Feng, F., Teng, S., Liu, K., Xie, J., Xie, Y., Liu, B., et al. (2020). Co-estimation of lithium-ion battery state of charge and state of temperature based on a hybrid electrochemical-thermal-neural-network model. *J. Power Sources* 455, 227935. doi:10.1016/j.jpowsour.2020.227935

Gao, X., Jia, Y., Zhang, W., Yuan, C., and Xu, J. (2022). Mechanics-driven anode material failure in battery safety and capacity deterioration issues: a review. *Appl. Mech. Rev.* 74 (6), 060801. doi:10.1115/1.4054566

He, Y., Deng, Z., Chen, J., Li, W., Zhou, J., Xiang, F., et al. (2024). State-of-health estimation for fast-charging lithium-ion batteries based on a short charge curve using graph convolutional and long short-term memory networks. *J. Energy Chem.* 98, 1–11. doi:10.1016/j.jechem.2024.06.024

Hou, W., Lu, Y., Ou, Y., Zhou, P., Yan, S., He, X., et al. (2023). Recent advances in electrolytes for high-voltage cathodes of lithium-ion batteries. *Trans. Tianjin Univ.* 29 (2), 120–135. doi:10.1007/s12209-023-00355-0

Jenu, S., Hentunen, A., Haavisto, J., and Pihlatie, M. (2022). State of health estimation of cycle aged large format lithium-ion cells based on partial charging. *J. Energy Storage* 46, 103855. doi:10.1016/j.est.2021.103855

Jiang, J., Zhao, S., and Zhang, C. (2021). State-of-Health estimate for the lithium-ion battery using chi-square and ELM-LSTM. *World Electr. Veh. J.* 12 (4), 228. doi:10.3390/wevj12040228

Khan, M. K., Houran, M. A., Kauhaniemi, K., Zafar, M. H., Mansoor, M., and Rashid, S. (2024). Efficient state of charge estimation of lithium-ion batteries in electric vehicles using evolutionary intelligence-assisted GLA–CNN–Bi-LSTM deep learning model. *Heliyon* 10 (15), e35183. doi:10.1016/j.heliyon.2024.e35183

Kim, J., Oh, S., Kim, H., and Choi, W. (2023). Tutorial on time series prediction using 1D-CNN and BiLSTM: a case example of peak electricity

demand and system marginal price prediction. *Eng. Appl. Artif. Intell.* 126, 106817. doi:10.1016/j.engappai.2023.106817

Li, X., Yuan, C., and Wang, Z. (2020). State of health estimation for Li-ion battery via partial incremental capacity analysis based on support vector regression. *Energy* 203, 117852. doi:10.1016/j.energy.2020.117852

Li, R., Li, W., and Zhang, H. (2022). State of health and charge estimation based on adaptive boosting integrated with particle swarm optimization/support vector machine (AdaBoost-PSO-SVM) model for lithium-ion batteries. *Int. J. Electrochem. Sci.* 17 (2), 220212. doi:10.20964/2022.02.03

Liu, W., Placke, T., and Chau, K. T. (2022). Overview of batteries and battery management for electric vehicles. *Energy Rep.* 8, 4058–4084. doi:10.1016/j.egyr.2022.03.016

Liu, S., Nie, Y., Tang, A., Li, J., Yu, Q., and Wang, C. (2023). Online health prognosis for lithium-ion batteries under dynamic discharge conditions over wide temperature range. *eTransportation* 18, 100296. doi:10.1016/j.etran.2023.100296

Liu, H., Deng, Z., Che, Y., Xu, L., Wang, B., Wang, Z., et al. (2024). Big field data-driven battery pack health estimation for electric vehicles: a deep-fusion transfer learning approach. *Mech. Syst. Signal Process.* 218, 111585. doi:10.1016/j.ymssp.2024.111585

Liu Z., Z., Wang, Y., Vaidya, S., Ruehle, F., Halverson, J., Soljačić, M., et al. (2024) KAN: Kolmogorov-arnold networks. arXiv. Available at: http://arxiv.org/abs/2404.19756.

Ma, B., Yang, S., Zhang, L., Wang, W., Chen, S., Yang, X., et al. (2022). Remaining useful life and state of health prediction for lithium batteries based on differential thermal voltammetry and a deep-learning model. *J. Power. Sources* 548, 232030. doi:10.1016/j.jpowsour.2022.232030

Rojas, O. E., and Khan, M. A. (2022). A review on electrical and mechanical performance parameters in lithium-ion battery packs. *J. Clean. Prod.* 378, 134381. doi:10.1016/j.jclepro.2022.134381

Tian, J., Xiong, R., and Shen, W. (2020). State-of-Health estimation based on differential temperature for lithium ion batteries. *IEEE Trans. Power Electron.* 35 (10), 10363–10373. doi:10.1109/TPEL.2020.2978493

Tran, M.-K., Mathew, M., Janhunen, S., Panchal, S., Raahemifar, K., Fraser, R., et al. (2021). A comprehensive equivalent circuit model for lithium-ion batteries, incorporating the effects of state of health, state of charge, and temperature on model parameters. *J. Energy Storage* 43, 103252. doi:10.1016/j.est.2021.103252

Wang, Y., Tian, J., Sun, Z., Wang, L., Xu, R., Li, M., et al. (2020). A comprehensive review of battery modeling and state estimation approaches for advanced battery management systems. *Renew. Sustain. Energy Rev.* 131, 110015. doi:10.1016/j.rser.2020.110015

Wang, S., Liu, K., Wang, Y., Stroe, D.-I., Fernandez, C., and Guerrero, J. M. (2022). *Multidimensional lithium-ion battery status monitoring.* 1st ed. Boca Raton, FL: CRC Press, 23. doi:10.1201/9781003333791

Wang, C., Wang, R., Zhang, C., and Yu, Q. (2024). Coupling effect of state of charge and loading rate on internal short circuit of lithium-ion batteries induced by mechanical abuse. *Appl. Energy* 375, 124138. doi:10.1016/j.apenergy.2024.124138

Xiong, R., Li, L., Li, Z., Yu, Q., and Mu, H. (2018). An electrochemical model based degradation state identification method of Lithium-ion battery for all-climate electric vehicles application. *Appl. Energy* 219, 264–275. doi:10.1016/j.apenergy.2018.03.053

Xu, Z., Wang, J., Lund, P. D., and Zhang, Y. (2022). Co-estimating the state of charge and health of lithium batteries through combining a minimalist electrochemical model and an equivalent circuit model. *Energy* 240, 122815. doi:10.1016/j.energy.2021.122815

Xu, R., Wang, Y., and Chen, Z. (2023). A hybrid approach to predict battery health combined with attention-based transformer and online correction. *J. Energy Storage* 65, 107365. doi:10.1016/j.est.2023.107365

Yang, S., Zhang, C., Jiang, J., Zhang, W., Gao, Y., and Zhang, L. (2021a). A voltage reconstruction model based on partial charging curve for state-of-health estimation of lithium-ion batteries. *J. Energy Storage* 35, 102271. doi:10.1016/j.est.2021.102271

Yang, S., Zhang, C., Jiang, J., Zhang, W., Zhang, L., and Wang, Y. (2021b). Review on state-of-health of lithium-ion batteries: characterizations, estimations and applications. *J. Clean. Prod.* 314, 128015. doi:10.1016/j.jclepro.2021.128015

Yang, Y., Xu, Y., Nie, Y., Li, J., Liu, S., Zhao, L., et al. (2024). Deep transfer learning enables battery state of charge and state of health estimation. *Energy* 294, 130779. doi:10.1016/j.energy.2024.130779

Ye, L., Peng, D., Xue, D., Chen, S., and Shi, A. (2023). Co-estimation of lithium-ion battery state-of-charge and state-of-health based on fractional-order model. *J. Energy Storage* 65, 107225. doi:10.1016/j.est.2023.107225

Yu, Q., Nie, Y., Peng, S., Miao, Y., Zhai, C., Zhang, R., et al. (2023). Evaluation of the safety standards system of power batteries for electric vehicles in China. *Appl. Energy* 349, 121674. doi:10.1016/j.apenergy.2023.121674

Zhang, C., Luo, L., Yang, Z., Du, B., Zhou, Z., Wu, J., et al. (2024). Flexible method for estimating the state of health of lithium-ion batteries using partial charging segments. *Energy* 295, 131009. doi:10.1016/j.energy.2024.131009

Zhang, C., Zhu, Y., Dong, G., and Wei, J. (2019). Data-driven lithium-ion battery states estimation using neural networks and particle filtering. *Int. J. Energy Res.* 43 (14), er.4820–8241. doi:10.1002/er.4820

Zhang, S., Guo, X., Dou, X., and Zhang, X. (2020). A rapid online calculation method for state of health of lithium-ion battery based on coulomb counting method and differential voltage analysis. *J. Power Sources* 479, 228740. doi:10.1016/j.jpowsour.2020.228740

Zhang, C., Zhao, S., Yang, Z., and Chen, Y. (2022). A reliable data-driven state-of-health estimation model for lithium-ion batteries in electric vehicles. *Front. Energy Res.* 10, 1013800. doi:10.3389/fenrg.2022.1013800

Zhang, C., Zhao, S., Yang, Z., and He, Y. (2023a). A multi-fault diagnosis method for lithium-ion battery pack using curvilinear Manhattan distance evaluation and voltage difference analysis. *J. Energy Storage* 67, 107575. doi:10.1016/j.est.2023.107575

Zhang, C., Luo, L., Yang, Z., Zhao, S., He, Y., Wang, X., et al. (2023b). Battery SOH estimation method based on gradual decreasing current, double correlation analysis and GRU. *Green Energy Intelligent Transp.* 2 (5), 100108. doi:10.1016/j.geits.2023.100108

Zhang, Z., Ji, C., Liu, Y., Wang, Y., Wang, B., and Liu, D. (2024). Effect of aging path on degradation characteristics of lithium-ion batteries in low-temperature environments. *Batteries* 10 (3), 107. doi:10.3390/batteries10030107

Zhao, J., Feng, X., Pang, Q., Fowler, M., Lian, Y., Ouyang, M., et al. (2024). Battery safety: machine learning-based prognostics. *Prog. Energy Combust. Sci.* 102, 101142. doi:10.1016/j.pecs.2023.101142

Zheng, Y., Cui, Y., Han, X., and Ouyang, M. (2021). A capacity prediction framework for lithium-ion batteries using fusion prediction of empirical model and data-driven method. *Energy* 237, 121556. doi:10.1016/j.energy.2021.121556

Zhu, Y., Gu, X., Liu, K., Zhao, W., and Shang, Y. (2024). Rapid test and assessment of lithium-ion battery cycle life based on transfer learning. *IEEE Trans. Transp. Electrification*, 1. doi:10.1109/TTE.2024.3354107

frontiers | Frontiers in Energy Research

TYPE Original Research
PUBLISHED 05 November 2024
DOI 10.3389/fenrg.2024.1488718

OPEN ACCESS

EDITED BY
Chaolong Zhang,
Jinling Institute of Technology, China

REVIEWED BY
Zhenkun Liu,
Nanjing University of Posts and Telecommunications, China
Xing Yang,
Anhui Science and Technology University, China
Pei Shi,
Wuxi University, China

*CORRESPONDENCE
Weixiao Lu,
luweixiao00@163.com

RECEIVED 30 August 2024
ACCEPTED 22 October 2024
PUBLISHED 05 November 2024

CITATION
Fang H, Lin S, Zhu J and Lu W (2024) Application of deep forest algorithm incorporating seasonality and temporal correlation for wind speed prediction in offshore wind farm.
Front. Energy Res. 12:1488718.
doi: 10.3389/fenrg.2024.1488718

Application of deep forest algorithm incorporating seasonality and temporal correlation for wind speed prediction in offshore wind farm

Haipeng Fang[1], Shuo Lin[1], Jinglin Zhu[1] and Weixiao Lu[2]*

[1]Hainan Shenneng New Energy Co., LTD., Haikou, Hainan, China, [2]School of Atmospheric Physics, Nanjing University of Information Science and Technology, Nanjing, Jiangsu, China

Accurate prediction of wind speed is a prerequisite for the safe and accurate operation of wind power generation, however, WRF models typically do not produce sufficiently accurate wind speed predictions. This study proposed a Seasonal and Temporal Correlation - Deep Forest (STC-DF) model for offshore wind speed prediction. Different from traditional methods, the STC-DF model takes the advantages of the deep forest algorithm to automatically learn complex feature interactions without manual feature engineering. The model is designed to capture the seasonal and temporal characteristics of wind speed variations. To test the effectiveness of the proposed method, we applied the trained STC-DF model to an offshore wind farm in Hainan Province, China. Seven days of data from each season were selected for testing. The results show that the STC-DF model can effectively reduce the error caused by WRF forecast. The error index of the corrected wind speed reduced more than 40%, the accuracy of wind speed forecast increased 15%. And the method passed the multi-model comparison test and robustness experiment. These research results show that the STC-DF model has strong versatility and good correction ability, and is suitable for wind speed forecasting in different regions, which is a feasible method to improve the reliability of offshore wind power generation.

KEYWORDS

wind speed prediction, wind speed correction, deep forest, seasonality, temporal correlation, offshore wind farm

1 Introduction

Global climate change, energy supply and energy costs are becoming increasingly important to government authorities and society. As a result, countries are analyzing greater diversification of their sources of power generation towards renewable resources (Díaz and Soares, 2020). Renewable energy plays a key role in China's energy strategy (Zhang and Wang, 2022). Wind energy has the prospect of being an alternative source of energy for power generation and, unlike fossil fuels, it reduces the amount of carbon dioxide emitted into the atmosphere. This intermittent nature of energy has led to the development and improvement of wind forecasting systems (Pereyra-castro and Caetano, 2022). China is a vast country with a total of 300 million kilowatts of wind energy that can be exploited annually in the country (Qian et al., 2016). As the development of onshore wind power in

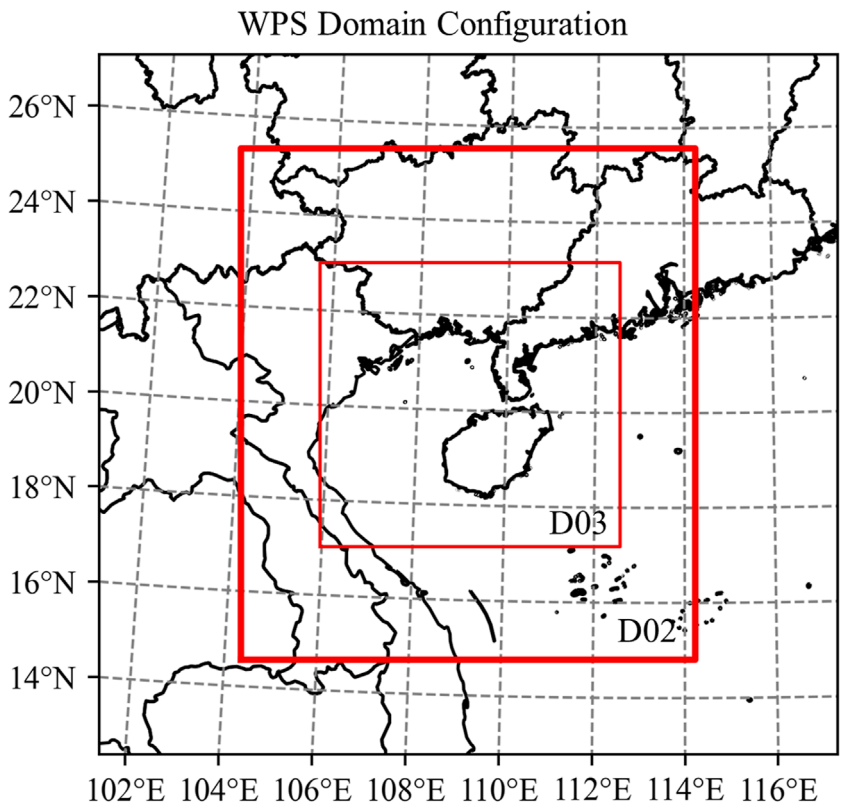

FIGURE 1
WRF model simulation area.

China is already relatively saturated, the development of offshore wind power will become an important means of addressing the fundamental interplay between future energy mix and supply patterns (Chen and Lin, 2022). The continental coastline is 18,400 km long (Zhang and Wang, 2022), with an island coastline of 14,247 km and a total coastline length of more than 32,600 km, there is great potential for the development of offshore wind resources. After more than two decades of industrialization and development, the offshore wind power industry has gradually moved from the demonstration stage to the commercialization stage, and is receiving more and more attention from national governments (Soares-Ramos et al., 2020; Irena, 2016). Wind speed prediction can effectively predict the future wind strength and power output of wind turbines, which provides data support for wind power operators to design wind turbine on-line strategies and maintenance plans, and can improve the competitiveness of wind power products in the energy market. Therefore, the accurate prediction of wind speed in offshore wind farms is of vital importance for the development of renewable energy.

Wind speed prediction today can be categorized into two schemes: data-driven schemes and physical schemes. Data-driven methods are currently a hot area for researchers in the field of wind power. It uses the intrinsic relationship of multi-source meteorological data to build mathematical and statistical models (Yang et al., 2005; Zeng et al., 2012), machine learning models (Liu et al, 2021a; Cassola and Burlando, 2012) and hybrid models (Papaefthymiou and Klockl, 2008; Liu et al, 2021b) and other prediction models to predict wind speed. However, the prediction step provided by traditional statistical model is difficult to meet the needs of China's wind farms (Zheng et al., 2011). Physical methods can be subdivided into two categories: numerical weather prediction methods (NWP) and spatial correlation methods (Zhang et al., 2020). The NWP method uses weather forecast data such as temperature, pressure, surface roughness, and obstacles to predict wind power, which is suitable for predicting wind power in power plants because it describes atmospheric motion without the need for large amounts of historical data (Yu et al., 2019). Currently, there are many different physical methods for wind speed prediction such as high-resolution limited area model (HIRLAM) (Landberg, 1999)、Mesoscale Model5 (MM5) (Salcedo-Sanz et al., 2009) and Weather Research and Forecasting (WRF) model (Zhao et al., 2017). Among them, the WRF model can provide ultra-high resolution and its Large Eddy Simulations (LES) scheme can effectively simulate the atmospheric motions of wind farms due to the fact that it is favored by wind farm operators (Prósper et al., 2019). However, numerical weather prediction results in large errors due to imperfect physical parameterization schemes, low resolution, and inaccurate topography. Due to the errors in wind speed prediction, it is difficult to meet the needs of wind farms in China (Xiong et al., 2023; Chang et al., 2015; Hu, 2016; Zhang et al., 2013). Meanwhile, physical algorithms have advantages in long-term forecasting. However,

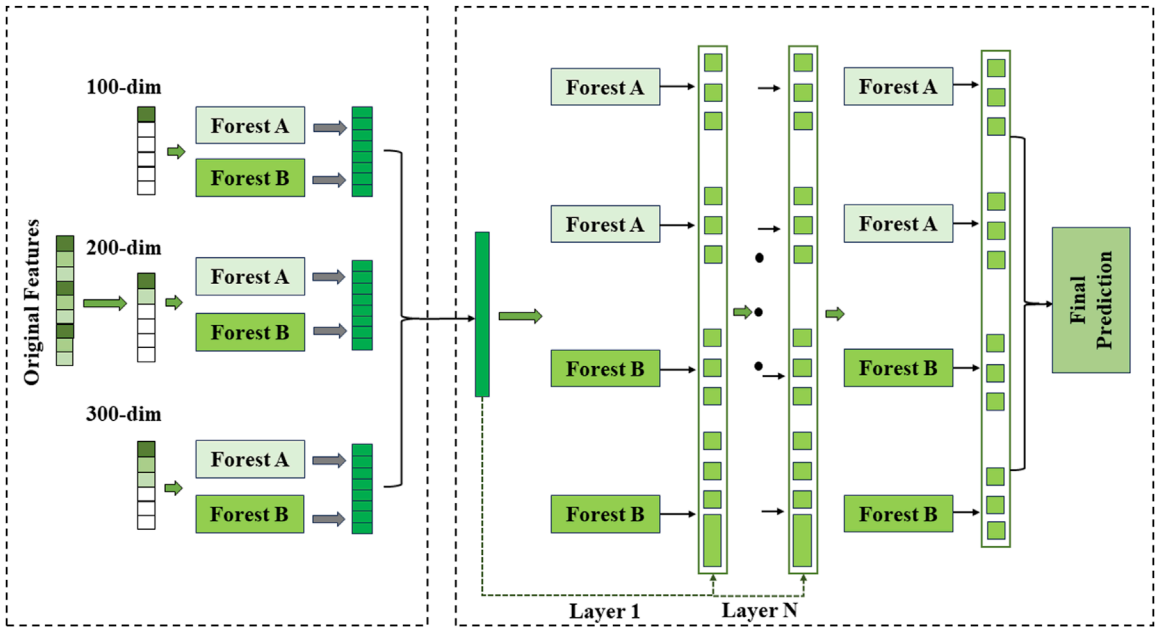

FIGURE 2
The structure of Deep Forest algorithm.

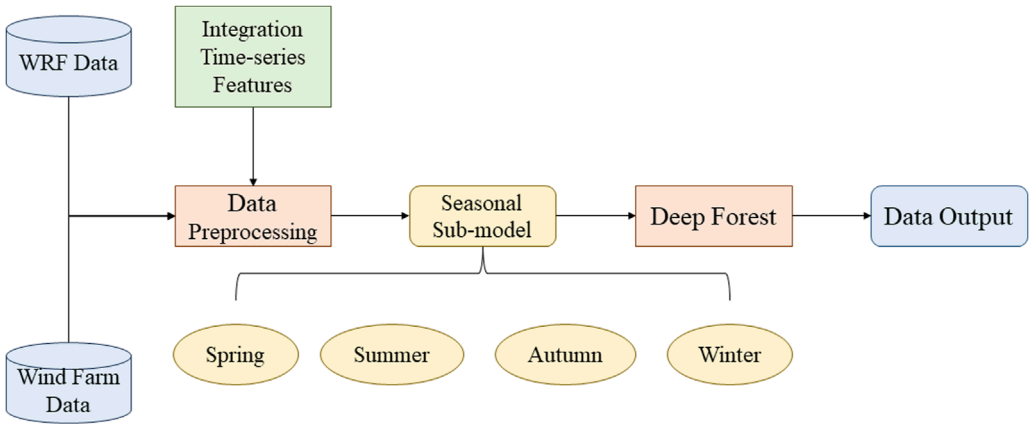

FIGURE 3
The flowchart of the proposed hybrid model.

they require a lot of computational time and are not suitable for short-term forecasting (Liu et al., 2015). Therefore, a single physical model needs to be assisted by other methods to realize high-precision wind power prediction in practical engineering applications.

Popular data-driven techniques mainly include signal processing, machine learning and information fusion (Zhang et al., 2023). In recent years, there has been a gradual increase in the research of using multiple meta-learners to combine to form highly interpretable models (Jiang et al., 2024; Liu et al., 2023; Liu et al., 2024a; Liu et al., 2024b), and the combination of signal processing and machine learning to construct hybrid models for wind speed prediction has become a hot topic (Jiang et al., 2023; Zhang et al., 2024). Literature (Chen et al., 2022) proposed a new wind speed prediction model that combines CEEMDAN, VMD, and LSTM. The error model combining VMD and LSTM can extract deeper features and improve the correction effect of the model. Zhang and Liu (2022) focused on post-processing the error signals and proposed an ELM-ICEEMDAN-ARIMA hybrid model for short-term wind speed forecasting. Zhou et al. (2023) proposed a hybrid prediction method for wind speed combining machine learning algorithms such as variational modal decomposition (VMD), principal component analysis (PCA) and random forest (RF). Xiong et al. (2023) extracted the wind speed

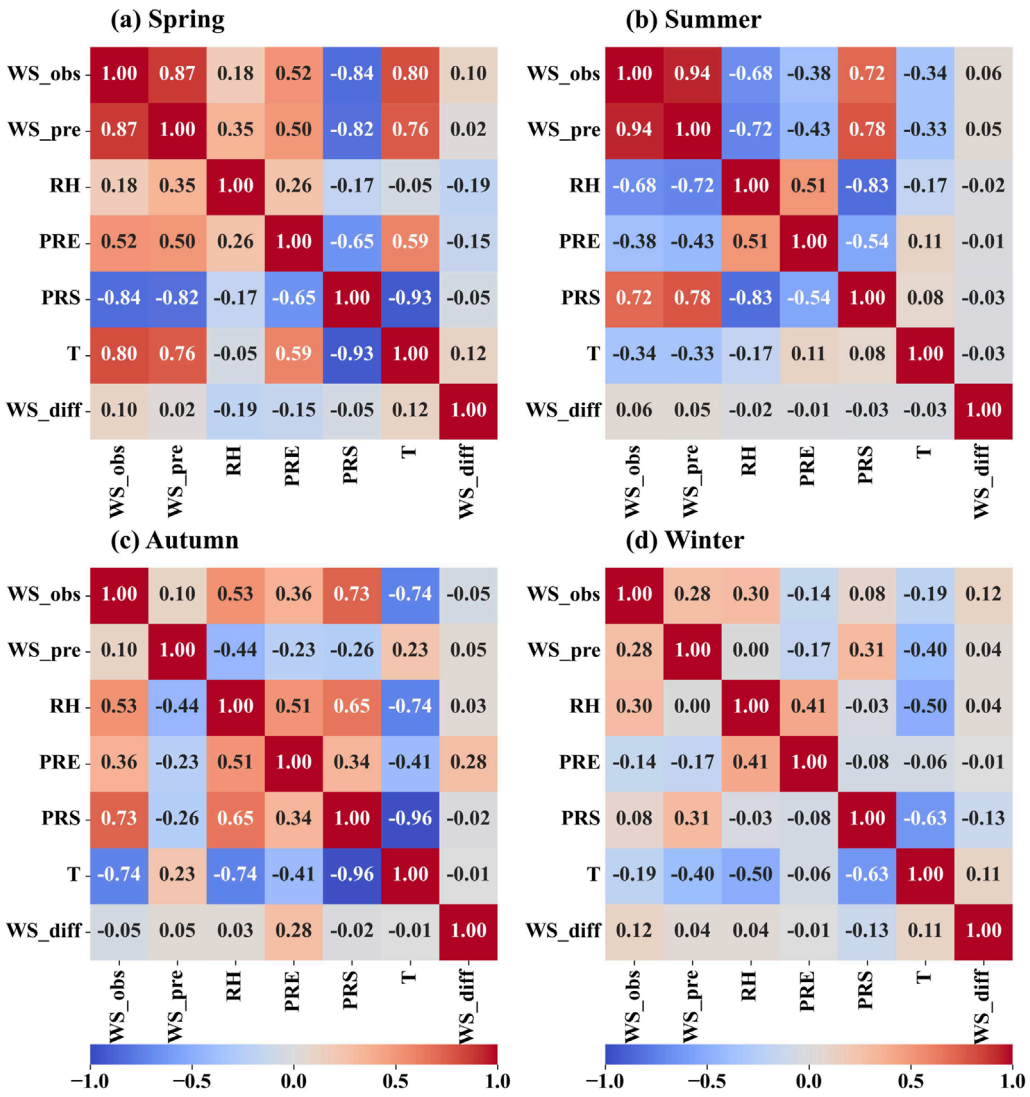

FIGURE 4
Correlation plots between the variables of the seasonal sub-models. **(A)** Spring, **(B)** Summer, **(C)** Aututmn, **(D)** Winter.

fluctuation features and labeled them using the fluctuation stable day model, and combined them with BO and LSTM for wind speed prediction. Establishing a suitable AI hybrid model to predict wind speed will be of great significance for the proper operation of wind farms.

Deep Forest is a cascade random forest algorithm based on deep models (Mao and Li, 2024), Compared to deep neural networks, it has fewer hyperparameters, lower data requirements, adaptive model complexity, and good robustness and generalization capabilities. Therefore, it is widely used in target recognition, image processing, text recognition, fault diagnosis, network intrusion detection, medical diagnosis, and other fields (Zhou and Feng, 2019). Mao introduced the idea of weight distribution in the cascade forest construction stage and proposed an improved DF algorithm based on information theory. This algorithm evaluates training samples to decide whether they enter the next level of training, thereby reducing the number of samples and improving the model's parallel training efficiency (Mao et al., 2022). Yin et al. (2020) applied the deep forest regression method to short-term load forecasting in power systems. The results showed that the default configuration parameters of the deep forest regression could improve short-term prediction accuracy and reduce the impact of experience on hyperparameter configuration of deep learning models. Liu et al. (2020) proposed a combined deep forest-based prediction model for short-term wind speed prediction. Wang et al. (2021) combined empirical modal decomposition and deep forests for wind speed prediction. Although the direct application of deep forests in wind speed prediction is not yet widespread, integrated learning methods have shown good potential in this field. Deep forest, as a powerful integrated learning algorithm, is expected to play a greater role in future wind speed prediction research.

However, offshore wind farms are subject to various factors due to their unique topographical characteristics, resulting in poor

TABLE 1 Evaluation of the seasonal sub-models forecast effect.

		RMSE (m/s)	rRMSE (%)	FA (%)	R
Spring	WRF	2.57	24.6	34.2	0.87
	STC-DF	1.78	18.8	47.5	0.94
Summer	WRF	3.77	24.5	11.9	0.94
	STC-DF	2.63	19.6	20.1	0.94
Autumn	WRF	2.94	35.4	12.5	0.1
	STC-DF	1.97	27	32	0.72
Winter	WRF	2.02	35.6	37.2	0.28
	STC-DF	1.32	21.3	56.2	0.72

wind speed stability. Wind speed prediction models will face greater challenges and need to be updated more frequently to adapt to the changes brought about by different influencing factors. In summary, the field of wind speed prediction has the following issues to be addressed:

(1) The influencing factors of wind speed prediction methods are not comprehensively considered. Wind speed exhibits seasonality, with variations in speed and volatility across different seasons. Seasonal factors have a significant impact on wind speed sequences.
(2) The feature factors input into wind speed prediction models are highly limited. Traditional prediction models only use wind speed data as input, without considering the impact of meteorological elements on wind speed variations and the historical autocorrelation of the input data. Therefore, it is difficult to capture subtle changes and short-term fluctuations in the data.

To address the above issues, we propose a model named Seasonal and Temporal Correlation - Deep Forest (STC-DF), which considers the impact of seasonal characteristic changes and temporal correlation of wind speed variations on wind speed prediction for offshore wind farms. The contributions of this study to the above two issues are as follows:

(1) Seasonal Training Correction Model: By extracting the main features from various meteorological elements of NWP predictions for each season, the input feature factors of the model are enriched. Appropriate models are selected for training and prediction on specific data to more accurately capture the randomness, intermittency, and volatility characteristics of actual wind speed.
(2) Incorporating Data Differencing: By including adjacent differences in predicted wind speed, trends and seasonality are eliminated, and lag effects are reduced. This reveals hidden patterns and relationships in the original time series, providing the model with more useful features and thereby improving prediction performance.

Through multi-model comparison test and robustness experiment, the effectiveness and generalizability of this method for wind speed prediction correction have been verified.

2 Data and methods

2.1 Data

The target wind farm for this study is an offshore wind farm in Hainan Province, and the wind speed data used are system derived wind speeds at the wind farm level with a time resolution of 15 min. The forecast data were generated by the WRF system, and since the turbine hub height is 70 m, 70-m wind speed (WS_pre), 2-m temperature (T), 2-m surface pressure (PRS), precipitation (PRE) and 2-m humidity (RH) were selected as input features for the correcting model. Connect all the data according to the timestamp and perform preprocessing such as fusion and cleaning. The data of the target wind farm in 2023 was selected as the study data. In the field of meteorology, seasons are usually divided according to the change of temperature patterns: spring (March-May), summer (June-August), autumn (September-November) and winter (December-February) (Linacre, 1992). The data from the last 7 days of each season was selected as the test set and the rest of the data was used as the training set.

2.2 Method

2.2.1 WRF model

In this study, the WRF regional mesoscale numerical prediction model is used to simulate the offshore wind farm, and the WRF model adopts a three-layer nested grid structure, with the grid numbers of 180 × 190, 100 × 90, and 110 × 110, and the grid spacings of 27 km, 9 km, and 3 km, respectively, and the initial field and boundary conditions are based on the Global Weather Forecast (GWF) data provided by the National Centers for Environmental Prediction (NCEP). The initial field and boundary conditions are based on the global weather forecast data provided by the National Centers for Environmental Prediction (NCEP) of the United States, with a temporal resolution of 7 days and a spatial resolution of 1° × 1°. Figure 1 shows the basic operation of the WRF model. In the WRF model setup, the physical process parameterization schemes, such as the Yonsei University boundary layer parameterization scheme (Hong et al., 2006), the Grell-Freitas convective parameterization scheme (Grell and Freitas, 2014), the RRTMG short- and long-wavelength radiation scheme (Iacono et al., 2008), and the Noah surface process scheme (Chen and Dudhia, 2001), are used. The time integration is based on the Runge-Kutta 3rd order scheme, and the computational time step is adaptively adjusted according to the CFL conditions.

2.2.2 Deep forest

Deep Forest (DF) (Zhou and Feng, 2019) is an integrated learning algorithm based on deep learning. The method stacks multiple random forest models together to form a deep network structure, and uses the output of each layer of random forest as the

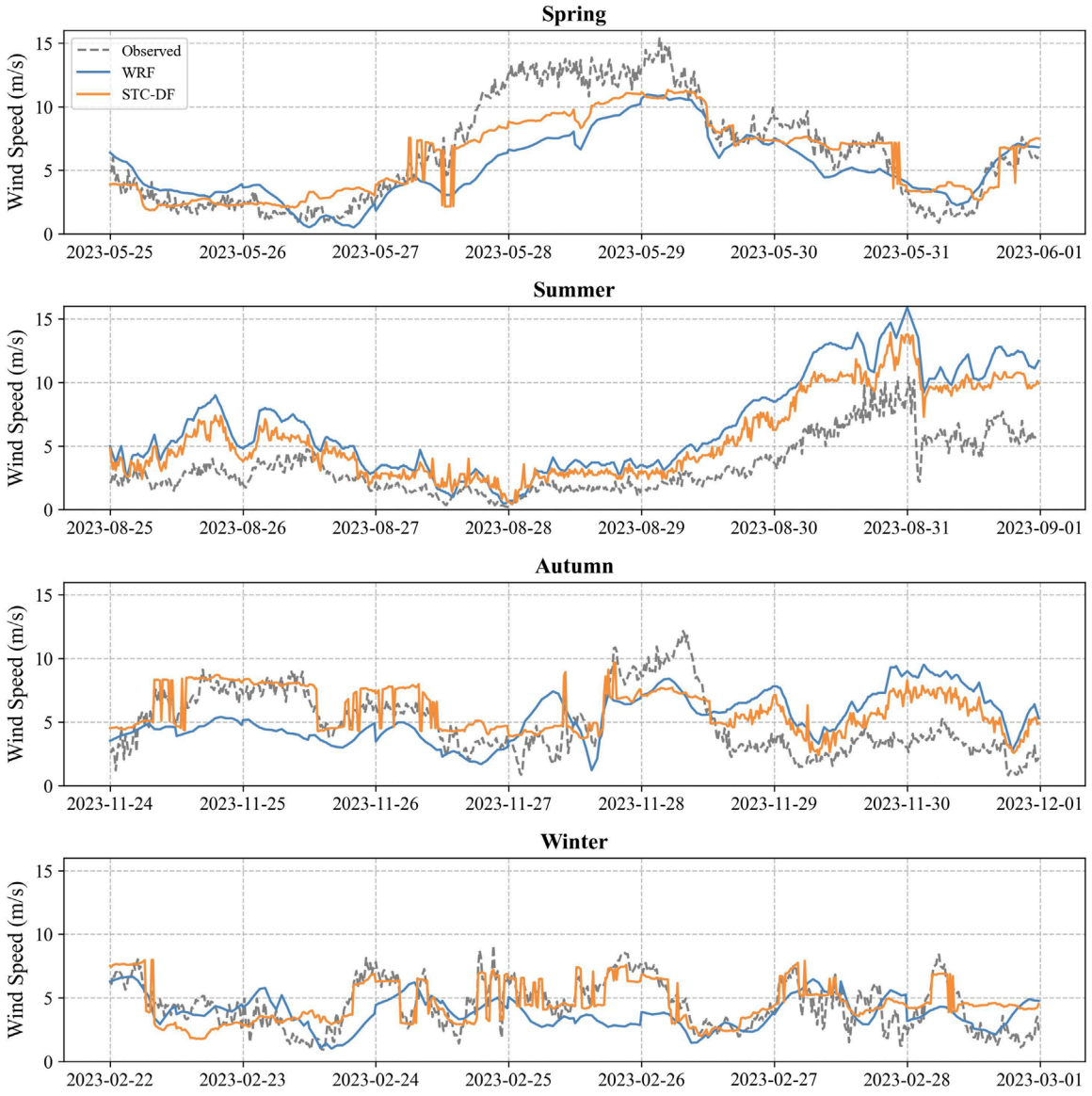

FIGURE 5
Comparison of observed wind speed, WRF forecast wind speed and STC-DF forecast wind speed time series in the seasonal sub-models.

input features of the next layer. Specifically, Deep Forest consists of the following steps:

Step1: gcForest employs a cascade structure to enable level-by-level processing, where each level of the cascade receives feature information processed by its predecessor level and outputs the results of its processing to the next level.

Step2: Each level is a collection of decision tree forests, i.e., a collection of sets, including different types of forests to encourage diversity. Each forest contains multiple trees, where the number of trees is a hyperparameter.

Step3: Each forest processes raw features to generate class vectors and augmented feature vectors, which are then used to train the forest in the next cascade. This process is implemented by multi-granularity scanning, where the original features are scanned using a sliding window to produce feature vectors of different sizes.

Step4: Each forest generates class vectors through k-fold cross-validation. During training, cross-validation is used to evaluate the performance of the entire cascade and terminate the training if necessary to prevent overfitting.

Step5: The number of classes in the cascade is automatically determined by estimating the performance of the entire cascade on the validation set, and the training process is terminated if there is no significant performance gain.

Unlike traditional integrated learning methods, Deep Forest is able to automatically learn the complex interactions between features without relying on manually designed feature engineering. In addition, the method has low computational complexity, is not easy to overfitting, and shows excellent classification performance

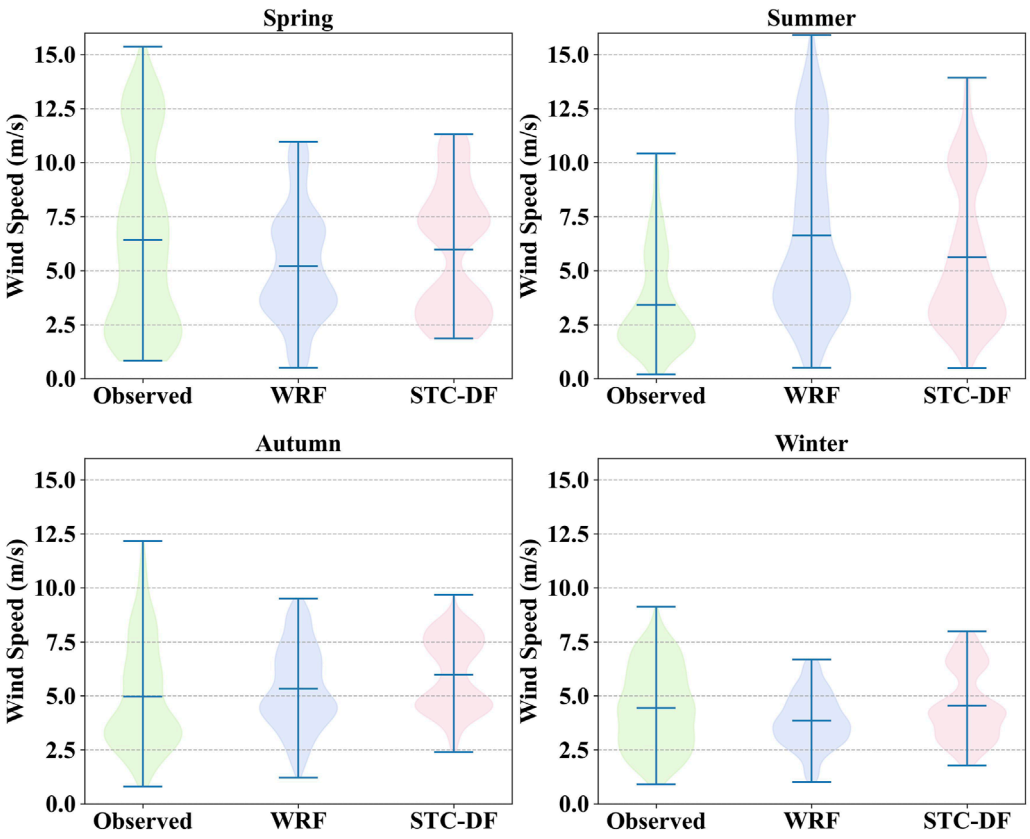

FIGURE 6
Distribution of wind speed in the seasonal sub-models.

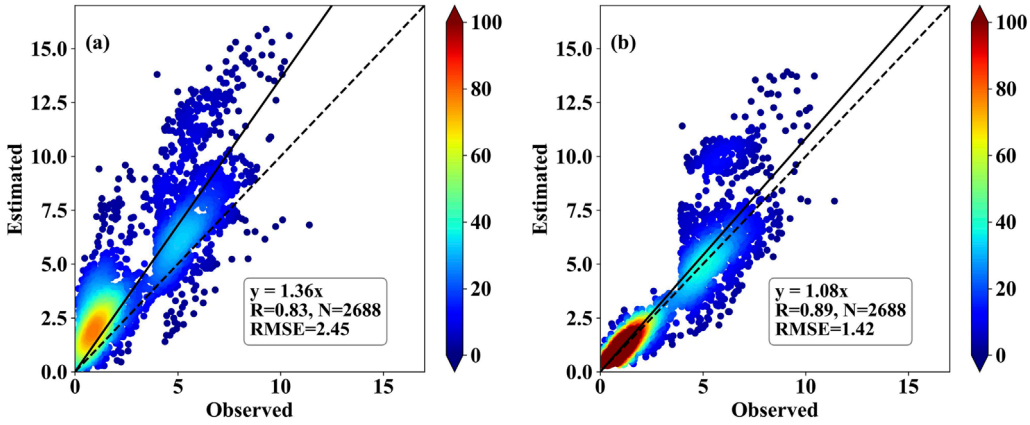

FIGURE 7
Regression scatter plot of predicted wind speed. **(A)** WRF model, **(B)** STC-DF model.

on multiple benchmark datasets. The structure of Deep Forest is shown in Figure 2.

2.2.3 Seasonal and temporal correlation - deep forest model

In order to better capture the relationship between seasonality, temporal correlation and meteorological factors in wind speed prediction problems, we propose to use STC-DF model to achieve better performance in wind speed prediction tasks. The model consists of the following main components:

(1) Seasonal sub-model: the year is divided into four seasons, and four sub-models are trained to capture the characteristics of wind speed changes in different seasons.

TABLE 2 The result of multi-model comparison test.

	RMSE (m/s)	rRMSE (%)	FA (%)	R
WRF	2.45	15.5	24	0.83
STC-DF	1.42	10.4	39	0.89
DF	2.17	14.6	29.1	0.68
RF	2.28	14.9	24.9	0.59
XGBoost	2.36	15.1	24.4	0.63
LightGBM	2.33	15	28.7	0.55
MLP	2.08	13.2	29.8	0.72
LSTM	1.76	11.9	31	0.84

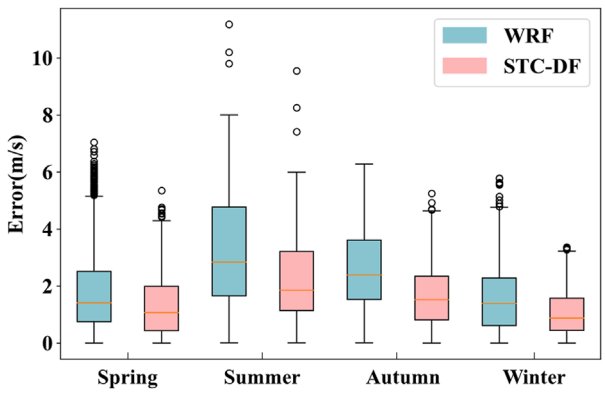

FIGURE 8
Boxplot distribution of errors for seasonal sub-models.

(2) Integration time-series features: In addition to the conventional features of temperature, humidity, pressure and other meteorological elements, the difference between the wind speed (WS_diff) at the previous moment and the current moment was also added to reflect the correlation in the time series.
(3) Deep forest model: The deep forest algorithm was used as the base model, and its powerful feature learning and non-linear modelling capabilities were used to predict wind speed.

The flowchart of the proposed hybrid model is given in Figure 3. The STC-DF model is carried out in the following three steps:

Step 1: Model training. Four sub-models were trained for different seasons. For each sub-model, the corresponding features were extracted and trained.
Step 2: Model predictions. Wind speed predictions were made by first identifying the season based on the current time and then using the appropriate sub-model to make the predictions. The predictions will reflect both seasonal and temporal correlations.
Step 3: Results evaluation. The accuracy of the model was evaluated by the wind speed evaluation index. In order to verify the validity as well as the generalizability of the model, multi-model comparison experiment and robustness experiment will be conducted for the model.

Through the integration of the above seasonal sub-models, time-series features and meteorological element features, the STC-DF Model is able to better learn the intrinsic law of wind speed change, and thus improve the accuracy and reliability of wind speed prediction.

2.2.4 Error analysis method

In order to evaluate the correction effect of the model, four error metrics, namely, Root Mean Square Errors (RMSE, Equation 1), Relative Root Mean Square Errors (rRMSE, Equation 2), Forecast Accuracy (FA, Equation 3) of wind speed, and Correlation Coefficient R (Equation 4), are chosen to measure the correction effect in this paper. The formulas for the error metrics are as follows:

$$RMSE = \sqrt{\frac{1}{n}\sum_{i-1}^{n}(\hat{y}_i - y_i)^2} \tag{1}$$

$$rRMSE = \frac{\sqrt{\frac{1}{n}\sum_{i=1}^{n}(y_i - \hat{y}_i)^2}}{\frac{i}{n}\sum_{i=1}^{n}y_i} \times 100\% \tag{2}$$

$$FA = \frac{N_r}{N_f} \times 100\% \tag{3}$$

$$R = \frac{\sum_{i=1}^{n}(x_i - \bar{x})(y_i - \bar{y})}{\sqrt{\sum_{i=1}^{n}(x_i - \bar{x})^2}\sqrt{\sum_{i=1}^{n}(y_i - \bar{y})^2}} \tag{4}$$

where $\hat{y}_i$ represents the i th predicted value, y_i denotes the i th observation, n is the total number of time samples, and $\bar{y}$ is the average of the observed values. Here, N_r stands for the number of samples with an absolute deviation of the wind speed forecast less than 1 m/s, while N_f is the number of samples forecasted.

3 Results and discussion

3.1 Result of seasonal sub-models

Four seasonal sub-models were developed using the above methodology to forecast corrected wind speeds for each of the four seasons of the offshore wind farm. The correlations between the variables of the test set in the seasonal sub-models are given in Figure 4, and the correlations between the observed wind speed and each of the variables are different for each season. Since DF possesses a natural anti overfitting property, i.e., it comes with a cross-validation process. It can achieve to a better result without any parameter tuning. There is a strong correlation between observed wind speed and WRF predicted wind speed in both spring and summer. Except in winter, the correlation between each variable and the observed wind speed is strong, and the positive and negative

values of the correlation will change significantly with the change of season. It can be seen that seasonal sub-model training for wind speed prediction correction is very necessary.

The forecast impact of the seasonal sub-models was assessed and compared with that of WRF (Table 1). The STC-DF model led to varying degrees of improvement in wind speed error correction across different seasons. The original WRF exhibited the largest and smallest prediction errors in summer and winter, respectively. The RMSE decreased by 30.74%, 30.24%, 32.99%, and 34.65% for the four seasons, all surpassing a 30% reduction. In autumn and winter, R showed the most significant increase, from 0.1 to 0.72 and from 0.28 to 0.72, respectively.

After counting the various error indicators of the seasonal sub-models, the prediction results are visualized. As shown in Figure 5 time series comparison chart, it can be intuitively seen that the seasonal sub-models improved the inaccuracy of WRF forecast wind speed in different degrees, making the corrected wind speed closer to the observed wind speed as a whole. Moreover, the models have the best correction effect in the middle of the wind speed, and the performance will be reduced when the wind speed is very high or very low. By observing the overall distribution of wind speed in the test set in the seasonal sub-models (Figure 6), it is not difficult to find that the wind speed forecast in summer is overall high, while the other three seasonal forecasts are overall low. Through the correction of the STC-DF model, the forecast deviation of the four seasons is reduced, and the quantiles are closer to the true values.

3.2 Result of STC-DF model

The corrected results of the seasonal sub-models were summarized to obtain the overall test set correction results. By comparing the regression scatter density plots of the forecast results from the WRF model and the STC-DF model (Figure 7), it can be seen that the forecast values of the STC-DF model are more convergent than those of the WRF model, with fewer outliers and a more concentrated distribution of data points. The forecast wind speed of the STC-DF model compared with that of the WRF model shows that the RMSE decreased from 2.45 m/s to 1.42 m/s, the rRMSE decreased from 15.5% to 10.4%. And the FA increased from 24% to 39%, R increased from 0.83 to 0.89. The error metric RMSE is reduced by 42.04%, which shows that the STC-DF model has considerable effect on wind speed correction.

3.3 Multi-model comparison test

In order to verify the effectiveness of the STC-DF model, we chose the DF, RF, XGBoost, LightGBM, MLP and LSTM algorithms for the wind speed data of the target wind farm to conduct a multi-model comparison test. The same data were chosen as the training set and test set in the experiment. The error values of the experimental results are given in Table 2. After comparison, the STC-DF model has lower RMSE and rRMSE, higher FA and R. The hybrid model proposed in this study can successfully reduce the errors brought by the WRF model and shows excellent performance.

3.4 Robustness experiment

In order to test the generality of the proposed method in this study, we applied the trained STC-DF model to an offshore wind farm in Guangdong Province for robustness experiment. Seven days of data are randomly selected from each season for the test, and the error distributions of the wind speed forecasted by the WRF model and those forecasted by the STC-DF model are shown in Figure 8. The method in this paper can effectively reduce the errors caused by WRF forecasts, and the outliers of predicted wind speed are reduced, with different degrees of improvement in each season. The RMSE of the sub-model forecast data in all seasons decreased from 2.78 m/s to 1.86 m/s, the FA increased from 25.4% to 42%, and the R increased from 0.57 to 0.8. The results fully demonstrate that the STC-DF model has strong generality, and it also has a better correction ability for wind speed of wind farm in different regions.

4 Conclusion and discussion

4.1 Conclusion

In order to solve the problem of feature extraction limitations and incomplete consideration of wind speed influence factors in wind speed correction methods, this study proposed a correction method based on deep forest algorithm integrating seasonal and temporal correlation. The proposed STC-DF model considered the seasonal difference and time correlation of wind speed, combined meteorological data and wind speed difference, and showed good performance in wind speed correction of offshore wind farms in Hainan Province and Guangdong Province. Compared with WRF data, the error index of the corrected wind speed reduced more than 40%, the accuracy of wind speed forecast increased 15%. In summary, the STC-DF model can effectively reduce the error caused by the WRF model forecast, improve the accuracy of the forecast, and contribute to the stable operation of the offshore wind farm, so as to improve the economic benefits of wind power.

4.2 Discussion

Through the robustness experiment, it is easy to see that the STC-DF model performed well for wind speed prediction in different offshore wind farms. However, due to the lack of data information of wind farms in different terrains, it is uncertain about the performance of the model in different terrain wind farms, such as mountain wind farms and plateau wind farms. In addition, since the wind farm data is only for 1 year, the time series input into the seasonal sub-model is not long enough, and the model still has room for improvement. The model is not effective in forecasting the extreme value of wind speed, and the amount of data input to the model will be increased in the future to get better prediction results. In the future research, stabilization models adapted to the characteristics of different wind farms or the number of hidden features to be mined according to different types of wind farms will also be considered.

Data availability statement

The datasets presented in this article are not readily available because The data that has been used is confidential. Requests to access the datasets should be directed to Weixiao Lu, luweixiao00@163.com.

Author contributions

HF: Data curation, Investigation, Writing–original draft. SL: Software, Writing–review and editing. JZ: Writing–review and editing, Validation. WL: Methodology, Visualization, Writing–original draft.

Funding

The author(s) declare that no financial support was received for the research, authorship, and/or publication of this article.

Conflict of interest

Authors HF, SL, and JZ were employed by Hainan Shenneng New energy Co., LTD.

The remaining author declares that the research was conducted in the absence of any commercial or financial relationships that could be construed as a potential conflict of interest.

Publisher's note

All claims expressed in this article are solely those of the authors and do not necessarily represent those of their affiliated organizations, or those of the publisher, the editors and the reviewers. Any product that may be evaluated in this article, or claim that may be made by its manufacturer, is not guaranteed or endorsed by the publisher.

References

Cassola, F., and Burlando, M. (2012). Wind speed and wind energy forecast through Kalman filtering of Numerical Weather Prediction model output. *Appl. energy* 99, 154–166. doi:10.1016/j.apenergy.2012.03.054

Chang, J., Peng, X., Fan, G., and Che, Y. (2015). Error calibration of numerical weather prediction with historical data. *Acta. Meteorologica. Sinica.* (2), 341–354. doi:10.11676/qxxb2015.021

Chen, C., Zhao, X., Bi, G., Xie, X., Gao, J., and Luo, Z. (2022). SSA-Res-GRU short-term wind speed prediction model based on multi-model decomposition. *Power Grid Technol.* 46 (08), 2975–2985. doi:10.13335/j.1000-3673.pst.2021.2510

Chen, F., and Dudhia, J. (2001). Coupling an advanced land surface–hydrology model with the Penn State–NCAR MM5 modeling system. Part I: model implementation and sensitivity. *Mon. weather Rev.* 129 (4), 569–585. doi:10.1175/1520-0493(2001)129<0569:caalsh>2.0.co;2

Chen, Y., and Lin, H. (2022). Overview of the development of offshore wind power generation in China. *Sustain. energy Technol. assessments* 53, 102766. doi:10.1016/j.seta.2022.102766

Díaz, H., and Soares, C. G. (2020). Review of the current status, technology and future trends of offshore wind farms. *Ocean. Eng.* 209, 107381. doi:10.1016/j.oceaneng.2020.107381

Grell, G. A., and Freitas, S. R. (2014). A scale and aerosol aware stochastic convective parameterization for weather and air quality modeling. *Atmos. Chem. Phys.* 14 (10), 5233–5250. doi:10.5194/acp-14-5233-2014

Hong, S. Y., Noh, Y., and Dudhia, J. (2006). A new vertical diffusion package with an explicit treatment of entrainment processes. *Mon. weather Rev.* 134 (9), 2318–2341. doi:10.1175/mwr3199.1

Hu, B. (2016). Experimental application of a probability method in predicting typhoon gusts on coastal islands. *Meteorological Sci. Technol.* 44 (02), 246–251. doi:10.19517/j.1671-6345.2016.02.013

Iacono, M. J., Delamere, J. S., Mlawer, E. J., Shephard, M. W., Clough, S. A., and Collins, W. D. (2008). Radiative forcing by long-lived greenhouse gases: calculations with the AER radiative transfer models. *J. Geophys. Res. Atmos.* 113 (D13). doi:10.1029/2008jd009944

Irena (2016). "Innovation outlook: off shore wind." Abu Dhabi: International Renewable Energy Agency.

Jiang, P., Liu, Z., Abedin, M. Z., Wang, J., Yang, W., and Dong, Q. (2024). Profit-driven weighted classifier with interpretable ability for customer churn prediction. *Omega* 125, 103034. doi:10.1016/j.omega.2024.103034

Jiang, Z., Che, J., He, M., and Yuan, F. (2023). A CGRU multi-step wind speed forecasting model based on multi-label specific XGBoost feature selection and secondary decomposition. *Renew. Energy* 203, 802–827. doi:10.1016/j.renene.2022.12.124

Landberg, L. (1999). Short-term prediction of the power production from wind farms. *J. wind Eng. industrial Aerodynamics* 80 (1-2), 207–220. doi:10.1016/s0167-6105(98)00192-5

Linacre, E. (1992). Climate data and resources: a reference and guide.

Liu, H., Tian, H. Q., Liang, X. F., and Li, Y. F. (2015). Wind speed forecasting approach using secondary decomposition algorithm and Elman neural networks. *Appl. Energy* 157, 183–194. doi:10.1016/j.apenergy.2015.08.014

Liu, M. D., Ding, L., and Bai, Y. L. (2021b). Application of hybrid model based on empirical mode decomposition, novel recurrent neural networks and the ARIMA to wind speed prediction. *Energy Convers. Manag.* 233, 113917. doi:10.1016/j.enconman.2021.113917

Liu, X., Lin, Z., and Feng, Z. (2021a). Short-term offshore wind speed forecast by seasonal ARIMA-A comparison against GRU and LSTM. *Energy* 227, 120492. doi:10.1016/j.energy.2021.120492

Liu, Z., De Bock, K. W., and Zhang, L. (2024a). Explainable profit-driven hotel booking cancellation prediction based on heterogeneous stacking-based ensemble classification. *Eur. J. Operational Res.* doi:10.1016/j.ejor.2024.08.026

Liu, Z., Jiang, P., Wang, J., Du, Z., Niu, X., and Zhang, L. (2023). Hospitality order cancellation prediction from a profit-driven perspective. *Int. J. Contemp. Hosp. Manag.* 35 (6), 2084–2112. doi:10.1108/IJCHM-06-2022-0737

Liu, Z., Jiang, P., Zhang, L., and Niu, X. (2020). A combined forecasting model for time series: application to short-term wind speed forecasting. *Appl. Energy* 259, 114137. doi:10.1016/j.apenergy.2019.114137

Liu, Z., Zhang, Y., Abedin, M. Z., Wang, J., Yang, H., Gao, Y., et al. (2024b). Profit-driven fusion framework based on bagging and boosting classifiers for potential purchaser prediction. *J. Retail. Consumer Serv.* 79, 103854. doi:10.1016/j.jretconser.2024.103854

Mao, Y., Geng, J., and Chen, L. (2022). Parallel deep forest algorithm improved by combining information theory. *Comput. Eng. Appl.* 58 (07), 106–115. doi:10.3778/j.issn.1002-8331.2103-0019

Mao, Y., and Li, W. (2024). Parallel deep forest algorithm based on mutual information and fusion weighting. *Comput. Appl. Res.* 41 (02), 473–481. doi:10.19734/j.issn.1001-3695.2023.05.0240

Papaefthymiou, G., and Klockl, B. (2008). MCMC for wind power simulation. *IEEE Trans. energy Convers.* 23 (1), 234–240. doi:10.1109/tec.2007.914174

Pereyra-castro, K., and Caetano, E. (2022). Wind-ramp predictability. *Atmosphere* 13 (3), 453. doi:10.3390/atmos13030453

Prósper, M. A., Otero-Casal, C., Fernández, F. C., and Miguez-Macho, G. (2019). Wind power forecasting for a real onshore wind farm on complex terrain using WRF high resolution simulations. *Renew. energy* 135, 674–686. doi:10.1016/j.renene.2018.12.047

Qian, Z., Pei, Y., Cao, L., Wang, J., and Jing, B. (2016). Review of wind power forecasting method. *High. Volt. Eng.* 42 (04), 1047–1060. doi:10.13336/j.1003-6520.hve.20160405021

Salcedo-Sanz, S., Pérez-Bellido, Á. M., Ortiz-García, E. G., Portilla-Figueras, A., Prieto, L., and Paredes, D. (2009). Hybridizing the fifth generation mesoscale model

with artificial neural networks for short-term wind speed prediction. *Renew. Energy* 34 (6), 1451–1457. doi:10.1016/j.renene.2008.10.017

Soares-Ramos, E. P., de Oliveira-Assis, L., Sarrias-Mena, R., and Fernández-Ramírez, L. M. (2020). Current status and future trends of offshore wind power in Europe. *Energy* 202, 117787. doi:10.1016/j.energy.2020.117787

Wang, Y., Wang, J., Wei, X., and Hurtado-Pérez, E. (2021). A cascade hybrid PSO feed-forward neural network model of a biomass gasification plant for covering the energy demand in an AC microgrid. *Energy Convers. Manag.* 232, 113896. doi:10.1016/j.enconman.2021.113896

Xiong, X., Zou, R., Sheng, T., Zeng, W., and Ye, X. (2023). An ultra-short-term wind speed correction method based on the fluctuation characteristics of wind speed. *Energy* 283, 129012. doi:10.1016/j.energy.2023.129012

Yang, X., Xiao, Y., and Chen, S. (2005). Wind speed and generated power forecasting in wind farm. *Proceedings-Chinese Soc. Electr. Eng.* 25 (11), 1. doi:10.1360/biodiv.050028

Yin, L., Sun, Z., Gao, F., and Liu, H. (2020). Deep forest regression for short-term load forecasting of power systems. *IEEE Access* 8, 49090–49099. doi:10.1109/access.2020.2979686

Yu, R., Gao, J., Yu, M., Lu, W., Xu, T., Zhao, M., et al. (2019). LSTM-EFG for wind power forecasting based on sequential correlation features. *Future Gener. Comput. Syst.* 93, 33–42. doi:10.1016/j.future.2018.09.054

Zeng, C., Ye, L., and Zhao, Y. (2012). Spatial model for short term wind power prediction considering wake effects. *Power Syst. Prot. Control* 40 (24), 59–142.

Zhang, C., Luo, L., Yang, Z., Du, B., Zhou, Z., Wu, J., et al. (2024). Flexible method for estimating the state of health of lithium-ion batteries using partial charging segments. *Energy* 295, 131009. doi:10.1016/j.energy.2024.131009

Zhang, C., Zhao, S., Yang, Z., and He, Y. (2023). A multi-fault diagnosis method for lithium-ion battery pack using curvilinear Manhattan distance evaluation and voltage difference analysis. *J. Energy Storage* 67, 107575. doi:10.1016/j.est.2023.107575

Zhang, J., and Liu, Z. (2022). Ultra short term wind speed interval prediction based on a hybrid model. *Power Syst. Prot. Control* 50 (22), 49–58. doi:10.19783/j.cnki.pspc.220241

Zhang, J., and Wang, H. (2022). Development of offshore wind power and foundation technology for offshore wind turbines in China. *Ocean. Eng.* 266, 113256. doi:10.1016/j.oceaneng.2022.113256

Zhang, Y., Guo, Z., Lin, Y., and Chi, D. (2013). Predictive capacity of mesoscale model for short-range wind speed forecasting at wind power farm. *Chin. J. Atmos. Sci.* 37 (04), 955–962. doi:10.3878/j.issn.1006-9895.2012.12092

Zhang, Y., Li, Y., and Zhang, G. (2020). Short-term wind power forecasting approach based on Seq2Seq model using NWP data. *Energy* 213, 118371. doi:10.1016/j.energy.2020.118371

Zhao, J., Guo, Y., Xiao, X., Wang, J., Chi, D., and Guo, Z. (2017). Multi-step wind speed and power forecasts based on a WRF simulation and an optimized association method. *Appl. energy* 197, 183–202. doi:10.1016/j.apenergy.2017.04.017

Zheng, Z. W., Chen, Y. Y., Huo, M. M., and Zhao, B. (2011). An overview: the development of prediction technology of wind and photovoltaic power generation. *Energy Procedia* 12, 601–608. doi:10.1016/j.egypro.2011.10.081

Zhou, S., Gao, Y., Duan, Z., Xi, X., and Li, Y. (2023). A robust error correction method for numerical weather prediction wind speed based on Bayesian optimization, Variational Mode Decomposition, Principal Component Analysis, and Random Forest: VMD-PCA-RF. *EGUsphere* 2023, 1–37. doi:10.5194/egusphere-2023-945

Zhou, Z. H., and Feng, J. (2019). Deep forest. *Natl. Sci. Rev.* 6 (1), 74–86. doi:10.1093/nsr/nwy108

Frontiers in
Energy Research

Advances and innovation in sustainable, reliable and affordable energy

Explores sustainable and environmental developments in energy. It focuses on technological advances supporting Sustainable Development Goal 7: access to affordable, reliable, sustainable and modern energy for all.

Discover the latest Research Topics

See more →

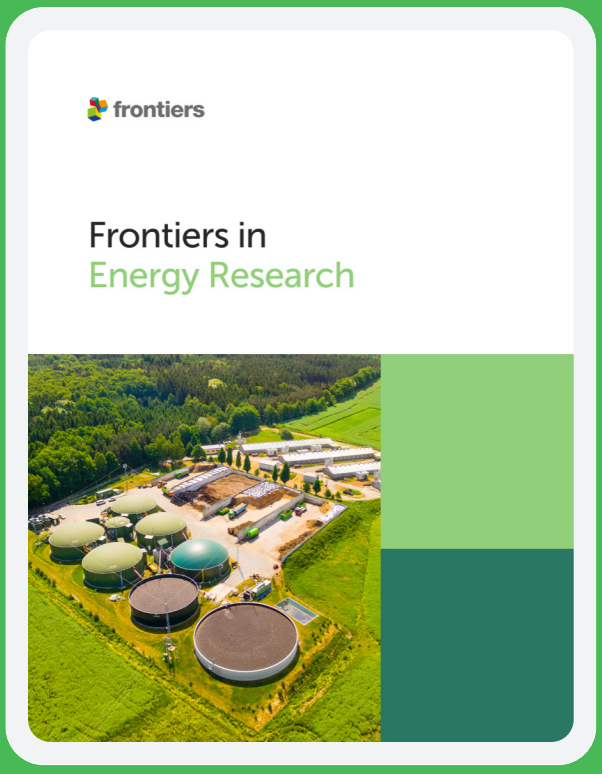

Frontiers

Avenue du Tribunal-Fédéral 34
1005 Lausanne, Switzerland
frontiersin.org

Contact us

+41 (0)21 510 17 00
frontiersin.org/about/contact